

# ON GASEOUS MICROFLOWS UNDER ISOTHERMAL CONDITIONS

Vom Fachbereich Produktionstechnik  
der  
UNIVERSITÄT BREMEN

zur Erlangung des Grades  
Doktor-Ingenieur  
genehmigte

Dissertation

von

Dipl.-Ing. Thomas Veltzke

Gutachter: Prof. Dr.-Ing. Jorg Thöming  
Prof. Dr.-Ing. Michael Schlüter  
(Technische Universität Hamburg-Harburg)

Tag der mündlichen Prüfung: 13. März 2013



# DECLARATION/ERKLÄRUNG

I herewith declare that I have produced this thesis without the prohibited assistance of third parties and without making use of aids other than those specified; notions taken over directly or indirectly from other sources have been identified as such. This work has not previously been presented in identical or similar form to any other German or foreign examination board.

Ich erkläre hiermit an Eides statt, dass ich die vorliegende Dissertationsschrift selbständig und ohne unerlaubte Hilfe angefertigt habe, andere als die angegebenen Quellen und Hilfsmittel nicht benutzt und die den benutzten Quellen wörtlich oder inhaltlich entnommenen Stellen als solche kenntlich gemacht habe. Weiterhin versichere ich, dass die Arbeit in gleicher oder ähnlicher Form noch keiner Prüfungsbehörde vorgelegt wurde.

---

Bremen, March 14, 2013

The PhD work was conducted from January 1, 2010 to November 25, 2012, under the supervision of Prof. Dr.-Ing. Jorg Thöming at the University of Bremen.



# ZUSAMMENFASSUNG

Strömungsprozesse von Gasen, und davon abhängige Wärme- und Stofftransportvorgänge in kleinsten Kanälen oder porösen Strukturen, sind für viele technische Anwendungen in diversen Ingenieurdisziplinen relevant. Diese so genannten Mikroströmungen treten zum Beispiel in geometrisch definierten Mikrokanälen von mikro- und nanoelektromechanischen Systemen (MEMS/NEMS) oder in hochporösen Katalysatorstrukturen auf, wobei das Strömungsverhalten unter anderem den Wärmeübergang und den Umsatz von Gasphasenreaktionen maßgeblich beeinflusst.

In Mikroströmungen befindet sich das strömende Gas in einem Zustand, der als *verdünnt* (engl. *rarefied*) bezeichnet wird. Dies ist der Fall, wenn der Abstand der Fließbegrenzung (z.B. Porendurchmesser) in der Größenordnung der mittleren freien Weglänge  $\lambda$  des Gases liegt. Das Verhältnis von  $\lambda$  zu einer charakteristischen Länge  $\ell$  wird als Knudsenzahl  $Kn$  bezeichnet welche reziprok proportional zu  $\ell$  und dem Druck des Gases ist. Somit können auch Gase in größeren Objekten verdünnt sein, wenn der Druck sehr gering ist. Dies ist beispielsweise in der Vakuumtechnik oder der Raumfahrt der Fall.

Abhängig von der dimensionslos quantifizierten Verdünnung zeigt sich, dass die kontinuumsmechanische Behandlung von Strömungen in und um sehr kleine Geometrien in vielen Fällen nicht möglich ist. Verdünnte Strömungen verhalten sich gänzlich anders als Kontinuumsströmungen. Somit kann die Forschung an Mikroströmungen zum Erkenntnisgewinn und generellen Verständnis von verdünnten Gasströmungen beitragen.

Kern dieser Arbeit ist die Modellierung von Gasströmungen in Mikrokanälen mit gleichbleibendem und sich über die Kanallänge veränderndem Querschnitt. Ein Mikrokanal ist als einfachste denkbare Geometrie eines verdünnten Strömungsvorgangs sowohl Teil von MEMS als auch ein Modell für komplexere Strukturen. Wenn die Physik der Strömung in Mikrokanälen durch ein Modell korrekt wiedergegeben werden kann, trägt dies zum generellen, phänomenologischen Verständnis von Strömungsprozessen bei. Eine mathematische Formulierung, welche die prediktive, nichtempirische Bestimmung von integralen Strömungsparametern (z.B. Druckverlust oder Massenflussrate) erlaubt, ist somit nicht nur ein nützliches Werkzeug zur Auslegung von Bauteilen in MEMS/NEMS, sondern erlaubt auch den Gewinn neuer, grundlegender Erkenntnisse.

Konsequenterweise ist die Zusammenstellung und Analyse existierender Modellierungsansätze für verdünnte Gasströmungen grundlegender Bestandteil der vorliegenden Arbeit. Es werden generelle Schwächen von Transportmodellen aufgezeigt, die dem aktuellen Stand der Forschung entsprechen. Die analysierten Unzulänglichkeiten existierender Modelle stellen gleichwohl die Motivation zur Entwicklung eines alternativen Ansatzes dar.

Im Rahmen dieser Doktorarbeit ist ein Transportmodell entwickelt worden, welches auf der Superposition von Stofftransportmechanismen beruht und unabhängig vom Verdünnungsgrad gültig ist. Dieses Modell wird anhand einer eingangs aufgestellten Hypothese über die

verdünnte Strömung durch Kanäle mit leicht veränderlichem Querschnitt entwickelt. Das mathematische, auf der entwickelten Hypothese beruhende Modell wird auf zweifache Weise evaluiert. Zunächst erfolgt der Vergleich integraler Messgrößen aus der Literatur mit den analytisch und prediktiv berechneten Werten, wobei eine erstaunliche Übereinstimmung von Messdaten und Modellierung auftritt.

Darüber hinaus sind eigene Messungen an Kanälen mit veränderlichem Querschnitt durchgeführt worden. Die Beschreibung der hergestellten Mikrostrukturen und des Messaufbaus ist ein weiterer zentraler Aspekt in der vorliegenden Dissertation. Auch für Messgrößen von Strömungen in diesen asymmetrischen Kanälen ist die Vorhersage durch das Modell sehr akkurat, was aufgrund der Einfachheit der mathematischen Formulierung überrascht.

Ein weiterer Aspekt der Arbeit widmet sich dem Einfluss der Oberflächenchemie auf das Verhalten von Mikroströmungen. Die Analyse des entwickelten Modells zeigt für hohe Verdünnungsgrade von Gasen, dass die Oberflächendiffusion einen signifikanten Beitrag am Gesamtstofftransport aufweist. Anhand des entwickelten Gesamtmodells können Daten für die Langmuir-Adsorption von Gasen an Oberflächen aus Mikrokanalversuchen abgeleitet werden. Diese Möglichkeit könnte die Entwicklung eines neuartigen Adsorptionsmessverfahren ermöglichen. Da Oberflächendiffusion grundlegend von der Wechselwirkungsstärke der Gasmoleküle mit der Kanalwand abhängt, wird die Möglichkeit der Oberflächenfunktionalisierung auf das Verhalten von Mikroströmungen theoretisch analysiert und experimentell bestätigt. Es kann prinzipiell gezeigt werden, dass eine Silanisierung von geätzten Siliziumkanälen einen signifikant messbaren Einfluss auf die Gaspermeabilität hat, wenn die Verdünnung ausreichend hoch ist.

# ABSTRACT

Flow processes of gases and related heat and mass transfer properties in smallest channels or porous structures are of utmost interest for many technical application in engineering science. This so-called *microflows* occur for instance in geometrically defined microchannels which are parts of Micro/Nano Electro Mechanical Systems (MEMS/NEMS) or in porous catalysts or filters. In such applications the heat transfer or the yield in gas phase reactions is crucially dependent on the flow behavior.

In microflows the fluid gas phase is in a state called *rarefied*, when the distance of solid boundaries (e.g. pore diameter) is on the same order of magnitude as the gaseous mean free path  $\lambda$ . The ratio of  $\lambda$  to a characteristic length  $\ell$  is defined as the Knudsen number which is reciprocally proportional to  $\ell$  and the pressure of the bulk gas. Hence, also gases in larger structures can be rarefied if the pressure is sufficiently low. For instance in vacuum applications or high altitude aerodynamics gaseous rarefaction has to be taken into account.

Depending on the dimensionless quantified rarefaction it is commonly known that continuum fluid dynamics fail for modeling gas flows in (and around) very small geometries. Rarefied flows behave totally different as continuum flows. Hence research on gaseous microflows can contribute to the general understanding of rarefaction effects.

Central aspect of the current thesis is the modeling of integral quantities of gaseous flows in micro structures with uniform and alongside varying cross section. A microchannel is the simplest geometry in which rarefaction effects can be observed and can as well be considered as a model for more complex geometries. A mathematical model which allows for the predictive and non-empirical calculation of integral flow properties (e.g. pressure loss or mass flow rate) is not only a useful tool for design of MEMS/NEMS devices, but also bears the chance of gaining new, basic insights.

Consequently, a basic aspect of the current work is the review and analysis of existing approaches in modeling gas microflows. General weaknesses of commonly used transport models are revealed and critically discussed. This analysis simultaneously represents the motivation for development of an alternative approach.

In the framework of this PhD thesis a transport model is developed which is based on the superposition of transport mechanisms and is unrestrictively valid over the whole range of rarefaction. The model is developed by means of a raised hypothesis on a rarefied flow in a slightly tapered duct. The derived mathematical formulation is twofold evaluated. First, comparison is carried out of measured values found in literature to analytically and predictively calculated curves, where a strikingly good accordance of data and model is found. Further, own measurements on microchannels with slightly varying cross section are performed. The presentation of manufactured microstructures and the experimental set-up is another central aspect of the current thesis. Even for measured values on these asymmetric ducts, the prediction of the model is thoroughly accurate which does surprise due to the simplicity of the mathematical formulation.

Furthermore the influence of surface chemistry on microflows is investigated in this work. Analysis of the derived model shows that for increasing rarefaction surface diffusion gains significant contribution to the entire flow rate. By means of the complete model data for Langmuir adsorption of gases on surfaces can be derived. This finding may contribute to the development of a novel measuring technique for gas adsorption on low-surface materials under ambient conditions.

Since surface diffusion is crucially dependent on the interaction strength of gas molecules to the solid surface, the possibility of surface functionalization for affecting the properties of gaseous microflows is theoretically analyzed and experimentally confirmed. In principle, it can be shown that a silanization of etched silicon channels causes a significantly measurable effect on the gas permeability when rarefaction is sufficiently high.

# ACKNOWLEDGEMENTS

I am heartily thankful to my supervisors, Prof. Jorg Thöming and Dr. Michael Baune, whose encouragement, supervision and support from the preliminary to the concluding level enabled me to work on this topic autonomously and to finish my PhD work in concise time.

This thesis would not have been possible without the infrastructure of the University of Bremen and the Center for Environmental Research and Sustainable Technology (UFT). My work was funded by German Research Foundation (DFG) within the Graduate College 1375 "Non-metallic Porous Structures for Physical-Chemical Functions". Substitutional for the Graduate College I would like to show my gratitude to Prof. Georg Grathwohl, Dr. Michaela Wilhelm, and Janet Heienbrock.

I am grateful to all my colleagues, but especially to George Okoth, Mirko Weinhold, and Jürgen Ulpts for the neat collaboration. Further I would like to thank the students I have supervised during my work: Carlos Eduardo Santana de Souza, Karen Vielhaus, Alexander Franz, Philipp Vogler, Natalia Herzog, Jens Reinhold, Helen Niemeyer, Philipp Ciaciuch, Dimitri Dargel, Florian Meierhofer, Hendrik Zachariassen, and Holger Stumpf.

I would like to thank Prof. Lucio Colombi Ciacchi who contributed valuable suggestions and insight and Prof. Alan Chaffee for the invitation to Melbourne.

Lastly, I offer my regards to all of those who supported me in any respect during the completion of the project: First of all my former girl friend (now my wife) Wiebke, my parents and sister, and all friends.



# CONTENTS

List of Figures	xi
List of Tables	xiii
List of own publications	xv
List of supervised student work	xvii
Glossary	xix
1 Introduction	1
1.1 Rarefied gas flows . . . . .	2
1.2 Hypothesis and thesis aim . . . . .	4
1.3 Thesis structure . . . . .	6
2 Experimental research on isothermal gas microflows	7
2.1 An overview . . . . .	7
2.2 Measuring gaseous microflows - A brief review . . . . .	9
2.3 Rarefaction effects observed in experiments . . . . .	12
3 Background theory and mathematical modeling	17
3.1 Governing equations . . . . .	17
3.1.1 Boltzmann equation . . . . .	18
3.1.2 Navier-Stokes equations . . . . .	19
3.2 Modeling gaseous microflows - A brief review . . . . .	23
3.3 Approach of tangential momentum accommodation . . . . .	25
3.3.1 Poiseuille flow with Maxwellian boundary condition . . . . .	26
3.3.2 Temperature influence on the TMAC . . . . .	27
3.3.3 Influence of surface topology . . . . .	28
3.3.4 Further inconsistencies of the Maxwellian approach . . . . .	30
3.4 The CDS model of superimposed flows . . . . .	31
3.4.1 Convection . . . . .	31
3.4.2 Molecular spatial diffusion . . . . .	33
3.4.3 Convection and free molecular flow in slightly tapered channels . . . . .	35
3.4.4 Diodicity effect in slightly tapered ducts . . . . .	39
3.4.5 Surface diffusion . . . . .	41
3.4.6 Maxwell-Stefan approach for modeling surface diffusion . . . . .	42
3.4.7 Superposition of mass flow contributions . . . . .	44
3.5 Theoretical opportunities of functionalization of the microchannel surface . . . . .	45
3.5.1 Hypothetic effect of surface chemistry on flow behaviour . . . . .	46

---

3.5.2	Approach and selection of possible functionalization agents . . . . .	48
4	Validation of the CDS model by literature data	51
4.1	Slip flow and beginning transition regime . . . . .	52
4.2	Free molecular regime . . . . .	56
4.3	Discussion of findings . . . . .	58
5	Experimental section	63
5.1	Microchannel production . . . . .	63
5.1.1	Micromilled aluminum channels . . . . .	64
5.1.2	Etched silicon channels . . . . .	65
5.2	Mass flow measurement . . . . .	66
5.2.1	Experimental set-up . . . . .	67
5.2.2	Data acquisition . . . . .	68
5.2.3	Continuous test procedure . . . . .	70
5.2.4	Twofold evaluation of set-up and test procedure . . . . .	71
5.2.5	Analysis of distribution of measurements and random errors . . . . .	74
5.3	Surface functionalization . . . . .	76
5.3.1	Apparatus for silanization reaction . . . . .	76
5.3.2	Procedure of functionalization . . . . .	77
5.3.3	Verification of altered surface chemistry . . . . .	77
6	Theoretical evaluation of experimental findings	79
6.1	Pressure driven gas flow in slightly tapered ducts . . . . .	79
6.2	Rarefaction dependency of the gas diode effect . . . . .	82
6.3	Influence of functionalization on gaseous mass flow . . . . .	84
7	Conclusions	87
7.1	Impact upon modeling gaseous microflows . . . . .	89
7.2	Outlook on future work . . . . .	89
	Bibliography	91
	Appendix A	103
	Appendix B	129

# LIST OF FIGURES

1.1	Rarefied gas flows in technical applications . . . . .	2
1.2	Characteristic length scales of typical microfluidic components . . . . .	3
1.3	The gas flow diode effect as a function of gaseous rarefaction . . . . .	5
2.1	Operation principle of calorimetric mass flow sensors/controllers . . . . .	10
2.2	Measuring ranges of MFS used in experiments on gaseous microflows . . . . .	11
2.3	Effects of moderately rarefied gas flows in straight microchannels . . . . .	14
2.4	Reduced mass flow rate $G$ versus rarefaction in terms of $\text{Kn}_m$ . . . . .	14
3.1	Gas flow models and their practical usability limited to rarefaction . . . . .	24
3.2	Schematic of tube Poiseuille flow with slip/no-slip boundary conditions . . . . .	25
3.3	Variation of the TMAC with temperature . . . . .	28
3.4	Variation of the TMAC for different values of surface roughness . . . . .	29
3.5	Comparison of TMAC for first and second order Maxwellian approach . . . . .	30
3.6	Schematic of a rectangular channel with alongside varying cross section . . . . .	35
3.7	Theoretical limitations of the diodicity in slightly tapered ducts . . . . .	40
3.8	Qualitative Langmuir adsorption isotherm . . . . .	42
3.9	Qualitative contribution of transport mechanism to the total flow rate . . . . .	43
3.10	Hydroxylated silicon surface obtained by MD simulations . . . . .	47
3.11	Silanization reaction of a hydroxylated silicon surface . . . . .	48
4.1	Experimentally obtained Reynolds number versus pressure ratio . . . . .	53
4.2	Dimensionless mass flow rate as a function of the rarefaction . . . . .	54
4.3	Diffusive proportion of mass flow in tubes as a function of the rarefaction . . . . .	55
4.4	Diffusive proportion of gaseous microflows in rectangular channels . . . . .	56
4.5	Reduced mass flow rate $G$ over a wide range of rarefaction . . . . .	57
4.6	Segregation of mass transport mechanism . . . . .	59
5.1	Microchannels produced by micromilling in aluminum . . . . .	64
5.2	Tapered microchannels produced by deep reactive-ion etching . . . . .	65
5.3	Sectional drawing of the experimental apparatus . . . . .	66
5.4	Assembling of a channel system into the fixture . . . . .	67
5.5	Interface of hardware and software of the experimental set-up . . . . .	68
5.6	Exemplary analysis of data obtained using the continuous method . . . . .	70
5.7	Estimation of $V_i$ and constant volume method for mass flow measurement . . . . .	72
5.8	Twofold validation of the continuous test procedure . . . . .	73
5.9	Statistical distribution of mass flow data . . . . .	75
5.10	Set-up for silanization of the microchannel surface . . . . .	76
5.11	Verification of silanization procedure. . . . .	78

6.1	Reduced molar flow rate in one channel versus mean Knudsen number . . . .	80
6.2	Influence of direction of perfusion on mass flow rate in asymmetric ducts . . .	81
6.3	Experimental and modeled diodicity versus mean Knudsen number . . . . .	83
6.4	Experimentally observed influence of surface chemistry on gas microflow . . .	85
A.1	Photos of experimental the set-up . . . . .	103

# LIST OF TABLES

2.1	Overview on experimental work on gas flows in long microducts . . . . .	8
2.2	Qualitative comparison of reviewed mass flow measuring techniques . . . . .	13
3.1	Moments of an ideal gas derived from velocity distribution function . . . . .	20
3.2	Experimental TMACs derived by microduct experiments . . . . .	29
3.3	Dimensions of examined microchannels . . . . .	39
4.1	Geometrical properties and experimental conditions in gas flow experiments .	51
4.2	Properties of gases used in cited literature . . . . .	52
4.3	Duct geometry and material, and experimental conditions . . . . .	57
4.4	Geometric properties of ducts used in mass flow experiments in literature . .	58
4.5	Adapted adsorption parameters for regression of model to experimental data	60
5.1	Dimensions of examined microchannels . . . . .	63
5.2	Technical specification of all instruments used in gas flow experiments . . . .	67
5.3	Properties of gases used in gas flow experiments . . . . .	74
5.4	Experimental data for performing the Anderson-Darling test . . . . .	75
B.1	Experimental results obtained on uniform channel <i>RC20</i> . . . . .	129
B.2	Experimental results obtained on micromilled tapered duct <i>Al-3</i> . . . . .	130
B.3	Experimental results obtained on etched tapered duct system <i>Si-5</i> . . . . .	130
B.4	Experimental results obtained on etched tapered duct system <i>Si-7</i> . . . . .	131
B.5	Experimental results obtained on etched tapered duct system <i>Si-9</i> . . . . .	132
B.6	Experimental results obtained on silanized tapered duct system <i>Si-9</i> . . . . .	136



# LIST OF OWN PUBLICATIONS

## Scientific articles

T. Veltzke & J. Thöming (2012) An analytically predictive model for moderately rarefied gas flow. *J. Fluid Mech.*, **698** 406–422

T. Veltzke, M. Baune & J. Thöming (2012) The contribution of diffusion to gas microflow: An experimental study. *Phys. Fluids*, **24** 082004

T. Veltzke, M. Baune & J. Thöming (2012) The contribution of surface diffusion to mass flow rate in microscale ducts. *MicroFlu12, 3<sup>rd</sup> European conference on Microfluidics, Heidelberg, 3-5 December 2012, SHF ed. ISSN 2108-4718*

## Conferences

T. Veltzke & J. Thöming. The contribution of diffusion to gas micro flow. *1<sup>st</sup> European Conference on Gas Micro Flows, 6-8 June 2012, Skiathos Island, Greece* (oral presentation)

T. Veltzke, M. Baune & J. Thöming. The contribution of surface diffusion to mass flow rate in microscale ducts. *3<sup>rd</sup> European Conference on Microfluidics, 3-5 December 2012, Heidelberg, Germany* (poster & oral presentation)



# LIST OF SUPERVISED STUDENT WORK

- N. Herzog & P. Vogler. Funktionalisierung von Membranen mit konischen Makroporen zur Steigerung der Selektivität von  $N_2$  zu  $CO_2$ . Bachelor's Thesis, April 2010 to September 2010.
- K. Vielhaus & A. Franz. Vergleich von Membranen mit konischen Makroporen zu konventionellen Membranen im Hinblick auf die  $N_2/CO_2$ -Trennung. Bachelor's Thesis, April 2010 to September 2010.
- J. Reinhold. Molekülstreuung an Oberflächen: Qualitative Untersuchungen durch Experimente und molekulardynamische Simulation. Bachelor's Thesis, October 2010 to December 2010.
- H. Niemeyer. Untersuchung des Einflusses von Gas-Wand Wechselwirkungen auf den Massenfluss in Mikrokanälen. Diploma Thesis, December 2010 to March 2011.
- P. Ciaciuch, D. Dargel & F. Meierhofer. Development of a novel membrane technology for gas separation in industrial processes. Master's project, December 2010 to March 2011.
- H. Zachariassen. Aufbau der Gasanalytik zur Bestimmung realer Trennfaktoren von Membranen mit langen asymmetrischen Poren. Bachelor's Thesis, June 2011 to September 2011.
- H. Stumpf. Untersuchung der Abhängigkeit des Verhältnisses von Eintritts- und Austrittsquerschnitt rechteckiger Mikrokanäle auf die Stofftransportmechanismen verdünnter Gase. Master's Thesis, December 2011 to June 2012.
- J. Reinhold. Molecular dynamics simulations on surface scattering of gases on functionalised surfaces. Master's project, January 2012 to April 2012.



# GLOSSARY

Symbol	Description/Value	Unit
<i>Roman</i>		
$a$	Adsorption site spacing, Eq. (3.76)	m
$A$	Cross-sectional area	m <sup>2</sup>
$B_1$	First RTD constant, $B_1 = 3.9083 \times 10^{-3}$	°C <sup>-1</sup>
$B_2$	Second RTD constant, $B_2 = -5.775 \times 10^{-7}$	°C <sup>-2</sup>
$c$	Absolute molecular velocity, $c = \zeta + u$	m s <sup>-1</sup>
$\bar{c}$	Most probable molecular velocity, $\bar{c} = \sqrt{2\mathfrak{R}T}$	m s <sup>-1</sup>
$c_p$	Heat capacity at constant pressure, $c_p = \mathfrak{R} + c_v$	J kg <sup>-1</sup> K <sup>-1</sup>
$c_s$	Speed of sound	m s <sup>-1</sup>
$c_v$	Heat capacity at constant volume, $c_v = c_p - \mathfrak{R}$	J kg <sup>-1</sup> K <sup>-1</sup>
$C$	Integration constant	<i>a.u.</i>
$d$	Tube diameter	m
$d_h$	Hydraulic diameter, $d_h = 4A/P$	m
$D$	Diodicity	-
$D_F$	Fickian diffusion coefficient	m <sup>2</sup> s <sup>-1</sup>
$D_{Kn}$	Knudsen diffusion coefficient	m <sup>2</sup> s <sup>-1</sup>
$D_{MS}$	Maxwell-Stefan diffusivity	m <sup>2</sup> s <sup>-1</sup>
$D_S$	Surface diffusion coefficient	m <sup>2</sup> s <sup>-1</sup>
$e_i$	Standard deviation of value $i$	<i>a.u.</i>
$E_{dif}$	Activation energy of diffusion, Eq. (3.76)	J
$f$	Velocity distribution function, $f(\tau, r, c)$	-
$F$	External force	N
$G$	Reduced mass flow rate	-
$G^j$	Reduced mass flow rate in slightly tapered ducts	-
$\Delta G_A$	Energy of adatom formation, Eq. (3.76)	J
$h$	Height of rectangular channel	m
$\hbar$	Planck's constant, $6.626 \times 10^{-34}$	J s
$I$	Electrical current	A
$J$	Flux	mol m <sup>-2</sup> s <sup>-1</sup>
$k$	Boltzmann constant, $1.381 \times 10^{-23}$	J K <sup>-1</sup>

$K$	Correction factor for rect. channels (Bruus, 2008)	-
$K_L$	Langmuir constant	$\text{Pa}^{-1}$
$\text{Kn}$	Knudsen number	-
$\ell$	Characteristic length, related to $\text{Kn}$	m
$l$	Duct length, arbitrary cross section	m
$L$	Lattice parameter, Figure 3.4	Å
$L_s$	Slip length, Figure 3.2	m
$m$	Mass	kg
$\dot{m}$	Mass flow rate	$\text{kg s}^{-1}$
$M$	Molar mass	$\text{kg mol}^{-1}$
$M(\Phi)$	Moments of velocity function $\Phi(c)$ , Table 3.1	<i>a.u.</i>
$\text{Ma}$	Mach number	-
$n$	Number	-
$\dot{N}$	Reduced molar flow rate	$\text{mol Pa}^{-1} \text{s}^{-1}$
$p$	Pressure, $p = \rho \Re T$	Pa
$p_{ij}$	Stress tensor, $p_{ij} = p\zeta_{ij} + \sigma_{ij}$	$\text{N m}^{-2}$
$p^*$	Initial pressure, section 5.2.4	Pa
$P$	Perimeter	m
$P_{\text{AD}}$	Threshold value of Anderson-Darling test, Eq. (5.9)	-
$P$	Pressure ratio, $P = p_i/p_o$	-
$q$	Amount adsorbed	$\text{mol m}^3$
$q^*$	Maximum amount adsorbed	$\text{mol m}^3$
$r$	Position	m
$r^*$	Tube radius, section 3.4.1	m
$R$	Universal gas constant, 8.314	$\text{J mol}^{-1} \text{K}^{-1}$
$R^2$	Coefficient of determination	-
$R$	Electric resistance	$\Omega$
$R_H$	Heater resistance, calorimetric MFS/MFC	$\Omega$
$R_T$	RTD resistance, calorimetric MFS/MFC	$\Omega$
$\Re$	Specific gas constant, $\Re = R/M = k/m$	$\text{J kg}^{-1} \text{K}^{-1}$
$\text{Re}$	Reynolds number	-
$S$	Dimensionless mass flow rate	-
$S_{\text{AD}}$	Function of $Z$ , Anderson-Darling test, Eq. (5.9)	-
$S_p$	Pumping speed of the turbo pump, Eq. (2.3)	$\text{kg Pa}^{-1} \text{s}^{-1}$
$T$	Absolute temperature	K
$u$	Fluid velocity	$\text{m s}^{-1}$
$\bar{u}$	Integral fluid velocity over cross section	$\text{m s}^{-1}$
$u_s$	Slip velocity, Figure 3.2	$\text{m s}^{-1}$
$U$	Voltage	V

$V$	Volume	$\text{m}^3$
$w$	Width of rectangular channel	$\text{m}$
$W$	Local Maxwell distribution, $W(\rho, u, T)$	-
$X$	Diffusive proportion of total mass flow rate	-
$z$	Number of neighboring adsorption sites, Eq. (3.76)	-
$Z$	Cumulative distribution function, Eq. (5.9)	-
<i>Greek</i>		
$\alpha$	Tangential momentum accommodation coefficient	-
$\alpha, \gamma$	Ratio of inlet diameter to outlet diameter	-
$\Gamma$	Duct aspect ratio, $\Gamma = P^2/4A$	-
$\delta, \delta^*$	Equivalent diameter	$\text{m}$
$\zeta_{ij}$	Kronecker delta	-
$\eta$	Number density	$\text{m}^{-3}$
$\theta$	Temperature, Celsius scale, $\theta = T - 273.15$	$^{\circ}\text{C}$
$\theta$	Surface coverage	-
$\kappa$	Ratio of specific heats, $\kappa = c_p/c_v$	-
$\lambda$	Gaseous mean free path	$\text{m}$
$\Lambda^j$	Diffusive conductivity, Table 3.3	$\text{m}^2$
$\mu$	Dynamic viscosity	$\text{Pa s}$
$\nu_0$	Oscillation frequency of ads. molecule, $\nu_0 = kT/h$	$\text{s}^{-1}$
$\xi$	Molecular collision frequency	$\text{s}^{-1}$
$\rho$	Density, $\rho = m/V$	$\text{kg m}^{-3}$
$\sigma$	Molecular collision diameter	$\text{m}$
$\sigma_{\text{LJ}}$	Lattice parameter, Figure 3.4	$\text{\AA}$
$\sigma_{ij}$	Friction stress tensor	$\text{N m}^{-2}$
$\varsigma$	Thermal velocity	$\text{m s}^{-1}$
$\tau$	Time	$\text{s, h}$
$\phi$	Gaussian distribution function	-
$\varphi$	Dimensionless disturbance function	-
$\Phi$	Velocity function, $\Phi(c)$	<i>a.u.</i>
$\chi$	Device constant, calorimetric MFS/MFC	$\text{K}^2 \text{s J}^{-1}$
$\psi$	Molar concentration	$\text{mol m}^{-3}$
$\Psi$	Convective conductivity, Table 3.3	$\text{m}^3$
$\omega$	Arbitrary value, Eq. 4.1	<i>a.u.</i>

*Index*

$C, D, S$	Convection, Diffusion, Surface diffusion
$dif, noz$	Diffusor, nozzle

<i>g</i>	Gravimetric
<i>i, o</i>	Inlet, outlet
<i>l, s</i>	Large, small
<i>m</i>	Mean

*Abbreviations*

AO	Analog output
BGK	Bhatnagar-Gross-Krook
CAD	Computer-aided design
CCL	Cercignani-Lampis-Lord
CDS	Convection Diffusion Surface diffusion
CVD	Chemical vapour deposition
DFG	German Research Foundation
DRIE	Deep reactive-ion etching
DSMC	Direct Simulation Monte Carlo
DVM	Discrete Velocity Method
GE	General Electric
IMSAS	Institute for Microsensors, -actuators and -systems, University of Bremen
INOX	Acier inoxydable (French)
KIT	Karlsruher Institut für Technologie
LBM	Lattice Boltzmann Method
LFM	Laboratory for Precision Machining, University of Bremen
LJ	Lennard-Jones
M-S	Maxwell-Stefan
MD	Molecular dynamics
MEMS/NEMS	Micro/Nano Electro Mechanical Systems
MFS/MFC	Mass flow sensor/controller
MTES	Methyltriethoxysilane, $C_7H_{18}O_3Si$
NI	National Instruments
OTS	Octadecyltrichlorosilane, $C_{18}H_{37}Cl_3Si$
PDMS	Polydimethylsiloxane, $CH_3[Si(CH_3)_2O]_nSi(CH_3)_3$
R13	Regularized 13 moments equation
RTD	Resistance temperature detector
SEM	Scanning electron microscope
TMAC	Tangential momentum accommodation coefficient
UFT	Center for Environmental Research and Sustainable Technology, University of Bremen
WIKA	WIKA Alexander Wiegand SE & Co. KG





# 1 INTRODUCTION

What are gaseous microflows? And what is different compared to "normal" gas flows and microflows of a liquid? Why research on gaseous microflows?

In contrast to a liquid or a solid, the density of a gas is very low. Density can be simply assumed as the amount of molecules in a given volume. To give an example: An one litre bottle filled with water contains roughly  $3.34 \times 10^{25}$  H<sub>2</sub>O molecules. An "empty" bottle with the same volume contains only  $2.68 \times 10^{22}$  gas molecules<sup>1</sup> - less than a thousandth part.

As long as the temperature exceeds 0 K (and this seems to be a law of nature), molecules are moving. As is well known, this omnipresent motion is termed thermal motion and consequently, molecules collide inevitably with each other or with molecules of a neighboring aggregate phase.

One can imagine: The given amount of H<sub>2</sub>O molecules collide more frequently with each other than the gas molecules. Hence the distance one gas molecule travels between two intermolecular collisions is much higher compared to the distance a water molecule has to go<sup>2</sup>. The average of the distances of all molecules is referred to as the mean free path  $\lambda$  which for a gas is a function of pressure  $p$  (amount of molecules in an enclosed volume), temperature  $T$  (mobility of molecules) and a parameter regarding the size of molecules  $\sigma$ :

$$\lambda = \frac{kT}{\sqrt{2}\pi\sigma^2p}. \quad (1.1)$$

Here  $k$  is the Boltzmann constant. As mentioned previously, molecules self-evidently collide also with neighboring phase; for instance with the solid inner wall of tube (to get to the nucleus of story). When considering a gaseous flow through a tube, gas molecules have intermolecular collisions and collisions with the wall. If the tube diameter is relatively large, the frequency of collisions with the solid is negligible. However, when the tube diameter is very small (micro), gas-wall collisions have to be taken into account.

This answers the first question: In gaseous microflows, molecular collisions with the solid boundary are not negligible. The state of the gas is referred to as *rarefied*.

By means of the ratio of gas-solid collisions to intermolecular collisions, the second question is easy to be answered. Macroscopic properties of a gas (e.g. density, thermal conductivity, sonic speed) are defined by intermolecular collisions (quantified with  $\lambda$ ). However, when collisions with the boundary are frequent, macroscopic properties become different and hence flow behaviour and heat transfer are observed to vary from "normal" gas flows. Also, since the mean free path of a liquid is such low, it is (more or less) regardless whether a liquid flows through a wide or a tiny tube<sup>3</sup>. A liquid phase is never rarefied.

---

<sup>1</sup>Assumed are ambient conditions and the air being a mixture of oxygen and nitrogen.

<sup>2</sup>For purposes of illustration only, this statement is simplified since it disregards the interaction strength of molecules. The mean free path of a liquid is only on the order of magnitude of the particle diameter.

<sup>3</sup>As long the Reynolds number  $Re$  is identical. Of course capillary forces, surface wetting, gravity and other external forces do affect the flow with respect to tube diameter.

The last question raised, can be formulated more specific: Why should an *engineer* do research on gaseous microflows?

To answer that question, first a dimensionless parameter has to be introduced which quantifies the previously mentioned rarefaction: The Knudsen number  $\text{Kn}$ . The Knudsen number gives information about the ratio of gas-solid collisions to intermolecular collisions. Consequently  $\text{Kn}$  is defined as the ratio of the gaseous mean free path to an arbitrary characteristic length  $\ell$ . By means of Eq. (1.1) follows

$$\text{Kn} = \frac{\lambda}{\ell} = \frac{kT}{\sqrt{2}\pi\sigma^2 p \ell}, \quad (1.2)$$

with  $\ell$  being for instance the distance between two walls or the diameter of a tube. Hence rarefaction increases with decreasing  $p$  and  $\ell$ . Thus, in many technical application rarefied conditions occur accompanied by macroscopic effects which are not explainable by means of "classical" fluid dynamics. As it is the task of an engineer to develop novel applications and to optimize existing devices concerning costs and size, a deep understanding of gaseous rarefaction is crucial.

Besides investigation of effects in micron-sized technical application, research on microflows allows to gain insight in general rarefaction problems (e.g. re-entry of a spacecraft) since  $T$ ,  $p$ , and  $\ell$  are linked by means of the Knudsen number.

## 1.1 Rarefied gas flows

As indicated in Figure 1.1, research on rarefied gas flows is of utmost interest due to manifold applications in the emerging area of Micro/Nano Electro Mechanical Systems (MEMS/NEMS) and Lab-on-a-Chip technologies as well as in the classical rarefaction problems, high

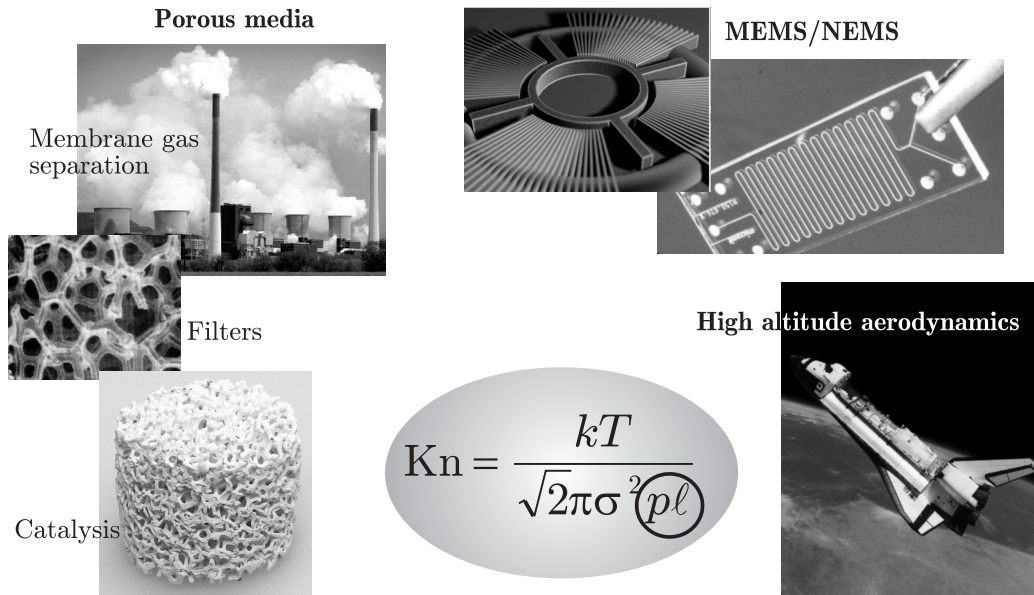


**Figure 1.1:** Rarefied gas flows in technical applications are linked by means of temperature, pressure and characteristic length. Single picture credits are given in the bibliography.

altitude aerodynamics and vacuum technology. Just wherever  $Kn$  significantly exceeds zero, rarefaction effects occur and affect macroscopic quantities of flow processes or heat transfer problems. Further examples for rarefied gas flows in engineering science are gaseous mass transfer in porous media (filters, membranes, catalysts), micro heat exchanger, and hard disc drives of computers (Gravesen *et al.*, 1993; Ho & Tai, 1996, 1998; Rostami *et al.*, 2002; Bruus, 2008).

As one might imagine (and as Eq. (1.2) indicates), a flow can be non-rarefied (e.g. ventilation hole,  $Kn \rightarrow 0$ ), a little bit rarefied (e.g. microchannel at atmospheric pressure,  $Kn \ll 1$ ), more rarefied (e.g. welding defects,  $Kn \approx 1$ ) or extremely rarefied (e.g. turbomolecular pump,  $Kn > 50$ ). By means of  $Kn$  several flow regimes are classified with respect to occurrent effects. The first classification system to differentiate between the various flow regimes within a rarefied gas is proposed by Schaaf & Chambré (1961) which solely depends on the magnitude of the local Knudsen number. A graphical representation of flow regimes experienced by a range of microfluidic devices by Beskok (2001) is adapted by Barber & Emerson (2006) and shown in Figure 1.2.

The flow regimes are classified in:

- *Continuum regime* ( $Kn < 0.01$ ): Here the continuum and thermodynamic equilibrium assumptions are appropriate. However, Gad-el-Hak (1999) suggested that the breakdown in the thermodynamic equilibrium assumption is discernible at  $Kn$  as low as 0.001 (Barber & Emerson, 2006).
- *Slip-flow regime* in the range of  $0.01 < Kn < 0.1$  where slight deviations from continuum assumptions are observable.
- *Transition flow regime* in the range of  $0.1 < Kn < 10$  where the continuum and thermodynamic equilibrium assumptions begin to break down, and alternative methods of analysis must be employed.
- *Free molecular regime* for  $Kn > 10$  where the conditions can be described as being a free molecular flow. Under such conditions, the mean free path of the molecules is far greater than the characteristic length scale, and consequently, molecules reflected from a solid surface travel on average many length scales before colliding with other molecules. The intermolecular collisions are thus negligible in comparison to the collisions between the gas molecules and the walls of the flow domain (Barber & Emerson, 2006).

Observable rarefaction effects exist - no engineer is able to change that. Consequently these effects, and the governing physical laws behind, have to be understood for development and optimization of devices in which gases are rarefied. Mathematical models which can describe

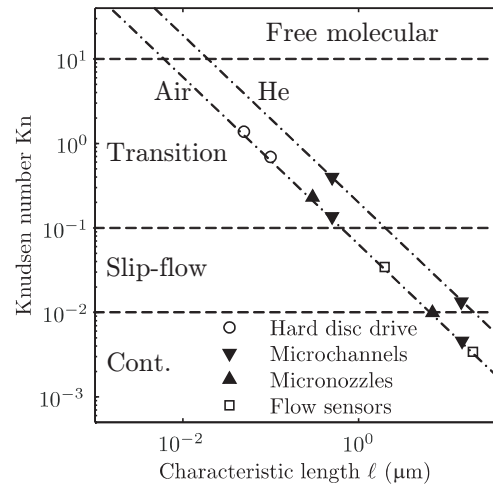


**Figure 1.2:** Characteristic length scales of typical microfluidic components and the corresponding Knudsen number at ambient conditions. Figure is taken from Barber & Emerson (2006).

or predict (what is much better) macroscopic properties of rarefied gas flows by means of microscopic analysis, are crucial for engineering.

## 1.2 Hypothesis and thesis aim

The first step of modeling is making assumptions. Consider two compartments filled with gas at different pressure levels connected by a small tube (e.g. 100  $\mu\text{m}$  in diameter) with length large compared to diameter. Striving for equilibrium, gas is transported by means of superimposed transport mechanisms (which is the main hypothesis) from the high-pressure compartment at inlet pressure  $p_i$  to the low-pressure compartment at outlet pressure  $p_o$ .

When  $p_i$  and  $p_o$  at the inlet and the outlet of the given tube are relatively high (e.g. ambient pressure),  $\lambda$  according to Eq. (1.1) is low and the macroscopic properties of the gas are defined by intermolecular collisions. The collective of molecules acts as a continuous phase and the flow mechanism under such conditions is referred to as *convection*.

However, the molecular nature of the gas has always to be taken into account, although mathematical formulations of convection (e.g. Poiseuille equation) yield sufficient results even when the gas is slightly rarefied. In the two-compartment system described above, gas molecules under thermal motion collide with each other and with the walls of the compartments. Since *pressure* is determined as the amount of molecules in a given volume, the collision frequency of molecules with the walls is higher in the high-pressure compartment at  $p_i$ .

Now both compartments have *one* hole - the tube inlet - with area  $A$  which is the cross-sectional area of the tube. Hence more molecules "collide" with the hole in the upstream compartment and migrate along the pressure gradient than vice versa. A mathematical expression of the transport mechanism referred to as molecular spatial diffusion is given by Knudsen (1909) in the beginning of the last century.

The explicit working hypothesis is that every gaseous flow at standard temperature in long ducts - regardless the flow regime (Figure 1.2) - is well described when superimposing convection with spatial diffusion mechanism. Only the distribution of transport mechanism to the entire flow is shifted with Kn: With increasing rarefaction spatial diffusion becomes dominant while convection diminishes.

Consequently the first aim of this thesis is to **develop a mathematical formulation of the hypotheses and to evaluate the model for uniform ducts by means of experimental data.**

Now consider a duct with slightly varying cross section as it is shown in Figure 1.3. From (a) to (c) the mean pressure  $p_m = 0.5(p_i + p_o)$  decreases (Kn increases), indicated by the amount of molecules at the duct inlet.

The convective flow rate, which is expressed by Poiseuille's law modified with the *lubrication approximation* for the use in circular ducts with slightly varying cross section (Bird *et al.*, 2007), is decreasing with  $p_m$  and increasing rarefaction, respectively. Following the lubrication approximation, the convective mass flow is independent of the direction of perfusion.

As mentioned earlier, the flow rate caused by molecular spatial diffusion depends on  $\Delta p = p_i - p_o$  and on the area of the "hole". Consequently the contribution of directed diffusion is higher when at identical  $p_i$  the entrance is larger (left-hand side in Figure 1.3) for the duct being perfused like a nozzle. In the case of the diffuser (right-hand side in Figure 1.3) only few molecules enter the duct. With increasing rarefaction and diminished convection, diffusion

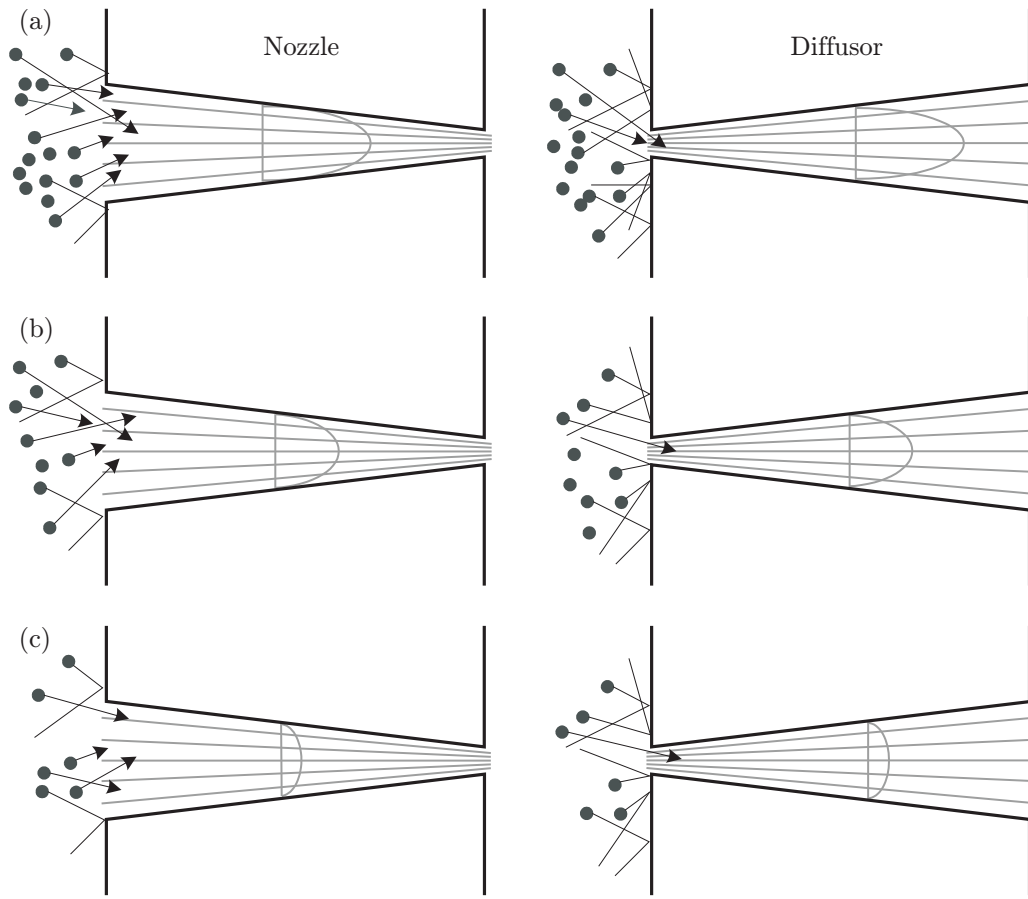


**Figure 1.3:** The gas flow diode effect as a function of gaseous rarefaction. On the left-hand side the duct is perfused as a nozzle. On the right-hand side the direction of perfusion is reversed. From (a) to (c) rarefaction increases due to the reduced  $p_m$ .

becomes dominant and the dependency on the direction of perfusion does likewise.

The second aim of the thesis is to **give the experimental proof of the outlined diode effect** and to **refine the superposition model for the prediction of experimental data obtained on slightly tapered ducts**.

As already pointed out in section 1.1, rarefied gas flows are of high interest for manifold technical and scientific application. Thus, besides general understanding of the physics, specific tools in the form of mathematical models are required for engineering without concerning with kinetic theory. And here too, as usual, the simpler the model, the faster the calculation, the higher the efficiency.

Hence a third aim can be formulated as follows: **This work is supposed to contribute to both, the general insight in gaseous microflows, and the development of a straightforward and "engineer-friendly" mathematical formulation.**

### 1.3 Thesis structure

In the previous section the working hypothesis is suggested and corresponding aims are formulated. By means of the following stated structure, the way to achieve the objectives should be demonstrated.

At first a general introduction on the topic of experimental work on gaseous microflows is given. This includes discussion about measuring methods which has relevance for the experimental section of this work. Further the experimentally observed rarefaction effects are specified and resulting problems for modeling flows under rarefied conditions are outlined.

The central element of this thesis is the development of an alternative transport model valid for the whole range of rarefaction as well as for straight and slightly tapered ducts, based on the hypothesis of the flow being a superposition of transport mechanism. For this purpose, first basic equations are given as theoretical background for mathematical modeling. Also a brief review about the topic of modeling rarefied gas flows is presented, which equally constitutes arguments and motivation on *why* this approach has been developed. Furthermore, a theoretical analysis about gaining insight on gaseous microflows by means of alteration of the surface chemistry of microducts is given.

The developed model is proved in duplicate. In chapter 4 the derived equations are used to describe experimental data given in literature for the slip-flow and the beginning transition regime in a predictive manner. Furthermore the model is also evaluated for a wide range of rarefaction in section 4.2.

The second evaluation of the model, and hence of the formulated hypothesis, is done by own microflow experiments on long ducts with slightly varying cross section. Here first the manufacturing methods of the different types of ducts, and the geometrical properties are shown. Further the experimental set-up and procedure, including measuring techniques, data acquisition, validation, and error analysis, are presented in detail.

Experimental results are shown in comparison to predictive calculations in chapter 6.

Finally, analytical and experimental results as well as general findings are discussed and an outlook on further work is given.

# 2 EXPERIMENTAL RESEARCH ON ISOTHERMAL GAS MICROFLOWS

During the last decades, experimental research on gas microflows has attracted vast attention due to the emerging field of micro/nano electromechanical systems (MEMS/NEMS) and Lab-on-a-Chip techniques. In detail, some of these applications may include mass flow sensors, pipe networks, micropumps or gaseous devices in analytic instruments as gas chromatograph or mass spectrometer. Gas flows through channels of various lengths and cross sections are basic elements of such systems and can be considered as a model for more complicated geometries.

This section aims to give a brief overview first about experimental work on isothermal gas microflows including the measurement techniques used in subject literature. Secondly, observed rarefaction effects are discussed concerning problems of "classical" transport models.

## 2.1 An overview

At the beginning of the last century Knudsen (1909) reported about experiments on gas flows through tubes performed by Kundt & Warburg (1875) and later by Warburg (1876), where measured values significantly deviated from Poiseuille's law. The same observations are made by Christiansen (1890) who performed gas flow experiments between parallel plates with a very small distance. Animated by these first publications on rarefied gas effects, Knudsen aimed to find the governing physical laws which cause the transition from the Poiseuille flow to the free molecular flow. The experimental approach by Knudsen is the first and a very extensive study (see Table 2.1) about relationships between gaseous pressure and tube diameter. He found the rarefaction effects to depend on the ratio of the gas mean free path as a function of the pressure to the tube diameter - A non-dimensional value which consequently is referred to as Knudsen number (Eq. (1.2) on page 2).

After Knudsen's studies a lot of experimental works are published of which only an excerpt is listed in Table 2.1. Several alleged influence parameters on rarefaction effects are studied, such as the influence of

- nature of the gas (Knudsen, 1909; Lund & Berman, 1966b; Arkilic, 1997; Sazhin *et al.*, 2001; Maurer *et al.*, 2003; Ewart *et al.*, 2007a; Graur *et al.*, 2009; Yamaguchi *et al.*, 2011, 2012),
- channel surface, including roughness (Peiyi & Little, 1983; Turner *et al.*, 2004; Tang *et al.*, 2007; Demsis *et al.*, 2010) and chemistry (Sazhin *et al.*, 2001; Hadj-Nacer *et al.*, 2012),
- cross section (Araki *et al.*, 2002; Tang *et al.*, 2007; Varoutis *et al.*, 2009) and tube diameter (Lalonde, 2001; Tang *et al.*, 2007; Yamaguchi *et al.*, 2011, 2012).

In summary it can be concluded that gas flows in microducts with various *but alongside uniform* cross section are widely studied in the last decades.

**Table 2.1:** Experimental work on gas flows in long, micro-sized ducts with uniform cross section. Knudsen number stated by the authors is either calculated using outlet pressure  $p_o$  or mean pressure  $p_m = 0.5(p_i + p_o)$ . The characteristic length is either diameter  $d$  for tubes, channel height  $h$  for rectangular channels or hydraulic diameter for the geometries studied by Varoutis *et al.* (2009).

Reference	Cross section	Kn	
Knudsen (1909)	Circular	0.00136 – 620 (mean)	
Lund & Berman (1966b)		0.0048 – 5.61 (mean)	
Lalonde (2001)		0.001 – 0.017 (mean)	
Shinagawa <i>et al.</i> (2002)		0.0021 – 2.5 (mean)	
Asako <i>et al.</i> (2005)		0.00018 (mean)	
Ewart <i>et al.</i> (2006)		0.003 – 0.289 (mean)	
Ewart <i>et al.</i> (2007a)		0.003 – 0.309 (mean)	
Ewart <i>et al.</i> (2008)		0.003 – 30 (mean)	
Marino (2009)		0.055 – 9.3 (mean)	
Yang & Garimella (2009)		0.0564 – 1.08 (outlet)	
Perrier <i>et al.</i> (2011)		0.3 – 30 (mean)	
Yamaguchi <i>et al.</i> (2011)		0.04 – 0.3 (mean)	
Hadj-Nacer <i>et al.</i> (2012)		0.00022 – 0.3 (mean)	
Yamaguchi <i>et al.</i> (2012)		0.05 – 0.3 (mean)	
Shih <i>et al.</i> (1996)		Rectangular	0.185 – 0.216 (mean)
Arkilic <i>et al.</i> (1997a)			0.155 (outlet)
Arkilic <i>et al.</i> (2001)			0.029 – 0.438 (outlet)
Jang <i>et al.</i> (2002)	0.00115 (outlet)		
Zohar <i>et al.</i> (2002)	0.053 – 0.169 (mean)		
Maurer <i>et al.</i> (2003)	0.002 – 0.8 (mean)		
Colin <i>et al.</i> (2004)	0.017 – 0.466 (outlet)		
Hsieh <i>et al.</i> (2004)	0.001 – 0.024 (outlet)		
Turner <i>et al.</i> (2004)	0.0005 – 0.03 (mean)		
Jang & Wereley (2006)	0.0017 (outlet)		
Ewart <i>et al.</i> (2007b)	0.023 – 41.412 (mean)		
Huang <i>et al.</i> (2007)	0.003 – 0.4 (mean)		
Jang & Wereley (2007)	0.0137 (outlet)		
Graur <i>et al.</i> (2009)	0.007 – 30 (mean)		
Pitakarnnop <i>et al.</i> (2010)	0.043 – 1, 837 (mean)		
Hong <i>et al.</i> (2012)	0.0008 – 0.0018 (outlet)		
Harley <i>et al.</i> (1995)	Trapezoidal		0.001 – 0.4 (mean)
Szalmas <i>et al.</i> (2012)		0.05 – 0.36 (outlet)	
Varoutis <i>et al.</i> (2009)	Rect., Circ., Trap., Trian.	0.007 – 14.992 (mean)	
Demsis <i>et al.</i> (2010)		Rect., Circ.	0.002 – 0.024 (mean)
Tison (1993)	Capillary leaks	?	
Cooper <i>et al.</i> (2004)	Carbon nanotubes	?	
Roy <i>et al.</i> (2003)	Nanopores	1.410 – 1.684 (outlet)	
Velasco <i>et al.</i> (2012)	Nanopores	0.00015 – 55 (mean)	

Surprisingly, gas flows in channels with varying cross section are not studied so far. A first experimental investigation on flows in microchannels with slightly varying cross section is carried out by the author (Veltzke *et al.*, 2012a). Hence, being a central element of this thesis, it is worth focusing the measurement techniques commonly used in the stated references.

The following section gives a brief review on measuring gaseous microflows with their advantages and disadvantages. This review is being presented against the background of the experimental set-up developed during the PhD work and presented in chapter 5.

## 2.2 Measuring gaseous microflows - A brief review

Following Morini *et al.* (2011) the flow rate through microchannels can be measured directly by means of appropriate instruments (mass or volumetric flow meters) or indirectly by checking the value taken by other measurable quantities (e.g. pressure, forces, weight, volume, temperature).

The first named can be divided in the groups of volumetric flow sensors and mass flow sensors (MFS) and are commercially available. This fact constitutes a genuine benefit since the time for the development of an experimental set-up is significantly reduced. Here an advantage of the volumetric flow sensors in comparison to the mass flow sensors is the independence of the measured quantity on the fluid tested. Whereas MFS can be used only with the fluid for which they have been calibrated.

The measuring principle of commercial flow meters can be roughly divided in non-thermal flow sensors which use mechanical working principles such as

- drag force (i.e. using silicon cantilevers),
- pressure measurements (i.e. using capacitive and/or piezoresistive pressure sensors), or
- the Coriolis principle,

and thermal flow sensors. Since drag force, pressure difference and Coriolis force strongly depend on the density of the working fluid, the measurement technique is very temperature-susceptible. Depending on the measurement of temperature, thermal flow sensors do not suffer from these disadvantage. According to Nguyen (1997) thermal flow sensors employed in commercially available flow meters are classified in sensors which measure the

- effect of the flowing fluid on a hot body (micro hot-wire and micro hot-film sensors),
- delay of a heat pulse over a known distance (time-of-flight sensors),
- asymmetry of temperature profile around a micro heater which is modulated by the fluid flow (calorimetric sensors).

The last mentioned calorimetric sensors are most popular (Morini *et al.*, 2011) for industrial, analytic and scientific application. Since a calorimetric mass flow sensor is used in the experimental part of this work (chapter 5), the measuring principle is subsequently explained.

As schematically shown in Figure 2.1 the flow is directed and a partial quantity flows through a thin tube indicated as *sensor* bypassing the main tube with the laminar flow device. The partial quantity is heated ( $R_H$ ) and thus the measured temperatures  $T_1$  and  $T_2$  deviate as a function of the mass flow. Temperature difference  $\Delta T$  and mass flow rate  $\dot{m}$  are directly proportional in terms of

$$\Delta T = \chi c_p \dot{m}, \quad (2.1)$$

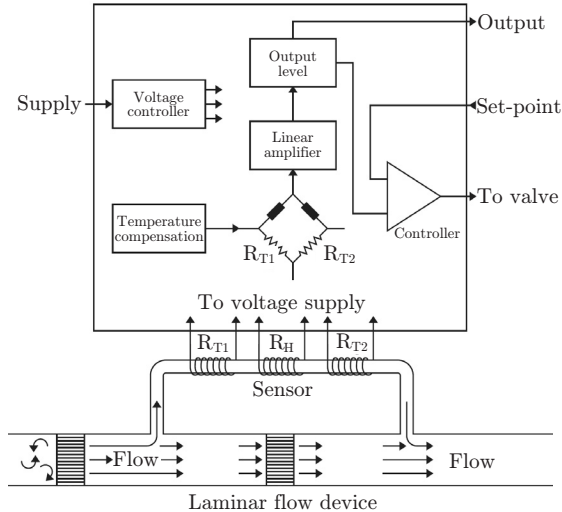


**Figure 2.1:** Operation principle of calorimetric mass flow sensors/controllers (MFS/MFC).

for example Marino (2009) used 20,000 INOX tubes with inner diameter of  $110\ \mu\text{m}$  as probe and an Series 5800 mass flow controller (MFC) by Brook Instruments with range from  $0.1 \dots 200 \times 10^{-8}\ \text{kg s}^{-1}$ . In the experiment the test gas is fed to an upstream chamber through the MFC. Downstream after the probe the flow goes to a second large chamber where the low pressure is kept by a turbomolecular pump and a Root pump. In both chambers the pressure is measured and the gas flow is kept constant by the MFC based on the calorimetric measurement principle. Thus the pressure drop is obtained as a function of the controlled mass flow.

A similar set-up is the TRANSFLOW set-up of the KIT<sup>1</sup> presented by Varoutis *et al.* (2012) for measurements of vacuum gas flows in the range of  $10^{-4} < \text{Kn} < 10^3$ . Here a constant flow rate is dosed via five MKS-647C into a large vessel (dosing dome) which is connected by the test channel to the pump dome. In both domes the pressure is measured and the pressure drop is obtained as a function of the constantly controlled gas flow.

Tang *et al.* (2007) used four different volumetric flow meters (Cole-Parmer/3290702; /3290706; /3290712; /3290715) for each specific measuring range. In their experiment the design is a little different compared to Marino (2009). Here the pressure before and after (atmosphere) the test channels is constant and the mass flow is measured as a function of the pressure difference.

The set-up of Celata *et al.* (2007) is quite similar to that of Tang *et al.* (2007), but here only one MFS (EL-Flow by Bronkhorst,  $0 \dots 5\ \text{ml min}^{-1}$ ) is used. In series with the commercial MFS they used a pipette of known diameter as a second independent mass flow measuring technique, in which the gas flow is carrying up a thin film of soapy water. The velocity at which the meniscus travels through the pipette is recorded with a highspeed camera and the volumetric flow rate is calculated. This method is referred to as the *droplet tracking method* and is also used by e.g. Shih *et al.* (1996) and Colin *et al.* (2004).

From the measurement principle and the definition of Kn according to Eq. (1.2), it is obvi-

with  $c_p$  being the heat capacity at constant pressure and  $\chi$  is a device constant. Temperatures  $T_1$  and  $T_2$  are measured by resistance temperature detectors (RTD) which are assembled in the Wheatstone bridge shown in Figure 2.1. The signal which corresponds the electrical potential between the resistors of the Wheatstone bridge is linearly amplified and can be measured as a voltage or current signal.

In experimental studies on flows in microducts (see Table 2.1) calorimetric sensors are not very common since the measuring range is restricted to relatively high mass flow rates (Figure 2.2). In subject literature this disadvantage is compensated by multiplying the amount of microducts. For

<sup>1</sup>KIT - Karlsruher Institut für Technologie, Institut für Technische Physik (ITEP)

ous that a dilemma occurs for measuring highly-rarefied flows with calorimetric-based MFS: When using the sensor under low pressure, only few molecules are in the thin sensing tube (Figure 2.1) and no sufficient measurement of the temperature profile is possible.

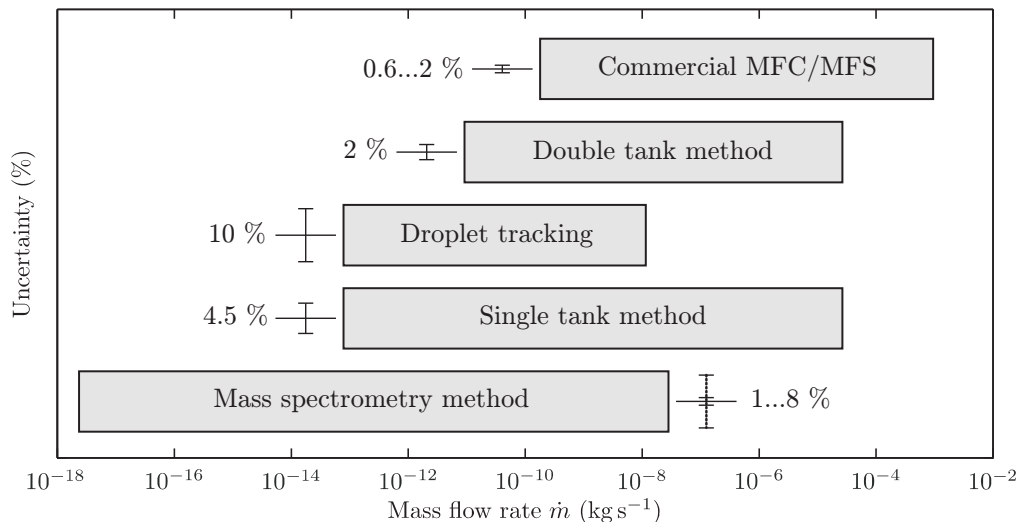


**Figure 2.2:** Measuring ranges of mass flow sensors used in experiments on gaseous microflows (Following Morini *et al.* (2011)).

In contrary to the usage of calorimetric mass flow sensors/controllers, indirect measurement techniques are widely disseminated in research on microfluidics. In principle the experimental set-up of Knudsen (1909) is used till now. Here two chambers with pressure gauges are connected by the test channel. At the beginning of the experiment, a  $\Delta p$  is applied by a pump which causes a flow through the test channel. During the experiment pressures in both chambers are observed and the mass flow rate can be calculated as the changing of substance per unit time using the ideal gas law. The equation of state is

$$\dot{m} = \frac{p}{\Re T} \frac{\partial V}{\partial \tau} + \frac{V}{\Re T} \frac{\partial p}{\partial \tau} - \frac{pV}{\Re T^2} \frac{\partial T}{\partial \tau}, \quad (2.2)$$

with  $V$  being the volume of the chamber which is observed. Further  $\Re$  is the specific gas constant,  $T$  the temperature and  $\tau$  the time. From Eq. (2.2) it becomes clear that each measuring value ( $p$ ,  $T$ ,  $V$  and  $\tau$ ) has to be measured very precisely since the measuring error is four-times propagated. Especially the estimation of the volume, including all fittings, valves, manufacturing errors, etc., is very demanding even nowadays. This method is referred to as the *single tank constant volume method* which for instance is used by Ewart *et al.* (2006, 2007a,b); Graur *et al.* (2009); Pitakarnnop *et al.* (2010). For the references cited here, the experimental rigs only vary in the way how the pressure is measured.

Beside the lot of measured values (and errors), another weakness of this method is the temperature fluctuation of the gas due to the compression into the tank.

Arkilic *et al.* (1997a,b, 2001) used a two-tank modified constant-volume accumulation technique to measure the mass flow rate, as the single-tank procedure would not ensure the thermal stability needed for their experiment. In this case, Eq. (2.2) is not sufficient to calculate the mass flow rate, as both upstream and downstream pressures vary during the experiment.

Instead, the pressure difference between the two tanks (both located downstream of the microchannel) is measured.

The most sensitive technique for the measurement of very low gaseous mass flow rates is based on mass spectrometry as it is first used by Tison (1993) and recently by Velasco *et al.* (2012) for measuring the flow in geometrically defined nanopores. Here the low-pressure side of the test channel (or pore) is equipped with a turbo pump, a Pirani gauge, a calibrated leak, and a residual gas analyzer, while the high-pressure side has a connection to a source of gas and conventional capacitance pressure gauges. The measured mass flow rate is proportional to the outlet pressure  $p_o$  in terms of

$$\dot{m} = p_o S_p, \quad (2.3)$$

with  $S_p$  being the pumping speed of the turbo pump. This method has by far the lowest limit in measuring range, but a series of complex operation steps are involved in the test so that the final determination of flow rate is dependent on the ratio of measured quantities instead of their absolute values, which reduces the sensitivity of possible fluctuations (Morini *et al.*, 2011).

As a conclusion of this section, Figure 2.2 shows the measuring ranges of all methods discussed. As mentioned earlier, the dilemma of calorimetric MFS/MFC between Knudsen number and measuring range can easily be shifted by the amount of test channels. Thus the main disadvantage of the commercial mass flow sensors/controllers can be compensated to some extent.

Finally the advantages and disadvantages of all measurement techniques are summarized in Table 2.2.

As a result of this review and the advantages and disadvantages of all known measurement techniques, the calorimetric measurement method is chosen for mass flow measurement in this PhD work. As shown in chapter 5.1.2, the amount of test channels is adjusted to achieve a mass flow range which is reliably measurable.

### 2.3 Rarefaction effects observed in experiments

In rarefied gas flows macroscopic effects are observable which cannot be explained by means of neither the continuum theory nor analytic approaches derived from kinetic theory. As mentioned earlier, Knudsen (1909) found the measured mass flow rate under rarefied conditions to be significantly higher than predicted by Poiseuille's law which describes viscous flows reliably. In Figure 2.3a experimental data of Arkilic *et al.* (1997b) of a slightly-rarefied helium flow in a rectangular microchannel is shown as a function of the pressure ratio  $P = p_i/p_o$ . The curve is calculated by means of Poiseuille's law according to Eq. (3.40) on page 33. The higher the rarefaction, the higher the underestimation of data by the model.

On the other hand, analytical models for molecular spatial diffusion (Knudsen diffusion), which can be derived directly from kinetic theory, also fail when predicting gaseous flow rates of low and moderately rarefied gases (Figure 2.3b). The argon mass flow data shown in Figure 2.3b is taken from Ewart *et al.* (2007a) and plotted versus the product of  $p_m$  and the driving force  $\Delta p$ . The curve is calculated by means of Eq. (3.49) on page 35.

Hence moderately rarefied gas flows are clearly distinguished from viscous flow in the con-

**Table 2.2:** Qualitative comparison concerning general advantages and disadvantages of reviewed techniques used for measuring gaseous microflows.

Technique	Pro	Contra
Calorimetric sensor	<ul style="list-style-type: none"> <li>• "Plug-and-play" saves time for development of an experimental set-up</li> <li>• Low costs of purchase</li> <li>• Low susceptibility to temperature at ambient conditions</li> <li>• Easy adjustment of the measuring range by increasing the amount of test channels</li> <li>• Low uncertainty in comparison to other techniques</li> </ul>	<ul style="list-style-type: none"> <li>• Restricted measuring range</li> <li>• Lower limit of measuring range is high in comparison to other techniques</li> </ul>
Single tank constant volume	<ul style="list-style-type: none"> <li>• Wide measuring range is possible (depends on tank volume)</li> <li>• Most commonly used; a lot of experience is available</li> </ul>	<ul style="list-style-type: none"> <li>• An individual development is necessary</li> <li>• Relatively high uncertainty</li> <li>• Costly due to the requirement of high-accurate gauges</li> <li>• Indirect measurement causes error propagation</li> </ul>
Two-tank constant volume	<ul style="list-style-type: none"> <li>• Wide measuring range is possible (depends on tank volume)</li> <li>• No susceptibility to temperature at ambient conditions</li> </ul>	<ul style="list-style-type: none"> <li>• An individual development is necessary</li> <li>• Costly due to the requirement of high-accurate gauges</li> <li>• Indirect measurement causes error propagation</li> <li>• Mass flow calculation is much more complicated compared to single tank method</li> </ul>
Mass spectrometry method	<ul style="list-style-type: none"> <li>• Measuring range covers lowest mass flow rates</li> </ul>	<ul style="list-style-type: none"> <li>• Extremely sophisticated development</li> <li>• Restricted measuring range</li> <li>• Extremely high costs (mass spectrometer)</li> </ul>

tinuum regime and from molecular diffusion at high rarefaction. They are an intermediate of the two border cases referred to as slip flow and transition regime flow (Veltzke *et al.*, 2012a). This intermediate is particularly evident when plotting the reduced mass flow rate  $G$  (mass flow rate divided by calculated mass flow rate of molecular spatial diffusion) versus the rarefaction in terms of the mean Knudsen number  $Kn_m$  (Eq. (3.2) in section 3.1).

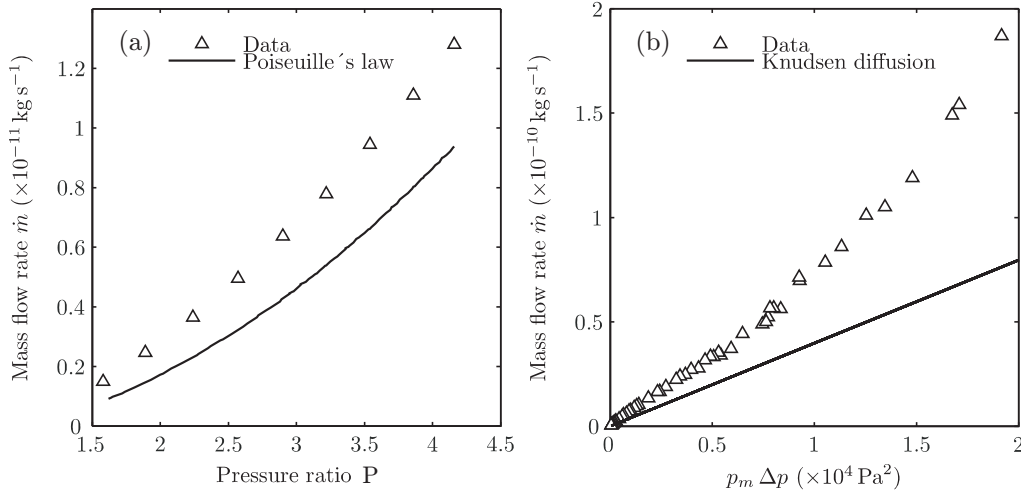


**Figure 2.3:** Effects of moderately rarefied gas flows in straight rectangular microchannels. In (a) the helium mass flow rate in a microchannel with high aspect ratio is plotted against the pressure ratio  $P = p_i/p_o$  (Arkilic *et al.*, 1997b). The curve is predictively calculated by means of Poiseuille's law according to Eq. (3.40) in section 3.4.1 with geometric dimensions and gas properties stated in the primary literature. In (b) the experimental mass flow rate of argon in a microtube measured by Ewart *et al.* (2007a) is plotted versus the product of  $p_m$  and the driving force  $\Delta p$ . The curve is calculated by means of an analytical model describing molecular spatial diffusion derived from kinetic theory (Eq. (3.49) in section 3.4.2).

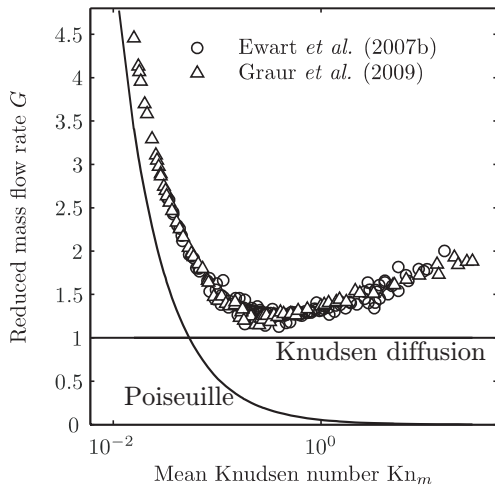


**Figure 2.4:** Reduced mass flow rate as a function of rarefaction in terms of the mean Knudsen number. The experimentally observable minimum of  $G$  is referred to as Knudsen minimum.

In Figure 2.4  $G$  decreases with increasing rarefaction until a minimum is reached. This minimum is referred to as Knudsen minimum. For very low  $\text{Kn}_m$  Poiseuille's law can sufficiently describe the results, but already slightly rarefied conditions cause a severe underestimation of data. The same applies for the model of molecular spatial diffusion: It underestimates experimental data throughout the range of rarefaction. An interesting finding and a challenge for basic research is that  $G$  increases with rarefaction after Knudsen's minimum. Such a behaviour is seldom in mass and heat transfer processes and thus it is not trite to understand the governing physical laws. Consequently modeling of the whole range of rarefaction is complex as it is shown in section 3.2.

Actually the stated examples of rarefaction effects of isothermal gas flows in long uniform channels are without direct impact on

any technical application. Except for long pipes in vacuum systems it is hard to find real

devices which are that simple. Nevertheless, long tubes and channels may be considered as models of more complex geometries and it is necessary to understand the microscopic effects causing unexpected behaviors of macroscopic properties (e.g. mass flow rate or pressure drop).

In section 1.1 some technical and scientific applications are exemplarily given in which gaseous flows are rarefied. For the task of optimization of those, or implementation of novel scientific and industrial techniques, it is crucial to fully understand and to model flows in the conceivably simplest geometries.



# 3 BACKGROUND THEORY AND MATHEMATICAL MODELING

This chapter is subdivided in three blocks in which the background theory, the modeling approach and theoretical investigation on surface functionalization are given.

The central element of this PhD work is the novel approach for modeling gaseous microflows. The first block of this chapter indicates *why* this approach has been developed and provides the required basics. Here especially one important value, the tangential momentum accommodation coefficient (TMAC) is discussed. Also a brief review on the topic of modeling gaseous microflows is given.

The second block deals with the derivation of the novel transport model which is called CDS model referring to **con**vection, **diff**usion and **surf**ace diffusion. Parts of this block are already published in peer-reviewed journals (Veltzke & Thöming, 2012; Veltzke *et al.*, 2012a,b) or submitted for publication.

The last block of this chapter theoretically emphasizes the opportunities of surface functionalization on knowledge gain in the field of rarefied gas flows.

## 3.1 Governing equations

Not a transport equation but the most important value in the context of this work is the Knudsen number  $\text{Kn}$  already stated in Eq. (1.2) on page 2. The Knudsen number as a measure of the gaseous rarefaction can be expressed by means of several physical properties and other dimensionless numbers:

$$\text{Kn} = \frac{\mu}{\rho\ell} \sqrt{\frac{\pi m}{2kT}} = \frac{\text{Ma}}{\text{Re}} \sqrt{\frac{\kappa\pi}{2}}. \quad (3.1)$$

Here  $\mu$  is the dynamic viscosity,  $m$  the molecular mass and  $\rho$  the density. All macroscopic gaseous properties can be obtained by finding the moments of the velocity distribution function  $f(\tau, r, c)$ , when  $f$  is known (Shen, 2005) ( $\tau$  is time,  $r$  is position and  $c$  is absolute molecular velocity). Consequently other dimensionless numbers are linked to  $\text{Kn}$  also: The Mach number  $\text{Ma}$  is defined as the ratio of gaseous velocity  $u$  to the speed of sound  $c_s = \sqrt{\kappa kT/m}$ , with  $\kappa$  being the ratio of specific heats. Further  $\text{Re}$  is the Reynolds number being the ratio of inertial forces ( $\rightarrow u$ ) to viscous forces ( $\rightarrow \mu$ ).

In this work special emphasis is placed on universality of the equations concerning the cross-sectional geometry of microducts. For that purpose the hydraulic diameter  $d_h = 4A/P$  is used as characteristic length  $\ell$  of the Knudsen number.  $A$  is the cross-sectional area and  $P$  is the perimeter of duct indifferent whether its shape is circular, rectangular or trapezoidal. Since  $\text{Kn}$  depends on the pressure, which is different from the inlet of a duct ( $p_i$ ) to the outlet

$(p_o)$ , the mean Knudsen number

$$\text{Kn}_m = \frac{kT}{\sqrt{2}\pi\sigma^2 p_m \ell} = \frac{kTP}{\sqrt{8}\pi\sigma^2 (p_i + p_o) A}, \quad (3.2)$$

is used for quantification of an integral rarefaction over the length  $l$  of the duct. The collision diameter  $\sigma$  can be derived by means of the simplest molecular model (hard sphere model) with assumption of two billiards: Two molecules with diameter  $d_1$  and  $d_2$  collide when their distance is less than  $\sigma_{12} = 0.5(d_1 + d_2)$  (Shen, 2005). For a single gas,  $\sigma$  equals the molecule diameter.

While  $\text{Kn}_m$  provides information about the state of the (integral) gaseous flow, solutions of transport equations are needed to describe measurable values like mass flow rate or pressure drop. As shown by means of Eq. (3.1), the Knudsen number can be expressed according to  $\text{Re}$  and  $\text{Ma}$  which both depend on the fluid velocity  $u$ . Also the integral velocity in a duct  $\bar{u}$  is directly related to the volumetric flow rate (see section 3.4.1), and hence the aim is to find an expression for  $u$  being a function of position, state and velocity of gas molecules in the duct.

The first of the following two sections emphasizes the Boltzmann equation as the most general equation describing the statistical behaviour of a fluid in thermodynamic nonequilibrium. On the basis of the Boltzmann equation the Navier-Stokes equations are derived as a set of differential equations, which can be analytically solved for some specific flow problems like Couette flow or Poiseuille flow in (long) ducts. The derivation of the Navier-Stokes equations is given in subsection 3.1.2.

### 3.1.1 Boltzmann equation

In the previous section the velocity distribution function  $f$  is mentioned to serve for the derivation of macroscopic gaseous properties. This is possible by means of the assumption of equilibrium or using the elemental "1/6-distribution" (Hänel, 2004). Unfortunately these assumptions are invalid for a general situation of thermodynamical nonequilibrium and hence the problem is how to find  $f$ .

The Boltzmann equation is an universally valid conditional equation which describes  $f$  of a molecule in time  $\tau$ , space  $r$ , and absolute velocity  $c$ . The absolute velocity of a molecule is the sum of  $u$  and the thermal velocity  $\varsigma$ . The Boltzmann equation is derived as an accounting equation for the conservation of molecules in a given volume  $\Delta V$ . The number of molecules

$$\Delta n(\tau, r, c) = f(\tau, r, c)\Delta V \Delta c \quad (3.3)$$

is temporarily changed by transport due to  $c$  and external forces  $F$ . For the sake of conservation, this transport term equals the collision term which includes the changing of  $\Delta n$  due to reversible, elastic collisions

$$(\Delta n_\tau + \Delta n_r + \Delta n_c)_{\text{Transport}} = (\Delta n^+ - \Delta n^-)_{\text{Collision}}, \quad (3.4)$$

with

$$\Delta n_\tau = \frac{\partial f}{\partial \tau} \Delta V \Delta c \Delta \tau; \quad (3.5a)$$

$$\Delta n_r = \left( c_x \frac{\partial f}{\partial x} + c_y \frac{\partial f}{\partial y} + c_z \frac{\partial f}{\partial z} \right) \Delta V \Delta c \Delta \tau; \quad (3.5b)$$

$$\Delta n_c = \left( \frac{\partial f}{\partial c_x} \frac{F_x}{m} + \frac{\partial f}{\partial c_y} \frac{F_y}{m} + \frac{\partial f}{\partial c_z} \frac{F_z}{m} \right) \Delta V \Delta c \Delta \tau; \quad (3.5c)$$

$$\Delta n^+ = \int_{c_1} \int_{A_c} (f f_1 g) dA_c dc_1 \Delta V \Delta c \Delta \tau; \quad (3.5d)$$

$$\Delta n^- = \int_{c_1} \int_{A_c} (f' f'_1 g) dA_c dc_1 \Delta V \Delta c \Delta \tau. \quad (3.5e)$$

For a detailed description of each contribution to transport term and collision term, reference is made to Shen (2005). In German language, an extensive and very descriptive derivation of the Boltzmann equation is given by Hänel (2004).

Combining now Eqs. (3.3), (3.4), and (3.5) the Boltzmann equation writes

$$\frac{\partial f}{\partial \tau} + \sum_{i=1}^3 c_i \frac{\partial f}{\partial x_i} + \sum_{i=1}^3 \frac{F_i}{m} \frac{\partial f}{\partial c_i} = \int_{c_1} \int_{A_c} g (f f_1 - f' f'_1) dA_c dc_1, \quad (3.6)$$

with  $i = 1, 2, 3$  denoting the components in  $x$ ,  $y$ , and  $z$ -direction. Eq. (3.6) can be found in many other notations in the literature.

Being a basic concept of the kinetic theory, the Boltzmann equation is unrestrictedly valid in nonequilibrium thermodynamics including the thermodynamic equilibrium also. Hence Eq. (3.6) is independent of gaseous rarefaction and describes the state of the gas in all flow processes correctly. So why continuing work on modeling gaseous microflows?

The Boltzmann equation is a mathematically very complex integro-differential equation (unpleasant for engineers). Hence, analytical solutions are only possible by means of approximation procedures for very simple problems. For instance, for small deviations from thermodynamic equilibrium the conversation equations of the continuum theory can be obtained when using the Chapman-Enskog expansion of the moments of the Boltzmann equation (Hänel, 2004). This derivation is shown in the following section.

General solutions are only possible by means of numerical methods like Direct Simulation Monte Carlo (DSMC) or Lattice Boltzmann Method (LBM). For many flow problems these methods are inappropriate due to the computational effort for the determination of velocity, position, and state of all molecules at every time step (Gad-el-Hak, 1999).

It can be concluded that kinetic theory is unrestrictedly valid but limited in its applicability. Hence it is worth focusing on derivation of time saving analytical approaches in addition to numerical methods.

### 3.1.2 Navier-Stokes equations

This work focuses the derivation of a transport model for isothermal gas flows. Thus the conversation equations for mass and momentum are needed, which is a set of differential equations called Navier-Stokes equations.

For derivation of the transport term of a general conversation equation, the moments of the Boltzmann equation are used. Therefore Eq. (3.6) is multiplied with a velocity function  $\Phi(c)$

and integrated over  $c$ :

$$\frac{\partial}{\partial \tau} \int \Phi f dc + \frac{\partial}{\partial x_i} \int \Phi c_i f dc = \int_c \int_{c_1} \int_{A_c} \Phi g (f f_1 - f' f'_1) dA_c dc_1 dc. \quad (3.7)$$

Here the derivatives with respect to time and space are put in front of the integral sign since they are independent of the integration over velocity. In contrast to Eq. (3.6), the moments equation is written in tensor notation and the term including  $F_i$  is omitted since the impact of external forces (e.g. gravity) is negligible for a gas flow (Hänel, 2004).

**Table 3.1:** Moments of an ideal gas derived from velocity distribution function with  $c = \varsigma + u$  (Hänel, 2004).

$\Phi(c)$	Moment $M(\Phi) = \int \Phi f dc$	Physical value
$m$	$m \int f dc = \rho$	Density
$mc_i$	$m \int (\varsigma_i + u_i) f dc = \rho u_i$	Momentum
$m\varsigma_i\varsigma_j$	$m \int (\varsigma_i + \varsigma_j) f dc = p_{ij} = p\zeta_{ij} - \sigma_{ij}$	Stress tensor
	$\frac{1}{3} \sum_i p_{ii} = \frac{m}{3} \int \varsigma^2 f d\varsigma = p$	Pressure
	$\sigma_{ij} = p\zeta_{ij} - p_{ij}$	Friction stresses
$mc_i c_j$	$m \int (\varsigma_i + u_i)(\varsigma_j + u_j) f dc = \rho u_i u_j + p\zeta_{ij} - \sigma_{ij}$	Momentum flux and stress tensor

Referring to basic literature on kinetic theory, some basic moments of  $\Phi$  are given in Table 3.1. Since mass ( $\Phi(c) = m$ ) can not be created or annihilated in a flow process, the collision term on the right-hand side of Eq. (3.7) is zero and the Boltzmann moments equation reduces to

$$\frac{\partial \rho}{\partial \tau} + \frac{\partial}{\partial x_i} (\rho u_i) = 0. \quad (3.8)$$

This expression is the well-known continuity equation. The transport term for momentum is obtained analogously with the appropriate moment given in Table 3.1:

$$\frac{\partial}{\partial \tau} (\rho u_i) + \frac{\partial}{\partial x_i} (\rho u_i u_j + p_{ij}) = 0; \quad (3.9a)$$

$$\frac{\partial}{\partial \tau} (\rho u_i) + \frac{\partial}{\partial x_i} (\rho u_i u_j) = -\frac{\partial p_{ij}}{\partial x_i}. \quad (3.9b)$$

The collision term is also zero for this moment since  $f f_1$  equals  $f' f'_1$  in case of an ideal elastic molecular collision. For small deviations from thermodynamic equilibrium, the still unknown stress tensor  $p_{ij} = p\zeta_{ij} - \sigma_{ij}$  on the right-hand side of Eq. (3.9b) can be determined by means of the Chapman-Enskog expansion (Chapman & Cowling, 1970) of a modified Boltzmann equation.

Due to the complexity of the collision term of the Boltzmann equation, a simplification is introduced by Bhatnagar *et al.* (1954) describing the approximation of a distribution function to Maxwell's speed distribution (Shen, 2005):

$$\frac{\partial f}{\partial \tau} + c_i \frac{\partial f}{\partial x_i} + \frac{F_i}{m} \frac{\partial f}{\partial c_i} = \xi (W - f), \quad (3.10)$$

with  $\xi$  being the molecular collision frequency and  $W = W(\rho, u, T)$  is a local Maxwell distribution. Here Eq. (3.6) is written in tensor notation with the simplified right-hand side.

Referring to the initial letters of the three authors, this equation is termed Bhatnagar-Gross-Krook (BGK) model. The stress tensor  $p_{ij}$  in Eq. (3.9) is subsequently derived by means of the Chapman-Enskog expansion of the BGK model.

Therefore the BGK model stated in Eq. (3.10) is written by disregarding external forces  $F$  (negligible impact) as

$$\frac{\partial f}{\partial \tau} + c_i \frac{\partial f}{\partial x_i} = \xi (W - f), \quad (3.11)$$

or written in terms of the substantial derivation as

$$\frac{Df}{D\tau} = \xi (W - f) \quad \text{with} \quad \frac{D}{D\tau} = \frac{\partial}{\partial \tau} + c_i \frac{\partial}{\partial x_i}. \quad (3.12)$$

Now this expression is non-dimensionalized by means of a characteristic length  $\ell$ , thermal velocity  $\varsigma_0$ , number density  $\eta$  and the mean free path  $\lambda$  (see Eq. (1.2) in section 1.1):

$$x_i = \bar{x}_i \ell; \quad \tau = \bar{\tau} \ell \varsigma_0^{-1}; \quad c_i = \bar{c}_i \varsigma_0; \quad f = \bar{f} \eta \varsigma_0^{-3}; \quad \xi = \bar{\xi} \varsigma_0 \lambda^{-1}. \quad (3.13)$$

By means of the Knudsen number defined in Eq. (1.2), the dimensionless BGK model writes

$$\text{Kn} \frac{D\bar{f}}{D\bar{\tau}} = \bar{\xi} (\bar{W} - \bar{f}). \quad (3.14)$$

As this equation clearly shows, the dimensionless velocity distribution function  $\bar{f}$  approaches the Maxwellian distribution  $\bar{W}$  for thermodynamic equilibrium ( $\text{Kn} \rightarrow 0$ ). In this case the BGK model yields the conversation equations of a frictionless flow without thermal conduction termed Euler equations. In contrast, the Navier-Stokes-(Fourier) equations are in order of magnitude one ( $\text{Kn}^1$ , compare Figure 3.1).

Following the Chapman-Enskog expansion, the velocity distribution function is a power series which is

$$\bar{f} = \text{Kn}^0 \bar{f}^{(0)} + \text{Kn}^1 \bar{f}^{(1)} = \bar{W} + \text{Kn} \bar{f}^{(1)}, \quad (3.15)$$

for order of magnitude one (Navier-Stokes). Combining now Eqs. (3.14) and (3.15) the BGK model with first-order approximation is written as

$$\text{Kn} \frac{D}{D\bar{\tau}} (\bar{f}^{(0)} + \text{Kn} \bar{f}^{(1)}) = \bar{\xi} (\bar{W} - \bar{f}^{(0)} - \text{Kn} \bar{f}^{(1)}). \quad (3.16)$$

With  $\bar{f}^{(0)} = \bar{W}$  and dividing Eq. (3.16) by  $\text{Kn}$  follows

$$\frac{D\bar{f}^{(0)}}{D\bar{\tau}} = -\bar{\xi} \bar{f}^{(1)}. \quad (3.17)$$

This is the BGK model in first order of the Chapman-Enskog expansion. The first order distribution function  $\bar{f}$  is redefined by means of

$$\bar{f} = \bar{W} + \bar{W} \varphi, \quad (3.18)$$

with  $\varphi$  being a dimensionless disturbance. Combining this expression to the right-hand side

of Eq. (3.15), the disturbance is

$$\varphi = \text{Kn} \frac{\bar{f}^{(1)}}{\bar{W}}, \quad (3.19)$$

which is much smaller than unity (Hänel, 2004). Due to this limitation  $\bar{f}$  approximates  $\bar{W}$  when  $\varphi$  approaches zero. Using again dimensioned variables (recalculated according to Eq. (3.13)), the BGK model according to Eq. (3.11) writes

$$\frac{\partial f}{\partial \tau} + c_i \frac{\partial f}{\partial x_i} = -\xi f \varphi. \quad (3.20)$$

Now  $\varphi$  is the last unknown variable which results from the Maxwellian distribution  $W$  and the collision frequency  $\xi$ . For the (extensive) derivation of the disturbance, reference is made to Hänel (2004). Finally Eq. (3.18), termed as the complete distribution for nonequilibrium, is written as

$$f = W \left( 1 - \frac{1}{\xi} \left[ \left( \frac{M\zeta^2}{2RT} - \frac{5}{2} \right) \frac{\zeta_i}{T} \frac{\partial T}{\partial x_i} + \frac{2M\zeta_i\zeta_j}{RT} \left( \frac{\partial u_i}{\partial x_j} + \frac{\partial u_j}{\partial x_i} - \frac{2}{3} \frac{\partial u_k}{\partial x_k} \zeta_{ij} \right)^{-1} \right] \right), \quad (3.21)$$

with the universal gas constant  $R$  and molar mass  $M$ . With this expression, the BGK model for the first order Chapman-Enskog expansion is solved for small deviations from thermodynamic equilibrium. By means of this equation, the unknown stress tensor in Eq. (3.9) can be derived.

According to the stress tensor stated in Table 3.1,  $p_{ij}$  is split in a pressure term  $p\zeta_{ij}$  and friction stresses  $\sigma_{ij}$ . Due to the isotropic nature of the pressure,  $p$  is defined as the mean of the stresses in their main direction:

$$p \equiv \frac{1}{3} (p_{xx} + p_{yy} + p_{zz}) = \frac{m}{3} \int \zeta^2 f d\zeta. \quad (3.22)$$

Thus Eq. (3.9b) is written as

$$\frac{\partial}{\partial \tau} (\rho u_i) + \frac{\partial}{\partial x_i} (\rho u_i u_j) = -\frac{\partial p}{\partial x_i} + \frac{\partial \sigma_{ij}}{\partial x_i}. \quad (3.23)$$

The friction stresses correspond

$$\sigma_{ij} = \mu \left( \frac{\partial u_i}{\partial x_j} + \frac{\partial u_j}{\partial x_i} - \frac{\mu_u}{\mu} \frac{\partial u_k}{\partial x_k} \zeta_{ij} \right), \quad (3.24)$$

and Eq. (3.23) in combination with Stoke's hypothesis ( $\mu_u/\mu = 2/3$ , (Bird, 1976)) yields the equation of momentum conservation of the Navier-Stokes equations.

Disregarding the divergence of the macroscopic velocity  $\partial u_k/\partial x_k$  and using vector notation in Cartesian coordinates, the set of differential equations for conservation of mass and momentum of a fluid is obtained as

$$\frac{\partial \rho}{\partial \tau} + \nabla \cdot (\rho \mathbf{u}); \quad (3.25)$$

$$\frac{\partial}{\partial \tau} (\rho u_x) + u_x \frac{\partial}{\partial x} (\rho u_x) + u_y \frac{\partial}{\partial y} (\rho u_x) + u_z \frac{\partial}{\partial z} (\rho u_x) = -\frac{\partial p}{\partial x} + \mu \left( \frac{\partial^2 u_x}{\partial x^2} + \frac{\partial^2 u_x}{\partial y^2} + \frac{\partial^2 u_x}{\partial z^2} \right);$$

$$\begin{aligned} \frac{\partial}{\partial \tau} (\rho u_y) + u_x \frac{\partial}{\partial x} (\rho u_y) + u_y \frac{\partial}{\partial y} (\rho u_y) + u_z \frac{\partial}{\partial z} (\rho u_y) &= -\frac{\partial p}{\partial y} + \mu \left( \frac{\partial^2 u_y}{\partial x^2} + \frac{\partial^2 u_y}{\partial y^2} + \frac{\partial^2 u_y}{\partial z^2} \right); \\ \frac{\partial}{\partial \tau} (\rho u_z) + u_x \frac{\partial}{\partial x} (\rho u_z) + u_y \frac{\partial}{\partial y} (\rho u_z) + u_z \frac{\partial}{\partial z} (\rho u_z) &= -\frac{\partial p}{\partial z} + \mu \left( \frac{\partial^2 u_z}{\partial x^2} + \frac{\partial^2 u_z}{\partial y^2} + \frac{\partial^2 u_z}{\partial z^2} \right). \end{aligned}$$

For modeling macroscopic quantities of a flow (e.g. mass flow rate), the velocity field of the flow has to be known. By means of numerical and analytical (for some simplified flows like Poiseuille flow and Couette flow) solutions of the Navier–Stokes equations, the velocity field can be calculated, and macroscopic quantities can be obtained.

The Navier–Stokes equations derived in this section are used for further modeling in section 3.4.1. In the following sections the modeling of gaseous microflows is emphasized by means of a brief review on state-of-the-art in general and the Maxwellian boundary condition in particular.

### 3.2 Modeling gaseous microflows - A brief review

The emerging development of micro devices like Micro/Nano Electro Mechanical Systems (MEMS/NEMS) or Lab-on-a-Chip devices by new manufacturing techniques has raised the necessity for a deeper understanding of the physical laws governing the fluid flow inside. In such systems the mean free path of the fluid molecules can be in the same order of magnitude as the height or diameter of the duct. This circumstance causes deviation from continuum flow behaviour and consequently the need for distinct approaches for modeling gas flows at the microscale.

From a macroscopic perspective gaseous microflows differentiate from the continuum behaviour to the effect that the mathematical models overestimate the pressure loss or underestimate the gaseous mass flow likewise (Figure 2.3 on page 14). The physical effects causing this deviation are insufficiently understood so far (Veltzke *et al.*, 2012a).

Nevertheless, there are several approaches starting from the continuum theory on the one hand and from the kinetic theory on the other hand to describe flow processes in this deeply interesting intermediate range. A diagram summarising the mathematical approaches is given by Gad-el-Hak (1999) which is shown in Figure 3.1 as a continued and supplemented version. According to Gad-el-Hak (1999) there are basically two possible kinds of model concept. On the one hand the molecular models which regard the molecular nature of a gas and on the other hand the continuum models which ignore the same. The discrete molecular approaches require numerical methods and thus computational calculation. The higher the rarefaction the more applicable the discrete molecular models embodied by e.g. Discrete Velocity Method (DVM), Direct Simulation Monte Carlo (DSMC) or Molecular Dynamics (MD) simulations. As indicated in Figure 3.1 the molecular approaches are further divided in statistical and deterministic models. For an extensive review on this topic reference is made to Gad-el-Hak (1999) and Reese *et al.* (2003).

For the use over the whole range of Kn molecular methods are inappropriate due to the considerable computational power which is needed for the determination of velocity, position, and state of all particles at every time step (Gad-el-Hak, 1999).

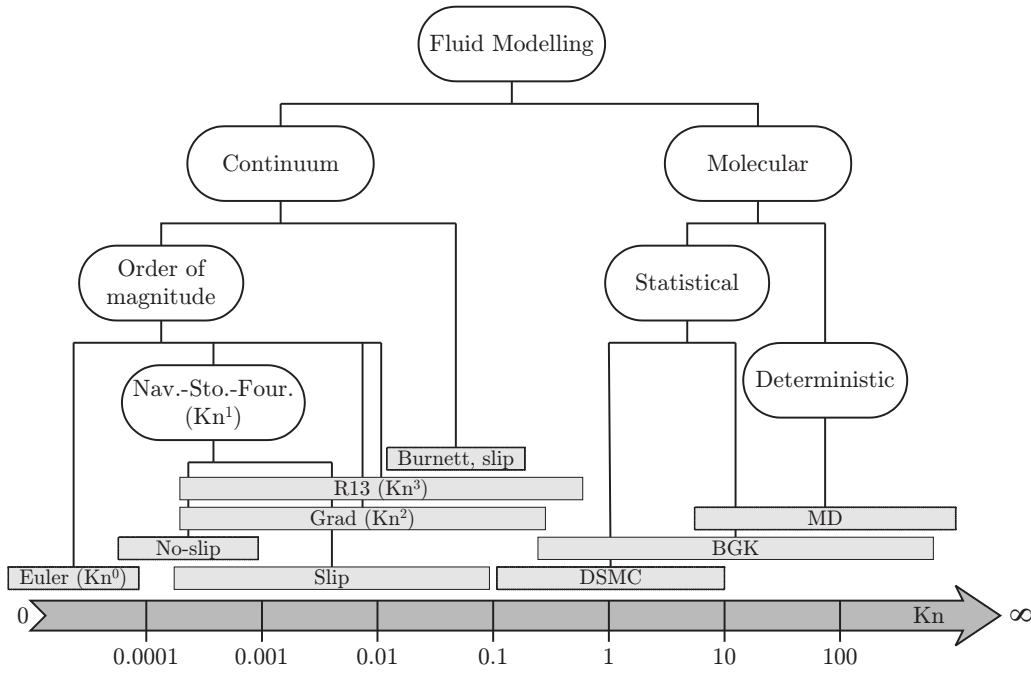


**Figure 3.1:** Gas flow models following Gad-el-Hak (1999) and their practical usability as a function of the rarefaction. No claim for completeness. Limits are taken from Gad-el-Hak (1999) and Struchtrup & Taheri (2011). Since the usability of the numerical methods strongly depends on the computational power, the lower limits of DSMC, MD, and other numerical methods will be shifted to lower Knudsen numbers in the future.

Continuum models like Navier-Stokes equations and Burnett equations can be solved comparatively easily with a few simplifying assumptions. Since the gas density and velocity are defined as averages over volume elements that are large in comparison to the molecular nature (Gad-el-Hak, 1999), the macroscopic quantities can be predicted reliably. Up to  $Kn \approx 0.001$  the mathematically easy Poiseuille equation is in acceptable agreement with measured data of flows in microducts (Struchtrup & Taheri, 2011).

The definition of the gas being a continuous phase becomes invalid with increasing rarefaction due to the decreasing number of molecules per unit volume. All experiments on rarefied gas flow show that the measured mass flow is higher than predicted by the solution of continuum models (Knudsen, 1909; Arkilic, 1994; Shih *et al.*, 1996; Arkilic *et al.*, 1997a,b; Jang *et al.*, 2002). Obviously there is "something missing" in the Navier-Stokes equations when the fluid is rarefied. Further the deviation increases with rarefaction (Maurer *et al.*, 2003; Ewart *et al.*, 2006, 2007a,b; Yamaguchi *et al.*, 2011) as it has been shown in section 2.3.

Therefore in literature emerge (roughly divided) two possibilities of correction approaches to compensate the above mentioned underestimation: The *slip* approach and the *volume* or *mass diffusion hydrodynamic* approach. The commonest slip approach is the use of the Maxwellian boundary condition (Maxwell, 1879) to solve the Navier-Stokes equations (Maurer *et al.*, 2003; Ewart *et al.*, 2006; Yamaguchi *et al.*, 2011; Arkilic *et al.*, 2001; Jang *et al.*, 2002; Hsieh *et al.*, 2004; Colin *et al.*, 2004; Graur *et al.*, 2009; Pitakarnnop *et al.*, 2010) or the Burnett equations (Stevanovic, 2007) as a function of the tangential momentum accommoda-

tion coefficient (TMAC). This approach is described in more detail in the following section. Also the regularized 13 moment equations (*R13*) presented by Struchtrup & Torrilhon (2007) and Grad's method (Grad, 1949) make use of momentum and energy accommodation coefficients as boundary conditions.

An alternative slip model based on the Langmuir adsorption isotherm is mathematically derived by Myong (2004). Furthermore Brenner (2011) presented a boundary condition assuming slip as an effect of gradients in the mass density of the fluid at the wall.

Approaches which add a term representing molecular spatial diffusion to the convection term (Poiseuille's law) are published by Pollard & Present (1948), Lund & Berman (1966a) and currently by Dadzie *et al.* (2008), Dadzie & Reese (2010), and Dongari *et al.* (2011). An overview is recently given by Dadzie & Brenner (2012).

For further reading on the topic of modeling gaseous flows, reference is made to the review papers of Gad-el-Hak (1999), Struchtrup & Taheri (2011), and Zhang *et al.* (2012) and the book of Karniadakis & Beskok (2002).

### 3.3 Approach of tangential momentum accommodation

A compromise to use the continuum models even for gas microflows, is the definition of slip boundary conditions unlike the classical wall adherence condition (Figure 3.2). This approach regards the molecular nature of the gas in the distinction of diffusively and specularly reflected molecules after a collision with the wall. The fraction of diffusively scattered molecules defines the tangential momentum accommodation coefficient (TMAC):

$$\alpha = \frac{\sum_n mc_i - \sum_n mc_o}{\sum_n mc_i}. \quad (3.27)$$

Here  $n$  is the total number of gas molecules in the sample with mass  $m$ ,  $i$  is the initial value, and  $o$  is the final value before and after the molecules collide with the solid surface. The concept of diffuse and specular reflection is first introduced by Maxwell (1879) and is helpful to understand gas surface scattering (Arya *et al.*, 2003). It is assumed that a fraction of gas molecules adsorb on the surface and desorb diffusely after a certain residence time with a velocity and direction that is independent of the incident velocity and direction. The angular distribution in case of diffuse reflection is described by Knudsen's cosine law (Knudsen, 1916; Feres & Yablonsky, 2004). The other fraction of gas molecules is reflected specularly.

Of course this concept is a simplified assumption and hence it is permanently advanced by various scientific approaches. For instance, a substantial progress is introduced by Cercignani & Lampis (1971) who derived a phenomenological model with accommodation coefficients for momentum and energy. Later this approach has been modified by Lord (1991). This so-called Cercignani-Lampis-Lord (CLL) reflection model is described in detail by Shen (2005). One

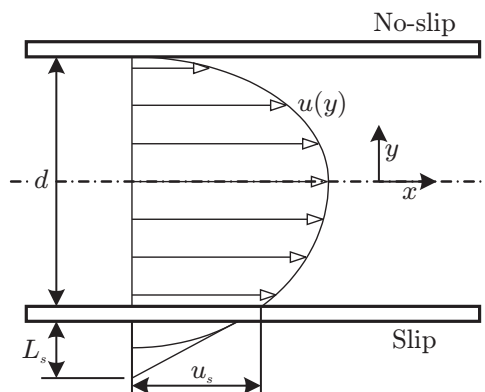


**Figure 3.2:** Schematic of tube Poiseuille flow considering no-slip and slip boundary conditions.

of the most detailed reviews on the topic of molecular momentum transport at fluid-solid interfaces is recently given by Cao *et al.* (2009).

One fundamental objective is to understand the impact of gas surface interactions on the TMAC. During the last decades, gas surface scattering has been extensively investigated using different experimental and theoretical methods and approaches. A current review is given by Agrawal & Prabhu (2008).

Theoretical approaches for estimating the TMAC are computer simulations, such as the deterministic MD simulations (Sun & Faghri, 2003; Arya *et al.*, 2003; Cao *et al.*, 2005, 2006; Finger *et al.*, 2007; Sun & Li, 2008, 2010, 2011; Spijker *et al.*, 2010), Monte Carlo simulations (e.g. DSMC) (Sun & Faghri, 2003), or the simulation of other theoretical models (Feres & Yablonsky, 2004; Ambaye & Manson, 2006; Fan & Manson, 2009). Here angular distributions and accommodation coefficients are calculated.

An experimental approach for derivation of the TMAC is the molecular beam scattering experiment. Here commonly noble gas molecules with high energy strike a clean noble metal surface (Cook & Hoffbauer, 1997, 1998; Nagard *et al.*, 1998; Rettner, 1998; Wight & Miller, 1998; Day *et al.*, 2003; Kondo *et al.*, 2005; Lu & Morris, 2011). By detecting the reflected molecules, scattering angle distribution, time of flight distributions, and momentum accommodation can be determined for various gas-surface systems.

Another experimental approach is the measurement of gaseous mass flows in defined microchannels. Using the transport model based on Poiseuille's law with the Maxwellian boundary condition (see section 3.3.1), the TMAC can be estimated by fitting the data points. Other efforts to indirectly measure the TMAC are summarized by Agrawal & Prabhu (2008).

Hence it can be concluded that the TMAC is an empirical value which in microflow experiments is mostly found to be ranging between 0.8 and unity. Unfortunately, when using other measuring techniques, the TMAC is ranging from 0.7 to 1.02 (rotating cylinder method (Timiriadze, 1913; Kuhlthau, 1949; Agrawal & Prabhu, 2008)) or from 0.4 to 1.2 (molecular beam experiment (Doughty & Schaetzle, 1969; Seidl & Steinheil, 1974; Cao *et al.*, 2009)). Further, results of MD simulations (being the only deterministic simulation technique) yield also different results which are consistently lower than results obtained in experiments (Cao *et al.*, 2005, 2006; Sun & Li, 2011).

The empirical nature of the TMAC is important and must be taken into account for further argumentation in the following sections.

### 3.3.1 Poiseuille flow with Maxwellian boundary condition

The definition of boundary conditions including the TMAC for solving the continuum-based Navier-Stokes equations enables to use continuum models with their advantages stated in section 3.2. As indicated in Figure 3.1 the analytical calculation of gas flows is possible up to  $\text{Kn} \leq 1$  with sufficient accuracy (Struchtrup & Taheri, 2011). Commonest in pertinent literature is the Maxwellian slip boundary condition

$$u(y = \pm d/2) = \lambda \frac{2 - \alpha}{\alpha} \left( \frac{\partial u}{\partial y} \right) \quad (3.28)$$

(Maxwell, 1879), which is used from zeroth to second order. Here  $\lambda$  is the gas mean free path according to Eq. (1.2) and  $u$  is the fluid velocity as a function of the ordinate axis  $y$  according to Figure 3.2. The TMAC  $\alpha$  can vary from zero (specular accommodation) to one (complete, or diffuse accommodation) as described earlier.

Following Eq. (3.28) the mean velocity of the flow profile shown in Figure 3.2 is high (lower part) when the accommodation is incomplete ( $\alpha \rightarrow 0$ ). Consequently, the mass flow rate than is higher compared to no-slip conditions (upper part), when the TMAC is smaller than unity. When assuming no-slip conditions, the fluid velocity at the wall equals the velocity of the wall.

For using this approach in an predictive manner the TMAC has to be known. However, due to its empirical nature this is impossible and  $\alpha$  is used as an adaption parameter for fitting experimental data (Arkilic, 1994; Jang *et al.*, 2002; Maurer *et al.*, 2003; Hsieh *et al.*, 2004; Ewart *et al.*, 2006; Stevanovic, 2007; Graur *et al.*, 2009; Pitakarnnop *et al.*, 2010; Yamaguchi *et al.*, 2011, 2012; Hadj-Nacer *et al.*, 2012). Nevertheless, being a value which describes the interaction of gas molecules with the channel walls, the TMAC may give some information about effects of wall characteristics (such as surface chemistry and topology) or influence of temperature on gas-surface interactions.

The impact factors on the TMAC usually include the gas-solid pairs and their interaction potentials, varieties of surface conditions such as temperature, adsorbents, lattice configurations, and surface roughness (Cao *et al.*, 2009). However, influence parameters on the TMAC is an issue controversially discussed in the literature (Gabis *et al.*, 1996; Karniadakis & Beskok, 2002; Agrawal & Prabhu, 2008). Exemplarily the temperature influence and the influence of the surface roughness are highlighted subsequently.

### 3.3.2 Temperature influence on the TMAC

Briefly summarized, results in literature show that the TMAC decreases with increasing temperature and kinetic energy of the molecules, respectively. By means of MD simulations this correlation is shown in Figure 3.3. Common explanation is, that it is less likely that a gas molecule adsorbs on the surface and is scattered diffusely later at high temperatures. Thus the scattering behaviour is more specular and the TMAC according to Eq. (3.27) is low.

Experimental investigations on the temperature influence of the TMAC are commonly performed by means of the molecular beam experiment. For instance Engel (1978) measured the angular scattering distribution in the scattering plane to be "more specular" at 1020 K compared to 300 K. Microchannel experiments on the temperature influence with respect to tangential momentum accommodation are not carried out so far.

The most common method to determine the temperature influence on the TMAC is MD simulation (Arya *et al.*, 2003; Cao *et al.*, 2005; Sun & Li, 2008; Spijker *et al.*, 2010; Sun & Li, 2011). All investigations confirm the dependency shown in Figure 3.3.

The crucial question is, if TMACs obtained in molecular beam experiments or MD simulations provide any valuable insight for modeling gas flows in microsystems. As figured out in section 3.3, the TMAC mainly depends on the method with which it is derived, since e.g. an artificial surface used in MD simulations is definitively not comparable to a technical surface. Thus, for instance, using  $\alpha = 0.19$  obtained by Yamamoto (2002) for platinum-argon at 300 K

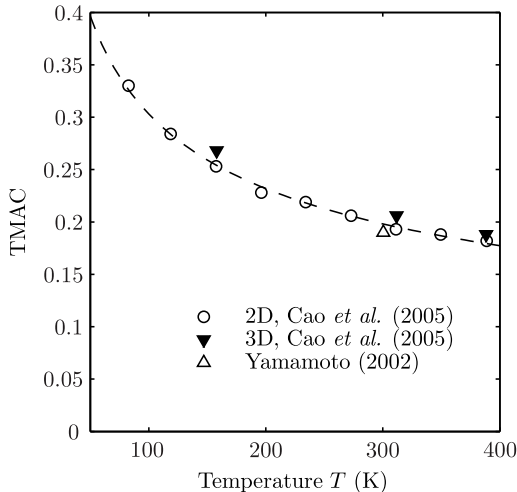


**Figure 3.3:** Variation of the TMAC with temperature. Data points are obtained by two-dimensional MD simulation of an argon Couette flow (Cao *et al.*, 2005) and three-dimensional MD simulations by Yamamoto (2002) and Cao *et al.* (2005). The dashed line represents a fitting function. Figure is taken from Cao *et al.* (2005) and slightly modified.

ing (Day *et al.*, 2003; Cao *et al.*, 2006; Sun & Li, 2011). This correlation obtained in MD simulation is shown in Figure 3.4.

Similarly to investigations on temperature influence, the most common methods for studying influence of surface topology are molecular beam experiment and numerical simulation techniques.

Again Engel (1978) obtained the scattering of an oxygen beam on a palladium surface to be much more specular when the surface is uncovered with adsorbate (which refers to roughness). Further Blanchard & Ligrani (2007) measured the TMAC on walls of different roughnesses using a unique technique and found the TMAC to strongly decrease with roughness which is counterintuitive and completely contrary to other findings in literature. However, it seems that these findings are ignored by the scientific community since the publication is not cited in the context of tangential momentum accommodation (except for the review paper of Agrawal & Prabhu (2008)). On the contrary, other experimental works qualitatively affirmed the findings of Engel (1978).

No inconsistencies concerning TMAC and surface roughness are reported when using numerical simulation: The degression of TMAC with decreasing roughness (Figure 3.4) is throughout confirmed by MD simulations (Arya *et al.*, 2003; Cao *et al.*, 2006; Sun & Li, 2011), DSMC (Sun & Faghri, 2003), and other approaches (Feres & Yablonsky, 2004; Ambaye & Manson, 2006; Fan & Manson, 2009).

would yield an exorbitantly higher mass flow rate compared to experimental data of Arkilic *et al.* (2001) (when using the Maxwellian approach).

Consequently arises a general point of criticism of the use of Maxwell’s boundary condition for modeling gas microflows. The next subsection shows another example of the discrepancy between a generally accepted dependency of the TMAC and findings obtained in microflow experiments.

### 3.3.3 Influence of surface topology

It is intuitive and commonly accepted that the TMAC increases with surface roughness. When considering a tennis ball (gas molecule) being thrown under a certain angle of incidence on a plane street, specular scattering is more likely than after hitting a stony field. Increasing surface roughness yields a higher probability of diffuse scattering

But again the question must be raised if these findings are related in any way to gaseous flows through microducts. Experimental work with the explicit aim to investigate the impact of surface roughness is very difficult and thus rare.

Nevertheless, Tang *et al.* (2007) investigated flow characteristics for nitrogen and helium in stainless steel microtubes, fused silica microtubes and fused silica square microchannels. Also Turner *et al.* (2004) systematically studied the influence of relative surface roughness, Knudsen number and Mach number of helium and nitrogen flows in etched silicon channels. Further, TMACs derived by flow experiments through microducts are summarized in Table 3.2 with respect to the surface roughness of the respective duct. Pitakarnnop *et al.* (2010)

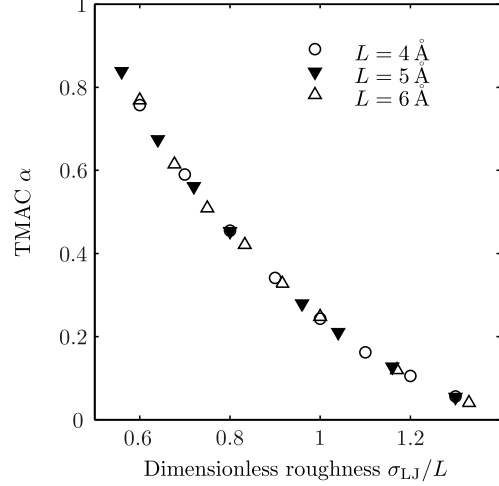


**Figure 3.4:** Variation of the TMAC for different values of the lattice parameters in MD simulation. The lattice parameter  $L$  corresponds the roughness of the surface. Figure is taken from Arya *et al.* (2003) and slightly modified.

**Table 3.2:** Experimental tangential momentum accommodation coefficients derived by microduct experiments.

References	Roughness (nm)	Gas	TMAC
Arkilic <i>et al.</i> (2001)	0.65	Ar	0.80
		N <sub>2</sub>	0.83
		CO <sub>2</sub>	0.88
Maurer <i>et al.</i> (2003)	20	He	0.91
		N <sub>2</sub>	0.87
Colin <i>et al.</i> (2004)	?	He	0.93
		N <sub>2</sub>	0.93
Graur <i>et al.</i> (2009)	<20	He	0.93
		Ar	0.91
		N <sub>2</sub>	0.96
Pitakarnnop <i>et al.</i> (2010)	5-8	Ar	1.00
Yamaguchi <i>et al.</i> (2011)	?	Ar	0.81
		N <sub>2</sub>	0.79

performed their measurements at rectangular channels with a typical roughness of 5 – 8 nm which is considerably lower than the surface roughness Graur *et al.* (2009) stated. Nevertheless Pitakarnnop *et al.* (2010) measured the higher TMAC which dissents the common state of the art as well as MD simulation and other numerical methods (as mentioned previously). This also dissents the explicit investigations: Tang *et al.* (2007) concluded that surface roughness in microchannels is found to affect the friction factor while Turner *et al.* (2004) found no significant effect at all.

The inconsistent findings of the surface roughness influence on the TMAC strengthen the doubts about the reasonableness of the Maxwellian boundary condition for modeling microflows.

Beneath temperature influence and the (alleged) impact of surface roughness, other inconsistencies arise from reviewing the literature on microflow experiments. More examples and a conclusion on this part of the thesis is given in the following subsection.

### 3.3.4 Further inconsistencies of the Maxwellian approach

In Table 3.2 a variety of references is listed allowing for the investigation of dependencies of the TMAC on nature of the gas, which is another influence parameter discussed in literature. By means of microflow experiments Arkilic *et al.* (2001) and Graur *et al.* (2009) derived the TMAC of argon to be significantly lower than of nitrogen. However Yamaguchi *et al.* (2011) found the reverse. Colin *et al.* (2004) measured  $\alpha$  of helium and nitrogen to be identical on the contrary to Maurer *et al.* (2003) who found the value of helium to be significantly higher.

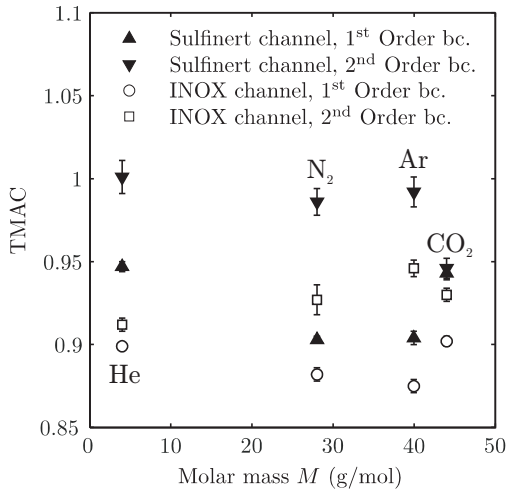


**Figure 3.5:** Comparison of TMAC for first and second order Maxwellian approach. Experiments are performed by Hadj-Nacer *et al.* (2012) on two etched microchannels, one of which is sulfinert. TMAC values are obtained for different gases using solution of Navier-Stokes equations with Maxwellian boundary condition of first and second order. Figure is taken from Hadj-Nacer *et al.* (2012) and slightly modified.

Summary is obvious: The TMAC stronger depends on the order of the boundary condition than on the nature of the gas and the surface (topology and chemistry) of the tube.

Although the impact of the TMAC on the mass flow rate might be minor in the moderately rarefied regime (Arkilic *et al.*, 2001), the shown inconsistencies led doubt that a TMAC-based

Inconsistent findings on the TMAC in microflow experiments do not only occur due to alleged influence parameters but also due to the order of the Maxwellian boundary condition with which they are derived. Hadj-Nacer *et al.* (2012) measured the mass flow rate of helium, nitrogen, argon and carbon dioxide through microtubes under isothermal conditions. Further, two surface materials (stainless steel and sulfinert steel) are considered. TMAC values for each gas-surface combination are obtained by means of solution of Navier-Stokes equations with Maxwellian boundary condition of first and second order. The results shown in Figure 3.5 are plotted versus the nature of the gas sorted by means of molar mass  $M$ . While the TMAC as a function of  $M$  first decreases for the first order boundary condition in both channels, the reverse behaviour is observed for the stainless steel tube when using the second order boundary condition. The sulfinert tube in addition to second order boundary condition yields a (more or less) steady decrease of TMAC with increasing molar mass.

approach can describe the observed rarefaction effects (see section 2.3) correctly. Furthermore it appears inconsistent to solve differential equations embodying the continuum model with a boundary condition based on the molecular one. Moreover, when using models that are based on the Maxwellian boundary condition, it is impossible to predict the mass flow rate due to the randomness of TMAC and its crucial dependency on the method with which it can be obtained.

Concerning quantitative determination of the TMAC it can be concluded that  $\alpha$  mainly depends on the method of determination (molecular beam, MD, microchannel, etc.) while other parameters discussed (temperature, surface roughness, etc.) are only of minor influence.

This points of criticism motivate to work on development of alternative modeling approaches. In this PhD work a superposition model is derived which is presented in the following section and evaluated in chapter 4.

### 3.4 The CDS model of superimposed flows

The mathematical model presented here is based on the superposition of convection, molecular spatial diffusion (Knudsen diffusion) and surface diffusion. The entire mass flow rate  $\dot{m}$  as target dimension is

$$\dot{m} = \dot{m}_C + \dot{m}_D + \dot{m}_S. \quad (3.29)$$

Following, convection is indicated with subscript index  $C$ , molecular spatial diffusion with  $D$  and surface diffusion with  $S$ . The derivation of the convective term (section 3.4.1) and the term of molecular spatial diffusion (section 3.4.2) is published by the author in (Veltzke & Thöming, 2012). The second part, the derivation of both transport mechanism for flows in ducts with slightly varying cross section, has been published in (Veltzke *et al.*, 2012a). The derivation of the term describing surface diffusion is accepted for publication in a peer-reviewed proceedings paper (Veltzke *et al.*, 2012b).

#### 3.4.1 Convection

The explanation of the Navier-Stokes equations, phenomenologically describing the conversation of momentum, or deduced from the Boltzmann equation, is well known in basic literature (Geankoplis, 1972; Sherman, 1990; Panton, 1996). The complete set of equations is derived from the BGK model in section 3.1.2.

For the derivation of the convective transport contribution a two-dimensional, laminar and steady flow without body forces in a long tube and in a rectangular channel is considered. The height  $h$  of the rectangular channel is assumed to be much smaller than its width  $w$  ( $h \ll w$ ). Further assumptions are expressed in the two boundary conditions for line symmetry of the velocity profile and wall adherence

$$\left. \frac{\partial u}{\partial r} \right|_{r=0} = 0, \quad u|_{r=r^*} = 0; \quad (3.30a)$$

$$\left. \frac{\partial u}{\partial y} \right|_{y=0} = 0, \quad u|_{y=\pm \frac{h}{2}} = 0, \quad (3.30b)$$

where  $u$  is the fluid velocity in the direction of the current and  $r^*$  the radius of the tube. The steady-state, streamwise conservation of momentum for an infinitesimal volume element is given by the Navier-Stokes equation according to Eq. (3.25) on page 22 in  $x$ -direction

$$\rho \left( u_r \frac{\partial u}{\partial r} + \frac{u_\varphi}{r} \frac{\partial u}{\partial \varphi} + u \frac{\partial u}{\partial x} \right) = -\frac{\partial p}{\partial x} + \mu \left( \frac{1}{r} \frac{\partial}{\partial r} \left( r \frac{\partial u}{\partial r} \right) + \frac{1}{r^2} \frac{\partial^2 u}{\partial \varphi^2} + \frac{\partial^2 u}{\partial x^2} \right), \quad (3.31)$$

in cylindrical coordinates for a tube. Analogous follows for the rectangular channel in Cartesian coordinates

$$\rho \left( u \frac{\partial u}{\partial x} + u_y \frac{\partial u}{\partial y} \right) = -\frac{\partial p}{\partial x} + \mu \left( \frac{\partial^2 u}{\partial x^2} + \frac{\partial^2 u}{\partial y^2} \right). \quad (3.32)$$

In Eqs. (3.31) and (3.32) the non-steady-state term and the term describing tensions in normal direction (see Eq. (3.25)) are equal zero. While the radial and swirl components, respectively the velocity components in  $y$ -direction are zero for laminar flow, Eqs. (3.31) and (3.32) reduce to

$$\frac{1}{r} \frac{\partial}{\partial r} \left( r \frac{\partial u}{\partial r} \right) = \frac{1}{\mu} \frac{\partial p}{\partial x}; \quad (3.33a)$$

$$\frac{\partial^2 u}{\partial y^2} = \frac{1}{\mu} \frac{\partial p}{\partial x}. \quad (3.33b)$$

Twofold integration yields the velocity  $u$  as a function of  $r$  and  $y$ , respectively and two integration constants:

$$u = \frac{1}{4\mu} \frac{\partial p}{\partial x} r^2 + C_1 \ln(r) + C_2; \quad (3.34a)$$

$$u = \frac{1}{2\mu} \frac{\partial p}{\partial x} y^2 + C_1 y + C_2. \quad (3.34b)$$

The integration constant  $C_1$  is calculated with the boundary condition for line symmetry (3.30) to zero. For the second constant follows

$$C_2 = \frac{1}{4\mu} \frac{\partial p}{\partial x} r^{*2}; \quad (3.35a)$$

$$C_2 = \frac{1}{2\mu} \frac{\partial p}{\partial x} \left( \frac{h}{2} \right)^2. \quad (3.35b)$$

Utilizing both integration constants, the velocity profiles for both geometries are written as

$$u = \frac{1}{4\mu} \frac{\partial p}{\partial x} (r^2 - r^{*2}); \quad (3.36a)$$

$$u = \frac{1}{2\mu} \frac{\partial p}{\partial x} \left( y^2 - \left( \frac{h}{2} \right)^2 \right). \quad (3.36b)$$

For the calculation of the flow rate the average velocity  $\bar{u}$  is required. By cross-sectional averaging of Eq. (3.36)  $\bar{u}$  is obtained as

$$\bar{u} = \frac{1}{\pi r^{*2}} \int_0^{r^*} \frac{2\pi r}{4\mu} \frac{\partial p}{\partial x} (r^2 - r^{*2}) dr = \frac{r^{*2}}{8\mu} \frac{\partial p}{\partial x}; \quad (3.37a)$$

$$\bar{u} = \frac{2}{h} \int_{-\frac{h}{2}}^{+\frac{h}{2}} \frac{1}{2\mu} \frac{\partial p}{\partial x} \left( y^2 - \left( \frac{h}{2} \right)^2 \right) dy = \frac{h^2}{12\mu} \frac{\partial p}{\partial x}. \quad (3.37b)$$

Note that the pressure drop across the length  $l$  of the duct is assumed to be linear ( $\Delta p/l$ ) and thus small that compression or expansion does not cause significant inequalities of temperature. For Mach numbers less than 0.3 the ratio of the mean pressure  $p_m$  to the outlet pressure  $p_o$  is used as a correction factor regarding the compressibility of the gaseous fluid (Bird *et al.*, 2007). Multiplying the average velocity  $\bar{u}$  with the compressibility correction factor and the cross section of the duct yields the outlet volumetric flow rate  $\dot{V}_o$ . The convective mass flow rate  $\dot{m}_C$  can be written in terms of  $\dot{V}_o$  based on the equation of state of an ideal gas as

$$\dot{m}_C = \frac{M\dot{V}_o p_o}{RT}. \quad (3.38)$$

Hence Eq. (3.37) altogether with the above mentioned substitutions applied to Eq. (3.38) yields

$$\dot{m}_C = \frac{\pi d^4 M p_m \Delta p}{128 \mu R T l}; \quad (3.39a)$$

$$\dot{m}_C = \frac{h^3 w M p_m \Delta p}{12 \mu R T l}, \quad (3.39b)$$

where  $d = 2r^*$  is the tube diameter. This solution of the Navier-Stokes equations is also known as Poiseuille's law for compressible fluids (Bird *et al.*, 2007) and can be written in its most general form as

$$\dot{m}_C = \frac{K A^3 M p_m \Delta p}{2 P^2 \mu R T l} \begin{cases} K = 1 & \text{circ.} \\ K = \frac{2}{3} - \frac{2}{3} \sum_{j=5}^{\infty} \frac{192 \min(h,w)}{j^5 \pi^5 \max(h,w)} \tanh \left( j \pi \frac{\max(h,w)}{2 \min(h,w)} \right) & \text{rect.} \end{cases}, \quad (3.40)$$

for ducts with circular and any rectangular cross section. Here  $A$  is the cross-sectional area (either  $\pi d^2/4$  or  $hw$ ) and  $P$  the perimeter (either  $\pi d$  or  $2(h+w)$ ). The correction factor  $K$  for rectangular channels of any aspect ratio is taken from Bruus (2008).

### 3.4.2 Molecular spatial diffusion

Spatial diffusive transport in a microchannel or microtube can be considered as pore diffusion including bulk, Knudsen and surface diffusion as well as capillary condensation (Cussler, 2009), whereby the contribution of each mechanism depends on the ratio of the gaseous mean free path  $\lambda$  to the pore size.

The mathematical expression of steady diffusive flux in general is analogous to Ohm's law whereby the flux  $J$  corresponds the current, a local concentration gradient  $\partial\psi/\partial x$  the voltage, and the Fickian diffusivity  $D_F$  the conductivity. This correlation is embodied in Fick's first law (Fick, 1855)

$$J = -D_F \frac{\partial\psi}{\partial x}, \quad (3.41)$$

where  $D_F$  varies with the kind of diffusion mechanism and thus depends on flow phenomena. A general overview is given by Cussler (2009) and specified for transport in porous solids by Cunningham & Williams (1980) and Kaerger & Ruthven (1992).

Is  $\lambda$  on the same order of magnitude as the characteristic length of the duct, molecules collide statistically more frequently with the solid wall than with each other (Cussler, 2009). In that case Knudsen diffusion is the dominant diffusive transport mechanism and the corresponding diffusion coefficient is crucially dependent on molecular collision properties. The Knudsen diffusion coefficient can be estimated by arguments corresponding to the kinetic theory by means of the simplest distribution of molecule position of rigid spheres.

For that purpose a volume element containing a large amount of rigidly spherical molecules is considered. In contrary to the random walk of the thermal motion it is assumed that the molecules are located solely on the three axes of a Cartesian coordinate system. Hence there are only six possible directions of motion ( $\pm x$ ,  $\pm y$  and  $\pm z$ ). The distance between the centers of the volume elements is equal to  $\lambda$  (Cunningham & Williams, 1980). As the molecular velocities obey the Maxwellian distribution, the most probable molecular velocity is

$$\bar{c} = \sqrt{\frac{2RT}{M}}, \quad (3.42)$$

Since the volume element is in contact with adjacent units, changing of mass is proportional to the flow of molecules across the boundary area  $A_x$ . Hence the molar flow rate in one direction of the  $x$ -axis of the coordinate system is

$$\dot{n}_x^\pm = \pm \frac{1}{6} \lambda A_x \bar{c} \frac{\partial \psi}{\partial x}, \quad (3.43)$$

with the molar concentration  $\psi$  in mol per unit volume. The entire changing of substance results from the balance of the molar flow rates from the left and the right unit across the boundary

$$\dot{n}_x = \frac{1}{6} \lambda A_x \bar{c} \frac{\partial \psi}{\partial x} - \left( -\frac{1}{6} \lambda A_x \bar{c} \frac{\partial \psi}{\partial x} \right) = \frac{1}{3} \lambda A_x \bar{c} \frac{\partial \psi}{\partial x}. \quad (3.44)$$

Written in terms of the diffusive flux  $J$  as molar flow rate per unit area, Eq. (3.44) can be compared with Fick's first law according Eq. (3.41)

$$J = -D_F \frac{\partial \psi}{\partial x} = \frac{1}{3} \lambda \bar{c} \frac{\partial \psi}{\partial x}. \quad (3.45)$$

Because flow is considered only in the direction of the  $x$ -axis,  $A_x$  equals the cross-sectional area  $A$  of the duct. The comparison in Eq. (3.45) yields the diffusion coefficient for Knudsen diffusion  $D_{\text{Kn}}$  with  $\lambda$  replaced by the hydraulic diameter  $d_h = 4A/P$  and with the molecular velocity according to Eq. (3.42):

$$D_F = D_{\text{Kn}} = -\frac{4A}{3P} \sqrt{\frac{2RT}{M}}. \quad (3.46)$$

As mentioned earlier, the steady diffusive flux  $J$  is proportional to a local concentration gradient  $\partial \psi / \partial x$  which is the driving force for molecular spatial diffusion. Because the flux is defined as the amount of substance per unit time and area, the spatial diffusive mass flow rate is

$$\dot{m}_D = JMA. \quad (3.47)$$

The concentration  $\psi$  in Eq. (3.41) can be expressed by the amount of substance  $n$  per unit

volume  $V$ . With the equation of state of an ideal gas, Eq. (3.47) then is rewritten with Fick's first law as

$$\dot{m}_D = -D_{\text{Kn}} \frac{MA \Delta p}{RT l}, \quad (3.48)$$

when assuming a linear pressure drop over the length of the duct. It should be noted that this simplification (already used for deriving the convective term) is due to the aim to develop an approach which is mathematically easy to handle. Here it is emphasized that the gradient is not linear as it was experimentally shown by e.g. Turner *et al.* (2004).

With  $D_{\text{Kn}}$  according to Eq. (3.46), the molecular spatial mass flow rate can be written as

$$\dot{m}_D = \frac{4A^2 \Delta p}{3Pl} \sqrt{\frac{2M}{RT}}, \quad (3.49)$$

which for the tube with  $A = \pi d^2/4$  and  $P = \pi d$  is an expression already stated by Knudsen (1909) or Kennard (1938).

Regarding the hypothesis formulated in section 1.2, it is worth noting that diffusive transport is linear proportional to cross-sectional area and pressure gradient. This relationship also becomes important when extending the superposition model to channels with slightly varying cross section.

### 3.4.3 Convection and free molecular flow in slightly tapered channels

Concerning tapered ducts reference is being made to the channel acting as *nozzle* or *diffusor* for both possible directions of perfusion. A schematic of a channel with alongside varying rectangular cross section is given in Figure 3.6 with all geometrical dimensions needed for modeling.

The entire mass flow as a superposition of only the convective term derived in section 3.4.1 and the term embodying molecular spatial diffusion derived in the previous section is

$$\dot{m}^j = \left( \frac{\Psi M p_m}{\mu RT} + \frac{\Lambda^j}{3} \sqrt{\frac{2M}{RT}} \right) \Delta p, \quad (3.50)$$

with geometric properties substituted by  $\Psi$  and  $\Lambda$  and superscript index  $j = \langle \text{noz}, \text{dif} \rangle$  denoting the direction of perfusion. Further  $\Psi$  is referred to as *convective conductivity* and  $\Lambda$  as *diffusive conductivity*. According to Eq. (3.40), the convective conductivity for ducts with arbitrary uniform cross section is

$$\Psi = \frac{KA^3}{2P^2l}, \quad (3.51)$$

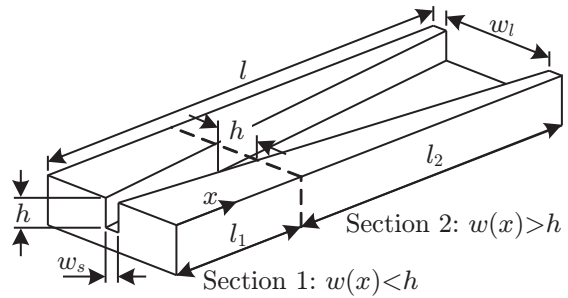


**Figure 3.6:** Schematic of a rectangular channel with alongside varying cross section.

with  $K$  stated in Eq. 3.40. Correspondingly, for the diffusive conductivity applies

$$\Lambda = \frac{4A^2}{Pl}, \quad (3.52)$$

according to Eq. (3.49). For a channel with slightly varying rectangular cross section as shown in Figure 3.6,  $\Psi$  and  $\Lambda$  will appear a little more complicated but can be derived non-empirical and consistently analytic also. This derivation is given subsequently.

Referring to the *lubrication approximation* stated by Bird *et al.* (2007) the convective mass flow rate in a slightly tapered tube is

$$\dot{m}_C^j = \frac{\pi d_o^4 M p_m \Delta p}{128 \mu R T l} \frac{3\gamma_j^3}{\gamma_j^2 + \gamma_j + 1}. \quad (3.53)$$

Here  $\gamma_j = d_i/d_o$  is the ratio of inlet diameter to outlet diameter. Since Eq. (3.53) holds for circular cross section, an equivalent outlet diameter  $\delta_o$  for tapered channels with rectangular cross section is needed. This diameter is derived by comparison of Poiseuille's law for tube and rectangular channel (Eqs. (3.39) and (3.40)) without predefinition whether width or height is larger:

$$\frac{\pi \delta_o^4}{128l} = \frac{K \min(h, w)^3 \max(h, w)^3}{8l (\max(h, w)^2 + 2\max(h, w)\min(h, w) + \min(h, w)^2)}. \quad (3.54)$$

Solving Eq. (3.54) to  $\delta_o$  yields

$$\delta_o = \sqrt[4]{\frac{16K \min(h, w)^3 \max(h, w)^3}{\pi (\max(h, w)^2 + 2\max(h, w)\min(h, w) + \min(h, w)^2)}}. \quad (3.55)$$

According to Figure 3.6 the varying cross section of the channel is due to the constantly changing width. Moreover, the small width  $w_s$  is smaller while the large width  $w_l$  is greater than the height ( $w_s < h < w_l$ ). Consequently two different  $K$  exist for the small aperture ( $K_s = K(w_s, h)$ ) and for the wide aperture ( $K_l = K(h, w_l)$ ). Referring to Eq. (3.54) the two different outlet diameter for *nozzle*-like and *diffusor*-like perfusion are

$$\delta_{o,noz} = \sqrt[4]{\frac{16K_s w_s^3 h^3}{\pi (h^2 + 2hw_s + w_s^2)}}; \quad (3.56a)$$

$$\delta_{o,dif} = \sqrt[4]{\frac{16K_l h^3 w_l^3}{\pi (w_l^2 + 2w_l h + h^2)}}. \quad (3.56b)$$

As mentioned earlier,  $\gamma_j$  is the ratio of the inlet to the outlet equivalent diameter and is calculated for the *nozzle*-case to

$$\gamma_{noz} = \frac{\delta_{i,noz}}{\delta_{o,noz}} = \frac{\delta_{o,dif}}{\delta_{o,noz}} = \sqrt[4]{\frac{K_l w_l^3 h^2 + 2hw_s + w_s^2}{K_s w_s^3 w_l^2 + 2w_l h + h^2}} = \gamma_{dif}^{-1}, \quad (3.57)$$

which is reciprocal for the reverse direction of perfusion. Using Eqs. (3.53) and (3.56) the

mass flow in *nozzle*-direction is

$$\dot{m}_C^{noz} = \frac{\pi \delta_{o,noz}^4 M p_m \Delta p}{128 \mu R T l} \frac{3 \gamma_{noz}^3}{\gamma_{noz}^2 + \gamma_{noz} + 1} = \frac{K_s w_s^3 h^3 M p_m \Delta p}{8 (h^2 + 2 h w_s + w_s^2) \mu R T l} \frac{3 \gamma_{noz}^3}{\gamma_{noz}^2 + \gamma_{noz} + 1}, \quad (3.58)$$

and for the reverse *diffusor*-direction

$$\dot{m}_C^{dif} = \frac{\pi \delta_{o,dif}^4 M p_m \Delta p}{128 \mu R T l} \frac{3 \gamma_{dif}^3}{\gamma_{dif}^2 + \gamma_{dif} + 1} = \frac{K_l h^3 w_l^3 M p_m \Delta p}{8 (w_l^2 + 2 w_l h + h^2) \mu R T l} \frac{3 \gamma_{dif}^3}{\gamma_{dif}^2 + \gamma_{dif} + 1}, \quad (3.59)$$

which is exactly equal to Eq. (3.58). Thus, the laminar convective mass flow in a tapered, rectangular channel does not depend on the direction of perfusion and hence the convective conductivity is defined as

$$\Psi_{taper} = \frac{K_s w_s^3 h^3}{8 (h^2 + 2 h w_s + w_s^2) l} \frac{3 \gamma_{noz}^3}{\gamma_{noz}^2 + \gamma_{noz} + 1} = \frac{K_l h^3 w_l^3}{8 (w_l^2 + 2 w_l h + h^2) l} \frac{3 \gamma_{dif}^3}{\gamma_{dif}^2 + \gamma_{dif} + 1}. \quad (3.60)$$

Consequently only the diffusive component of the entire mass flow differs in dependency on the ratio of inlet cross section to outlet cross section.

For verification again a uniform cross section is considered with  $w_s = w_l = w$  and  $w \gg h$ . Then  $K_s = K_l = K$  according to Eq. (3.40) is approaching 2/3 and  $\gamma$  as the ratio of inlet to outlet equivalent diameter equals one. Thus Eqs. (3.58) and (3.59) are equal to Eq. (3.39b).

Since molecular spatial diffusion depends crucially on the closest distance of the walls of a system (the characteristic length  $\ell$  of Kn), the channel in Figure 3.6 is divided in two sections: Section 1 has width as the closest distance where section 2 has height as the closest distance. Thus the duct is considered as a series connection of two transport resistors and therefore the entire diffusive conductivity is

$$\Lambda_{taper}^j = \frac{\Lambda_1^j \Lambda_2^j}{\Lambda_1^j + \Lambda_2^j}. \quad (3.61)$$

According to Eq. (3.52) the diffusive conductivity is proportional to the cross-sectional area  $A_1$  which is different for the *nozzle*-direction and the *diffusor*-direction. Focussing section 1 in the case of the duct being perfused as a *nozzle*,  $A_1^{noz}$  is obtained by multiplying the narrow side area  $w_s h$  with the ratio of the average width  $\bar{w} = 0.5(w_s + h)$  to the large side width of section 1 (which is equal to  $h$ ). For the reverse direction  $w_s h$  is multiplied with  $w_s/\bar{w}$  for  $A_1^{dif}$ , respectively. Following Eq. (3.52) the diffusive conductivity in section 1 can be written as

$$\Lambda_1^{noz} = \frac{w_s A_1^{noz}}{l_1} = \frac{w_s^2 \bar{w} (w_l - w_s)}{(h - w_s) l}; \quad (3.62a)$$

$$\Lambda_1^{dif} = \frac{w_s A_1^{dif}}{l_1} = \frac{w_s^3 h (w_l - w_s)}{\bar{w} (h - w_s) l}. \quad (3.62b)$$

Since the Knudsen number in section 2 is low in comparison to section 1, assumption is being made that the dependency on the aperture area as minor. Adapting the *lubrication*

approximation by Bird *et al.* (2007) in analogy to Eq. (3.60) an expression written as

$$\Lambda_2^j = \frac{\pi(\delta_{o,j}^*)^3}{4l_2} \frac{2\alpha_j^2}{\alpha_j + 1} \quad (3.63)$$

is obtained for the diffusive conductivity in section 2 with  $\delta_{o,j}^*$  being the outlet equivalent diameter. In analogy to  $\gamma_j$ ,  $\alpha_j = \delta_{i,j}^*/\delta_{o,j}^*$  is the ratio of inlet to outlet equivalent diameter of section 2. Again, the equivalent diameters for both directions of perfusion are found by equalizing the diffusive conductivities of tube and rectangular channel:

$$\delta_{o,j}^* = \sqrt[3]{\frac{4hA_{2,o}^j}{\pi}}. \quad (3.64)$$

According to Figure 3.6, the outlet areas are  $A_{2,o}^{noz} = h^2$  and  $A_{2,o}^{dif} = hw_l$ , respectively. Hence for both ratios of inlet to outlet equivalent diameter follows

$$\alpha_{noz} = \frac{\delta_{i,noz}^*}{\delta_{o,noz}^*} = \frac{\delta_{o,dif}^*}{\delta_{o,noz}^*} = \sqrt[3]{\frac{w_l}{h}} = \alpha_{dif}^{-1}. \quad (3.65)$$

Using Eq. (3.63) with  $l_2 = l(w_l - h)/(w_l - w_s)$  and considering the duct being perfused as a *nozzle*, diffusive conductivity in section 2 is

$$\Lambda_2^{noz} = \frac{h^3(w_l - w_s)}{(w_l - h)l} \frac{2\alpha_{noz}^2}{\alpha_{noz} + 1} = \frac{h^2w_l(w_l - w_s)}{(w_l - h)l} \frac{2\alpha_{dif}^2}{\alpha_{dif} + 1} = \Lambda_2^{dif}, \quad (3.66)$$

which is exactly equal in both directions since the approach is the same as used for derivation of the convective term. Finally Eqs. (3.62) and (3.66) are applied to Eq. (3.61) which yields

$$\Lambda_{taper}^{noz} = \frac{2w_s^2\bar{w}h^3(w_l - w_s)\alpha_{noz}^2}{2h^3(h - w_s)l\alpha_{noz}^2 + w_s^2\bar{w}(w_l - h)l(\alpha_{noz} + 1)}; \quad (3.67a)$$

$$\Lambda_{taper}^{dif} = \frac{2w_s^3w_lh^3(w_l - w_s)\alpha_{dif}^2}{2\bar{w}w_lh^2(h - w_s)l\alpha_{dif}^2 + w_s^3h(w_l - h)l(\alpha_{dif} + 1)}, \quad (3.67b)$$

for the diffusive conductivities in both directions of perfusion.

For verification of the derived expression, Eq. (3.61) is written as

$$\Lambda_{taper}^j = \frac{\Lambda_n^j \Lambda_k^j}{\Lambda_n^j + \Lambda_k^j} = \frac{\Lambda_k^j}{1 + \Lambda_k^j/\Lambda_n^j}, \quad (3.68)$$

with  $n, k = \langle 1, 2 \rangle$ ,  $n \neq k$ . In the case of a channel with uniform cross section  $l_n$  is zero while  $l_k$  equals  $l$  consequently. Since  $l_1$  in Eq. (3.62) and  $l_2$  in Eq. (3.63) is the denominator, Eq. (3.62) approaches infinity when  $l_1$  is zero. The same applies for Eq. (3.63) when  $l_2$  approaches zero. Hence Eq. (3.68) writes

$$\Lambda_{taper}(\Lambda_n \rightarrow \infty) = \Lambda_k, \quad (3.69)$$

without  $j$  which is redundant when cross section is constant. With  $w_s = w_l = \bar{w} = w$  and  $\alpha = 1$  follows

$$\Lambda_k = \Lambda_1 = \Lambda_2 = \frac{\min(h, w)^2 \max(h, w)}{l}, \quad (3.70)$$

which is equal to Eq. (3.52). Thus it is proved that the expression derived for the diffusive conductivity of slightly tapered ducts yields the same result for a channel with uniform cross section as the equation derived in section 3.4.2.

Finally all expressions for the conductivity in ducts with various geometries are summarized in Table 3.3 with  $\gamma_j$  and  $\alpha_j$  according to Eqs. (3.57) and (3.65).

**Table 3.3:** Mathematical expressions of geometrical properties of three different ducts considered in this work. Here subscript index  $s$  denotes *small* while  $l$  stands for *large* (see Figure 3.6) and  $\bar{w}$  is  $0.5(w_s + h)$  (Veltzke *et al.*, 2012a).

	Circular	Rectangular $w \gg h$	Varying rectangular cross-section $w_l > h > w_s$
$\Psi$	$\frac{\pi d^4}{128l}$	$\frac{h^3 w}{12l}$	$\frac{K_s w_s^3 h^3}{8(h^2 + 2hw_s + w_s^2)l} \frac{3\gamma_{noz}^3}{\gamma_{noz}^2 + \gamma_{noz} + 1} = \frac{K_l h^3 w_l^3}{8(w_l^2 + 2w_l h + h^2)l} \frac{3\gamma_{dif}^3}{\gamma_{dif}^2 + \gamma_{dif} + 1}$
$\Lambda$	$\frac{\pi d^3}{4l}$	$\frac{h^2 w}{l}$	$\frac{2w_s^2 \bar{w} h^3 (w_l - w_s) \alpha_{noz}^2}{2h^3 (h - w_s) l \alpha_{noz}^2 + w_s^2 \bar{w} (w_l - h) l (\alpha_{noz} + 1)}$ $\frac{2w_s^3 w_l h^3 (w_l - w_s) \alpha_{dif}^2}{2\bar{w} w_l h^2 (h - w_s) l \alpha_{dif}^2 + w_s^3 h (w_l - h) l (\alpha_{dif} + 1)}$
$A$	$\frac{\pi d^2}{4}$	$hw$	$h_k w_k; \quad k \in s, l$
$P$	$\pi d$	$2(h + w)$	$2(h_k + w_k); \quad k \in s, l$
$\ell$	$d$	$h$	$2\left(\frac{A_s}{P_s} + \frac{A_l}{P_l}\right); \quad \text{with } A \text{ and } P \text{ of a rectangle}$

From the superposition of convection and molecular spatial diffusion expressed by Eq. (3.50), it can already be seen that the diverse mass flows in opposing direction of a tapered duct depend on the diffusive term, more specific, on the diffusive conductivities according to Eq. (3.67). Further the disparity in perfusion direction increases when  $p_m$  decreases and thus diffusion is the dominating transport mechanism when the gas is rarefied.

For an expression of Eq. (3.50) independent of the driving force  $\Delta p$ , the reduced molar flow rate is introduced as

$$\dot{N}^j = \frac{\dot{m}^j}{M\Delta p} = \left( \frac{\Psi p_m}{\mu RT} + \frac{\Lambda^j}{3} \sqrt{\frac{2}{MRT}} \right), \quad (3.71)$$

which is expressed by means of the mean Knudsen number according to Eq. (3.2) with  $\ell$  being the characteristic length stated in Table 3.3 as

$$\dot{N}^j = \frac{\Psi k}{\sqrt{2}\pi\mu\sigma^2\ell R} \text{Kn}_m^{-1} + \frac{\Lambda^j}{3} \sqrt{\frac{2}{MRT}}. \quad (3.72)$$

This expression shows the dependency on the rarefaction more clearly: With increasing  $\text{Kn}_m$  the convective term approaches zero and hence the diffusive term (being a function of  $\Lambda^j$ ) is gaining in importance. Thus the dependency on the direction of perfusion increases with rarefaction.

### 3.4.4 Diodicity effect in slightly tapered ducts

To quantitatively describe the dependency on the direction of perfusion, a dimensionless value referred to as diodicity  $D$ , being the ratio of the molar flow rate in nozzle-direction to the

molar flow rate in diffusor-direction is introduced as

$$D = \frac{\dot{N}^{noz}}{\dot{N}^{dif}} = \frac{\frac{\Psi k}{\sqrt{2\pi\mu\sigma^2\ell R}} \text{Kn}_m^{-1} + \frac{\Lambda^{noz}}{3} \sqrt{\frac{2}{MRT}}}{\frac{\Psi k}{\sqrt{2\pi\mu\sigma^2\ell R}} \text{Kn}_m^{-1} + \frac{\Lambda^{dif}}{3} \sqrt{\frac{2}{MRT}}} = \frac{\frac{a}{c} + \frac{b}{c} \text{Kn}_m}{\frac{a}{c} + \text{Kn}_m}; \quad (3.73a)$$

$$\frac{a}{c} = \frac{3\Psi k}{2\pi\mu\sigma^2\ell\Lambda^{dif}} \sqrt{\frac{MT}{R}}; \quad \frac{b}{c} = \frac{\Lambda^{noz}}{\Lambda^{dif}}. \quad (3.73b)$$

Hence an predictive expression for  $D$  is obtained being a function only of the mean Knudsen number, nature of gas, temperature and geometrical properties of the duct. From Eq. (3.73b) and Table 3.3 it can be seen that  $D$  is independent of the length of the duct as long as  $l$  is considered to be large compared to  $\ell$ .

In the case of a duct with uniform cross section  $\Lambda^{noz}$  equals  $\Lambda^{dif}$  and  $D$  is unity regardless whether rarefaction is high or low.

Since the reduced molar flow rate (Eq. (3.72)) decreases with increasing rarefaction in the continuum and slip-flow regime down to Knudsen's minimum (Knudsen, 1909; Gaede, 1913; Lund & Berman, 1966a; Graur *et al.*, 2009) instead of approaching zero, the diodicity must be limited. From Eq. (3.73a) it can be seen that  $D$  increases with rarefaction and approaches  $b/c$  for  $\text{Kn}_m \rightarrow \infty$ . The higher  $b/c$  which equals the ratio of  $\Lambda^{noz}$  to  $\Lambda^{dif}$ , the higher the diodicity at infinite high rarefaction.

But since  $\Lambda^{noz}$  and  $\Lambda^{dif}$  are linked in terms of the geometrical properties  $w_s$ ,  $w_l$  and  $h$  (Table 3.3),  $D$  is also limited in terms of the geometry of the duct itself and can be analyzed in terms of the ratio of  $A_l$  to  $A_s$  (which is  $w_l/w_s$  for constant  $h$  and  $h_l/h_s$  for constant  $w$ ) and  $h/w_s$  (see Figure 3.6).

In Figure 3.7a the diodicity for  $\text{Kn}_m \rightarrow \infty$  is shown as a function of  $A_l/A_s$ . For a constant

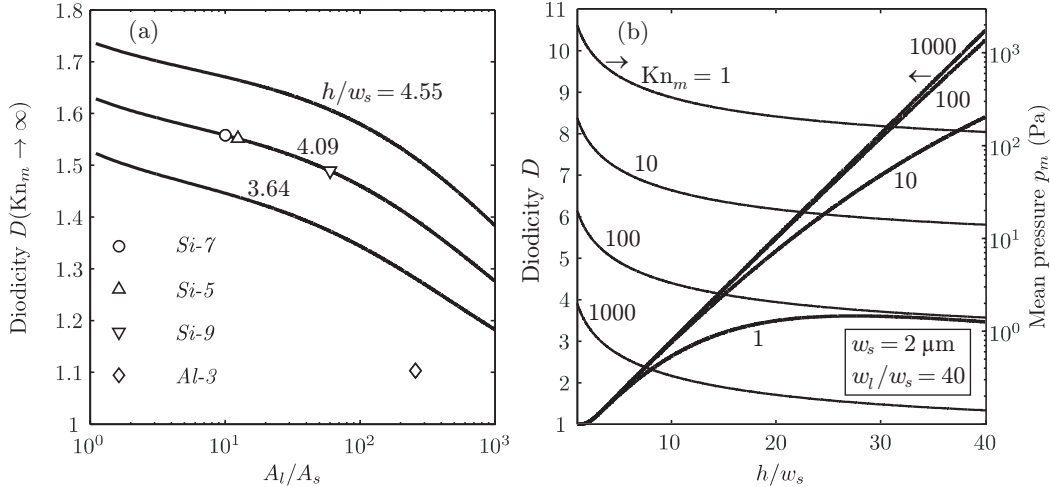


**Figure 3.7:** Diodicity for  $\text{Kn}_m \rightarrow \infty$  according to Eq. (3.73a) versus  $A_l/A_s$  (a). Curves are calculated for different ratios of  $h$  to  $w_s$ . Symbols for the four ducts with slightly varying cross section used in gas flow experiments are calculated with geometrical properties stated in Table 5.1 in section 5.1. In (b) the diodicity and the mean pressure are plotted against the ratio of  $h$  to  $w_s$  for  $\text{Kn}_m = 1, 10, 100$  and 1000. Curves are calculated for a fictional duct with  $w_s = 2 \mu\text{m}$  and  $w_l$  being 40 times  $w_s$ .

ratio of  $h$  to  $w_s$   $D(\text{Kn}_m \rightarrow \infty)$  decreases with increasing  $A_l/A_s$  and approaches unity when the ratio moves towards infinity. This finding first occurs to be contradictory to the hypothesis formulated in section 1.2 but the derivation of  $\Lambda^j$  (section 3.4.3) clarifies that  $\Lambda^{\text{noz}}$  as well as  $\Lambda^{\text{dif}}$  increase with  $w_l$  and thus the ratio decreases.

Further  $D(\text{Kn}_m \rightarrow \infty)$  increases with  $h/w_s$  because a diminishing  $w_s$  (at constant  $A_l/A_s$ ) yields a decrease of both  $\Lambda^{\text{noz}}$  and  $\Lambda^{\text{dif}}$  and hence the ratio increases.

In Figure 3.7b the diodicity (thick curves) is plotted as a function of  $h/w_s$  for a fictional duct with  $w_s = 2 \mu\text{m}$  and  $w_l/w_s = 40$  at different mean Knudsen numbers according to Eq. (3.2). In general the diodicity is high for large  $\text{Kn}_m$  as it is pointed out earlier. The diodicity increases with  $h/w_s$  at constant  $\text{Kn}_m$  since section 1 in Figure 3.6, which is crucial for the mathematical derivation of  $\Lambda^j$ , increases also. For the constant  $\text{Kn}_m$  in Figure 3.7b, the thin curves represent the mean pressure  $p_m$  which decreases with increasing rarefaction. Further  $p_m$  decreases when  $h$  rises and  $w_l$  and  $w_s$  remain constant (see Eq. (1.2) on page 2 and  $\ell$  in Table 3.3).

Thus it can be concluded that the diode effect is limited to the geometry itself and to the rarefaction due to the very low pressures which are essential when a micro structure is given. Operating a duct with slightly varying cross section at e.g.  $\text{Kn}_m = 1000$  is impossible due to the size restrictions of the manufacturing processes and the mass flow measurement at pressures on the order of magnitude of 1 Pa.

### 3.4.5 Surface diffusion

In membrane and catalysis science surface diffusion is the dominating mass transport mechanism when the pore size is on the order of magnitude of a few nanometers (Kaerger & Ruthven, 1992). Extensive theoretical and experimental studies on the dependency of gaseous surface diffusion on pore size, temperature, and other influence parameters including gas mixtures are given by Moon *et al.* (2005); Thornton *et al.* (2009); Markovic *et al.* (2009a,b); Petkovska *et al.* (2011). Furthermore, MD simulations can contribute to the understanding of surface diffusion and can, to some extent, substitute costly and time consuming experiments Pohl & Heffelfinger (1999); Skoulidas & Sholl (2005); Krishna & van Baten (2009). Besides the books of Kaerger & Ruthven (1992) and Cussler (2009), a current and clear review on the topic of gas surface diffusion in porous structures is given by Medved & Černý (2011).

Since pore size is related to gaseous rarefaction, surface diffusion is assumed here to contribute to the entire flow rate in microscale ducts when the pressure is sufficiently low.

Due to thermal motion, gas molecules collide inevitably with a close-by surface and can be reflected, get adsorbed, or also migrate on the surface, dependent on the ratio of gas-gas to gas-solid interaction strength (Kolasinski, 2001). In case of an ideal surface a monolayer or a layer with a thickness of several molecules is formed. More realistic is the formation of islands due to high-energetic defect sites like steps and kinks or functional groups (Oura *et al.*, 2003). The adsorption process can therefore be considered as the first step of surface diffusion. Simultaneously and consequently, the adsorption process is a mass transport resistance: No surface diffusion without previous adsorption.

After adsorption of molecules from the bulk, the second step is the directed motion of the adsorbed phase when a concentration gradient is present. Commonly, the activated, or site-

hopping mechanism is used to describe submonolayer surface diffusion (Smith & Metzner, 1964; Mason *et al.*, 1967; Roybal & Sandler, 1972). For the description of further possible surface diffusion mechanisms reference is made to the book of Oura *et al.* (2003).

### 3.4.6 Maxwell-Stefan approach for modeling surface diffusion

Crucial for the amount adsorbed are temperature (which corresponds to the kinetic energy  $kT$ ) and the pressure of the bulk phase (representing the concentration of molecules in the bulk). Assuming isothermal conditions, the amount adsorbed is a function of the pressure. With increasing  $p$  the thermodynamic equilibrium between bulk phase and adsorbate phase is shifted to a higher surface coverage  $\theta$  which is the ratio of amount adsorbed  $q$  to the maximum amount adsorbed  $q^*$ . The isotherm developed by Langmuir (1933) has proven to be useful in explaining

experimental data and for theoretical deliberation (Myong, 2004). The expression for  $\theta$  according to Langmuir's isotherm is

$$\theta = \frac{q}{q^*} = \frac{pK_L}{1 + pK_L}, \quad (3.74)$$

with  $K_L$  being the Langmuir constant. The Langmuir adsorption isotherm is characterized by the fact that the gradient  $\Delta q/\Delta p$  increases with decreasing  $p$  (Figure 3.8). For an isothermal, pressure driven gas flow,  $\Delta p = p_i - p_o$  is the difference of inlet pressure to outlet pressure. Thus, for a given  $\Delta p$  the difference of adsorbed gas molecules  $\Delta q$  increases with rarefaction ( $\text{Kn} \propto p^{-1}$  according to Eq. (1.2)).

When the amount adsorbed at the duct inlet  $q_i$  is related to  $p_i$  and  $q_o$  depends on  $p_o$  respectively, a concentration difference of adsorbate  $\Delta q$  occurs over the length of the duct. This difference, which is the driving force of surface diffusion, increases with decreasing absolute pressure and increasing Knudsen number, respectively.

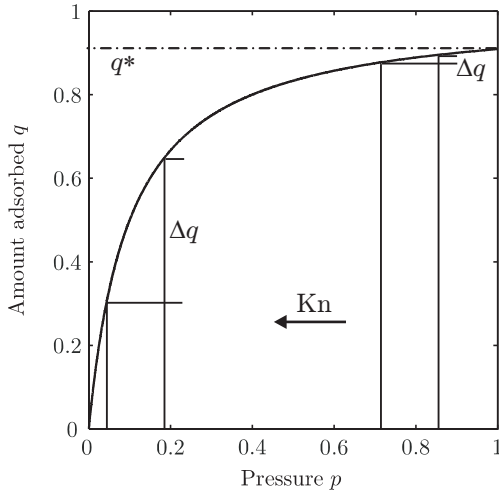


**Figure 3.8:** Qualitative Langmuir adsorption isotherm. The concentration difference of adsorbed gas molecules  $\Delta q$  due to a constant  $\Delta p$  in the gas phase decreases with increasing pressure  $p$  and decreasing  $\text{Kn}$  respectively. The coverage is limited to the maximum amount adsorbed  $q^*$  which depends on the kind of gas and on topology and chemistry of the solid surface.

In Figure 3.9 the contribution of the transport mechanism to an isothermal gas flow caused by  $\Delta p$  is illustrated qualitatively with respect to the rarefaction. At high absolute pressure the surface of the duct is completely covered with the maximum amount that can be adsorbed (Figure 3.8) and thus  $q_i \approx q_o \approx q^*$ . Thus  $\Delta q$  is near zero and hence there is no contribution of surface diffusion. The entire mass flow is dominated by convection superimposed with a negligible contribution of molecular spatial diffusion (Veltzke & Thöming, 2012).

With decreasing pressure the amount adsorbed at the duct outlet is significantly smaller than  $q^*$  and  $q_i$  and thus a  $\Delta q$  occurs with the result of surface diffusion mass flow. The relative contribution of convection abates. Under very low pressure (high  $\text{Kn}$ ) the entire coverage is low but the difference is high (see Figure 3.8). Thus the entire flow is determined by Knudsen

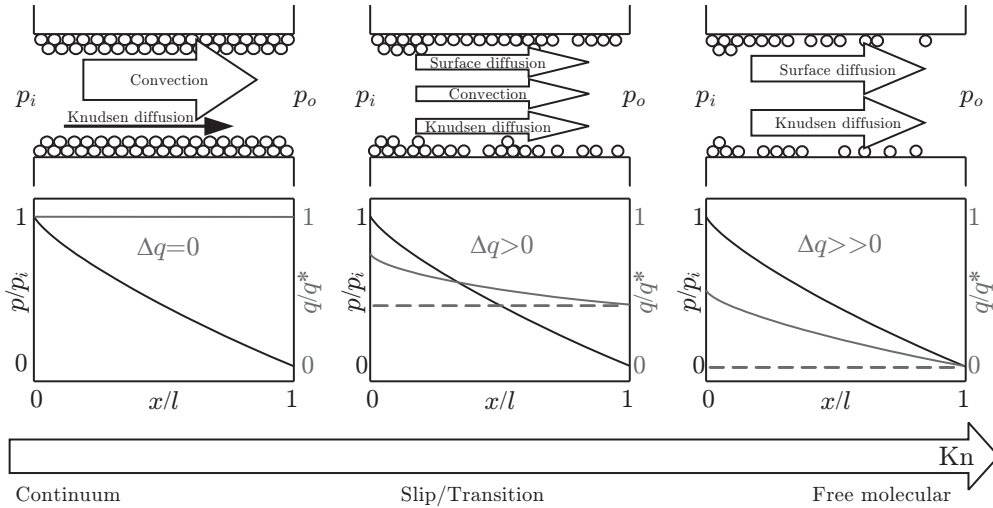


**Figure 3.9:** Qualitative contribution of transport mechanism to the total flow. The driving force  $\Delta q$  for surface diffusion depends on absolute pressure of the bulk which corresponds the gaseous rarefaction according to Eq. (1.2) on page 2.

diffusion superimposed with surface diffusion.

So far, this hypothesis only concerns the dependence of the driving force on the bulk pressure. The dependence of the diffusivity is vice versa since low bulk pressure causes low coverage and hence only very few molecules which can migrate on the surface. Thus the absolute surface diffusion flux results from the driving force as well as from the surface coverage. In general the Maxwell-Stefan (M-S) approach is chosen to describe diffusion of two or more species as these mass flows always depend on each other. This is also the case for surface diffusion of single gas where two separate species occur: Molecules in gas bulk phase ( $p$ ) and those adsorbed on the surface ( $q$ ). Basic assumption is that bulk phase and adsorbate phase are in an equilibrium state. Following Krishna & Wesselingh (1997), the M-S approach combined with the Langmuir adsorption isotherm (which implicitly implies equilibrium) yields a reasonable expression for the description of surface diffusion phenomena which is proven by experimental work and simulation (Moon *et al.*, 2005; Markovic, 2009; Krishna & van Baten, 2009). The Maxwell-Stefan diffusivity  $D_{MS}$  of the flux  $J$  in a single component system

$$J = -D_{MS} \frac{\partial \theta}{\partial x} = -D_{S} q^* \frac{1}{1 - \theta} \frac{\partial \theta}{\partial x}, \quad (3.75)$$

is also referred to as *corrected diffusivity* (Ruthven, 1984) since it depends on  $\theta$  in contrast to Fickian diffusivity  $D_F$  (compare Eq. (3.41) on page 33). According to Eq. (3.75) the M-S diffusivity decreases with surface coverage (Krishna & Wesselingh, 1997) which confirms the hypothesis stated above.

Thus, under a given rarefaction,  $D_{MS}$  must increase with the surface area of a microscale duct because the absolute amount adsorbed increases also. This qualitatively explains the increase of  $G$  after Knudsen's minimum in Figure 2.4 on page 14.

For modeling the third mass transfer term, assumption is being made that at every longitudinal increment  $\partial x$  the adsorbed phase is in thermodynamical equilibrium to the gas phase in

terms of the Langmuir isotherm (Figure 3.8). According to the M-S approach by Krishna & Wesselingh (1997) the flux  $J$  according to Eq. (3.75) along the walls of a duct is proportional to the surface diffusion coefficient  $D_S$ . According to Oura *et al.* (2003)  $D_S$  for mass diffusion at real surfaces is given by an Arrhenius approach depending on the activation energy of diffusion  $E_{\text{dif}}$  and the energy of adatom formation  $\Delta G_A$ :

$$D_S = \frac{\nu_0 a^2}{z} \exp\left(-\frac{\Delta G_A + E_{\text{dif}}}{kT}\right). \quad (3.76)$$

Here  $a$  is the adsorption site spacing and  $z$  is the number of neighboring sites (which is  $z = 2$  when assuming transport only along the coverage gradient). Further  $\nu_0$  is the oscillation frequency of the adsorbed molecule which is  $kT$  divided by Planck's constant, and thus only affected by temperature.

Separation of variables in Eq. (3.75) and integration from  $x = 0$  to  $l$  and from inlet coverage  $\theta_i$  to outlet coverage  $\theta_o$  respectively, yields

$$J = -\frac{D_S q^*}{l} \log\left(\frac{1 - \theta_i}{1 - \theta_o}\right) = \frac{D_S q^*}{l} \log\left(\frac{p_i K_L + 1}{p_o K_L + 1}\right). \quad (3.77)$$

To obtain the surface diffusion mass flow rate, Eq. (3.77) is multiplied with cross-sectional area and molar mass

$$\dot{m}_S = \frac{A}{l} D_S q^* M \log\left(\frac{p_i K_L + 1}{p_o K_L + 1}\right). \quad (3.78)$$

From Eq. (3.78) it can be seen that  $\dot{m}_S$  increases with mean pressure and approaches zero when  $p_o \rightarrow p_i$ . Corresponding to intuition,  $\dot{m}_S$  increases with surface diffusivity  $D_S$  and maximum amount adsorbed  $q^*$ .

Here it has to be mentioned for the sake of completeness that the assumption of adsorption-desorption equilibrium for modeling surface diffusion under steady-state conditions lacks accuracy because adsorption and desorption rates are assumed to be constant at every longitudinal position of the duct (Argönül *et al.*, 2007).

Nevertheless, it can be expected that the adsorption and desorption process occur on a microscopic time scale which is completely different to those of migration of the adsorbed gas molecules, as it is pointed out by Brenig (1987). Hence assumption is being made that a *quasi*-equilibrium state between the moving bulk and adsorbate phase exists. Hence the use of the expression of Langmuir (1933) for mathematical modeling has its justification.

### 3.4.7 Superposition of mass flow contributions

According to Eq. (3.29) on page 31 the derived equations for the three transport mechanism are added to obtain the entire mass flow rate. Consequently the entire mass flow rate is

$$\dot{m} = \frac{A}{Pl} \left( \frac{KA^2 M p_m \Delta p}{2P\mu RT} + \frac{4A\Delta p}{3} \sqrt{\frac{2M}{RT}} + PD_S q^* M \log\left(\frac{p_i K_L + 1}{p_o K_L + 1}\right) \right), \quad (3.79)$$

being the sum of convective transport according to Eq. (3.40), molecular spatial diffusion corresponding Eq. (3.49) and surface diffusion expressed by Eq. (3.78).

For the purpose of a dimensionless expression of  $\dot{m}$ , the reduced mass flow rate  $G$  is introduced

as the ratio of the entire mass flow rate  $\dot{m}$  to the mass flow rate of molecular spatial diffusion  $\dot{m}_D$  according to Eq. (3.49):

$$G = \dot{m} \frac{3Pl}{4A^2\Delta p} \sqrt{\frac{RT}{2M}} = \frac{3KPp_m}{32\Gamma\mu} \sqrt{\frac{M}{2RT}} + 1 + \frac{3\Gamma D_S q^*}{P\Delta p} \sqrt{\frac{RTM}{2}} \log\left(\frac{p_i K_L + 1}{p_o K_L + 1}\right), \quad (3.80)$$

with  $\Gamma = P^2/(4A)$  being the ratio of squared perimeter to cross-sectional area and  $K$  according to Eq. (3.40). Hence  $\Gamma$  is a measure of the aspect ratio of the duct: For a tube  $\Gamma = \pi$  reaches its minimum since the ratio of enclosed volume to duct surface is minimal. For a rectangular channel with high aspect ratio  $\Gamma$  increases with  $w/h$ .

Using the left-hand side of Eq. (3.80), experimentally determined mass flow rates can be non-dimensionalized independent of the cross-sectional shape of the duct.

Finally Eq. (3.80) is expressed as a function of rarefaction in terms of the mean Knudsen number according to Eq. (3.2) as

$$G = \frac{3Kk}{64\pi\sigma^2\mu \text{Kn}_m} \sqrt{\frac{MT}{R}} + 1 + \frac{3\Gamma D_S q^*}{P\Delta p} \sqrt{\frac{RTM}{2}} \log\left(\frac{p_i K_L + 1}{p_o K_L + 1}\right). \quad (3.81)$$

From this expression it can be clearly seen that the convective contribution decreases with increasing rarefaction. Per definition the contribution of molecular spatial diffusion is throughout unity and independent of  $\text{Kn}_m$ . The contribution of surface diffusion increases first of all with the aspect ratio expressed by  $\Gamma$ , secondly with decreasing absolute pressure of the gaseous phase (low  $p_i$  and  $p_o$  yields high  $\dot{m}_S$ ) and thirdly with surface diffusivity  $D_S$  (Eq. (3.76)) and maximum amount adsorbed  $q^*$ .

This analytical investigation of the derived expression is in excellent agreement to the hypothesis stated in section 3.4.6 and qualitatively sketched in Figure 3.9 on page 43.

In the following chapter, the mathematical models derived in this work are evaluated by means of experimental results taken from literature.

As mentioned above, the contribution of surface diffusion is affected by parameters regarding the Langmuir adsorption model and the surface diffusivity. Hence the surface chemistry of the duct walls and the interaction of gas molecules with the surface is assumed to have significant influence on the mass flow rate when rarefaction increases.

In the last section of this chapter hypothetical correlations between gaseous mass flow rate and surface chemistry and gas-surface interactions are discussed. Consequently the opportunities of functionalization of the microchannel surface are highlighted. Based on theoretical considerations, functionalization agents are reviewed with the aim to functionalize a test channel. The experimental approach is described in section 5.3 and the results are given in section 6.3.

### 3.5 Theoretical opportunities of functionalization of the microchannel surface

In sections 3.3.2, 3.3.3, and 3.3.4 influence parameters on the tangential momentum accommodation coefficient, and thus on the behaviour of micro flows were discussed. The impact factors include the gas-solid pairs and their interaction due to chemical potentials, varieties of surface conditions such as lattice configurations, surface roughness, and presence of adsor-

bents (Cao *et al.*, 2009).

In section 3.4.6 the surface chemistry was identified to influence the gaseous flow rate when rarefaction and aspect ratio  $\Gamma$  of the duct are high. Following Eq. (3.81) the reduced mass flow rate  $G$  depends on  $D_S$  according to Eq. (3.76) and on  $q^*$  and  $K_L$  from the Langmuir equation (Eq. (3.74)). These three parameters strongly depend on the interaction strength of the gas molecules to the surface. Hence the surface chemistry is crucial for  $G$  when the requirements for dominance of the surface diffusion term (high Kn and  $\Gamma$ ) are given (compare Figure 3.9).

If it is possible to specifically enhance or reduce  $D_S$  or  $q^*$  for a given gas by means of altering the surface chemistry of a microchannel, surface functionalization may open novel opportunities on knowledge gain in the field of rarefied gas flows.

In the following subsection, hypothetical effects of the surface chemistry on rarefied flows are discussed with respect to the surface diffusion term of the derived model (Eq. (3.78)). Based on these theoretical considerations a selection of possible functionalization agents is given in section 3.5.2.

In the experimental part of this thesis, one of the considered agents is used for surface functionalization of etched silicon microchannels (section 5.3). A comparison of gas flow experiments on the same channels before and after functionalization is given in section 6.3.

### 3.5.1 Hypothetic effect of surface chemistry on flow behaviour

According to the hypothesis formulated in section 3.4.6 and illustrated by means of Figure 3.9, surface diffusion is the only transport mechanism which is affected by the surface.

The first step of gaseous surface diffusion (heterodiffusion) is the adsorption of bulk molecules at the surface. Adsorbed molecules are referred to as *adparticles*. In most cases, the adparticle becomes mobile due to thermal activation and its motion is described as a random walk. In the presence of a concentration gradient, the random walk motion of many particles results in their net diffusion motion in the direction opposite to the direction of the gradient (Oura *et al.*, 2003).

The preceding adsorption process and the surface diffusion itself are affected by many factors such as gas-solid interactions, formation of surface phase (Oura *et al.*, 2003), presence of defect sites (related to surface roughness), and temperature. Strikingly, the same influence parameters are identified when referring to tangential momentum accommodation.

Under ambient conditions, gas molecules adsorb by means of *physisorption*, which is defined by its significantly weaker binding strength compared to *chemisorption*. The binding of gas molecules to the surface is due to intermolecular forces without electron transfer (Bathen & Ciprian, 2006). These are

- coulombic attractions of charged molecules,
- attractive forces between two dipole or quadrupole,
- dipole-ion interactions, and
- van-der-Waals forces between neutral particles, and neutral and polar particles, respectively.

Gas adsorption at surfaces is as wide-ranging as widely studied. For further reading reference is made to Kolasinski (2001) and further basic literature (Brunauer, 1945; Somorjai, 1972; Atkins, 1978).

As already mentioned in section 3.4.6, adsorption takes place at high-energetic sites (steps, kinks, functional groups) and defects. An extensive introduction on surface science is given by Oura *et al.* (2003). Concerning detailed data on structural defects at surfaces reference is made to Henzler & Ranke (1993).

Thus, when covering or replacing the high-energetic sites of a surface by means of an irreversible chemical functionalization, gas adsorption and hence surface diffusion can be altered. As a proof of principle of the stated considerations, a hydroxylated silicon surface is assumed and shown in Figure 3.10. Here the example of hydroxylated silicon is chosen since experiments of gaseous microflows are often performed on channels etched in silicon, whereby the surface is hydroxylated. As illustrated by means of the MD simulated silicon surface by Cole *et al.* (2007) in Figure 3.10, the topmost atom layer features unsaturated bindings. After contact with oxygen of the ambient air, a passivating oxidation layer is spontaneously formed and the surface gains an energetically stable state.

Following Zhang (2001), real silicon surfaces are covered by an amorphous layer with a thickness of 5–20 Å. Due to the humidity of the ambient air, polar hydroxyl groups are formed which cause hydrophilic behaviour of the surface. The coverage typically ranges from 4.6 to 5.5 OH groups per nm<sup>2</sup> (Zhuravlev, 1987; Vansant *et al.*, 1995).

Furthermore, water molecules adsorb at this strong polar surface to the effect that real silicon surfaces are always covered with a thin water film (Wiegand, 2001; Cole *et al.*, 2007).

How do gas molecules (e.g. argon, nitrogen, carbon dioxide) interact with such a surface? As figured out by Shamir *et al.* (1999), argon and nitrogen interact even at room temperature with a hydroxylated silicon surface. Shamir *et al.* attribute the interaction potential (which causes adsorption) to an induced polarization of the neutral gas molecules by means of the negative charge of the surface.

Furthermore, carbon dioxide also adsorbs at a silicon surface at room temperature as it is experimentally shown by Antonini & Hochstrasser (1972) and Ueno & Bennett (1978). The higher the concentration of OH groups at the surface, the more CO<sub>2</sub> molecules adsorb (Ueno & Bennett, 1978). Due to the relative strong quadrupole of the carbon dioxide molecule (Xu *et al.*, 2008), the interaction to the surface of an etched channel is considered to be higher compared to higher-symmetric gases with less degrees of freedom (e.g. noble gases, nitrogen).

Nevertheless, all the considered gases adsorb at the surface of etched microchannels and hence a contribution of spatial surface diffusion exists when a concentration gradient is present. Consequently a functionalization of the surface should qualitatively alter the flow behaviour (permeability) of all gases.

In the following subsection, functionalization methods and agents are analyzed with respect to alter the interaction potential of the surface.

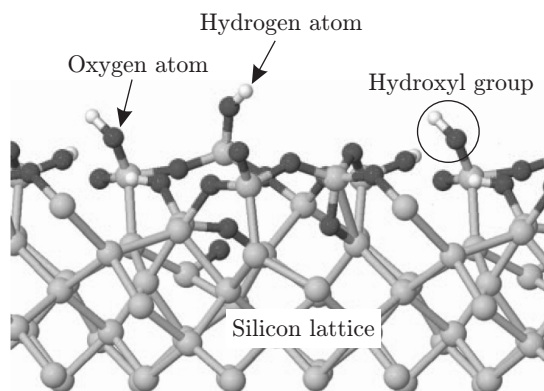


**Figure 3.10:** Hydroxylated silicon surface obtained by MD simulation by Cole *et al.* (2007). Hydroxyl groups are bound onto a naturally oxidized silicon surface.

### 3.5.2 Approach and selection of possible functionalization agents

Due to the previously discussed characteristic of the silicon surface, it is assumed that a modification of the hydroxyl groups causes an alteration of gas-wall interactions. Hence an enhancement of the amount of OH groups should increase the interaction potential, while a removal should act as vice versa. For both cases, an alteration of the flow behaviour under high rarefaction is expected.

As mentioned in the last section and illustrated by means of Figure 3.10, an etched silicon surface is saturated with a specific concentration of OH groups. Hence an irreversible, energetically stable increase of the OH concentration is difficult to achieve. One possibility is the plasma activation of a silicon surface as described by Olbrechts *et al.* (2006) or Habib *et al.* (2010). When the surface is exposed to the plasma, adsorbed molecules like hydroxyl groups and organic contaminants are removed (Kissinger & Kissinger, 1991; Habib *et al.*, 2010). Further, oxygen radicals are implemented in the existing amorphous layer (Olbrechts *et al.*, 2006). Both effects yield additional binding sites for adsorption of (new) hydroxyl groups. After exposition to the atmospheric ambience, a huge amount of new OH groups is formed spontaneously.

This method is used for preparation of a microchannel by Tan *et al.* (2010). Here the hydrophilicity of a polydimethylsiloxane (PDMS) microchannel is enhanced for microflow experiments with water.

Nevertheless, the enhanced OH concentration is temporarily unstable. It is observed that the polarity of the surface steadily decreases with time (Kissinger & Kissinger, 1991; Wiegand, 2001; Habib *et al.*, 2010; Tan *et al.*, 2010). The duration until the initial concentration is regained varies from 20 h (Habib *et al.*, 2010) over seven days (Tan *et al.*, 2010) up to 20 days (Kissinger & Kissinger, 1991).

On the other hand, a temporarily stable reduction of OH groups is simple to achieve by means of chemical functionalization. One possibility is the silanization as it is shown in Figure 3.11. In the reaction scheme octadecyltrichlorosilane (OTS,  $C_{18}H_{37}Cl_3Si$ ) is shown as a

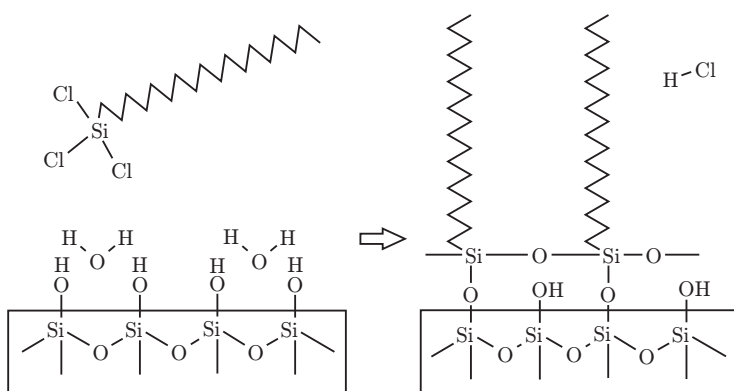


**Figure 3.11:** Silanization reaction of a hydroxylated silicon surface with a monolayer of adsorbed water. Own illustration following Zhuang *et al.* (2007) and Yang (2008).

possible agent to silanize a hydroxylated silicon surface.

According to Figure 3.11, even a monolayer of adsorbed water is sufficient for that the hydrolysable headgroup of the OTS molecule binds strongly at the surface. For each bound molecule, three hydrochloric acid molecules are released. After silanization, the nonpolar

chain of eighteen carbon atoms protrude at the surface like trees. Due to the cross-linking of the OTS, a highly-ordered monolayer is formed and the concentration of effective OH groups is significantly reduced (Kirkpatrick & Muhlstein, 2007).

Silanization can be performed by means of a liquid reaction or by deposition from the vapour phase (chemical vapour deposition, CVD).

For liquid reactions it has been shown that the OTS molecules often agglomerate, and deposition is very inhomogeneous. Thus the surface roughness is significantly enhanced (Dong *et al.*, 2006; Yang, 2008). In contrary, by means of CVD a very homogeneous monolayer can be deposited without negative alteration of surface roughness (Dong *et al.*, 2006).

Consequently a suitable agent and an appropriate method for functionalization is identified. In section 5.3 the microchannel treatment with OTS by means of a self-constructed set-up is described. In section 6.3 it is shown by means of microflow experiments with various gases, if the functionalization has any influence on the gaseous flow behaviour.



# 4 VALIDATION OF THE CDS MODEL BY LITERATURE DATA

The derived model is applied to the prediction of experimental data of gaseous flows in microchannels and microtubes with uniform cross section. A selection of experimental work is already stated in Table 2.1 on page 8. All experimental results which are used to evaluate the model derived in the previous chapter have been performed under isothermal conditions around room temperature with helium, argon, nitrogen and air as working gases (Table 4.1). The Reynolds number and the Mach number are consistently low so that the assumptions stated in section 3.4.1 are complied. In Table 4.1 the geometric properties of the test ducts

**Table 4.1:** Values of geometrical and process parameters in gas flow experiments taken from literature. Temperatures marked with  $\dagger$  are not stated in primary literature and assumed as room temperature (298 K).

References	Geometry and size		Gases	$T$ (K)
	Circ., $\ell = d$ ( $\mu\text{m}$ )	$l$ (mm)		
Lalonde (2001)	3.9, 20.3, 52.8	20.4, 20.4, 100	Air	294, 298
Ewart <i>et al.</i> (2006)	25.2	53	N <sub>2</sub>	296.5
Ewart <i>et al.</i> (2007a)	25.27	53	He, Ar, N <sub>2</sub>	298 <sup>†</sup>
Marino (2009)	110	150	N <sub>2</sub>	298 <sup>†</sup>
Perrier <i>et al.</i> (2011)	49.6	18.2	He, Ar, N <sub>2</sub>	296.5
Yamaguchi <i>et al.</i> (2011)	535.6	46.9	N <sub>2</sub>	293
	Rect., $\ell = h; w$ ( $\mu\text{m}$ )			
Shih <i>et al.</i> (1996)	1.2; 40	4	Ar	293
Arkilic (1994)	1.33; 52.25	7.5	He	314
Arkilic <i>et al.</i> (1997a)	1.33; 52.3	7.49	Ar	293
Arkilic <i>et al.</i> (1997b)	1.33; 52.25	7.5	He	314
Zohar <i>et al.</i> (2002)	0.53, 0.97; 40	4	Ar, N <sub>2</sub>	293
Ewart <i>et al.</i> (2007b)	9.38; 492	9.39	He	$\sim$ 296
Gaur <i>et al.</i> (2009)	9.38; 492	9.39	Ar, N <sub>2</sub>	$\sim$ 293
Pitakarnnop <i>et al.</i> (2010)	1.88; 21.1	5	He, Ar	298.5
	Diverse, $\ell = d_h$ (mm)			
Varoutis <i>et al.</i> (2009)	$\approx$ 16	1,277	N <sub>2</sub>	298 <sup>†</sup>

stated in primary literature are given as well as the characteristic length of the Knudsen number  $\ell$  according to Table 3.3 on page 39. Also temperatures  $T$  and the gases used in experiments are stated to indicate which physical properties are used for calculation. The appropriate gas properties are given in Table 4.2.

**Table 4.2:** Properties of gases used in cited literature. The molecular diameter of Air is calculated as the weighted average of the diameters of N<sub>2</sub> and O<sub>2</sub>. The values for the molecular diameter are taken from Cussler (2009). Values in brackets are unused here but stated for completeness.

Gas	$M$ (g mol <sup>-1</sup> )	$\sigma$ (pm)	$\mu$ (10 <sup>-5</sup> Pa.s)		
			293 K	298 K	314 K
He	4.003	255.1	1.997	2.019	2.088
Ar	39.95	354.2	2.255	2.286	(2.383)
N <sub>2</sub>	28.01	379.8	1.746	1.769	(1.841)
Air	28.96	373.1	1.812	1.836	(1.912)

the appropriate equations. When fitting a curve to a set of data (section 4.2), fitting parameters are varied until the coefficient of determination reaches a maximum (least-squares fitting).

This chapter is sub-divided with respect to the order of rarefaction. Following Figure 1.2 on page 3, first the the so-called slip-flow regime and the beginning transition regime ( $0.01 < \text{Kn} < 0.3$ , section 1.1), are focused in detail. After that the whole range of Kn up to 30 is regarded. Finally the findings of comparison of experimental data to the analytical model derived are briefly discussed.

## 4.1 Slip flow and beginning transition regime

The measured mass flow rate  $\dot{m}$  is put into a non-dimensional form using the Reynolds number

$$\text{Re} = \frac{\rho_o \bar{u}_o \ell}{\mu} = \frac{\rho_o \dot{V}_o \ell}{\mu A} = \frac{\dot{m} \ell}{\mu A}, \quad (4.2)$$

with  $\rho_o$  being the gas density at the duct outlet and  $\bar{u}_o$  is the mean velocity just there. Further the product of the volumetric flow rate at the outlet  $\dot{V}_o$  with  $\rho_o$  equals  $\dot{m}$ . The geometric properties, cross-sectional area  $A$  and  $\ell$ , are calculated according to Table 3.3 on page 39 and stated for both geometries (tube and rectangular channel with high aspect ratio) in Table 4.1.

The modeled mass flow rate according to Eq. (3.50) on page 35 is recalculated likewise as

$$\text{Re} = \frac{d^2 p_o}{\mu R T \ell} \left( \frac{d M p_o}{64 \mu} (P^2 - 1) + \frac{1}{3} \sqrt{2 M R T} (P - 1) \right); \quad (4.3a)$$

$$\text{Re} = \frac{h^2 p_o}{3 \mu R T \ell} \left( \frac{h M p_o}{8 \mu} (P^2 - 1) + \sqrt{2 M R T} (P - 1) \right), \quad (4.3b)$$

for tube and rectangular channel with  $h \ll w$  as a function of the pressure ratio  $P = p_i/p_o$ . The convective and diffusive conductivities in Eq. (3.50) are replaced by  $\Psi$  and  $\Lambda$  stated in Table 3.3.

Figure 4.1 shows Re as a non-dimensional measure of the mass flow rate as a function P.

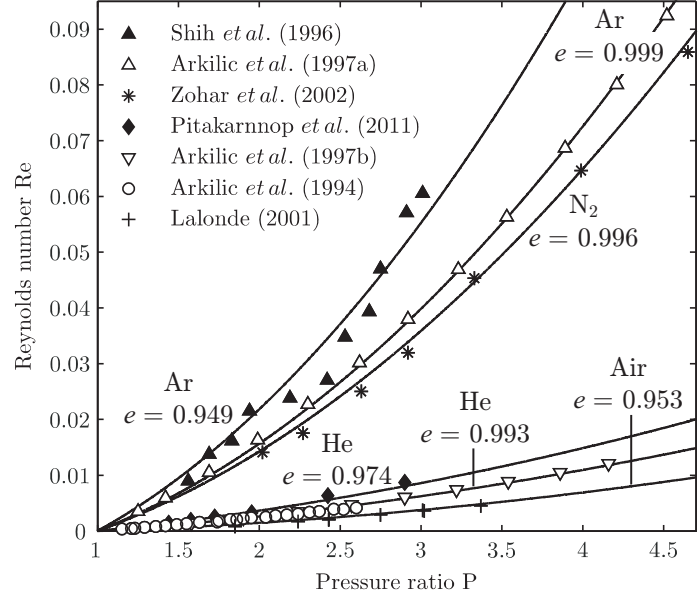
For the quantification of the quality of the derived model, the coefficient of determination  $e$  is used. According to Steel & Torrie (1980)  $e$  is defined as

$$e = 1 - \frac{\sum_{i=1}^n (\omega_i - \hat{\omega}_i)^2}{\sum_{i=1}^n (\omega_i - \bar{\omega})^2}, \quad (4.1)$$

where  $\omega_i$  is the value of the data point (e.g. Re,  $S$ ,  $G$ ),  $\bar{\omega}$  is the average of these and  $\hat{\omega}_i$  is the predicted value calculated with

The experimental mass flows are extracted from the given literature and non-dimensionalized according to Eq. (4.2) for the microchannel experiments and for the microtube data of Lalonde (2001). The geometries of the ducts required for these calculations are specified in Table 4.1 and  $\mu$  is given in Table 4.2. For the microduct experiments shown in Figure 4.1 the outlet pressure  $p_o$  is always kept constant. The quality of the simulation is quantified by the value of  $e$  according to Eq. (4.1) which clearly shows that all experimental data are invariably well predicted.

**Figure 4.1:** Mass flow rate given as Reynolds number versus pressure ratio  $P$  for various channel geometries, gases, temperatures (Table 4.1) and outlet pressures. Comparison of experimental data (symbols) and predictions (lines) yield coefficients of determination  $e$  close to unity. The experimental outlet pressure is kept constant to  $\blacktriangle$ ;  $*$ ;  $\nabla$ ;  $\circ$ ,  $p_o = 100$  kPa;  $\triangle$ , 101.3 kPa;  $\blacklozenge$ , 50 kPa and  $+$ , 102.7 kPa. (Veltzke & Thöming, 2012)



Comparing exemplarily argon flows in rectangular channels, the channel of Shih *et al.* (1996), although smaller in cross-section, yields a higher permeability compared to the channel of Arkilic *et al.* (1997a), which is due to the smaller length. Also comparable are the data of Arkilic *et al.* for argon (Arkilic *et al.*, 1997a) and helium (Arkilic *et al.*, 1997b) generated in the same channel. Due to the distinctly higher molar mass and the lower temperature (see Eq. (4.3b)) the argon flow is much higher despite identical outlet pressure.

Furthermore, another dimensionless mass flow rate  $S$  is introduced as the ratio of the total mass flow rate according to Eq. (3.50) on page 35 to the convective proportion according to Eq. (3.39) on page 33

$$S = \frac{\dot{m}}{\dot{m}_C} = 1 + \frac{\Lambda\mu}{3\Psi p_m} \sqrt{\frac{2RT}{M}}. \quad (4.4)$$

The mean pressure  $p_m$  can be expressed by means of the mean Knudsen number  $\text{Kn}_m$  as a measure of the rarefaction. Thus Eq. (3.2) on page 18 is reconverted to  $p_m$  and applied in Eq. (4.4)

$$S = 1 + \frac{64\pi}{3} \frac{\mu\sigma^2 \text{Kn}_m}{k} \sqrt{\frac{R}{MT}}; \quad (4.5a)$$

$$S = 1 + 8\pi \frac{\mu\sigma^2 \text{Kn}_m}{k} \sqrt{\frac{R}{MT}}. \quad (4.5b)$$

The predicted dimensionless mass flow rate  $S$  is independent of any geometrical property such as length, diameter, width and height and is also independent of the driving force ( $P$  or  $\Delta p$ ). Only the gas ( $\mu(T)$ ,  $\sigma$ ,  $M$ ) affects  $S$ . The comparison of geometries in Eq. (4.5) shows that the only difference consists on a constant factor ( $64\pi/3$  and  $8\pi$ ) which is approximately 2.5 times higher for the tube.

While the model for convective gas flows at laminar and subsonic conditions according to Eq. (3.40) is proportional to the product of  $p_m$  and  $\Delta p$ , the diffusive mass flow according to Fick's first law is merely proportional to the pressure difference (Eq. (3.49) on page 35). Therefore the diffusive proportion of the total flow is high when the mean pressure is low, which is synonymous to a high rarefaction. For high absolute pressures or large pressure gradients the convective transport is dominant.

For an evaluation of the derived model over a wider range of rarefaction, the dimensionless mass flow rate  $S$  as the measured mass flow rate divided by Poiseuille's law for compressible fluids is plotted versus  $\text{Kn}_m$ . Figure 4.2 shows the data points given in literature and the corresponding predictions for tube and channel at room temperature. While  $S$  can be exactly predicted for the tube, the data points of the rectangular channels slightly diverge from the prediction with increasing rarefaction.

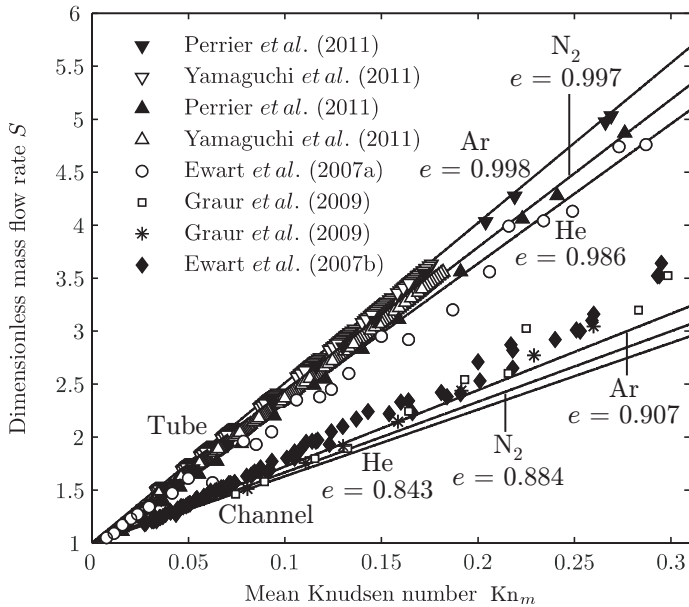


**Figure 4.2:** Dimensionless mass flow rate  $S$  as a function of the rarefaction and appendant predictions (lines). Predictions are calculated by means of Eq. (4.5) with  $T = 298$  K and gas properties given in Table 4.2. (Veltzke & Thöming, 2012)

As mentioned earlier, molecular spatial diffusion is considered as becoming the dominant transport mechanism as rarefaction increases. Thus the diffusive proportion  $X$  is introduced as the ratio of the diffusive mass flow rate according Eq. (3.49) to the total mass flow rate (Eq. (3.50))

$$X = \frac{\dot{m}_D}{\dot{m}} = \frac{\Lambda\mu RT\sqrt{2M}}{3\Psi Mp_m\sqrt{RT} + \Lambda\mu RT\sqrt{2M}}. \quad (4.6)$$

With the convective and diffusive conductivities  $\Psi$  and  $\Lambda$  Eq. (4.6) writes

$$X = \left( \frac{3}{64\pi} \frac{k}{\mu\sigma^2 \text{Kn}_m} \sqrt{\frac{MT}{R}} + 1 \right)^{-1}; \quad (4.7a)$$

$$X = \left( \frac{1}{8\pi} \frac{k}{\mu\sigma^2 \text{Kn}_m} \sqrt{\frac{MT}{R}} + 1 \right)^{-1}, \quad (4.7b)$$

for the tube and the rectangular channel with high aspect ratio. According to (4.7a) and (4.7b),  $X$  rises besides increasing rarefaction with rising viscosity of the gas. This is reasonable due to the inversely proportional dependency of the convective flow on the viscosity.

Since the viscosity of a gas increases with the power of 0.5 with temperature (Atkins & De Paula, 2006), the diminishing influence of the temperature is compensated or overcompensated when using the formula of Sutherland (1895).

Since  $X$  is linked to  $S$  in terms of

$$X = \frac{\dot{m}_D}{S\dot{m}_C}, \quad (4.8)$$

the experimental data can be recalculated accordingly, and are shown in Figures 4.3 and 4.4 where  $X$  is plotted versus the mean Knudsen number. Confirming the hypothesis, the

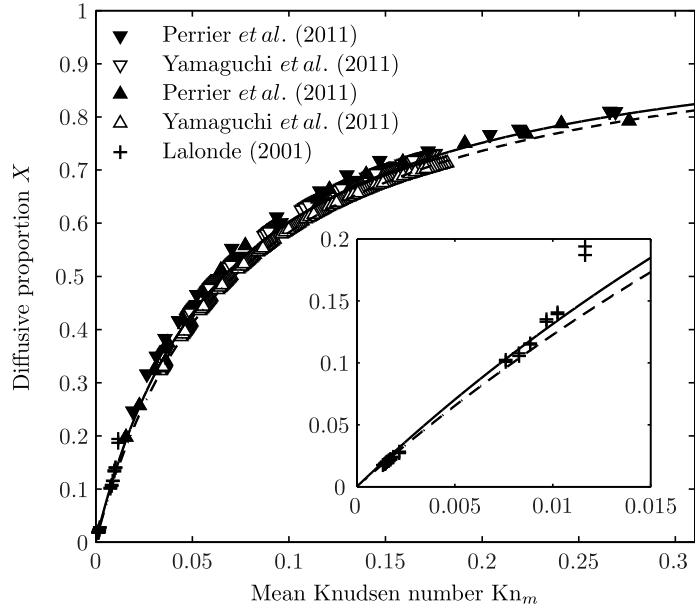


**Figure 4.3:** Diffusive proportion as a function of the rarefaction and appendant predictions (lines) for tubes. Predictions for helium (solid line) and nitrogen (dashed line) are calculated by means of Eq. (4.7a) with  $T = 298\text{K}$  and gas properties given in Table 4.2. (Veltzke & Thöming, 2012)

diffusive proportion increases with rarefaction regardless the cross-sectional geometry. Nevertheless, there are two remarkable differences:

- The indirectly measured diffusive proportion in the tube is significantly higher compared to the rectangular channel with high aspect ratio.
- While the calculation for the tubes match the data exactly (Figure 4.3), a deviation of curves and data is to be seen in Figure 4.4. The model underestimates the data when rarefaction increases.

Hence it must be supposed that diffusion is dependent on the duct geometry due to the ratio

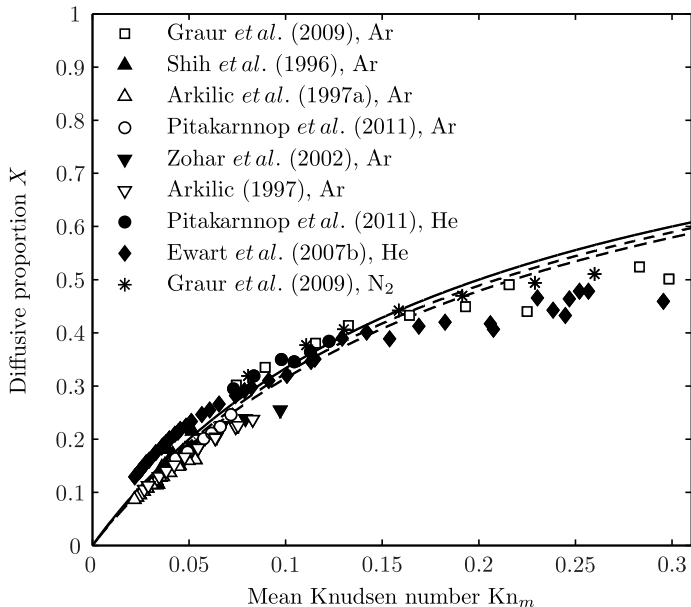


**Figure 4.4:** Diffusive proportion as a function of the rarefaction and appendant predictions (lines) for rectangular channels with high aspect ratio. Predictions for argon, nitrogen and helium are calculated by means of Eq. (4.7b) with  $T = 298$  K and gas properties given in Table 4.2. (Veltzke & Thöming, 2012)

of volume and area of the wall. Holding the minimum in that ratio, the tube reaches the maximal diffusive proportion. Thus it is likely that there is an influence of the wall at higher Knudsen numbers which affects other diffusion mechanism (Malek & Coppens, 2003; Cussler, 2009), which are negligible in the non-rarefied and slightly rarefied regime.

The rarefaction-dependent underestimation of data in channels with high aspect ratio ( $h \ll w$ ) by the evaluated model indicates the presence of an additional flow mechanism which is somehow related to the specific area of the duct wall. Also the contribution of this mechanism must be increasing with  $Kn$ .

In the following section a wider range of rarefaction is regarded to examine this hint.

## 4.2 Free molecular regime

The complete set of reviewed experimental mass flow data over a wide range of rarefaction ( $0.01 < Kn_m < 30$ ) is stated in Table 4.3 and plotted in Figure 4.5 as reduced mass flow rate  $G$  (Eq. (3.81) on page 45) against the mean Knudsen number  $Kn_m$ . Here  $G$  is calculated in terms of  $P$  and  $A$  instead of the channel height or tube diameter as it is done in primary literature. For the abscissa  $Kn_m$  is used as a function of  $d_h = 4A/P$  and mean pressure  $p_m$  according to Eq. (3.2). The geometrical properties for recalculation of data are stated in Table 4.4.

Up to  $Kn_m \approx 0.08$  all data follow the same trend indifferent whether the duct is rectangular with high aspect ratio or of any other cross-sectional shape. Starting in the range of Knudsen's minimum the trend of the data on rectangular channels diverge from the trend of data obtained in ducts with small  $\Gamma$ .

In the rectangular channel the flow rises distinctly with increasing rarefaction after the Knudsen minimum in contrast to the tube (and the other ducts with  $\Gamma/\pi \approx 1$ ) where the level of the flow almost stays constant. Here it is worth noting that the data of Varoutis *et al.* (2009)

**Table 4.3:** Duct geometry and material, temperature, and gases used in mass flow experiments over a wide range of rarefaction ( $0.01 < \text{Kn}_m < 30$ ) taken from literature.

References	Geometry	Surface	Temperature	Gas
Varoutis <i>et al.</i> (2009)	Circular Square Isosc. trapez. Equil. trian.	Stainless steel	Ambient	N <sub>2</sub>
Marino (2009)	Circular	INOX	20 °C	He
Yamaguchi <i>et al.</i> (2011)		Silica		
Ewart <i>et al.</i> (2007b)			291.6 - 297. K	He
Graur <i>et al.</i> (2009)	Rectangular		Ambient	N <sub>2</sub> , Ar, He

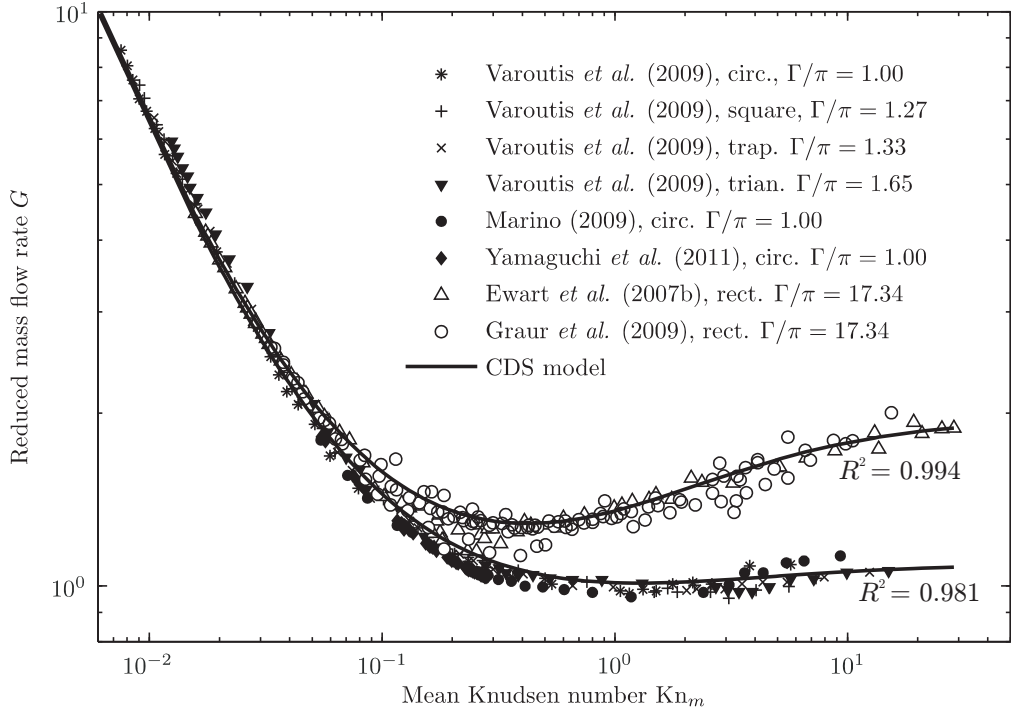


**Figure 4.5:** Reduced mass flow rate  $G$  versus  $\text{Kn}_m$ . Data for various duct cross-sections and gases are taken from literature (Table 4.3) and normalized using values stated in Table 4.4. Exemplarily plotted curves for data of Ewart *et al.* (2007b) obtained on a rectangular channel with high  $\Gamma$  and Varoutis *et al.* (2009) (circular cross section) are calculated according to the CDS model of superimposed flows (Eq. (3.81) on page 45) by adapting  $D_{Sq}^*$  and  $K_L$ . Fitting parameters are varied until the coefficient of determination  $R^2$  according to Eq. (4.1) reaches its maximum (least-squares fitting). All adaption parameters and appropriate  $R^2$  are stated in Table 4.5.

**Table 4.4:** Geometric properties of ducts used in mass flow experiments over a wide range of rarefaction ( $0.01 < \text{Kn}_m < 30$ ). All values are taken from cited literature.

Geometry	$d_h$ (m)	$l$ (mm)	$A$ (m <sup>2</sup> )	$P$ (m)	$\Gamma/\pi$
<i>Circular</i>	$d$		$\pi d/4$	$\pi d$	
Varoutis <i>et al.</i> (2009)	$15.96 \times 10^{-3}$	1277	$2.00 \times 10^{-4}$	$50.14 \times 10^{-3}$	1.00
Marino (2009)	$11.00 \times 10^{-5}$	150	$0.95 \times 10^{-8}$	$34.56 \times 10^{-5}$	1.00
Yamaguchi <i>et al.</i> (2011)	$53.56 \times 10^{-5}$	46.9	$2.25 \times 10^{-7}$	$16.83 \times 10^{-4}$	1.00
<i>Square</i>	$w$		$w^2$	$4w$	
Varoutis <i>et al.</i> (2009)	$15.89 \times 10^{-3}$	1277	$2.52 \times 10^{-4}$	$63.56 \times 10^{-3}$	1.27
<i>Isosc. trapez.</i>	$\frac{2(W+w)h}{W+w+2h/\sin\alpha}$		$\frac{W+2}{2}h$	$W + w + \frac{2h}{\sin\alpha}$	
Varoutis <i>et al.</i> (2009)	$16.48 \times 10^{-3}$	1277	$2.83 \times 10^{-4}$	$68.67 \times 10^{-3}$	1.33
<i>Equil. trian.</i>	$\frac{2}{3}b$		$\frac{4}{\sqrt{3}}b^2$	$3b$	
Varoutis <i>et al.</i> (2009)	$17.06 \times 10^{-3}$	1277	$3.78 \times 10^{-4}$	$88.65 \times 10^{-3}$	1.65
<i>Rectangular</i>	$(2wh)/(w+h)$		$wh$	$2(w+h)$	
Ewart <i>et al.</i> (2007b)	$18.41 \times 10^{-6}$	9.39	$4.61 \times 10^{-9}$	$10.02 \times 10^{-4}$	17.34
Graur <i>et al.</i> (2009)	$18.41 \times 10^{-6}$	9.39	$4.61 \times 10^{-9}$	$10.02 \times 10^{-4}$	17.34

obtained in four channels with different cross section (circular, square, trapezoidal, triangular) but nearly identical  $\Gamma$  show no significant distinction. The crucial difference between channels with high aspect ratio and all other ducts is the relative surface area of the walls which is extremely high for a high aspect ratio and minimal for circular cross section. Also the data obtained in steel tubes (Marino, 2009) and in a silica tube (Yamaguchi *et al.*, 2011) are without any considerable disparity.

The two exemplarily shown curves in Figure 4.5 are found by regression of Eq. (3.80) by adapting the Langmuir constant  $K_L$  and the product of  $D_S$  and  $q^*$ . The adapted parameters for each duct-gas combination are listed in Table 4.5 in the following section. As a measure for the quality of the regression the coefficient of determination according to Eq. (4.1) is used. Therefore a routine is written in MATLAB<sup>1</sup> to find  $K_L$  and  $D_S q^*$  which yield the maximum value for  $R^2$  of each data set.

The logarithmic behaviour of the derived model is in excellent agreement to the experimental data when adapting two parameters in the surface diffusion term. The terms for convection (Poiseuille's law) and Knudsen diffusion are consistently predictive. Knudsen's minimum is described reliably due to the decreasing contribution of convection and the emerging contribution of surface diffusion nearby the minimum.

### 4.3 Discussion of findings

A consistently predictive model is presented for the analytical calculation of microduct gas flows at low Mach number and moderate rarefaction ( $\text{Kn} < 0.3$ ). The entire mass flow rate is considered as a simple superposition of convective transport and molecular spatial diffusion since the surface diffusion term is negligible for low  $\text{Kn}$  (see Figure 4.6). The model is applied

<sup>1</sup>MATrix LABoratory, R2010b

to the simulation of experimental results given in literature. For all measurement series on microtubes the calculated curves match the data points accurately (Figures 4.2 and 4.3), which yields two consequences for modeling rarefied gas flows:

- A prediction of the mass flow rate (or pressure drop likewise) is possible without the assumption of wall slip in the so-called slip-flow and transition regime (Gad-el-Hak, 1999). Knowing geometrical dimensions of the duct, temperature, gas properties, and inlet- and outlet pressure, the resulting mass flow rate can be calculated without any adaption parameter, as which the TMAC can be termed.
- The classification of non-rarefied to moderately rarefied gas flows in continuum, slip and transition regime (Figure 1.2 on page 3) becomes obsolete when the flow is considered as a superposition of different flow mechanisms over the whole range of Kn.

For rectangular channels data and model diverge with increasing rarefaction ( $\text{Kn} > 0.15$ ) when assuming a superposition only of convection and molecular spatial diffusion. Nevertheless, predictions in the slip regime and beginning transition regime are throughout accurate (Figures 4.1, 4.4 and 4.5).

Concerning moderately rarefied flows it is shown that the diffusive proportion  $X$  and likewise the dimensionless mass flow rate  $S$  is not influenced by any variable regarding the surface topology. In consequence of the broad varying surface roughness (Table 3.2 on page 29) of the ducts the cited authors used, the results of Turner *et al.* (2004) are confirmed thus far, that surface roughness has no influence on mass transfer in slightly and moderately rarefied gas flows. Further the inconsistencies concerning the dependency of the TMAC on surface roughness (section 3.3.4) leads to reasonable doubts about the slip boundary condition and the state-of-the-art approach in modeling flow processes. Nevertheless there might be an influence of roughness at higher Knudsen numbers due to additionally superimposed surface diffusion which is dependent on molecular residence times at the wall (Malek & Coppens, 2003).

In both previous sections it is found that the ratio of channel surface to volume has significant influence on gaseous flows in microducts when rarefaction increases (Figure 4.5). The presented model enables to segregate the different transport mechanism as it is shown in Figure 4.6. Here the data of Ewart *et al.* (2007b) and Graur *et al.* (2009) measured on a rectangular silicon microchannel with high aspect ratio are shown. The derived model is plotted for the single transport mechanism. The convective contribution (thin solid line) descends steeply with increasing

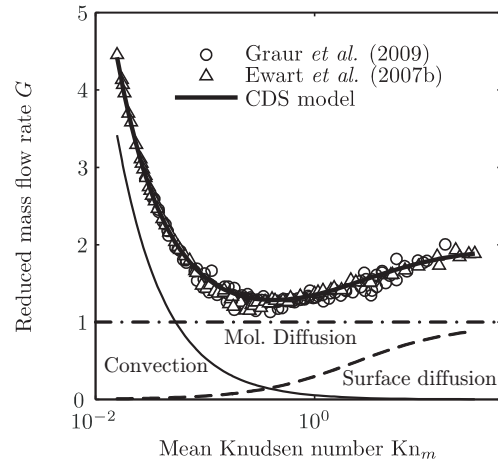


**Figure 4.6:** Segregation of mass transport mechanism in a rectangular channel with high aspect ratio. The reduced mass flow rate  $G$  according to Eq. (3.81) is plotted versus the mean Knudsen number  $\text{Kn}_m$  as a measure of gaseous rarefaction. The single contributions to  $G$  are calculated according to Eqs. (3.40), (3.49) and (3.78) with geometric properties stated in Table 4.4.

rarefaction and is negligible for  $\text{Kn}_m > 1$ . According to Eq. (3.81) on page 45, the contribution of molecular spatial diffusion (thin dotdashed line) is not affected by rarefaction and is unity by definition. The contribution of surface diffusion is shown as thin dashed curve. The thick curve is the total reduced mass flow rate shown in Figure 4.5 as the sum of the three transport mechanisms.

The contribution of surface diffusion is negligible for low rarefaction due to the complete coverage of the duct surface which causes the absence of a driving force. With increasing rarefaction surface diffusion gains importance which finds its expression in the rising of  $G$  after Knudsen's minimum. Due to the dependence of the Maxwell-Stefan diffusivity on the coverage  $\theta$ , this increase is degressive since only few molecules are adsorbed at the surface and can be transported by surface diffusion.

**Table 4.5:** Adaption parameters  $K_L$  and  $D_S q^*$  for regression of the model to experimental data, and coefficient of determination  $R^2$  according to Eq. (4.1). Langmuir adsorption parameters  $K_L$  and  $q_g^*$  of Harlick & Tezel (2003) and Moon *et al.* (2005) are measured by gas chromatography and gravimetric method at 40 °C and ambient temperature, respectively. Surface diffusion coefficient  $D_S$  is measured by Moon *et al.* (2005) using a modified Wicke-Kallenbach experiment. Cells indicated with †: changing of  $K_L$  and  $D_S q^*$  does not affect the values of neither  $G$  nor  $R^2$ ; Cells indicated with ‡: Not stated in primary literature, or no sufficient information for calculation.

Data source	Solid/gas	$K_L$ (Pa <sup>-1</sup> )	$D_S q^* V_{\text{duct}}$ ( $\frac{\text{mol m}^2}{\text{s}}$ )	$R^2$
Varoutis <i>et al.</i> (2009)	Steel/N <sub>2</sub>	/†	/†	0.982
		/†	/†	0.975
Marino (2009)	INOX/N <sub>2</sub>	/†	/†	0.963
Yamaguchi <i>et al.</i> (2011)	Silica/N <sub>2</sub>	/†	/†	0.998
Graur <i>et al.</i> (2009)		$8.493 \times 10^{-3}$	$1.119 \times 10^{-14}$	0.931
	Silica/Ar	$7.213 \times 10^{-3}$	$1.083 \times 10^{-14}$	0.886
	Silica/He	$2.389 \times 10^{-3}$	$1.105 \times 10^{-13}$	0.947
Ewart <i>et al.</i> (2007b)		$2.402 \times 10^{-3}$	$1.102 \times 10^{-13}$	0.994
<i>Chromatographic, gravimetric and Wicke-Kallenbach cell</i>			$D_S q_g^* m_{\text{sample}}$ ( $\frac{\text{mol m}^2}{\text{s}}$ )	
Harlick & Tezel (2003)	ZSM-5/N <sub>2</sub>	$2.906 \times 10^{-6}$	/‡	/‡
Moon <i>et al.</i> (2005)	MTES/N <sub>2</sub>	$4.827 \times 10^{-6}$	$2.102 \times 10^{-13}$	/‡

With finding  $K_L$  and  $D_S q^*$  by least-squares fitting for the optimal regression of  $G$ , adsorption data is "measured" by means of microflow experiments. For the evaluation of the adapted parameters and comparison with conventional measured  $K_L$  and  $D_S q^*$  focus is laid on the solid/gas combination silica/N<sub>2</sub>. The comparison is difficult to that effect that gravimetric or volumetric adsorption measurement of nitrogen is usually performed either at very low temperature, or on porous substrates with very high specific surface (e.g. Vycor glass, zeolites). This might explain why  $K_L$  measured by Harlick & Tezel (2003) and Moon *et al.* (2005) using gas chromatography and gravimetric method respectively, is three orders of magnitude lower compared to the result derived from the experiments of Graur *et al.* (2009) (Table 4.5). Another explanation for the discrepancy is the completely different pressure condition. Harlick & Tezel (2003) measured the amount of adsorbed ranging from 10 to 90 kPa and Moon *et al.* (2005) in a range from 5 to 12 kPa while the microchannel measurements by Graur *et al.* (2009) are performed under conditions down to 14 Pa.

Moon *et al.* (2005) also measured the M-S diffusivity *at zero loading* ( $D_S$ ) of nitrogen on their methyltriethoxysilane (MTES) templating silica layer using a modified Wicke-Kallenbach cell. They found  $D_S$  to be  $2.689 \times 10^{-8} \text{ m}^2 \text{ s}^{-1}$ . Using the gravimetric method for measuring nitrogen adsorption at 293 K, Moon *et al.* (2005) found  $K_L$  and  $q_g^*$  by fitting their data with the Langmuir model (Eq. (3.74) on page 42). They derived  $q_g^*$  to be  $0.0391 \times 10^{-3} \text{ mol g}^{-1}$ . For comparison with the data obtained from microflow experiments, the *absolute* amount adsorbed  $q^*$  (in  $\text{mol m}^{-3}$ ) on the one hand is multiplied with the volume of the duct  $V_{\text{duct}} = whl$  and on the other hand  $q_g^*$  (in  $\text{mol g}^{-1}$ ) with the mass of the sample  $m_{\text{sample}} = 2 \text{ mg}$ . Thus  $D_S q_g^* m_{\text{sample}}$  is  $2.102 \times 10^{-13} \text{ mol m}^2 \text{ s}^{-1}$  which is surprisingly close to the value of  $1.119 \times 10^{-14} \text{ mol m}^2 \text{ s}^{-1}$  which is derived from the microflow data of Graur *et al.* (2009) when using the CDS model according to Eq. (3.81).

This indicates that from mass flow measurements on microscale ducts at low pressure adsorption data could be obtained for materials with very low surface area.

Unfortunately no data is found for channels with high aspect ratio made of steel or another material than etched silicon. Further, Graur *et al.* (2009) used different gases for the measurements but no significant distinction between neither argon, helium nor nitrogen is to be seen (Figure 4.5, Table 4.3). These findings are not inconsistent with the depicted hypothesis of surface diffusion since no serious contribution is expected for the ducts with small  $\Gamma$  indifferent whether made of steel or silicon/silica. Also the different gases used for the experiments of Graur *et al.* (2009) are hardly different regarding the interaction strength to a silica surface. None of the used gases has a dipole or a significant quadrupole moment which causes a high interaction potential to the hydroxyl groups of the silica surface (section 3.5.1). Concerning the adsorption behaviour the measured gases act more or less similar.

As a conclusion of this chapter, it can be argued that the first aim of the thesis formulated on page 4 is sufficiently fulfilled. A mathematical formulation of the stated hypothesis is developed in section 3.4 which is thoroughly evaluated by means of experimental data taken from literature. For the slip-flow regime and the beginning transition regime the analytical model is consistently predictive. With increasing rarefaction the surface diffusion term gains importance and adaptation of two parameters is necessary. However, the shape of the curve (and hence the type of derived function) is in excellent agreement to data.



# 5 EXPERIMENTAL SECTION

This section covers all practical work and experiments presented within the current thesis. First, the investigated microchannels are object of contemplation including manufacturing, geometry and dimensions. In the second section of this chapter focus is laid on the measurement of gaseous mass flow. Herein the experimental set-up is presented being the fixture and periphery for the different microchannel systems. Further attention is payed to data acquisition, resolution of the sensors, analysis of the error distribution and two different methods for evaluating the mass flow measurement method. The third section deals with the functionalization of one microchannel system including apparatus and procedure as well as the verification of the performed functionalization.

## 5.1 Microchannel production

For the experimental studies of the current work two kinds of microchannels are used. On the one hand a single rectangular channel with constant cross section is manufactured with the purpose of validating the experimental set-up for mass flow measurement. Also this channel is used to perform measurements under moderate rarefaction to ensure that a measured diode effect on ducts with slightly varying cross section is not artificially caused by the experimental set-up itself. On the other hand microchannels with alongside slightly varying cross section (further referred to as *tapered microchannels*) are within the scope of experimental investigation (see section 3.4.4). The dimensions of all microchannels investigated in gas flow experiments are stated in Table 5.1.

**Table 5.1:** Dimensions of micromilled tapered notches and etched microchannels used in gas flow experiments. Systems with internal names *Si-7*, *Si-5* and *Si-9* consist of each five silicon wafers (Figure 5.2c) with a varying number of channels  $n$ . The varying number is due to the different ratios of large cross section  $A_l$  to small cross section  $A_s$ .

Name	Material	$n$	Small dimensions ( $\mu\text{m}$ )			Length (mm)
			$h$	$w$	$l$	
<i>RC20</i>	AlMg <sub>3</sub>	1	$20.0 \pm 0.03$	$100.08 \pm 0.06$	$30.01 \pm 0.1$	
<i>Al-3</i>	AlMg <sub>3</sub>	1	$h_s$	$h_l$	$w$	$l$
			$0.98 \pm 0.21$	$252.80 \pm 0.16$	$1007.50 \pm 3.13$	$11.05 \pm 0.1$
<i>Si-7</i>	Si(100)	$5 \times 429$	$w_s$	$h$	$w_l$	$l$
<i>Si-5</i>	Si(100)	$5 \times 350$	$2.2 \pm 0.01$	$9.0 \pm 0.03$	$22.1 \pm 0.08$	$15.0 \pm 0.1$
<i>Si-5</i>	Si(100)	$5 \times 350$	$2.2 \pm 0.03$	$9.0 \pm 0.03$	$27.4 \pm 0.11$	$7.5 \pm 0.07$
<i>Si-9</i>	Si(100)	$5 \times 75$	$2.2 \pm 0.02$	$9.0 \pm 0.03$	$132.0 \pm 0.17$	$15.0 \pm 0.1$

The channels are manufactured by means of two different production methods which are presented in the following subsections.

### 5.1.1 Micromilled aluminum channels

The rectangular channel with uniform cross section with  $20\ \mu\text{m}$  height (*RC20*) and the tapered duct with alongside varying height (*Al-3*) are manufactured by milling a long notch into a piece of aluminum ( $\text{AlMg}_3$ ) using raster fly-cutting. As schematically shown in Figure 5.1a, the notch is capped with another plain piece of aluminum with high quality optical surface. Both parts are screwed together and sealed by means of perfectly plain surfaces. All parts are manufactured by the LFM<sup>1</sup> using a Nanotech 350FG<sup>2</sup>. As cutting tool a diamond facet-tool with a cutting edge width of  $100\ \mu\text{m}$  is used. The cutting conditions are as follows: Spindle turning of  $2000\ \text{min}^{-1}$ ; feed rate of  $200\ \text{mm}\ \text{min}^{-1}$ ; cutting depth of  $25\ \mu\text{m}$  per cut when roughing and  $10\ \mu\text{m}$  for the finishing step.

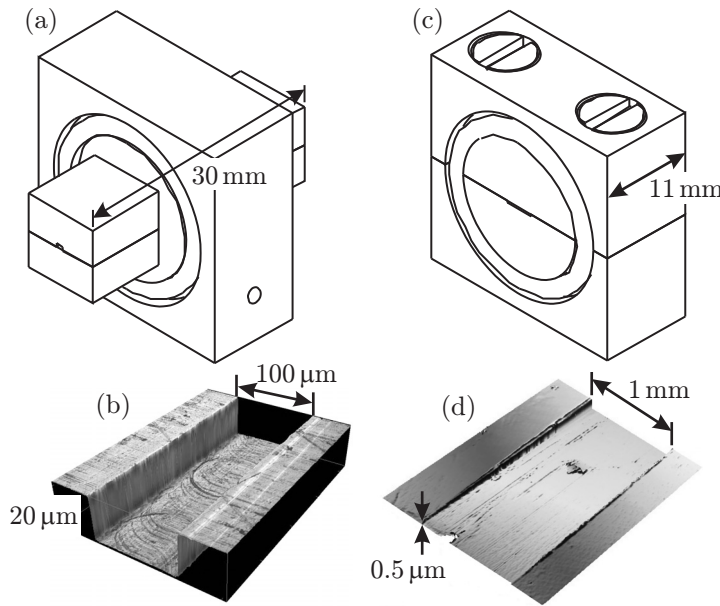


**Figure 5.1:** Microchannels milled in aluminum. A single channel with uniform cross-section is sealed with a plain aluminum cover with a high surface finish and assembled in an aluminum block (a). The gap is sealed with a two-component adhesive. Nominal channel geometries are checked using optical profilometry (b). In (c) the holding fixture of a single tapered channel is shown. The channel accrues by assembling one part with a milled notch with a plain part. High quality optical surfaces act as sealing. Channel length corresponds the block thickness. The notch of *Al-3* with a significant inclination (d) is visualized by optical profilometry.

The length  $l$  of the uniform rectangular channel shown in Figure 5.1a,b is  $30.01 \pm 0.1\ \text{mm}$  and thus large compared to height  $h = 20.0 \pm 0.03\ \mu\text{m}$  and width  $w = 100.08 \pm 0.06\ \mu\text{m}$ . Hence the channel is referred to as a *long channel* where entrance and outlet effects are negligible (Arkilic *et al.*, 2001).

The notch of duct *Al-3* shown in Figure 5.1d has a length of  $11.05 \pm 0.1\ \text{mm}$  which corresponds the thickness of the aluminum block. The height is changing from  $h_s = 0.98 \pm 0.21\ \mu\text{m}$  to  $h_l = 252.80 \pm 0.16\ \mu\text{m}$  while the width of  $w = 1007.50 \pm 3.13\ \mu\text{m}$  is constant.

Each notch width and depth are measured 20 times using optical profilometry (PL $\mu$ 2300, Sensofar) and arithmetic mean (Table 5.1) and uncertainty are calculated. The length is measured by means of direct light microscopy (also 20 times for calculation of arithmetic mean and uncertainty). Both test channels shown in Figure 5.1 can be assembled into the experimental set-up shown in Figure 5.3 in section 5.2.

<sup>1</sup>LFM - Laboratory for Precision Machining, University of Bremen

<sup>2</sup>Moore Nanotechnology Systems, Keene, NH, USA

### 5.1.2 Etched silicon channels

The second type of tapered microchannels is fabricated by deep reactive-ion etching (DRIE) in silicon Si(100) by the IMSAS<sup>3</sup>. This etching method is a standard procedure for production of micro electromechanical systems (MEMS). The processing root is described in detail by Franssila (2010).

The channels are etched in a rectangular wafer and capped with a glass plate by fusion bonding. Dependent on the geometry (internally named *Si-7*, *Si-5* and *Si-9*) each wafer contains  $n$  such channels. As indicated in the scheme in Figure 5.2a the cross-sectional area changes due to the alongside varying width. A more detailed scheme is already shown in Figure 3.6 on page 35.

The channel length  $l$  of  $15.0 \pm 0.1$  mm and  $7.5 \pm 0.07$  mm, respectively corresponds the length of the rectangular wafer the channels are etched in. The height  $h$  (or etching depth) is constant with  $9.0 \pm 0.03$   $\mu\text{m}$  for all three geometries. The 429 channels of *Si-7* have the lowest ratio of inlet to outlet cross-sectional area. Here the width is changing alongside one channel from  $w_s = 2.2 \pm 0.01$   $\mu\text{m}$  at the small aperture to  $w_l = 22.1 \pm 0.08$   $\mu\text{m}$  at the wide aperture. For *Si-9* the wide aperture  $w_l = 132.0 \pm 0.17$   $\mu\text{m}$  is much higher and thus one wafer only contains 75 channels. The width of channels of type *Si-5* is changing from  $w_s = 2.2 \pm 0.03$   $\mu\text{m}$  at the small aperture to  $w_l = 27.4 \pm 0.11$   $\mu\text{m}$  at the wide aperture but the length is different to *Si-7* and *Si-9* (Table 5.1). One *Si-5*-wafer has  $n = 350$  channels.

As indicated in Figure 5.2b,  $w_s$ ,  $w_l$  and  $h$  are measured for 20 channels using scanning electron microscopy (SEM) and arithmetic mean and uncertainty are calculated. The length is measured also for 20 channels using a direct light microscope. The mean surface roughness of the etched silicon and the glass cover is measured to be  $9.8 \pm 0.1$  nm using an optical profilometer (PL $\mu$ 2300, Sensofar).

According to Figure 5.2c five glass-covered wafers are combined to a stack with the purpose to achieve a mass flow which is reliably measurable (compare section 2.2). This bundle is inserted into a quadratic aluminum block (25 mm edge length, 10 mm thick) and sealed with a two-component adhesive. The aluminum block has two bores where thermocouples can be inserted for temperature monitoring during the gas flow measurement.

The aluminum block in which the channel bundle is inserted, is identical to the blocks of

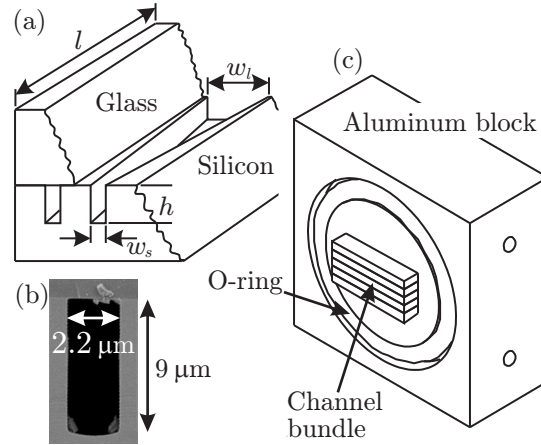


**Figure 5.2:** Tapered microchannels produced by deep reactive-ion etching (DRIE) in silicon wafers. Channels are capped with a glass plate by fusion bonding. Schematic (a) gives the crucial dimensions height  $h$ , small width  $w_s$ , large width  $w_l$  and length  $l$ . In (b) a SEM image of the narrow aperture of one channel is shown. All microscopic dimensions are measured on 20 channels using SEM for calculation of average and uncertainty. To enhance the mass flow, five wafers are combined to a stack which is assembled in an aluminum block (c).

<sup>3</sup>IMSAS - Institute for Microsensors, -actuators and -systems, University of Bremen

the micromilled single test channels. Thus, this channel can also be implemented into the subsequently presented rig.

## 5.2 Mass flow measurement

To obtain meaningful and reliable mass flow data on the previously presented channels, an experimental set-up is designed, constructed and build. The "heart" of the set-up is a temperature-controlled apparatus in which the aluminum blocks with the diverse microducts can be inserted. This rig embedded in its periphery is shown in Figure 5.3.

In the first subsection the hardware (apparatus and periphery) is presented. For detailed manufacturing drawings, photos, data sheets and ex-works calibration certificates of the measuring instruments, reference is made to Appendix A.

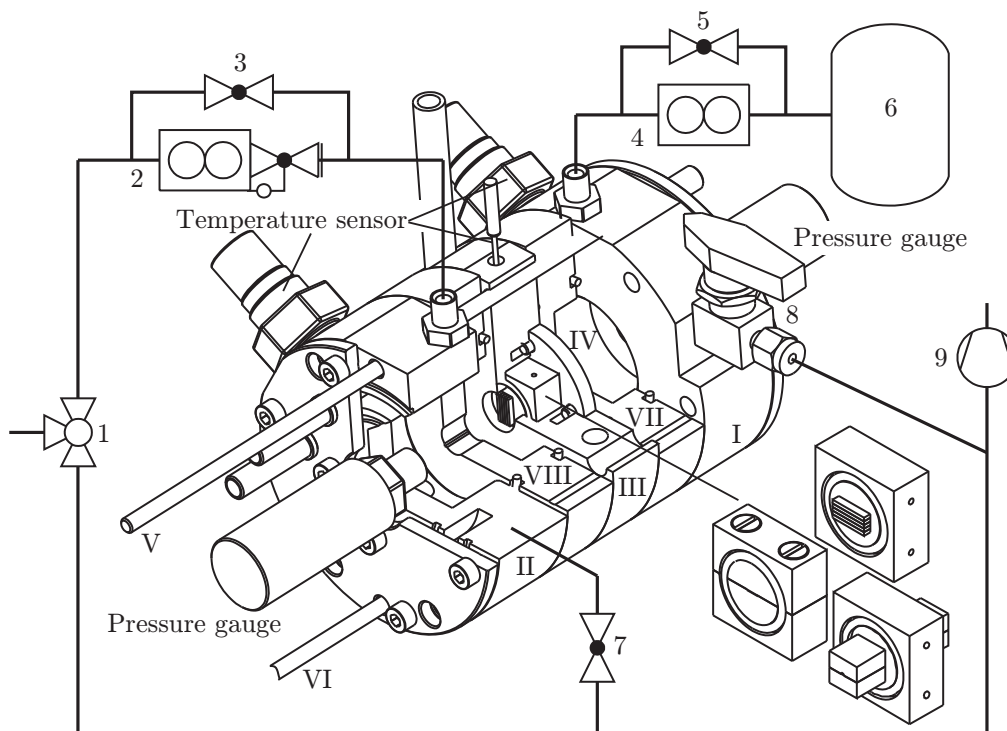


**Figure 5.3:** Sectional drawing of the experimental apparatus embedded in the process flow diagram of the set-up. Beyond the termed elements the set-up includes: Gas supply valve (1); mass flow controller (2); bypass valve (3,5); mass flow sensor (4); pressure vessel (6); ball valve (7,8); vacuum pump (9). All types of channels according to Figures 5.1 and 5.2 used for the experiments can be assembled into the apparatus. Parts indicated with roman numbers are explained in section 5.2.1.

The following subsections emphasise the experimental set-up, data acquisition in terms of analog and digital data processing, two different measurement methods including the evaluation and analysis of errors.

### 5.2.1 Experimental set-up

Figure 5.3 gives a sectional drawing of the experimental apparatus embedded in the process flow diagram of the set-up. The apparatus consists of two chambers in which temperature is measured by PT1000 resistance thermometers (WIKA, TF35) and absolute pressure is measured by a pressure gauge (GE Sensing, PMP4070). The inlet of the upstream chamber is connected to the gas supply (1) via a mass flow controller (2) (Bronckhorst, F-201CV-ABD-11-Z). The outlet of the downstream chamber is connected to a vessel (6) with a volume of 15 liters by a mass flow sensor (4) (Bronckhorst, F-110C-002-AGD-11-V). Technical specification and resolution of sensors are stated in Table 5.2. Both, the mass flow sensor

**Table 5.2:** Technical specification and resolution of the mass flow controller (MFC) and all sensors used in gas flow experiments. All stated values are manufacturer informations.

Value	Controller/Sensor	Range	Accuracy
Mass flow (C)	F-201CV, Bronckhorst	$2.084 \times 10^{-8} \dots 2.084 \times 10^{-7} \text{ kg s}^{-1}$	$\pm 0.5 \%^\dagger$
Mass flow (S)	F-110C, Bronckhorst	$2.918 \times 10^{-10} \dots 1.459 \times 10^{-8} \text{ kg s}^{-1}$	$\pm 2.0 \%^\dagger$
Pressure	PMP4070, GE Sensing	0.1 ... 160 kPa(a)	$\pm 0.04 \%^\dagger$
Temperature	TF35-PT1000, WIKA	-50 ... 300 °C	-

<sup>†</sup> Of the mean

(MFS) and mass flow controller (MFC) can be bypassed (valves 3 and 5) for evacuating and cleaning of the overall system. Furthermore, both chambers have a second connection to a vacuum pump (9) via ball valves 7 and 8 for this very purpose.

The two components bearing the two chambers (I and II in Figure 5.3) are equipped with a circular canal for thermal oil to temper the complete apparatus which is made of stainless steel. When a channel system is newly mounted into the apparatus or is turned over for measuring the permeability in opposite direction, the apparatus is assembled as described subsequently.

As indicated in Figures 5.1, 5.2 and 5.3 all channel systems are integrated in aluminum blocks of identical dimensions with O-rings at the front and back. First the aluminum block is laid into the milling pocket of the central disc (III in Figure 5.3) as it is shown in the exploded assembly drawing in Figure 5.4. The block is fixed by a smaller disc (IV) which presses the O-rings and hence seals the front and back of the central disc. Here four M4 screws are used to press IV into III.

The component with the downstream chamber (I) has two conduction pivots (V and VI in Figure 5.3) with a length of 25 cm. First one disc (VII) with O-rings at each side is slid

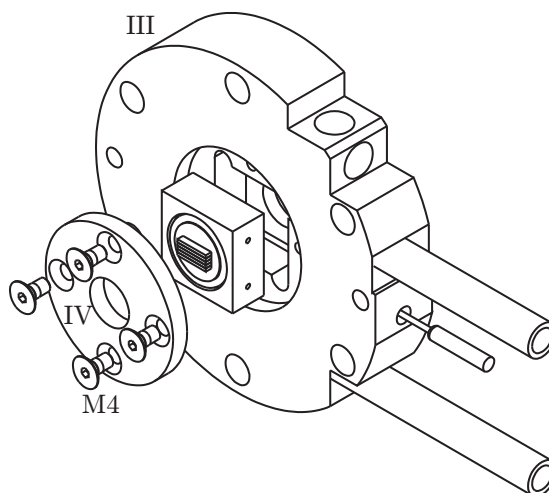


**Figure 5.4:** Assembling of a channel system (etched silicon channels) into the fixture.

on the pivots to touch component I. Then the same is done with the fixture (III) bearing the aluminum block with channels, another disc (VIII) identical to VII, and the component with the upstream chamber (II). Finally six long M8 screws are used to fix the whole apparatus.

### 5.2.2 Data acquisition

Each measuring device listed in Table 5.2 is connected to a power supply and creates an analog signal in return, which is proportional to the physical variable of interest (temperature, pressure and mass flow). The analog signals are converted into a digital signal for further processing and acquisition. As an A/D converter the NI USB-6211<sup>4</sup> of National Instruments is used. This device transforms voltage signals from  $-10$  to  $+10$  V into numerical values as schematically shown in Figure 5.5. Frequency of acquisition can be freely chosen and is adjusted to 6 Hz. Thus for each measured variable six values per second are acquired.

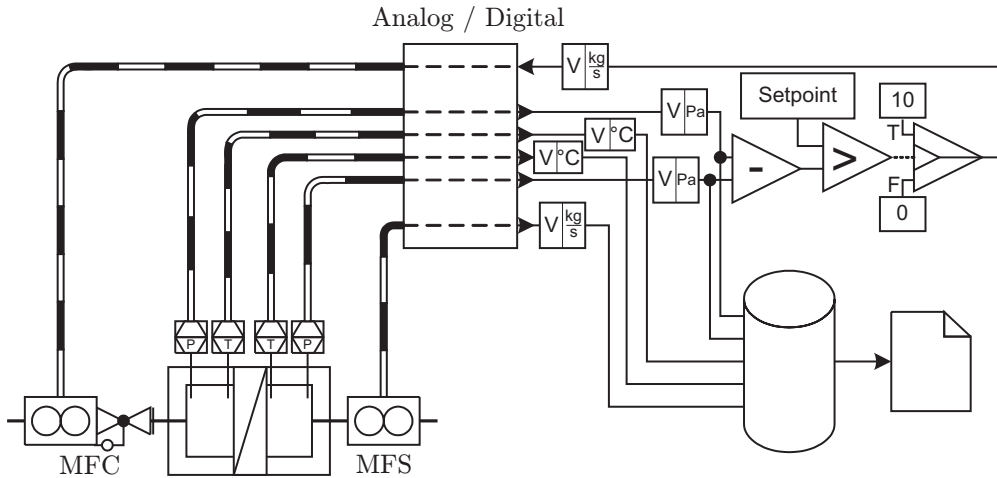


**Figure 5.5:** Interface of hardware and software of the experimental set-up. Analog voltage signals are converted to a digital signal and processed in a virtual instrument programmed in LabVIEW. Sensor calibration, pressure difference controlling and data acquisition are implemented in the virtual instrument. Data is acquired with a frequency of 6 Hz. Selected data (inlet and outlet pressure and temperature, mass flow) is exported to a txt-file.

The PT1000 resistance thermometers (indicated with T in Figure 5.5) receive a highly-constant current of  $I_{const} = 1$  mA. The PT1000 has an electrical resistance which is a function of temperature in terms of

$$R(\theta) = R_0 \left( 1 + B_1\theta + B_2\theta^2 \right), \quad (5.1)$$

with  $B_1 = 3.9083 \times 10^{-3} \text{ } ^\circ\text{C}^{-1}$  and  $B_2 = -5.775 \times 10^{-7} \text{ } ^\circ\text{C}^{-2}$ . The value  $R_0$  is the nominal resistance which is  $1000 \text{ } \Omega$  at  $\theta = 0 \text{ } ^\circ\text{C}$  (Nau, 2004). According to Ohm's law, a voltage signal

$$U(\theta) = R(\theta)I_{const}, \quad (5.2)$$

as a function of the temperature can be measured. As an example, following Eqs. (5.1) and (5.2) an electrical potential of  $U = 1.2$  V is induced at  $\theta = 48.5 \text{ } ^\circ\text{C}$ .

<sup>4</sup>NI USB-6211 with 16-Bit,  $250 \text{ kS s}^{-1}$  M series multifunction DAQ, Bus-Powered

The two pressure gauge indicated with p in Figure 5.5 return a voltage signal in the range of 0 to +10 V which proportionally covers the measuring range from 0 to 160 kPa(a).

The MFS returns a current signal of 4 mA from 0 to  $2.918 \times 10^{-10} \text{ kg s}^{-1}$  and 20 mA for  $\dot{m} \geq 1.459 \times 10^{-8} \text{ kg s}^{-1}$  (see Table 5.2). With a parallel connected shunt resistance of 500  $\Omega$  the current signal is proportionally converted to a voltage signal which can be received and processed by the NI USB-6211.

Further the NI USB-6211 has also channels for creating analog output (AO) signals by converting numerical values entered by the user into voltage signals from  $-10$  to  $+10$  V. One of the four AO-channels is connected to the MFC shown in Figure 5.5 to address the control valve of the device.

Following, the conversion of measured and created voltage signals in physical values of each measuring variable are described.

- a) *Temperature*: The digital voltage value  $U$  is converted to a temperature value with unit  $^{\circ}\text{C}$  within a SubVI in the virtual instrument programmed in LabVIEW<sup>5</sup>. Following Eqs. (5.1) and (5.2) the temperature is calculated to

$$\theta = -\frac{B_1}{2B_2} + \sqrt{\frac{B_1^2}{4B_2^2} - \frac{U_0 - U}{B_2 U_0}}, \quad (5.3)$$

with  $B_1$  and  $B_2$  stated earlier. The acquired temperature values measured in both chambers are permanently written into a txt-file while the virtual instrument is running.

- b) *Pressure and  $\Delta p$ -control*: Both PMP4070 gauge are calibrated by GESensing ex works. The calibration function for converting voltage into pressure with unit Pa is

$$p = 16019.78 \left[ \text{Pa V}^{-1} \right] U, \quad (5.4)$$

which is applied in two additional SubVIs according to Figure 5.5. Analogous to the temperature values, the pressure values are collected in the same txt-file for each time step (six values per second).

In the virtual instrument the pressure difference  $\Delta p = p_i - p_o$  is calculated and compared as the actual value to a setpoint value. This comparison yields a boolean value which is *true* if the setpoint value exceeds the actual value and *false* if vice versa. In the case of *true* a numerical constant with value 10 is converted into an analog signal of +10 V which is given to the MFC to fully open the control valve. In the case of *false* a zero is given to the MFC and the valve is shut.

By means of this simple boolean operation, control of  $\Delta p$  between both chambers is realized.

- c) *Mass flow*: Due to the measuring principle of the F-110C (commercial calorimetric mass flow sensor; see section 2.2), a calibration function for every single working gas exists. The calibrations are performed ex works by Bronckhorst, and curves are provided for

$$\dot{m}_{\text{N}_2} = 2.088 \times 10^{-8} \left[ \text{kg s}^{-1} \text{ V}^{-1} \right] U - 1.250 \times 10^{-11} \left[ \text{kg s}^{-1} \right]; \quad (5.5a)$$

$$\dot{m}_{\text{CO}_2} = 1.557 \times 10^{-8} \left[ \text{kg s}^{-1} \text{ V}^{-1} \right] U - 0.834 \times 10^{-11} \left[ \text{kg s}^{-1} \right]; \quad (5.5b)$$

<sup>5</sup>National Instruments LabVIEW, version 8.5

$$\dot{m}_{\text{Ar}} = 2.923 \times 10^{-8} \left[ \text{kg s}^{-1} \text{V}^{-1} \right] U - 1.667 \times 10^{-11} \left[ \text{kg s}^{-1} \right]; \quad (5.5c)$$

$$\dot{m}_{\text{O}_2} = 2.046 \times 10^{-8} \left[ \text{kg s}^{-1} \text{V}^{-1} \right] U - 1.250 \times 10^{-11} \left[ \text{kg s}^{-1} \right]; \quad (5.5d)$$

$$\dot{m}_{\text{CH}_4} = 1.616 \times 10^{-8} \left[ \text{kg s}^{-1} \text{V}^{-1} \right] U - 1.042 \times 10^{-11} \left[ \text{kg s}^{-1} \right]; \quad (5.5e)$$

$$\dot{m}_{\text{H}_2} = 2.098 \times 10^{-8} \left[ \text{kg s}^{-1} \text{V}^{-1} \right] U - 1.250 \times 10^{-11} \left[ \text{kg s}^{-1} \right]. \quad (5.5f)$$

Before starting a measurement the appropriate SubVI has to be activated by the user.

Analogous to the values of temperature and pressure the mass flow data is logged in the same manner.

In the following subsection the test procedure for mass flow measurement is presented with regard to the data acquisition.

### 5.2.3 Continuous test procedure

The apparatus shown in Figure 5.3 is brought to the desired operation temperature. Valves 3, 5, 7 and 8 are opened and the complete system is evacuated by the vacuum pump (9) to a pressure of 0.1 kPa while the gas supply is closed. Then the system is filled with the current working gas (e.g. nitrogen) to a pressure of 150 kPa. Afterwards, the supply valve is closed and the vacuum pump is switched on again. This procedure is repeated 10 times to ensure that the contamination of the system with other gases is negligible. After this preparatory cleaning procedure the system is brought to the desired working pressure and valves 3, 5, 7 and 8 are closed.

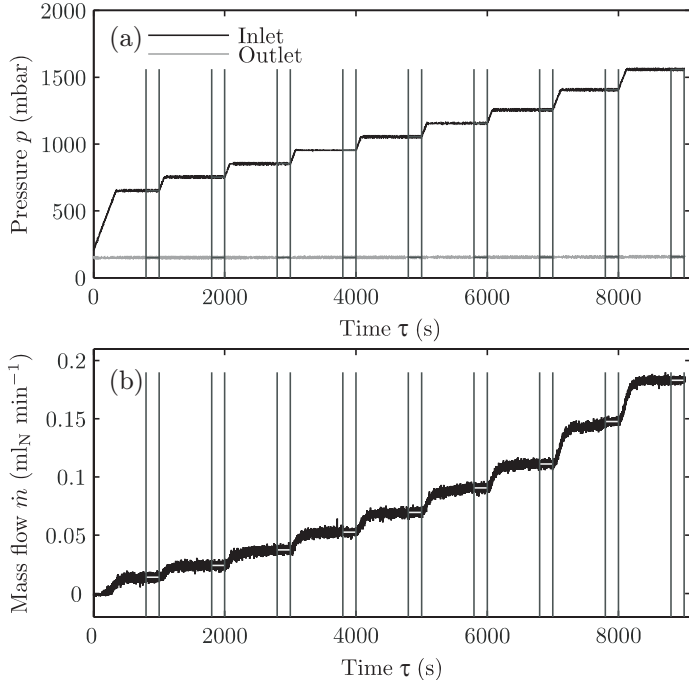


**Figure 5.6:** Exemplary analysis of data obtained using the continuous method. Measured inlet and outlet pressure versus time (a) and measured mass flow (F-110C) versus time (b). When the mass flow caused by a constant pressure difference reached steady state all values (pressure, temperature, mass flow) are averaged over 100 seconds (600 data points) and exported for further processing. Measurements are performed under isothermal conditions. The setting and control of different  $\Delta p$  is realized by a boolean operation implemented in the virtual instrument programmed in LabVIEW. Results are obtained in the framework of the Master's work of Stumpf (2012).

The mass flow measurements are performed automatically by the virtual instrument programmed in LabVIEW. In the virtual instrument (schematically shown on the right hand side

of Figure 5.5), a time schedule is implemented which gives a certain  $\Delta p$  to a certain time  $\tau$  as a setpoint value. As can be seen in Figure 5.6a, the pressure difference is changed by the program from 600 to 700 mbar at  $\tau = 2000$  s, exemplarily. Since the setpoint value is higher compared to the actual value, the boolean operation results in *true* and a numerical value of 10 is converted by the NI USB-6211 to a voltage signal of +10 V which fully opens the control valve of the MFC.

Via the MFC (9) the working gas is flowed into the upstream chamber until the desired pressure difference between both chambers is reached. Then the boolean operation results in *false* and the MFC closes its control valve. Here it is worth noting that the control valve operates within a fraction of a second. Thus the simple boolean operation is used to control  $\Delta p$  between both chambers very satisfactory, as it is proved by Figure 5.6a.

When the measured mass flow reached steady state (Figure 5.6b), the data (mass flow, inlet pressure and temperature, outlet pressure and temperature) is logged and averaged over 10 minutes (see vertical lines in Figure 5.6). Afterwards the next pressure difference is adjusted by the program. As indicated in the example in Figure 5.6 nine different  $\Delta p$  are adjusted and resulting mass flow rate is measured. This procedure is further referred to as one single measurement.

#### 5.2.4 Twofold evaluation of set-up and test procedure

The experimental set-up presented in section 5.2.1 allows for the performance of a second, independent procedure for mass flow measurement. This method is referred to as the *constant volume method* which is most commonly used for measuring gaseous mass flow in microducts (see section 2.2). Here this method is used for evaluation of the continuous test procedure presented in the previous subsection.

A second evaluation is performed using the channel with uniform rectangular cross section *RC20* shown in Figure 5.1a,b.

In the constant volume method the mass flow rate is indirectly determined by means of measuring the pressure variation in one of the chambers assuming quasi-steady state of an ideal gas. Using the equation of state, the time derivative of the mass in the inlet chamber is proportional to the temporal change of the inlet pressure

$$\dot{m} = \frac{\partial m_i}{\partial \tau} = \frac{V_i M}{RT} \frac{\partial p_i}{\partial \tau}, \quad (5.6)$$

where  $V_i$  is the volume of the inlet chamber. To calculate  $\dot{m}$  according to Eq. (5.6), the volume  $V_i$  has to be determined most exactly. From the CAD drawing the "pure" chamber volume can be derived but besides the manufacturing inaccuracies, the volumes of valves, tubes, fittings, and the pressure gauge remain unknown.

The precise volume of the inlet chamber is deduced from the pressure change occurring by changing the volume in syringe (50 mL) connected to the chamber via valve 7 in Figure 5.3. The complete volume can be estimated from Boyle's law (Arkilic, 1997)

$$V_{Boyle} = \frac{\Delta V p^*}{p^* - p} \left( 1 + \frac{p^* - p}{p^*} \right). \quad (5.7)$$

Here  $\Delta V$  is the volume difference caused by pulling the plunger of the syringe and  $p^*$  is the

initial pressure before expanding the volume. The plunger is pulled according to a  $\Delta V$  of 2 mL and the pressure in the inlet chamber is measured. Then the plunger again is pulled in steps of 2 mL to the 18 mL marking and the respective pressure is measured at every step. In Figure 5.7a the volume  $V_{Boyle}$  calculated by means of Eq. (5.7) is plotted against the difference of  $p^*$  and reduced pressure due to pulling the plunger. Data is fitted linear and the  $y$ -intercept conforms the complete chamber volume which is  $V_i = V_{Boyle}|_{p=p^*} = 2.112 \times 10^{-5} \text{ m}^3$ .

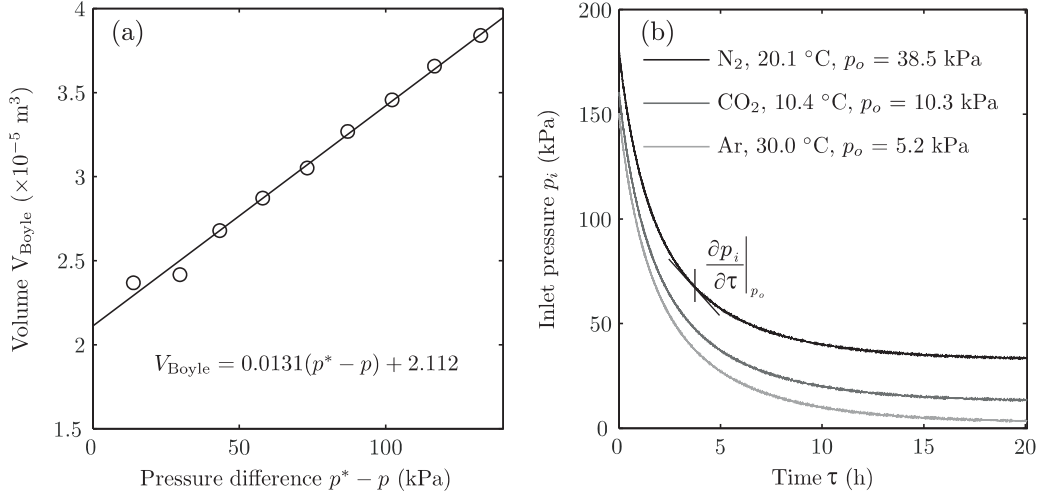


**Figure 5.7:** Estimation of inlet chamber volume  $V_i$  and constant volume method for mass flow measurement. In (a) the inlet chamber volume is obtained by plotting the volume of the chamber and a connected syringe versus the pressure difference which is changed by volume expansion due to pulling the plunger. The chamber volume conforms the  $y$ -intercept of the fitted line. In (b) the pressure in the inlet chamber  $p_i$  is measured versus time while the gas flows through the uniform rectangular channel into the outlet chamber connected to the pressure vessel (6 in Figure 5.3) at constant  $p_o$ . Three measurements are performed at different outlet pressures using different gases at different temperatures under isothermal conditions. By means of a tangent the gradient of  $p_i$  can be determined at each  $\Delta p$ . The gradient and the appendant  $p_i$  and  $p_o$  are exported for further processing.

After determination of  $V_i$ , discontinuous measurements are performed with the purpose to validate the continuous test procedure. In Figure 5.7b the inlet pressure is plotted versus time  $\tau$  for three experiments using different gases, temperature and outlet pressure. Here the rectangular channel with uniform cross section (*RC20*, Table 5.1; Figure 5.1a,b) is used for testing.

In detail the procedure is as follows: First the complete system shown in Figure 5.3 is brought to the specified temperature and then evacuated using vacuum pump (9) while valves 3, 5, 7 and 8 are opened and supply valve (1) is shut. Then the pump is switched off and the respective working gas is flowed into the system via valve 1 until the desired outlet pressure is reached. Afterwards valves 3, 7 and 8 are closed and the initial inlet pressure is adjusted using the MFC (2). With setting the MFC on zero, the experiment starts and data is logged until equilibrium is reached. By means of a tangent (see Figure 5.7b)  $\partial p_i / \partial \tau$  can be calculated at each  $\Delta p$  and the appendant  $p_i$ ,  $p_o$ ,  $T_i$ , and  $T_o$  are exported also.

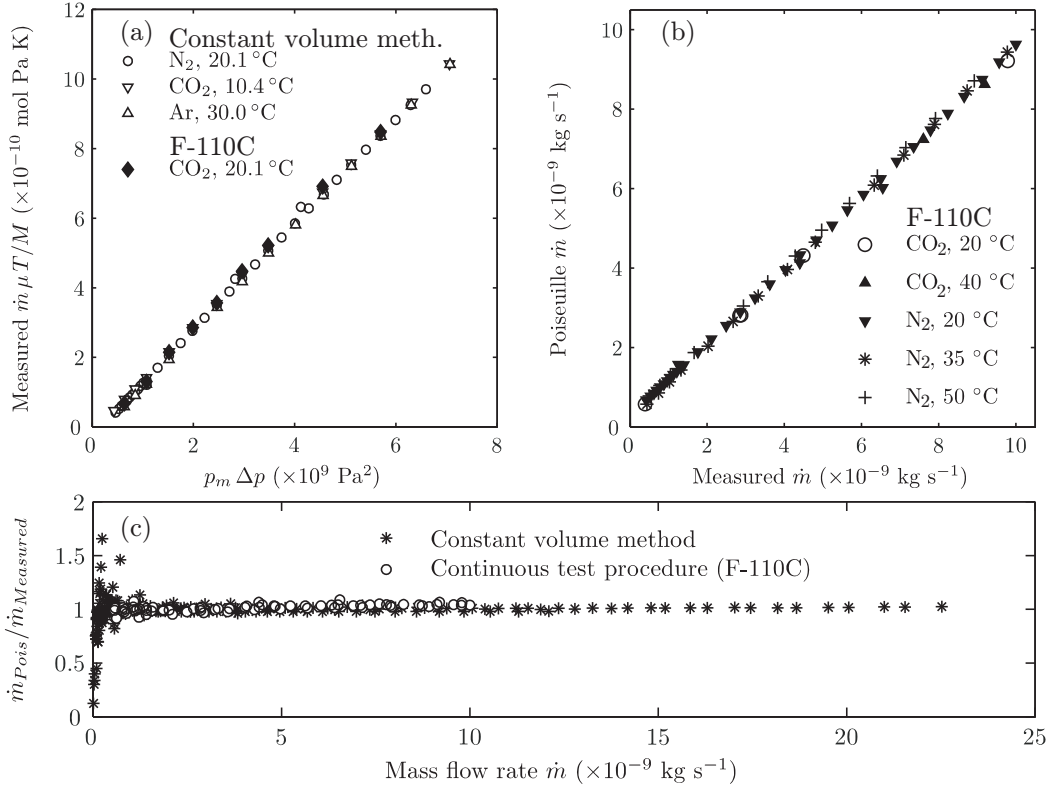


**Figure 5.8:** Twofold validation of the continuous test procedure and verification of the lower limit of the measuring range. In (a) the measured mass flow rate is related to  $\mu$ ,  $T$  and  $M$  and plotted versus the product of  $p_m$  and  $\Delta p$ . The open symbols refer to data estimated by means of the constant volume method. Mass flow rate is calculated according to Eq. (5.6) with  $\partial p_i / \partial \tau$  derived from discontinuous measurements (Figure 5.7b). Gas properties for calculation are given in Table 5.3. In (b) the mass flow calculated by means of Poiseuille’s law is plotted versus measured mass flow data obtained on *RC20* at  $Kn_m < 0.002$ . Geometrical values and gas properties used for calculation are stated in Tables 5.1 and 5.3. In (c) the ratio of calculated mass flow rate to measured mass flow rate is plotted against  $\dot{m}$  for finding the lower limits of the measuring range of both methods.

In Figure 5.8a the measured mass flow rate is related to dynamic viscosity  $\mu$ , temperature  $T$  and molar mass  $M$  and plotted versus the product of mean pressure  $p_m$  and  $\Delta p$ . The open symbols refer to data estimated by means of the constant volume method. The mass flow rate is calculated according to Eq. (5.6) with  $\partial p_i / \partial \tau$  derived from discontinuous measurements shown in Figure 5.7b. Gas properties  $\mu$  and  $M$  used for calculation are stated in Table 5.3.

Filled diamond symbols in Figure 5.8a are measured by means of the continuous procedure. Both methods are completely independent but show good quantitative agreement of data.

Furthermore, a lot of mass flow measurements using the continuous method are performed under very low rarefaction on the rectangular channel with uniform cross section. For a second, independent validation, measured mass flow rate is compared to the mass flow rate calculated by Poiseuille’s law according to Eq. (3.40) on page 33.

**Table 5.3:** Properties of gases used in gas flow experiments.

Gas	$M$ (g mol <sup>-1</sup> )	$\sigma$ (pm)	$\mu$ (10 <sup>-5</sup> Pa s)					
			10 °C	20 °C	30 °C	35 °C	40 °C	50 °C
N <sub>2</sub>	28.01	379.8	1.700	1.747	1.792	1.815	1.837	1.881
O <sub>2</sub>	31.99	362.0	1.961	2.017	2.072	2.100	2.127	2.180
Ar	39.95	354.2	2.194	2.256	2.317	2.347	2.378	2.437
CO <sub>2</sub>	44.01	394.1	1.400	1.449	1.497	1.521	1.544	1.592

Measurements are performed at different constant temperatures in the range from 20 to 50 °C using nitrogen and carbon dioxide as working gases. The pressure in the outlet chamber is adjusted to 100 kPa so that the mean Knudsen number is throughout smaller than 0.002 and Poiseuille’s law experientially yields reasonable results (Gad-el-Hak, 1999).

As clearly shown in Figure 5.8b the data points lie lined up on the angle bisector of the coordinate system and hence measured data are in very good agreement to the analytical solution.

Thus the method of measurement can be considered as proved by two different and independent strategies. The twofold validation of the measurement technique also implies the elimination of systematic errors. This means that the experimental procedure is consistent with negligible systematic errors compared to the random errors focused in the following subsection.

Furthermore, the range of measurement of both methods is checked by plotting the ratio of calculated mass flow rate to measured mass flow rate versus  $\dot{m}$  (Figure 5.8c). For both methods the lower limit is found to be approximately  $5 \times 10^{-10}$  kg s<sup>-1</sup> which is in quite good agreement to the manufacturer information of the F-110C (compare Table 5.2). Concerning range of measurement and resolution there is no considerable distinction between the continuous test method and the constant volume method performed at the set-up presented here. For this reason the continuous test procedure is used in this work since the method is easier to automate and hence less time-consuming.

### 5.2.5 Analysis of distribution of measurements and random errors

In experimental science a theoretical model is evaluated and proved based on the results of experimental evidence and thus the analysis of this evidence is crucial for the method in general. While systematic errors are proved to be negligible (subsection 5.2.4), a random error analysis is essential for evidence of the experimental results.

In this work all single measurements (as described in subsection 5.2.3) are performed at least in triplicate for stochastic validation. For the visualization of e.g. the mass flow rate as a function of  $\Delta p$  all data points can be simply plotted in a diagram without particular investigation of random errors.

However, for the determination of the indirectly measured diodicity (Eq. (3.73) on page 40)

$$D = \frac{\dot{m}_{noz} \Delta p_{dif}}{\dot{m}_{dif} \Delta p_{noz}} \sqrt{\frac{T_{noz}}{T_{dif}}}. \quad (5.8)$$

the random error is crucial for experimental evidence. The error of  $D$  must be calculated by means of an error propagation using mean values of the six parameters in Eq. (5.8) and appropriate errors. Since arithmetic mean and standard deviation are values appendant to the Gaussian distribution, a statistical test has to be performed to prove whether the data are normally distributed or not (Dytham, 2006). Hence a statistical test has to verify if it is permissible to use arithmetic mean and standard deviation (of three or more measured values) for calculation of  $D$  and other indirectly measured values.

**Table 5.4:** Arithmetic mean and standard deviation of data obtained by mass flow measurements for the Anderson-Darling test. All  $n = 8$  measurements are performed under identical conditions ( $\theta = 20^\circ\text{C}$ ,  $p_o = 7.6\text{ kPa}$ ) with nitrogen as working gas and five different  $\Delta p$ . The threshold value  $P_{\text{AD}}$  of the Anderson-Darling test is calculated according to Eq. (5.9).

$n$	$\Delta p$ (kPa)	$e_{\Delta p}$ (kPa)	$\dot{m}_m$ ( $10^{-10}\text{ kg s}^{-1}$ )	$e_{\dot{m}}$ ( $10^{-11}\text{ kg s}^{-1}$ )	$S_{\text{AD}}$	$P_{\text{AD}}$
8	15.0	0.62	3.189	2.084	-22.979	3.870
8	17.5	0.81	4.897	2.709	-21.765	3.710
8	25.0	0.55	10.712	2.501	-20.845	3.584
8	30.0	0.36	14.901	2.709	-20.638	3.555
8	45.0	0.75	29.634	3.751	-20.259	3.501

The Anderson–Darling test (Anderson & Darling, 1954) is one of many procedures commonly encountered to check if a set of data is normally distributed (Dytham, 2006). For the test eight single mass flow measurements under identical conditions (outlet pressure, temperature, nitrogen as working gas) are performed according to section 5.2.3. By means of the LabVIEW virtual instrument five different  $\Delta p$  are adjusted and arithmetic mean  $\dot{m}_m$  and standard deviation  $e_{\dot{m}}$  are calculated from the data set of  $n = 8$  single measurements (Table 5.4). The value  $P_{\text{AD}}$  is the probability of the data being normal distributed and is mathematically expressed by

$$P_{\text{AD}} = \sqrt{-S_{\text{AD}} - n}, \quad \text{with} \quad (5.9)$$

$$S_{\text{AD}} = \sum_{i=1}^n \frac{(2i-1)}{n} (\ln(Z_i) + \ln(Z_{n-i+1})).$$

Here  $Z$  is the cumulative distribution function. The parameter  $P_{\text{AD}}$  is a threshold value: If  $P_{\text{AD}} < 0.05$ , the data set significantly deviates from a normal distribution (Anderson & Darling, 1954). For all measured  $\Delta p$  stated in Table 5.4  $P_{\text{AD}}$  is throughout larger than 0.05 and the hypothesis that the mass flow data follow a Gaussian distribution cannot be refused.

This result is confirmed by Figure 5.9 where the probability of  $\dot{m}/\dot{m}_m$  is plotted versus the mass flow rate measured in single measurements related to the arithmetic mean  $\dot{m}_m$  of

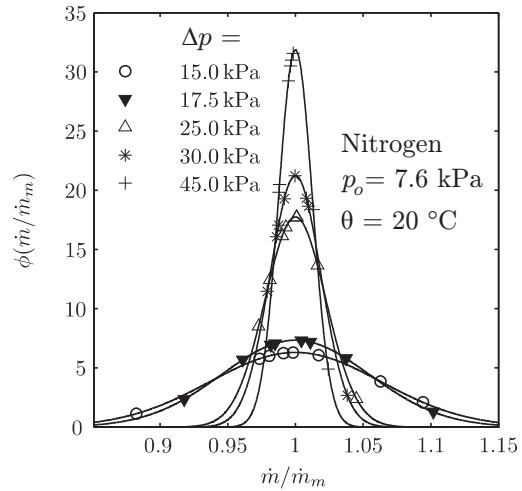


**Figure 5.9:** Statistical distribution of mass flow data for different  $\Delta p$ .

all eight measurements. The lines are fitted for Gaussian distribution by means of the least mean square method. For each  $\Delta p$  the data is in perfect agreement to the curves and thus a normal distribution is most likely.

As a consequence it is permissible to use arithmetic mean and standard deviation for calculation of indirectly measured values using the continuous test procedure at the experimental set-up.

### 5.3 Surface functionalization

As figured out in section 3.5.1, surface chemistry is discussed to influence the gas flow in microchannels under rarefied conditions. For a qualitative investigation a surface functionalization is chosen and performed with the aim to compare the permeability of an identical channel system before and after functionalization.

After obtaining mass flow data on one channel system (*Si-9*) with a hydroxylated silicon surface (subsection 3.5.1), the channel walls are functionalised by means of a silanization. As an agent octadecyltrichlorosilane (OTS,  $C_{18}H_{37}Cl_3Si$ , Merck, boiling pressure at room temperature approximately 2 kPa) is used in a vapour phase process (CVD) performed in a self-constructed apparatus.

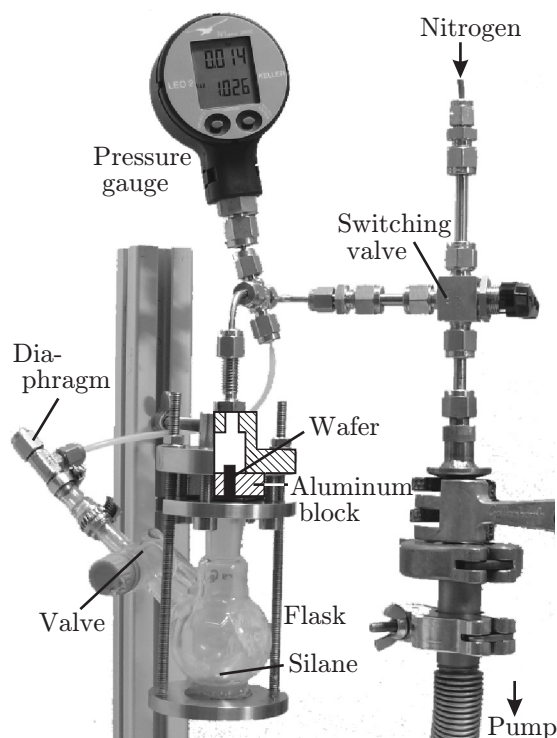


**Figure 5.10:** Set-up for silanization of the microchannel surface.

#### 5.3.1 Apparatus for silanization reaction

The aluminum block with the glass-capped silicon wafers shown in Figure 5.2c on page 65, is clamped between a disc with a centered bore and a kind of steam dome as shown in Figure 5.10. The O-rings at both sides of the aluminum block seal the connections against the atmosphere. Below the disc a two-necked flask is centered and pressed against the underneath of the disc by two threaded rods. Between the upper neck and the disc is another gasket. The second neck of the flask is equipped with a valve and a T-piece adapter with one outlet connected to the steam dome and the straight outlet sealed with a diaphragm. The steam dome is connected to a pressure gauge for monitoring and a valve which can be switched between a vacuum pump and a source for protective gas (nitrogen).

### 5.3.2 Procedure of functionalization

The silanization has to be performed under protective gas atmosphere due to the fact that the liquid silane reacts spontaneously with the humidity of the ambient air (compare section 3.5.2). Hence a preparatory procedure is performed before starting the silanization process. First the valve at the second bottleneck is opened and the switching valve is switched to the running vacuum pump. Thus the complete system is evacuated to a pressure of 0.1 kPa(a). Then the valve is switched to the nitrogen line until the pressure reaches 400 kPa(a) while the valve at the neck remains open. Then the valve is switched to the pump and the complete system is evacuated again. This procedure is repeated 10 times to ensure to remove the humidity in the set-up.

Afterwards the pressure in the system is adjusted to 200 kPa(a). Through the diaphragm a long cannula is stung and 4 mL of pure OTS are injected into the flask. The cannula is removed and the overpressure in the system prevents the ingress of ambient air. Then the switching valve is again opened to the pump and the pressure is carefully reduced to 10 kPa(a). Then the valve at the neck of the flask is closed. The pressure in the dome is further reduced to 0.1 kPa(a) and the pump remains running. Hence a pressure gradient occurs over the length of the channels, which are the sole connection between the flask containing the OTS and the vacuum pump. After three hours the OTS starts boiling and the silane vapour flows through the channels towards the pump. After another two hours the procedure is finished by turning off the vacuum pump and adjusting the pressure to 100 kPa(a). This duration for the functionalization procedure is chosen in reference to Dong *et al.* (2006). Then the valve at the neck of the flask is opened and the aluminum block is built out the functionalization apparatus.

Finally the aluminum block with the now silanized microchannels is again implemented in the experimental apparatus as shown in Figure 5.4.

### 5.3.3 Verification of altered surface chemistry

The identical procedure is completed at a second, identical wafer with the aim to prove if the functionalization is performed successfully. Therefore the aluminum block is carefully destroyed by grinding and thus the glass-covered silicon wafer is removed off its fixture. Following Wang & Lieberman (2003) the OTS molecules bind to the hydroxyl groups at the surface and form a highly ordered self-assembled monolayer (Figure 3.11 in section 3.5.2) which covers and thus inactivates the OH groups. Hence the comparison of the contact angle of (polar) water at the hydroxylated and the silanized surface is a straightforward qualitative indicator for the successful functionalization.

Using a reflected-light microscope with a camera, first a non-functionalized reference wafer is placed on the microscope stage and three channels are focused through the glass cover. Then a droplet of highly pure water is pipetted on the one end of the channels which directly is soaked in by capillary force. Photos of the water meniscus are taken through the glass cover (Figure 5.11a). The contact angle is quite low which indicates a polar surface due to a high concentration of hydroxyl groups. The same is done with the silanized wafer shown in Figure 5.11b where the contact angle is observed to be significantly larger compared to the reference wafer.

Thus it is shown that the surface chemistry of the channels is successfully altered and the majority of polar OH groups is inactivated.

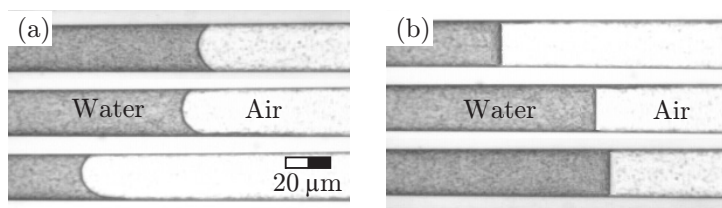


**Figure 5.11:** Verification of silanization procedure. Water meniscus in the channels is photographed through the glass cover as a qualitative proof for successful functionalization: Before (a) and after (b) silanization procedure.

In the following chapter experimental results obtained by means of the experimental set-up on the presented test channels are shown and discussed. Also the comparison between gas flows before and after silanization is provided.

# 6 THEORETICAL EVALUATION OF EXPERIMENTAL FINDINGS

In section 1.2 the hypothesis of this thesis is formulated and corresponding aims are stated. Here it is postulated that a slightly tapered duct acts as a gas diode to the effect, that the permeability is higher when it is perfused like a nozzle than vice versa. Further, as outlined by means of Figure 1.3 on page 5, this diode effect is expected to increase with rarefaction due to the diminishing contribution of convective transport to the entire flow. The first two sections of this chapter give the experimental proof of the outlined diode effect.

Furthermore, as a second evaluation of the model derived in chapter 3, experimental data obtained on slightly tapered microchannels (section 5.1) are used for comparison to predictively calculated curves.

Finally, the last section emphasizes the topic of surface functionalization of microchannels. Precedent, analytical investigations on the influence of the surface chemistry on microflows are carried out in section 3.5. The practical execution of the functionalization and the proof of the altered surface chemistry are described in section 5.3.

## 6.1 Pressure driven gas flow in slightly tapered ducts

As stated above and simulated by means of Eq. (3.73) on page 40, the diode effect is increasing with rarefaction (see Figure 3.7b on page 40). As a quantitative measure of the rarefaction in tapered ducts, the Knudsen number according to the left-hand side of Eq. (3.2) on page 18 is used with a slight modification: Since the characteristic length  $\ell$  varies alongside the channel, the hydraulic diameter at the small aperture and at the large aperture must be taken into account. For that purpose,  $\ell$  for varying rectangular cross-section stated in Table 3.3 on page 39 is used, and Eq. (3.2) writes

$$\text{Kn}_m = \frac{kT}{\sqrt{2}\pi\sigma^2 p_m \ell} = \frac{kT P_s P_l}{\sqrt{2}\pi\sigma^2 (p_i + p_o) (A_s P_l + A_l P_s)}. \quad (6.1)$$

For the ordinate, the mass flow rate (measured and calculated) is used in various representation as described subsequently.

The experiments on all four ducts with slightly varying cross section and the uniform reference channel (Table 5.1) are performed under isothermal conditions at 20 °C using carbon dioxide, argon and oxygen as working gases.

Exemplarily, the data measured on *Si-5* and *Si-9* are plotted in Figure 6.1 as reduced molar flow rate according to Eq. (3.72) on page 39 versus  $\text{Kn}_m$  according to Eq. (6.1). For all measurements performed,  $\dot{m}/(nM\Delta p)$  decreases with increasing  $\text{Kn}_m$ , which is likewise observed for the dimensionless  $G$  (see definition according to left-hand side of Eq. (3.80) on page 45

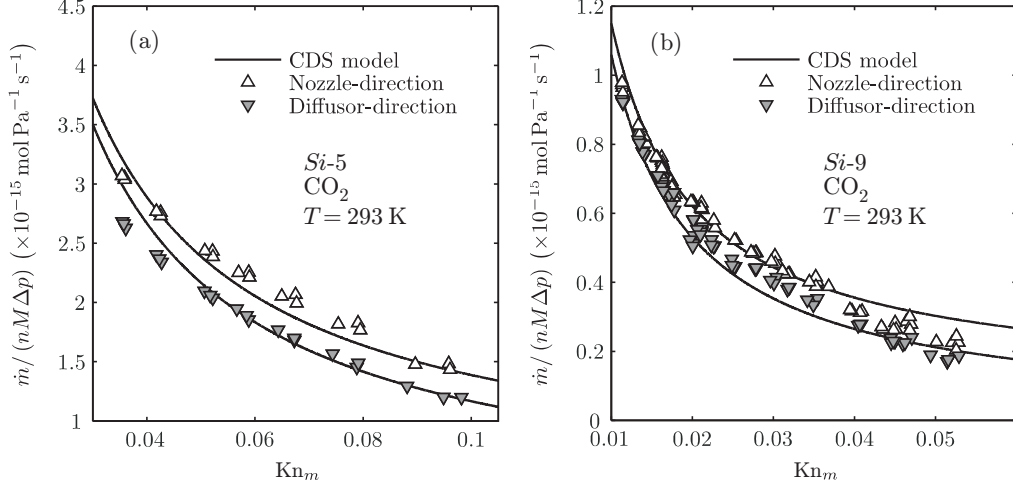


**Figure 6.1:** Reduced molar flow rate in one channel according to left-hand side of Eq. (3.71) on page 39 versus  $\text{Kn}_m$  according to Eq. (6.1). Two plots are shown exemplarily for all measurements performed in this work: Data in (a) is obtained on *Si-5* using carbon dioxide as working gas. In (b) the same gas is used for measurements on system *Si-9*. All experiments are performed at 20 °C. The curves shown in (a) and (b) are predicted for the flow in both directions of perfusion according to Eq. (3.72) with geometrical properties stated in Table 5.1 on page 63. Gas properties are given in Table 5.3 on page 74.

and Figure 4.5 on page 57). As clearly shown in Figure 6.1, the flow in nozzle-direction is throughout higher than in diffusor-direction, as it has been observed for all ducts with slightly varying cross section. Furthermore, the dependency on the direction of perfusion increases with  $\text{Kn}_m$ , and hence with gaseous rarefaction. As will be shown in the next section, this diode effect occurs qualitatively identical at the micromilled duct with slightly varying cross section *Al-3*, but not at the straight channel *RC20* (Figure 5.1 in section 5.1.1). This finding can therefore be considered as the experimental proof of the outlined diode effect and an indication for the correctness of the derived model, which is in good agreement to experimental data.

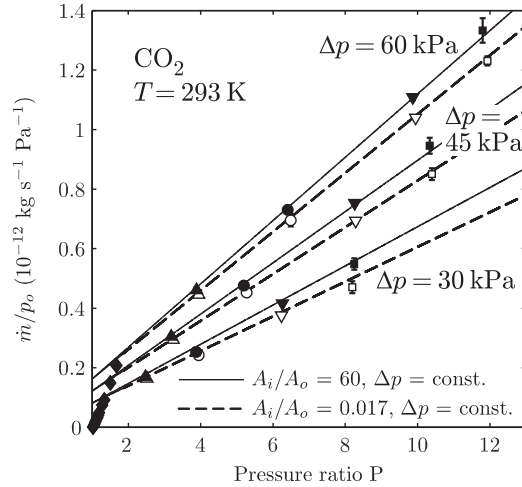
The rarefactional increase of the dependency on the direction of perfusion perfectly confirms the hypothesis illustrated by means of Figure 1.3. The rarefaction dependency can be visualized more clearly when using another depiction as shown in Figure 6.2. Here for depiction and interpretation of data the arithmetic mean of normalized mass flow rate  $\dot{m}/p_o$  and pressure ratio  $P = p_i/p_o$  are used. This is permissible since measured data are Gaussian distributed, as it is analyzed in section 5.2.5. The standard deviations  $e_{\dot{m}/p_o}$  and  $e_P$  are calculated according to the Gaussian error propagation to

$$e_{\dot{m}/p_o} = \sqrt{\left(\frac{\partial(\dot{m}/p_o)}{\partial \dot{m}} e_{\dot{m}}\right)^2 + \left(\frac{\partial(\dot{m}/p_o)}{\partial p_o} e_{p_o}\right)^2} = \sqrt{\left(\frac{e_{\dot{m}}}{p_o}\right)^2 + \left(-\frac{\dot{m} e_{p_o}}{p_o^2}\right)^2}; \quad (6.2a)$$

$$e_P = \sqrt{\left(\frac{\partial P}{\partial p_i} e_{p_i}\right)^2 + \left(\frac{\partial P}{\partial p_o} e_{p_o}\right)^2} = \sqrt{\left(\frac{e_{p_i}}{p_o}\right)^2 + \left(-\frac{P e_{p_o}}{p_o}\right)^2}. \quad (6.2b)$$

Here  $e_{\dot{m}}$  is the uncertainty of the mass flow rate and  $e_{p_i}$  and  $e_{p_o}$  are the uncertainties of inlet

**Figure 6.2:** Influence of ratio of inlet to outlet cross sectional area on mass flow under rarefied conditions. The normalized mass flow rate of  $\text{CO}_2$  measured on *Si-9* is plotted versus the pressure ratio  $P = p_i/p_o$ . Measurements are performed under isothermal conditions at  $20^\circ\text{C}$  at the following five outlet pressures: diamond,  $p_o = 90\text{ kPa}$ ; triangle (up),  $20\text{ kPa}$ ; circle,  $10\text{ kPa}$ ; triangle (down),  $5\text{ kPa}$  and square  $3\text{ kPa}$ . Filled symbols denote the nozzle-direction and the empty symbols the diffuser-direction. Predictions in nozzle-direction (solid lines) and diffuser-direction (dashed lines) are calculated for constant  $\Delta p$  using Eqs. (3.50), (3.60), and (3.67) with geometrical properties stated in Table 5.1 on page 63. Gas properties are given in Table 5.3 on page 74. Measurements are at least performed in triplicate. Horizontal and partly vertical error bars are smaller than symbols.



and outlet pressure. The value of  $e_{\dot{m}/p_o}$  and  $e_P$  corresponds the width of the vertical errorbar and horizontal errorbar, respectively. It is worth noting that  $\dot{m}$ ,  $p_i$  and  $p_o$  are the arithmetical averages of the performed measurements. By the way, all experimental results obtained in this PhD work are stated in Appendix B.

In Figure 6.2 the flow is consistently higher when the duct is perfused as a nozzle (filled symbols, solid lines). Following the hypothesis, this is a reasonable result since the amount of molecules hitting the aperture is higher. Further this finding is strongly supported by the fact that measured data (symbols) agree almost perfectly with analytical predictions (lines). According to Figure 6.2, the disparity of the flow in both directions is increasing with the pressure ratio since  $P$  is higher for constant  $\Delta p$  when the absolute pressure ( $p_o$ ) decreases. Hence this effect is directly dependent on the rarefaction. Spoken in terms of a convective component and a diffusive component according to Eq. (3.50): Spatial diffusion becomes more determining with increasing rarefaction until it dominates the flow behaviour under highly rarefied conditions. Furthermore, this experimental observation is qualitatively confirmed by simulations using a molecular kinetic approach<sup>1</sup> (Tantos & Valougeorgis, 2012).

However, from this proved finding it is unlikely whether the reverse can occur as Stevanovic (2007) reported when using the Maxwellian approach (compare section 3.3.1). She found that the simulated mass flow in a slightly diverging channel is higher than in a converging one. Spoken in terms of nozzle and diffuser, it is found that the permeability in the diffuser-direction is higher than vice versa. Nevertheless, it has to be noted that no experimental (or other) evaluation of the simulated curves are given in the paper of Stevanovic. This qualitative comparison indicates that gas flows in slightly tapered ducts are not describable by means of the Maxwellian slip approach but with the CDS superposition model (Veltzke & Thöming, 2012).

<sup>1</sup>This statement is attested by the author's private communication with Prof. Dimitris Valougeorgis from University of Thessaly, Department of Mechanical Engineering.

The following section focuses the diodicity  $D$ , which has been introduced in section 3.4.4 as the ratio of the permeability in nozzle-direction to the permeability in diffusor-direction. Also the experimental results obtained on the micromilled channels *RC20* and *Al-3* are presented subsequently.

## 6.2 Rarefaction dependency of the gas diode effect

According to the definition of  $D$  as  $\dot{N}^{noz}/\dot{N}^{dif}$  according to Eqs. (3.71) and (3.73a) on page 40, measured data is prepared as follows. For the diodicity  $D$  the mean and the standard deviation of all measured values (mass flow, inlet and outlet pressure) measured at identical  $p_i$  and  $p_o$ , is calculated. For each setting at least three measurements are performed. Using the mean of the measured values, the diodicity is obtained as

$$D = \frac{\dot{N}^{noz}}{\dot{N}^{dif}} = \frac{\dot{m}_{noz}\Delta p_{dif}}{\dot{m}_{dif}\Delta p_{noz}}. \quad (6.3)$$

In comparison to Eq. (5.8) on page 74, the temperature ratio  $T_{noz}/T_{dif}$  is omitted in this expression since adjustment of temperature is very precise in experimental procedure. Thus the appropriate error is calculated according to the Gaussian error propagation to

$$e_D = \sqrt{\sum \left( \frac{\partial D}{\partial z} ez \right)^2}; \quad z = \langle \dot{m}_{noz}, \dot{m}_{dif}, \Delta p_{noz}, \Delta p_{dif} \rangle. \quad (6.4)$$

For the abscissa the mean Knudsen number for the nozzle-direction and the diffusor-direction is calculated according to Eq. (6.1) and than again the mean is calculated:

$$\overline{\text{Kn}}_m = 0.5 \left( \text{Kn}_m^{noz} + \text{Kn}_m^{dif} \right). \quad (6.5)$$

The appropriate error is

$$e_{\overline{\text{Kn}}_m} = \sqrt{\sum \left( \frac{\partial \overline{\text{Kn}}_m}{\partial z} ez \right)^2}; \quad z = \langle \bar{T}, p_m, d_h \rangle. \quad (6.6)$$

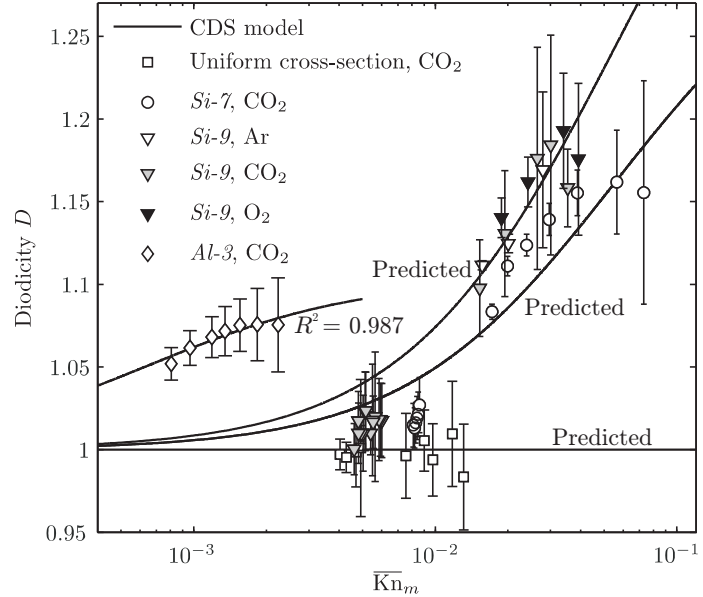
The complete set of raw data used for calculation of  $D$ ,  $\overline{\text{Kn}}_m$  and both errors is supplied in Appendix B.

In Figure 6.3 the diodicity according to Eq. (6.3) is plotted versus  $\overline{\text{Kn}}_m$  for all series except for the data obtained on *Si-5* shown in Figure 6.1(a). This is only for reasons of clarity since the diodicity measured on *Si-5* is nearly identical to the values obtained on *Si-7*.

For all measurements performed on ducts with slightly varying cross section, the diodicity increases with rarefaction. This experimental finding perfectly confirms the hypothesis stated in section 1.2 and illustrated in Figure 1.3 on page 5.

The diodicity obtained on the channel with uniform cross section (*RC20*) is unity and not affected by  $\overline{\text{Kn}}_m$  since no significant disparity in the direction of perfusion is observed. Hence the data is in good agreement to the horizontal line predictively calculated according to Eq. (3.73a). This finding also confirms, that the diode effect is not an artificial error of the experimental set-up or the measuring procedure.

**Figure 6.3:** Experimental and modeled diodicity as a function of gaseous rarefaction. Experiments are performed under isothermal conditions at 20 °C. All measurements are at least performed in triplicate and data is prepared according to Eqs. (6.1), (6.3), and (6.5). Vertical errorbars are calculated according to Eq. (6.4). Horizontal error bars are calculated according to Eq. (6.6) and are throughout smaller than symbols. Curves for *Si-7*, *Si-9* and the channel with uniform cross-section (*RC20*) are predicted using Eq. (3.73a). Curve for *Al-3* is fitted by the method of least squares by adapting  $a/c$  and  $b/c$  according to Eq. (3.73b) on page 40. Results are partly obtained in the framework of the Master’s work of Stumpf (2012).



Also  $D$  is predicted for etched channels *Si-7* and *Si-9*. The curve calculated for *Si-9* ( $A_l/A_s = 60.00$ ) is throughout higher than the curve for *Si-7* ( $A_l/A_s = 10.05$ ) which is confirmed by the experimental results. This finding perfectly validates the hypothesis concerning the influence of cross-sectional area  $A$  on the contribution of molecular spatial diffusion to the entire flow. By means of the data points of *Si-9* it can further be demonstrated that  $D$  is independent of the nature of the gas when  $\overline{Kn}_m$  is plotted on the abscissa. This finding gives further confirmation of the statement that gas microflows under slightly rarefied conditions are not influenced by the nature of the gas (controversially discussed influence parameter of the TMAC; see section 3.3.4).

The diodicity effect does not only occur on etched channels, since the same qualitative behaviour is observed on the notch with varying height milled into an aluminum block (*Al-3*, Figure 5.2(c) and (d) on page 65). The measured diodicity with  $\text{CO}_2$  as working gas (open diamonds) increases slightly with rarefaction and aims to a limit ( $D \approx 1.1$ ), as it is predicted by means of Figure 3.7(a) on page 40.

Since the model cannot easily be applied to that kind of geometry (note that the model is developed for the case of  $w_s < h < w_l$  (Veltzke *et al.*, 2012a)), the model according to Eq. (3.73a) (right-hand side) is fitted to data by adapting  $a/c$  and  $b/c$ . The curve obtained by the method of least squares perfectly agrees with the experimental diodicity. The fact that the diodicity does not depend on the surface material indicates once more the inconsistencies of the TMAC approach discussed in sections 3.3.2 to 3.3.4.

All experimental findings are in good qualitative and quantitative agreement to the hypothesis describing the diode effect and to the model of superimposed flows. Thus the second aim of the thesis (page 5) is fulfilled since an experimental proof of the outlined diode effect

is given, and the refined superposition model is evaluated for the prediction of experimental data obtained on slightly tapered ducts.

### 6.3 Influence of functionalization on gaseous mass flow

Before execution of the silanization reaction as described in section 5.3, gas flow measurements are performed on *Si-9* using argon and carbon dioxide as working gas. All experiments are multiply performed according to the procedure presented in section 5.2.3. All measurements are performed under isothermal conditions at 20 °C and raw data is given in Appendix B. For the depiction of data the non-dimensional reduced mass flow rate  $G$  (Eq. (3.80) on page 45) is used as a function of gaseous rarefaction. Since  $G$  in Eq. (3.80) is defined by means of geometrical properties  $A$  and  $P$ , the expression must be adapted for ducts with slightly varying cross section. Thus the reduced mass flow rate for tapered ducts is defined as

$$G^j = \frac{\dot{m}^j}{\dot{m}_D^j} = \dot{m}^j \frac{3}{\Lambda^j \Delta p} \sqrt{\frac{RT}{2M}}; \quad j = \langle noz, dif \rangle, \quad (6.7)$$

with diffusive conductivity  $\Lambda^j$  stated in Table 3.3 on page 39 and geometrical properties given in Table 5.1 on page 63. In Figure 6.4 the recalculated experimental results are plotted versus the mean Knudsen number according to Eq. (6.1). For all measurements performed,  $G^j$  is slightly higher when the channel surface is silanized. This effect is independent of the direction of perfusion since it occurs in nozzle-direction (a, c) as well as in diffuser-direction (b, d). Here again it has to be noted, that gas flow experiments are performed at one and the same channel bundle before and after silanization. Thus the observed effect cannot be attributed to slightly different geometrical properties or blocked single channels. The fact that permeability in silanized channels is higher, indicates that the enhancement of flow rate is actually due to the altered surface properties.

Vice versa (if the silanization would have reduced the permeability), it might have been argued that the relatively long chains of the OTS molecules (Figure 3.11 on page 48) shrink the cross-sectional area of the channels and the effect is only due to altered geometry. Nevertheless, despite the extremely slight reduction of cross section (OTS carbon chain has a length of roughly 2.7 nm) the silanization slightly enhances  $G^j$ . This finding generally confirms that surface functionalization bears potential for basic research on rarefied gas flows.

How does this finding correspond to the surface diffusion term of the derived model and to the analytical considerations of section 3.5?

By means of Figure 4.6 on page 59 it is found that surface diffusion is setting in at roughly  $\text{Kn}_m = 0.05$ . This is in good agreement to the current experimental results given in Figure 6.4, since a slight disparity occurs at even this order of rarefaction.

In section 3.5 the OH groups of the hydroxylated silicon surface of the channels are identified to cause interaction to gas molecules. By means of the silanization the majority of OH groups is inactivated as it is clearly demonstrated in Figure 5.11 on page 78. Following the surface diffusion term according to Eq. (3.78), the reduction of surface polarity must have increased the surface diffusivity  $D_S$  and/or the parameters of the Langmuir equation  $q^*$  and/or  $K_L$ . For further investigation of this statement, MD simulations is the method of choice. Even commercial MD programs (for instance Accelrys Materials Studio) provide good possibilities

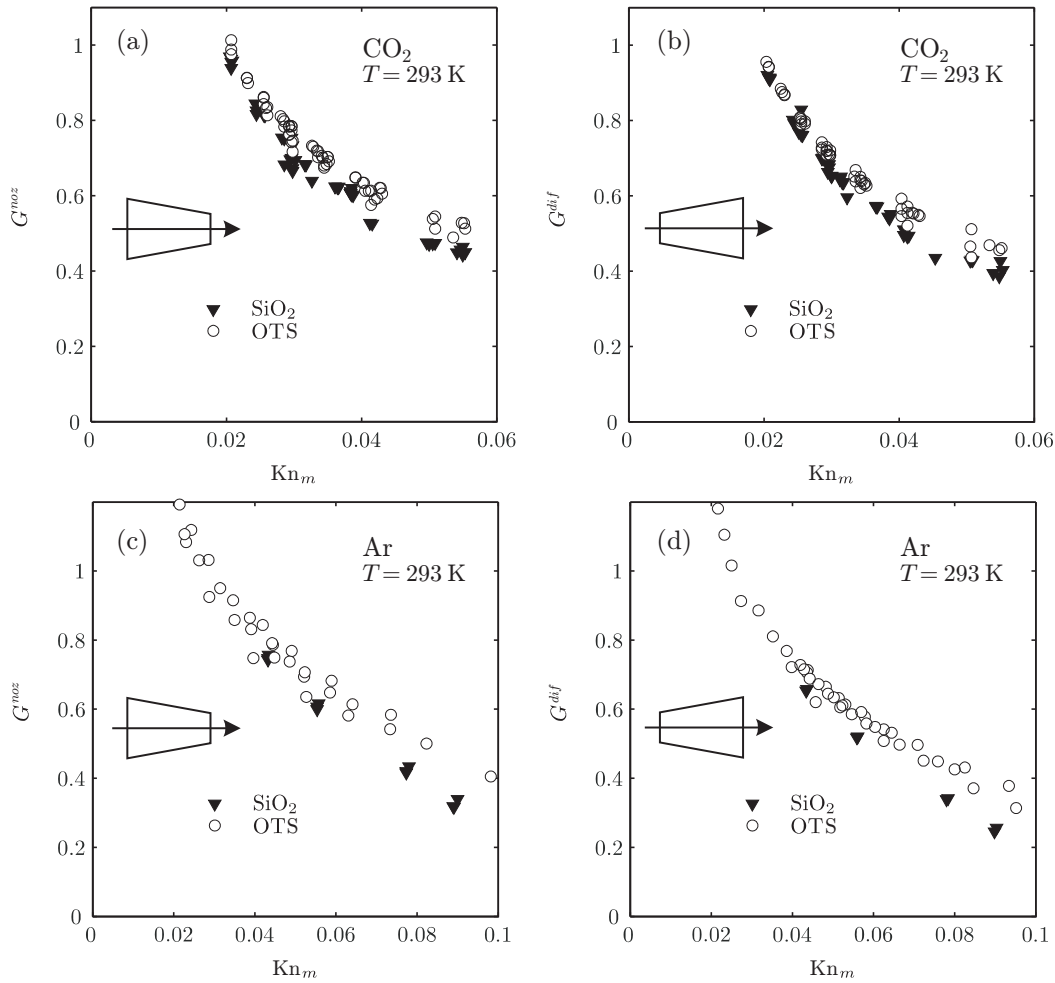


**Figure 6.4:** Experimentally observed influence of surface chemistry on gas microflow. Argon and carbon dioxide flow results through etched silicon channel bundle *Si-9* before and after silanization. The reduced mass flow rate  $G$  according to Eq. (3.80) on page 45 is plotted versus  $Kn_m$  according to Eq. (6.1). Measurements are performed under isothermal conditions at  $20^\circ\text{C}$  in each direction of the duct: (a) and (c) in nozzle-direction as well as (b) and (d) in diffuser-direction. Results are partly obtained in the framework of the Diploma work of Niemeyer (2011).

for analysis of the interaction strength of argon and carbon dioxide to an OTS monolayer.

For further discussion of this specific topic, reference is being made to section 7.2 in the last chapter. Here an outlook on future work is given. Besides this section, a general conclusion of the thesis is given with special focus on the impact of the presented work upon modeling gaseous microflows.



## 7 CONCLUSIONS

Based on the main hypothesis that gaseous mass transfer is always a superposition of various transport mechanisms, a consistently predictive model is presented for the analytical calculation of microduct gas flows under moderately rarefied conditions (up to  $\text{Kn} \approx 0.3$ ). Experimental results obtained on microducts with uniform cross section available in literature can be predicted reliably as well as own data measured on slightly tapered microchannels. The model is mathematically easy to handle so that mass flow rate or pressure loss can be calculated solely using a pocket calculator when duct geometry, gas properties, inlet pressure, outlet pressure, and temperature are known. Taking up the term used in section 1.2, the model is a straightforward and "engineer-friendly" mathematical formulation. The strikingly accurate prediction of experimental data indicates the correctness of the model and confirms the theoretical considerations.

By means of an additional term describing surface diffusion, the model is extended for the use over all regimes of rarefaction and termed CDS model (convection, diffusion and surface diffusion). The surface diffusion term is derived from the Maxwell-Stefan approach with assumption of Langmuir type adsorption, which yields a physically reasonable transport model in good agreement with experimental data taken from literature.

Under moderately rarefied conditions, micron-sized ducts with slightly varying cross section act as a gas flow diode. The experimentally observed diode effect increases with rarefaction. Measurements are performed on four ducts with different ratios of inlet to outlet cross section and one channel with uniform rectangular cross section as reference. Ducts are manufactured by "classic" deep reactive-ion etching of silicon and raster fly-cutting of aluminum. Thereby, the latter mentioned is a completely novel method for production of test channels for research on gaseous microflows. It is shown that the surface material has no influence on the experimentally obtained diodicity.

The diode effect, postulated by the working hypothesis and formulated in the developed model, is in excellent quantitative agreement to all measurements performed and presented in the current work. Analytical investigation of this approach shows that the contribution of convection to the entire mass flow rate decreases with increasing rarefaction and the flow is dominated by diffusion when the gas is moderately rarefied. The diffusive proportion strongly depends on the direction of perfusion since molecular spatial diffusion mass flow rate is proportional to the cross-sectional area of a duct. Further, the diode effect is independent of the length of the duct as long as  $l$  is considered to be large compared to width and height of the duct. The accuracy of prediction does surprise due to the simplicity of the mathematical formulation.

Considering the whole range of rarefaction, qualitative analysis of the CDS model shows that the amount adsorbed is higher at the duct inlet compared to the outlet and thus a concentration gradient occurs aligned to the pressure gradient in the bulk. This concentration

gradient represents the driving force for surface mass diffusion transport and furthermore increases with rarefaction. Thus the contribution of surface diffusion to the entire flow is negligible in the continuum regime but becomes increasingly important with rarefaction of the bulk gas. Hence the model of surface diffusion may contribute to the phenomenological understanding of the processes in the Knudsen layer (Zhang *et al.*, 2012).

From comparison of the model to experimental mass flow data on long ducts it can be summarized that:

- The cross-sectional shape of a duct has no influence on the reduced mass flow rate in the continuum, slip, and incipient transition regime when using the hydraulic diameter as reference value.
- Neither the kind of the tested gases (N<sub>2</sub>, He, Ar) nor the surface material of the duct (steel, etched silicon) does significantly influence the reduced mass flow rate.
- A significant disparity of permeability occurs between rectangular channels with high aspect ratio and nearly circular ducts in the transition and free molecular regime.

Thus the crucial difference is the aspect ratio (expressed by  $\Gamma$ ) of the duct representing the relative surface area of the walls which is extremely high for flat, rectangular channels and minimal for circular cross section (tube). The logarithmic behaviour of the derived model is in excellent agreement to the experimental data when adapting two parameters in the surface diffusion term. The terms for convection (Poiseuille's law) and molecular spatial diffusion are consistently predictive. Knudsen's minimum is described reliably due to the decreasing contribution of convection and the emerging contribution of surface diffusion nearby the minimum.

Hence a fundamental, physically reasonable transport model is presented which holds for the whole range of the Knudsen number. Consequently the (arbitrary) classification of the flow in continuum, slip-flow, transition, and free molecular regime (Figure 1.2 on page 3) should be modified when considering the flow as a superposition of different transport mechanism.

To conclude this topic, it is distinctly emphasized that the current thesis does not claim to supersede the kinetic theory. The presented modeling approach aims to contribute to the phenomenological understanding of gaseous flow processes and to provide a straightforward mathematical formulation. For more complex geometries, the calculation of macroscopic quantities is only possible by means of numerical methods like Direct Simulation Monte Carlo or Lattice Boltzmann Method.

Furthermore, the opportunities of surface functionalization on knowledge gain in the field of rarefied gas flows are discussed against the background of the developed surface diffusion term. Due to the theoretically analyzed chemical characteristics of a technical silicon surface, it is assumed that a modification of the hydroxyl groups causes an alteration of gas-wall interactions. Based on considerations regarding interactions of various gases with the OH groups, an appropriate chemical agent is identified and applied for the functionalization of a bundle of microchannels. By means of qualitative measurement of the water contact angle, it is shown that the surface chemistry of the channels is successfully altered and the majority of polar OH groups is inactivated.

The comparison of the permeability of gas flows before and after the treatment confirms that surface functionalization bears potential for basic research on rarefied gas flows.

## 7.1 Impact upon modeling gaseous microflows

An analytical approach is presented for the calculation of gaseous mass flow rate in microducts over the whole range of rarefaction. For all measurement series on microducts under moderately rarefied conditions, data points can be predicted accurately when using the superposition model presented in this thesis. This has impact upon modeling gaseous microflows since:

- A prediction of the mass flow rate is possible without the assumption of wall slip in the so-called slip-flow and transition regime. Knowing the size of the duct, the temperature, the gas properties, and the inlet and outlet pressure, the resulting mass flow rate can be calculated without any adaption parameter, such as the TMAC.
- The classification of non-rarefied into moderately rarefied gas flows in continuum, slip-flow and transition regimes becomes obsolete when the flow is considered as a superposition of different flow mechanisms over the whole range of Knudsen numbers.

Further, by means of the derived model it can be shown for the slip-flow regime and the beginning transition regime, that the diffusive proportion and likewise the dimensionless mass flow rate are not influenced by any variable regarding the surface topology. As a consequence of the broadly varying surface roughness (Table 3.2 on page 29) of the ducts the cited authors used, the results of Turner *et al.* (2004) can be confirmed thus far, that surface roughness has no influence on mass transfer in slightly and moderately rarefied gas flows. Further, the inconsistencies concerning the dependence of the TMAC on other parameters that are summarized in section 3.3, lead to reasonable doubts about the slip boundary condition and the state-of-the-art approach in modeling flow processes.

Analytical investigation of the present model shows that the diffusive proportion of the entire flow increases with the area of the channel entrance. The measurements of rarefied gas flows performed on slightly tapered microchannels confirmed that, since the mass flow is measured to be higher when the duct is perfused from the large to the narrow aperture (nozzle). Thus, more molecules impinge on the aperture and enter the duct on the high pressure side when the entrance cross section is large. Qualitative comparison with an approach using second order Maxwellian boundary condition shows that it is not possible to describe the flow in tapered ducts by means of slip correction. This leads to reasonable doubts about the use of the Maxwellian slip boundary condition in general.

It can be concluded that the results shown here might be an indicator for the rightness of the superposition approach for modeling gaseous microflows. Besides, suggestion is made to skip the term *slip-flow regime* and distinguish only three regimes according to the respective dominant transport mechanism.

## 7.2 Outlook on future work

Regarding the hypothesis that microflows under high rarefaction depend on the nature of the gas and on the material of the duct, experiments with gases including strong interactions with the surface should be performed. For glass or silica ducts, measurements with use of gases with a permanent dipole (e.g.  $\text{SO}_2$ ,  $\text{CHF}_3$ ) should clarify if rarefied phenomena depend on the contribution of surface diffusion being a function of gas–surface interactions.

As shown by means of the exemplarily performed surface functionalization, it is shown that chemical alteration of microduct surfaces is a promising method for knowledge gain in the field of rarefied gas flows. Other functional groups should be deposited at the surface of microducts for gas flow experiments over a wider range of rarefaction. Using MD simulations for analysis of the adsorption parameters and the surface diffusivity  $D_S$ , a better understanding of the dependency of the surface diffusion term on gas-solid interactions will be achieved. Probably MD simulations studies will clarify the discrepancy of adsorption data obtained by means of the superposition model and "conventionally" obtained data (see section 4.3).

Furthermore, it should be considered to apply the developed model for geometrically undefined ducts (porous structures). In analogy to the transport model of gases in porous membranes given by Melin & Rautenbach (2003), it is worth trying to express the CDS model by means of mean pore diameter, porosity, and tortuosity. Perhaps the derived model is even valid for isothermal gas flows in filters or gas separation membranes.

Finally, the limits of the diode effect simulated by means of the model (Figure 3.7 on page 40) should be studied using an experimental set-up which allows for investigation of a wider range of rarefaction. Furthermore, ducts with larger ratios of inlet to outlet cross-sectional area should be produced and investigated with respect to the dependency of the diode effect on geometric properties.

# BIBLIOGRAPHY

- A. Agrawal & S. V. Prabhu. Survey on measurement of tangential momentum accommodation coefficient. *J. Vac. Sci. Technol. A*, **26**:634–645, 2008.
- H. Ambaye & J. R. Manson. Calculations of accommodation coefficients for diatomic molecular gases. *Phys. Rev. E*, **73**:031202, 2006.
- T. W. Anderson & D. A. Darling. A test of goodness of fit. *J. Am. Statist. Assoc.*, **49**:765–769, 1954.
- J. F. Antonini & G. Hochstrasser. Surface states of pristine silica surfaces II.: UHV studies of the CO<sub>2</sub> adsorption-desorption phenomena. *Surf. Sci.*, **32**:665–686, 1972.
- T. Araki, M. S. Kim, H. Iwai, & K. Suzuki. An experimental investigation of gaseous flow characteristics in microchannels. *Microscale Therm. Eng.*, **6**:117–130, 2002.
- A. Argönül, L. Argönül, & F. J. Keil. The inconsistency in modeling surface diffusion with adsorption equilibrium. *J. Univ. Chem. Technol. Metallurgy*, **42**:181–186, 2007.
- E. B. Arkilic. Gaseous flow in micron-sized channels. Master’s thesis, Massachusetts Institute of Technology, Cambridge, MA, 1994.
- E. B. Arkilic. *Measurement of the Mass Flow and Tangential Momentum Accommodation Coefficient in Silicon Micromachined Channels*. PhD thesis, Massachusetts Institute of Technology, Cambridge, MA, 1997.
- E. B. Arkilic, M. A. Schmidt, & K. S. Breuer. TMAC measurement in silicon micromachined channels. *Proceedings of the 20th Symposium on Rarefied Gas Dynamics, Beijing, China*, 1997a.
- E. B. Arkilic, M. A. Schmidt, & K. S. Breuer. Gaseous slip flow in long microchannels. *J. Microelectromech. Syst.*, **6**:167–178, 1997b.
- E. B. Arkilic, K. S. Breuer, & M. A. Schmidt. Mass flow and tangential momentum accommodation in silicon micromachined channels. *J. Fluid Mech.*, **437**:29–43, 2001.
- G. Arya, H.-C. Chang, & E. J. Maginn. Molecular simulations of Knudsen wall-slip: Effect of wall morphology. *Mol. Simulat.*, **29**:697–709, 2003.
- Y. Asako, K. Nakayama, & T. Shinozuka. Effect of compressibility on gaseous flows in a micro-tube. *Int. J. Heat Mass Tran.*, **48**:4985–4994, 2005.
- P. Atkins. *Physical Chemistry*. Freeman, New York, 1978.
- P. Atkins & J. De Paula. *Physical chemistry*. Oxford University Press, Oxford, 8 edition, 2006.

- R. Barber & D. Emerson. Challenges in modeling gas-phase flow in microchannels: From slip to transition. *Heat Transfer Eng.*, **27**:3–12, 2006.
- D. Bathen & J. Ciprian. *Adsorption*. In: *Fluidverfahrenstechnik: Grundlagen, Methodik, Technik, Praxis* (Editor: R. Goedecke). Wiley-VCH, Weinheim, 2006.
- A. Beskok. Validation of a new velocity-slip model for separated gas microflows. *Numer. Heat Tr. B-Fund.*, **40**:451–471, 2001.
- P. L. Bhatnagar, E. P. Gross, & M. Krook. A model for collision processes in gases. I. small amplitude processes in charged and neutral one-component systems. *Phys. Rev.*, **94**:511–525, 1954.
- G. A. Bird. *Molecular Gasdynamics*. Clarendon Press, Oxford, 1976.
- R. B. Bird, W. E. Stewart, & E. N. Lightfoot. *Transport Phenomena*. John Wiley & Sons, New York, 2 edition, 2007.
- D. Blanchard & P. Ligrani. Slip and accommodation coefficients from rarefaction and roughness in rotating microscale disk flows. *Phys. Fluids*, **19**:063602, 2007.
- W. Brenig. Dynamics and kinetics of gas-surface interaction: Sticking, desorption and inelastic scattering. *Phys. Scripta*, **35**:329–331, 1987.
- H. Brenner. Beyond the no-slip boundary condition. *Phys. Rev. E*, **84**:046309, 2011.
- S. Brunauer. *Physical Adsorption*. Princeton University Press, New York, 1945.
- H. Bruus. *Theoretical Microfluidics*. Oxford University Press, Oxford, 2008.
- B.-Y. Cao, M. Chen, & Z.-Y. Guo. Temperature dependence of the tangential momentum accommodation coefficient for gases. *Appl. Phys. Lett.*, **86**:091905, 2005.
- B.-Y. Cao, M. Chen, & Z.-Y. Guo. Effect of surface roughness on gas flow in microchannels by molecular dynamics simulation. *Int. J. Eng. Sci.*, **44**(13–14):927–937, 2006.
- B.-Y. Cao, J. Sun, M. Chen, & Z.-Y. Guo. Molecular momentum transport at fluid-solid interfaces in MEMS/NEMS: A review. *Int. J. Mol. Sci.*, **10**:4638–4706, 2009.
- G. P. Celata, M. Cumo, S. J. McPhail, L. Tesfagabir, & G. Zummo. Experimental study on compressible flow in microtubes. *Int. J. Heat Mass Tran.*, **28**:28–36, 2007.
- C. Cercignani & M. Lampis. Kinetic models for gas-surface interactions. *Transport Theor. Stat.*, **1**:101–114, 1971.
- S. Chapman & T. G. Cowling. *The mathematical theory of non-uniform gases*. Cambridge University Press, Cambridge, 3 edition, 1970.
- C. Christiansen. Die atmolytische Strömung der Gase. *Ann. Phys.*, **277**:565–587, 1890.
- D. J. Cole, M. C. Payne, G. Csányi, S. M. Spearing, & L. Colombi Ciacchi. Development of a classical force field for the oxidized Si surface: Application to hydrophilic wafer bonding. *J. Chem. Phys.*, **127**:204704, 2007.

- S. Colin, P. Lalonde, & R. Caen. Validation of a second-order slip flow model in rectangular microchannels. *Heat Transfer Eng.*, **25**:23–30, 2004.
- S. R. Cook & M. A. Hoffbauer. Absolute momentum transfer in gas-surface scattering. *Phys. Rev. E*, **55**:R3828–R3831, 1997.
- S. R. Cook & M. A. Hoffbauer. Analyzing gas-surface interactions using the reduced force coefficients. *Phys. Rev. E*, **58**:504–511, 1998.
- S. M. Cooper, B. A. Cruden, M. Meyyappan, R. Raju, & S. Roy. Gas transport characteristics through a carbon nanotubule. *Nano Lett.*, **4**:377–381, 2004.
- R. E. Cunningham & R. J. J. Williams. *Diffusion in Gases an Porous Media*. Plenum Press, New York, 1980.
- E. L. Cussler. *Diffusion - Mass transfer in fluid systems*. Cambridge University Press, Cambridge, UK, 3 edition, 2009.
- S. K. Dadzie & H. Brenner. Predicting enhanced mass flow rates in gas microchannels using nonkinetic models. *Phys. Rev. E*, **86**:036318, 2012.
- S. K. Dadzie & J. M. Reese. A volume-based hydrodynamic approach to sound wave propagation in a monatomic gas. *Phys. Fluids*, **22**:016103, 2010.
- S. K. Dadzie, J. M. Reese, & C. R. McInnes. A continuum model of gas flows with localized density variations. *Physica A*, **387**:6079–6094, 2008.
- B. S. Day, S. F. Shuler, A. Ducre, & J. R. Morris. The dynamics of gas-surface energy exchange in collisions of Ar atoms with  $\omega$ -functionalized self assembled monolayers. *J. Chem. Phys.*, **119**:8084–8096, 2003.
- A. Demsis, S. V. Prabhu, & A. Agrawal. Influence of wall conditions on friction factor for flow of gases under slip condition. *Exp. Therm. Fluid Sci.*, **34**:1448–1455, 2010.
- J. Dong, A. Wang, K. Y. Simon Ng, & G. Mao. Self-assembly of octadecyltrichlorosilane monolayers on silicon-based substrates by chemical vapor deposition. *Thin Solid Films*, **515**:2116–2122, 2006.
- N. Dongari, S. K. Dadzie, Y. Zhang, & J. M. Reese. Isothermal micro-channel gas flow using a hydrodynamic model with dissipative mass flux. *Rarefied Gas Dynamics: Proceedings of the 27th International Symposium, Pacific Grove, CA*, pages 718–724, 2011.
- R. O. Doughty & W. J. Schaetzle. *Experimental determination of momentum accommodation coefficients at velocities up to and exceeding earth escape velocity*. In: *Rarefied Gas Dynamics*. Academic Press, New York-London, 2 edition, 1969.
- C. Dytham. *Choosing and using statistics: A biologist's guide*. Blackwell, Malden, MA, 2 edition, 2006.
- T. Engel. A molecular-beam investigation of He, CO, and O<sub>2</sub> scattering from D(111). *J. Chem. Phys.*, **69**:373–385, 1978.

- T. Ewart, I. A. Graur, P. Perrier, & J. G. Meolans. Mass flow rate measurements: From hydrodynamic to free molecular regime. *Proceedings of the 6th International Conference on Nanochannels, Microchannels, and Minichannels, Darmstadt, Germany*, pages 65–73, 2008.
- T. P. Ewart, P. Perrier, I. A. Graur, & J. G. Meolans. Mass flow rate measurements in gas micro flows. *Exp. Fluids*, **41**:487–498, 2006.
- T. P. Ewart, P. Perrier, I. A. Graur, & J. G. Meolans. Tangential momentum accommodation in microtube. *Microfluid. Nanofluid.*, **3**:689–695, 2007a.
- T. P. Ewart, P. Perrier, I. A. Graur, & J. G. Meolans. Mass flow rate measurements in a microchannel, from hydrodynamic to near free molecular regimes. *J. Fluid Mech.*, **584**:337–356, 2007b.
- G. Fan & J. R. Manson. Theory of direct scattering, trapping, and desorption in atom-surface collisions. *Phys. Rev. B*, **79**:045424, 2009.
- R. Feres & G. Yablonsky. Knudsen’s cosine law and random billiards. *Chem. Eng. Sci.*, **59**:1541–1556, 2004.
- A. Fick. Über Diffusion. *Ann. Phys.*, **170**:59–86, 1855.
- G. W. Finger, J. S. Kapat, & A. Bhattacharya. Molecular dynamics simulation of adsorbent layer effect on tangential momentum accommodation coefficient. *J. Fluids Eng.*, **129**:31–39, 2007.
- S. Franssila. *Introduction to Microfabrication*. John Wiley & Sons, Chichester, 2 edition, 2010.
- D. H. Gabis, S. K. Loyalka, & T. S. Srorvick. Measurements of the tangential momentum accommodation coefficient in the transition flow regime with a spinning rotor gauge. *J. Vac. Sci. Technol. A*, **14**:2592–2598, 1996.
- M. Gad-el-Hak. The fluid mechanics of microdevices-The Freeman scholar lecture. *J. Fluid. Eng.*, **121**:5–33, 1999.
- W. Gaede. Die Äußere Reibung der Gase. *Ann. Phys.*, **346**:289–336, 1913.
- J. G. Geankoplis. *Mass transport phenomena*. Holt, Rinehart & Winston, Inc., New York, 1972.
- H. Grad. On the kinetic theory of rarefied gases. *Commun. Pur. Appl. Math.*, **2**:331–407, 1949.
- I. A. Graur, P. Perrier, W. Ghazlani, & J. G. Meolans. Measurements of tangential momentum accommodation coefficient for various gases in plane microchannel. *Phys. Fluids*, **21**:102004, 2009.
- P. Gravesen, J. Branebjerg, & O. S. Jensen. Microfluidics – a review. *J. Micromech. Microeng.*, **3**:168–182, 1993.

- S. B. Habib, E. Gonzales, & R. F. Hicks. Atmospheric oxygen plasma activation of silicon (100) surfaces. *J. Vac. Sci. Technol. A*, **28**:476–485, 2010.
- M. Hadj-Nacer, P. Perrier, J. G. Meolans, I. A. Graur, & M. Wüest. Experimental study of the gas flows through channels with circular cross sections. *JPCS*, **362**:012025, 2012.
- J. C. Harley, Y. Huang, H. H. Bau, & J. N. Zemel. Gas flow in micro-channels. *J. Fluid Mech.*, **284**:257–274, 1995.
- P. J. E. Harlick & F. H. Tezel. Adsorption of carbon dioxide, methane and nitrogen: Pure and binary mixture adsorption for ZSM-5 with SiO<sub>2</sub>/Al<sub>2</sub>O<sub>3</sub> ratio of 280. *Sep. Purif. Technol.*, **33**:199–210, 2003.
- M. Henzler & W. Ranke. *Structural effects at surfaces*. In: *Physics of solid surfaces, Landolt Börnstein, New Series III* (Editor: G. Chiarotti). Springer, Berlin, 1993.
- D. Hänel. *Molekulare Gasdynamik*. Springer, Berlin, 2004.
- C. M. Ho & Y. C. Tai. MEMS and its applications for flow control. *J. Fluids Eng.*, **118**:437–447, 1996.
- C. M. Ho & Y. C. Tai. Micro-electro-mechanical-systems (MEMS) and fluid flows. *Annu. Rev. Fluid Mech.*, **30**:579–612, 1998.
- C. Hong, T. Yamada, Y. Asako, & M. Faghri. Experimental investigations of laminar, transitional and turbulent gas flow in microchannels. *Int. J. Heat Mass Tran.*, **55**:4397–4403, 2012.
- S.-S. Hsieh, H.-H. Tsai, C.-Y. Lin, C.-F. Huang, & C.-M. Chien. Gas flow in a long microchannel. *Int. J. Heat Mass Tran.*, **47**:3877–3887, 2004.
- C. Huang, J. W. Gregory, & J. P. Sullivan. Microchannel pressure measurements using molecular sensors. *J. Microelectromech. Syst.*, **16**:777–785, 2007.
- J. Jang & S. T. Wereley. Effective heights and tangential momentum accommodation coefficients of gaseous slip flows in deep reactive ion etching rectangular microchannels. *J. Micromech. Microeng.*, **16**:493–504, 2006.
- J. Jang & S. T. Wereley. Gaseous slip flow analysis of a micromachined flow sensor for ultra small flow applications. *J. Micromech. Microeng.*, **17**:229–237, 2007.
- J. Jang, Y. Zhao, S. T. Wereley, & L. Gui. Mass flow measurement of gases in deep-RIE microchannels. *Proceedings of IMECE2002 ASME International Mechanical Engineering Congress & Exposition, New Orleans, LA*, pages 17–22, 2002.
- J. Kaerger & D. M. Ruthven. *Diffusion in Zeolites and Other Microporous Solids*. Wiley-Interscience, New York, 1992.
- E. Karniadakis & A. Beskok. *Micro Flows: Fundamentals and Simulation*. Springer, New York, 2002.
- E. H. Kennard. *The kinetic theory of gases*. McGraw-Hill, New York, 1938.

- R. Kirkpatrick & C. L. Muhlstein. Performance and durability of octadecyltrichlorosilane coated borosilicate glass. *J. Non-Cryst. Solids*, **353**:2624–2637, 2007.
- G. Kissinger & W. Kissinger. Hydrophilicity of silicon wafers for direct bonding. *Phys. Status Solidi A*, **123**:185–192, 1991.
- M. Knudsen. Die Gesetze der Molekularströmung und der inneren Reibungsströmung der Gase durch Röhren. *Ann. Phys.*, **333**:75–130, 1909.
- M. Knudsen. Das Cosinusetz in der kinetischen Gastheorie. *Ann. Phys.*, **353**:1113–1121, 1916.
- K. W. Kolasinski. *Surface Science: Foundations of Catalysis and Nanoscience*. John Wiley & Sons, Chichester, 2001.
- T. Kondo, D. Mori, R. Okada, M. Sasaki, & S. Yamamoto. A molecular-beam study of the collision dynamics of methane and ethane upon graphitic monolayer on Pt(111). *J. Chem. Phys.*, **123**:114712, 2005.
- R. Krishna & J. M. van Baten. An investigation of the characteristics of Maxwell-Stefan diffusivities of binary mixtures in silica nanopores. *Chem. Eng. Sci.*, **64**:870–882, 2009.
- R. Krishna & J. A. Wesselingh. The Maxwell-Stefan approach to mass transfer. *Chem. Eng. Sci.*, **52**:861–911, 1997.
- A. R. Kuhlthau. Air friction on rapidly moving surfaces. *J. Appl. Phys.*, **20**:217–223, 1949.
- A. Kundt & E. Warburg. Über Reibung und Wärmeleitung verdünnter Gase. *Ann. Phys.*, **232**:177–211, 1875.
- P. Lalonde. *Etude expérimentale d'écoulements gazeux dans les microsystèmes à fluides*. PhD thesis, L'Institut National des Sciences Appliquées de Toulouse, 2001.
- I. Langmuir. Surface chemistry. *Chem. Rev.*, **13**:147–191, 1933.
- R. G. Lord. Some extensions to the Cercignani-Lampis gas-surface scattering kernel. *Phys. Fluids A-Fluid*, **3**:706–710, 1991.
- J. W. Lu & J. R. Morris. Gas-surface scattering dynamics of CO<sub>2</sub>, NO<sub>2</sub>, and O<sub>3</sub> in collisions with model organic surfaces. *J. Phys. Chem. A*, **115**:6194–6201, 2011.
- L. M. Lund & A. S. Berman. Flow and self-diffusion of gases in capillaries. Part I. *J. Appl. Phys.*, **37**:2489–2495, 1966a.
- L. M. Lund & A. S. Berman. Flow and self-diffusion of gases in capillaries. Part II. *J. Appl. Phys.*, **37**:2496–2508, 1966b.
- K. Malek & M.-O. Coppens. Knudsen self- and Fickian diffusion in rough nanoporous media. *J. Chem. Phys.*, **119**:2801–2811, 2003.
- L. Marino. Experiments on rarefied gas flows through tubes. *Microfluid. Nanofluid.*, **6**:109–119, 2009.

- A. Markovic. *Experimental and theoretical analysis of the mass transport through porous glass membranes with different pore diameters*. PhD thesis, Otto-von-Guericke-Universität, Magdeburg, 2009.
- A. Markovic, D. Stoltenberg, D. Enke, E. U. Schlünder, & A. Seidel-Morgenstern. Gas permeation through porous glass membranes. Part I. Mesoporous glasses-Effect of pore diameter and surface properties. *J. Membrane Sci.*, **336**:17–31, 2009a.
- A. Markovic, D. Stoltenberg, D. Enke, E. U. Schlünder, & A. Seidel-Morgenstern. Gas permeation through porous glass membranes. Part II. Transition regime between Knudsen and configurational diffusion. *J. Membrane Sci.*, **336**:32–41, 2009b.
- E. A. Mason, A. P. Malinauskas, & R. B. Evans. Flow and diffusion of gases in porous media. *J. Phys. Chem.*, **46**:3199–3216, 1967.
- J. Maurer, P. Tabeling, P. Joseph, & H. Willaime. Second-order slip laws in microchannels for helium and nitrogen. *Phys. Fluids*, **15**:2613–2621, 2003.
- J. C. Maxwell. On stresses in rarified gases arising from inequalities of temperature. *Phil. Trans. R. Soc. Lond.*, **170**:231–256, 1879.
- I. Medved & R. Černý. Surface diffusion in porous media: A critical review. *Micropor. Mesopor. Mat.*, **142**:405–422, 2011.
- T. Melin & R. Rautenbach. *Membranverfahren: Grundlagen der Modul- und Anlagenauslegung*. Springer, Berlin, 2 edition, 2003.
- J.-H. Moon, Y.-J. Park, M.-B. Kim, S.-H. Hyun, & C.-H. Lee. Permeation and separation of a carbon dioxide/nitrogen mixture in a methyltriethoxysilane templating silica/ $\alpha$ -alumina composite membrane. *J. Membrane Sci.*, **250**:195–205, 2005.
- G. L. Morini, Y. Yang, H. Chalabi, & M. Lorenzini. A critical review of the measurement techniques for the analysis of gas microflows through microchannels. *Exp. Therm. Fluid Sci.*, **35**:849–865, 2011.
- R. S. Myong. Gaseous slip models based on the Langmuir adsorption isotherm. *Phys. Fluids*, **16**:104–117, 2004.
- M. B. Nagard, P. U. Andersson, N. Markovi, & J. B. C. Pettersson. Scattering and trapping dynamics of gas-surface interactions: Theory and experiments for the Xe-graphite system. *J. Chem. Phys.*, **109**:10339, 1998.
- M. Nau. Elektrische Temperaturmessung mit Thermoelementen und Widerstandsthermometern. Technical report, JUMO GmbH & Co. KG, 2004.
- N. Nguyen. Micromachined flow sensors - a review. *Flow Meas. Instrum.*, **8**:7–16, 1997.
- B. Olbrechts, X. Zhang, Y. Betholet, T. Pardoën, & J. P. Raskin. Effect of interfacial SiO<sub>2</sub> thickness for low temperature O<sub>2</sub> plasma activated wafer bonding. *Microsyst. Technol.*, **12**:383–390, 2006.
- K. Oura, V. G. Lifshits, A. A. Saranin, A. V. Zotov, & M. Katayama. *Surface science*. Springer, Berlin, 2003.

- R. L. Panton. *Incompressible flow*. Wiley-Interscience, New York, 2 edition, 1996.
- W. Peiyi & W. A. Little. Measurement of friction factors for the flow of gases in very fine channels used for microminiature Joule-Thomson refrigerators. *Cryogenics*, **23**:273–277, 1983.
- P. Perrier, I. A. Graur, T. Ewart, & J. G. Meolans. Mass flow rate measurements in microtubes: From hydrodynamic to near free molecular regime. *Phys. Fluids*, **23**:042004, 2011.
- M. Petkovska, A. Markovic, M. Lazar, & A. Seidel-Morgenstern. Investigation of gas transport through porous membranes based on nonlinear frequency response analysis. *Adsorption*, **17**:75–91, 2011.
- J. Pitakarnnop, S. Varoutis, D. Valougeorgis, S. Geoffroy, L. Baldas, & S. Colin. A novel experimental setup for gas microflows. *Microfluid. Nanofluid.*, **8**:57–72, 2010.
- P. I. Pohl & G. S. Heffelfinger. Massively parallel molecular dynamics simulation of gas permeation across porous silica membranes. *J. Membrane Sci.*, **155**:1–7, 1999.
- W. G. Pollard & R. D. Present. On gaseous self-diffusion in long capillary tubes. *Phys. Rev.*, **73**:762–774, 1948.
- J. M. Reese, M. A. Gallis, & D. A. Lockerby. New directions in fluid dynamics: non-equilibrium aerodynamic and microsystem flows. *Philos. T. Roy. Soc. A*, **361**:2967–2988, 2003.
- C. T. Rettner. Thermal and tangential-momentum accommodation coefficients for N<sub>2</sub> colliding with surfaces of relevance to disk-drive air bearings derived from molecular beam scattering. *IEEE T. Magn.*, **34**:2387–2395, 1998.
- A. A. Rostami, A. S. Majumdar, & N. Saniel. Flow and heat transfer for gas flowing in microchannels: A review. *Heat Mass Transfer*, **38**:339–367, 2002.
- S. Roy, R. Raju, H. F. Chuang, B. A. Cruden, & M. Meyyappan. Modeling gas flow through microchannels and nanopores. *J. Appl. Phys.*, **93**:4870–4879, 2003.
- L. A. Roybal & S. I. Sandler. Surface diffusion of adsorbable gases through porous media. *AIChE J.*, **18**:39–42, 1972.
- D. M. Ruthven. *Principles of Adsorption and Adsorption Processes*. Wiley, New York, 1984.
- O. Sazhin, S. F. Borisov, & F. Sharipov. Accommodation coefficient of tangential momentum on atomically clean and contaminated surfaces. *J. Vac. Sci. Technol. A*, **19**:2499–2503, 2001.
- S. A. Schaaf & P. L. Chambré. *Flow of Rarefied Gases*. Princeton University Press, New York, 1961.
- M. Seidl & E. Steinheil. *Measurement of momentum accommodation coefficients on surfaces characterized by Auger Spectroscopy, SIMS and LEED*. In: *Rarefied gas dynamics: Ninth International Symposium on Rarefied Gas Dynamics* (Editors: M. Becker, M. Fiebig). DFVLR-Press, Porz-Wahn, 1974.

- N. Shamir, J. G. Mihaychuk, H. M. van Driel, & H. J. Kreuzer. Universal mechanism for gas adsorption and electron trapping on oxidized silicon. *Phys. Rev. Lett.*, **82**:359–361, 1999.
- C. Shen. *Rarefied gas dynamics*. Springer, Berlin, 2005.
- F. S. Sherman. *Viscous flow*. McGraw-Hill, New York, 1990.
- J. C. Shih, C. M. Ho, J. Q. Liu, & Y. C. Tai. Monatomic and polyatomic gas flow through uniform microchannels. *ASME-DSC*, **59**:197–203, 1996.
- H. Shinagawa, H. Setyawan, T. Asai, Y. Sugiyama, & K. Okuyama. An experimental and theoretical investigation of rarefied gas flow through circular tube of finite length. *Chem. Eng. Sci.*, **57**:4027–4036, 2002.
- A. I. Skoulidas & D. S. Sholl. Self-diffusion and transport diffusion of light gases in metal-organic framework materials assessed using molecular dynamics simulations. *J. Phys. Chem. B*, **109**:15760–15768, 2005.
- R. K. Smith & A. B. Metzner. Rates of surface migration of physically adsorbed gases. *J. Phys. Chem.*, **68**:2741–2747, 1964.
- G. A. Somorjai. *Principles of Surface Chemistry*. Prentice-Hall, Englewood Cliffs, NY, 1972.
- P. Spijker, A. J. Markvoort, S. V. Nedeia, & P. A. J. Hilbers. Computation of accommodation coefficients and the use of velocity correlation profiles in molecular dynamics simulations. *Phys. Rev. E*, **81**:011203, 2010.
- R. G. Steel & J. H. Torrie. *Principles and procedures of statistics: a biometrical approach*. McGraw-Hill, New York, 2 edition, 1980.
- N. D. Stevanovic. A new analytical solution of microchannel gas flow. *J. Micromech. Microeng.*, **17**:1695–1702, 2007.
- H. Struchtrup & P. Taheri. Macroscopic transport models for rarefied gas flows: A brief review. *IMA J. Appl. Math.*, **76**:672–697, 2011.
- H. Struchtrup & M. Torrilhon.  $H$  theorem, regularization, and boundary conditions for linearized 13 moment equations. *Phys. Rev. Lett.*, **99**:014502, 2007.
- H. Sun & M. Faghri. Effect of surface roughness on nitrogen flow in a microchannel using the direct simulation Monte Carlo method. *Numer. Heat Tr. A-Appl.*, **43**:1–8, 2003.
- J. Sun & Z.-X. Li. Effect of gas adsorption on momentum accommodation coefficients in microgas flows using molecular dynamic simulations. *Mol. Phys.*, **106**:2325–2332, 2008.
- J. Sun & Z.-X. Li. Two-dimensional molecular dynamic simulations on accommodation coefficients in nanochannels with various wall configurations. *Comput. Fluids*, **39**:1345–1352, 2010.
- J. Sun & Z.-X. Li. Three-dimensional molecular dynamic study on accommodation coefficients in rough nanochannels. *Heat Transfer Eng.*, **32**:658–666, 2011.
- W. Sutherland. The viscosity of mixed gases. *Philos. Mag.*, **40**:421–431, 1895.

- L. Szalmas, S. Colin, & D. Valougeorgis. Flow rate measurements of binary gas mixtures through long trapezoidal microchannels. *JPCS*, **362**:012003, 2012.
- S. H. Tan, N. T. Nguyen, Y. C. Chua, & T. G. Kang. Oxygen plasma treatment for reducing hydrophobicity of a sealed polydimethylsiloxane microchannel. *Biomicrofluidics*, **4**:32204, 2010.
- G. H. Tang, Z. Li, Y. L. He, & W. Q. Tao. Experimental study of compressibility, roughness and rarefaction influences on microchannel flow. *Int. J. Heat Mass Tran.*, **50**:2282–2295, 2007.
- C. Tantos & D. Valougeorgis. Rarefied gas flows through long rectangular channels of variable width and comparison with measurements. 2012.
- A. W. Thornton, T. Hilder, H. J. Hill, & J. M. Hill. Predicting gas diffusion regime within pores of different size, shape and composition. *J. Membrane Sci.*, **336**:101–108, 2009.
- A. Timiriazeff. Über die innere Reibung verdünnter Gase und über den Zusammenhang der Gleitung und des Temperatursprunges an der Grenze zwischen Metall und Gas. *Ann. Phys.*, **345**:971–991, 1913.
- S. Tison. Experimental data and theoretical modeling of gas flows through metal capillary leaks. *Vacuum*, **44**:1171–1175, 1993.
- S. E. Turner, L. C. Lam, M. Faghri, & O. J. Gregory. Experimental investigation of gas flow in microchannels. *J. Heat Trans.*, **126**:753–763, 2004.
- A. Ueno & C. O. Bennett. Infrared study of CO<sub>2</sub> adsorption on SiO<sub>2</sub>. *J. Catal.*, **54**:31–41, 1978.
- E. F. Vansant, P. Van Der Voort, & K. C. Vrancken. *Characterization and chemical modification of the silica surface*. Elsevier Science B. V., Amsterdam, 1995.
- S. Varoutis, S. Naris, V. Hauer, C. Day, & D. Valougeorgis. Computational and experimental study of gas flows through long channels of various cross sections in the whole range of the Knudsen number. *J. Vac. Sci. Technol. A*, **27**:89–100, 2009.
- S. Varoutis, T. Giegerich, V. Hauer, & C. Day. TRANSFLOW: An experimental facility for vacuum gas flows. *JPCS*, **362**:012027, 2012.
- A. E. Velasco, S. G. Friedman, M. Pevarnik, Z. S. Siwy, & P. Taborek. Pressure-driven flow through a single nanopore. *Phys. Rev. E*, **86**:025302, 2012.
- T. Veltzke & J. Thöming. An analytically predictive model for moderately rarefied gas flow. *J. Fluid Mech.*, **698**:406–422, 2012.
- T. Veltzke, M. Baune, & J. Thöming. The contribution of diffusion to gas microflow: An experimental study. *Phys. Fluids*, **24**:082004, 2012a.
- T. Veltzke, M. Baune, & J. Thöming. The contribution of surface diffusion to mass flow rate in microscale ducts. *MicroFlu12*, 3<sup>rd</sup> European conference on Microfluidics, Heidelberg, 3-5 December 2012, SHF ed. ISSN 2108-4718, 2012b.

- Y. Wang & M. Lieberman. Growth of ultrasMOOTH octadecyltrichlorosilane self-assembled monolayers on SiO<sub>2</sub>. *Langmuir*, **19**:1159–1167, 2003.
- E. Warburg. Über die Gleitung der Gase an Glaswänden. *Ann. Phys.*, **235**:399–415, 1876.
- M. Wiegand. *Auswirkungen einer Plasmabehandlung auf die Eigenschaften des Niedertemperatur-Waferbondens monokristalliner Siliziumoberflächen*. PhD thesis, Martin-Luther-Universität Halle-Wittenberg, 2001.
- A. C. Wight & R. E. Miller. Vibrational quenching of acetylene scattered from LiF(001): Trapping desorption versus direct scattering. *J. Chem. Phys.*, **109**:8626, 1998.
- X. Xu, X. Zhao, L. Sun, & X. Liu. Adsorption separation of carbon dioxide, methane, and nitrogen on h $\beta$  and Na-exchanged  $\beta$ -zeolite. *J. Nat. Gas Chem.*, **17**:391–396, 2008.
- H. Yamaguchi, T. Hanawa, O. Yamamoto, Y. Matsuda, Y. Egami, & T. Niimi. Experimental measurement on tangential momentum accommodation coefficient in a single microtube. *Microfluid. Nanofluid.*, **11**:57–64, 2011.
- H. Yamaguchi, Y. Matsuda, & T. Niimi. Tangential momentum accommodation coefficient measurements for various materials and gas species. *JPCS*, **362**:012035, 2012.
- K. Yamamoto. Slip flow over a smooth platinum surface. *JSME Int. J. B-Fluid T.*, **45**:788–795, 2002.
- S. R. Yang. *Zusammengesetzte Self-assembled Monolayers (SAMs) auf Siliziumoberflächen: Präparation und Charakterisierung*. PhD thesis, Johann Wolfgang Goethe-Universität, Frankfurt am Main, 2008.
- Z. Yang & S. V. Garimella. Rarefied gas flow in microtubes at different inlet-outlet pressure ratios. *Phys. Fluids*, **21**:052005, 2009.
- W.-M. Zhang, G. Meng, & X. Wei. A review on slip models for gas microflows. *Microfluid. Nanofluid.*, pages 1–38, 2012. doi: 10.1007/s10404-012-1012-9.
- X. G. Zhang. *Electrochemistry of silicon and its oxide*. Kluwer Academic/Plenum Publishers, New York, 2001.
- X. Y. Zhuang, O. Hansen, T. Knieling, C. Wang, P. Rombach, W. Lang, W. Benecke, M. Kehlenbeck, & J. Koblitz. Vapor-phase self-assembled monolayers for anti-stiction applications in MEMS. *J. Microelectromech. Syst.*, **16**:1451–1460, 2007.
- L. T. Zhuravlev. Concentration of hydroxyl groups on the surface of amorphous silicas. *Langmuir*, **3**:316–318, 1987.
- Y. Zohar, S. Y. K. Lee, W. Y. Lee, L. Jiang, & P. Tong. Subsonic gas flow in a straight and uniform microchannel. *J. Fluid Mech.*, **472**:125–151, 2002.

**Single picture credits** (Figure 1.1 on page 2)

Power plant

<http://solar-energie-boden.de/wp-content/uploads/2011/02/Kohlekraftwerk.jpg>

*Date of download: 1 June 2012*

Filter/Catalyst

*With friendly permission of Wiebke Veltzke and Ralf Sievering*

MEMS/NEMS

<http://www.ateforum.com/news/images/ATE/mems5.jpg>

<http://en.wikipedia.org/wiki/Lab-on-a-chip>

*Date of download: 1 June 2012*

Spaceshuttle

<http://www.nevadaspacegrant.com/wp-content/uploads/2010/01/Space-Shuttle.jpg>

*Date of download: 4 June 2012*

# APPENDIX A

This appendix contains detailed information about the experimental set-up presented in section 5.2. Besides photos and manufacturing drawings, data sheets and ex-works calibration documents of the measuring instruments are provided subsequently.

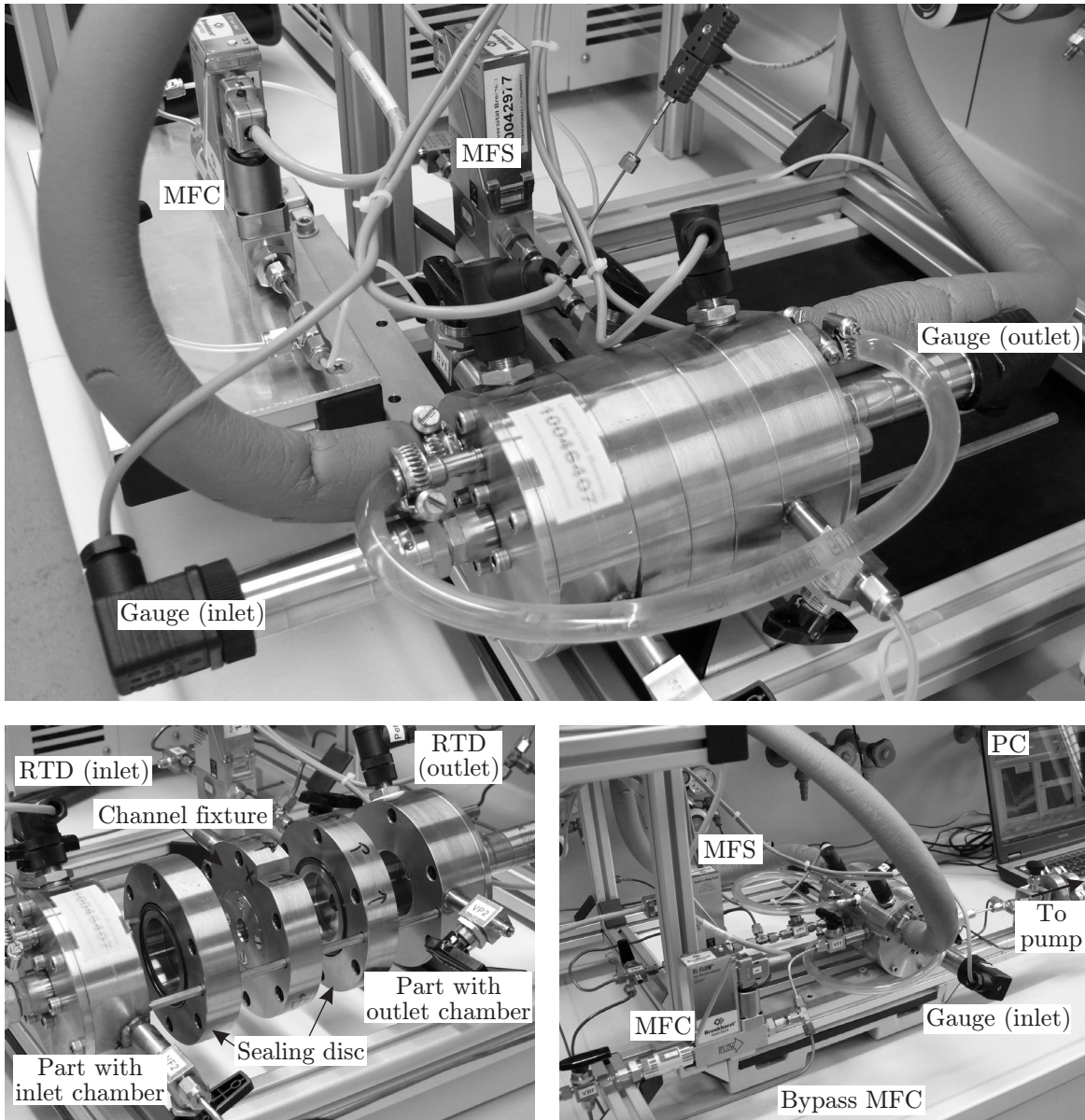
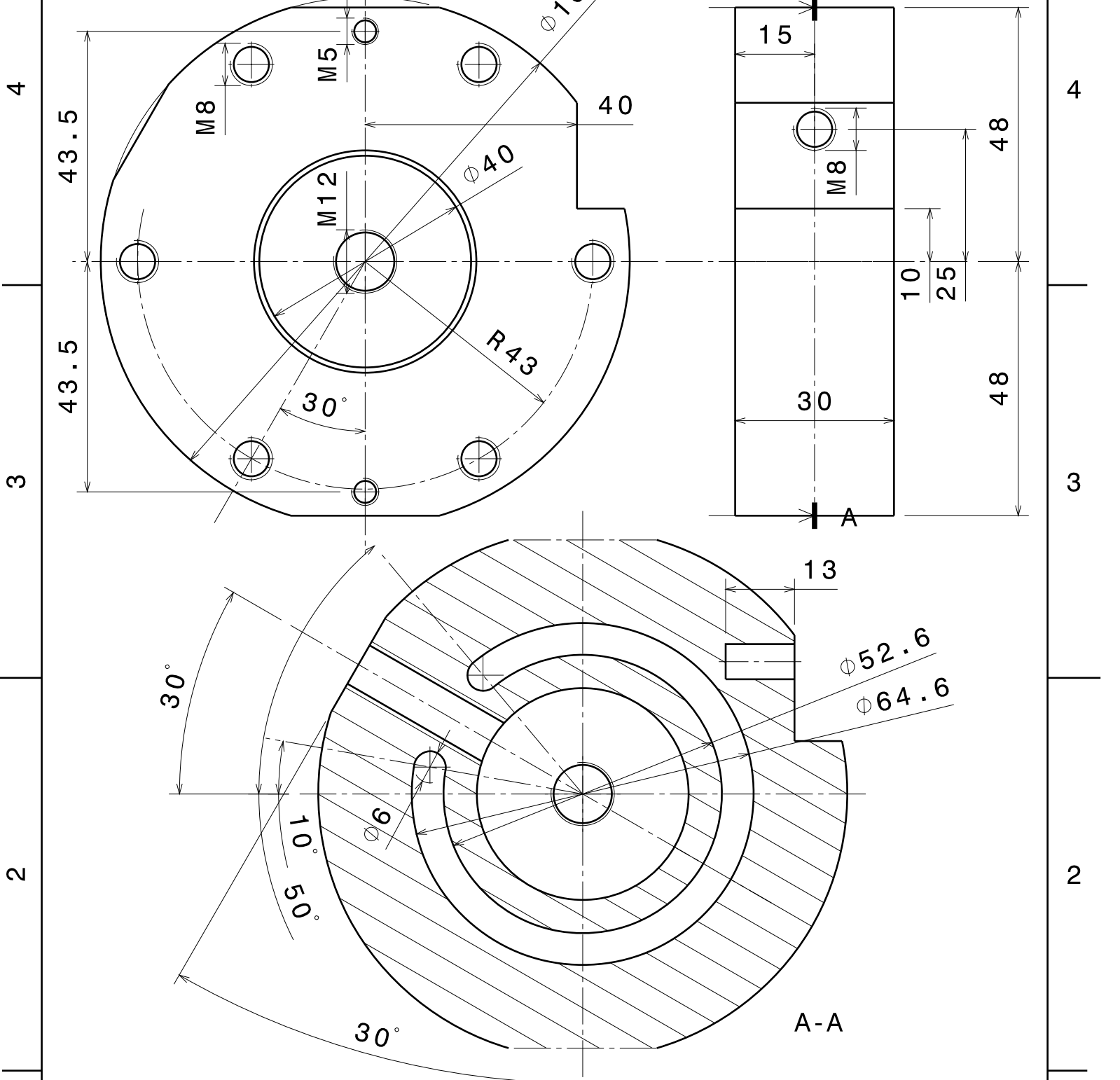


Figure A.1: Photos of the experimental set-up according to Figure 5.3 on page 66.



DESIGNED BY: <b>T. Veltzke</b>	
DATE: <b>June 1. 2010</b>	
MATERIAL: <b>Stainless Steel</b>	
<b>1.4301</b>	
SIZE <b>A4</b>	
SCALE <b>1:1</b>	WEIGHT (kg)

<b>Part with inlet chamber (1)</b>		DRAWING NUMBER	SHEET
		<b>1-1</b>	<b>1/4</b>

I	-
H	-
G	-
F	-
E	-
D	-
C	-
B	-
A	-

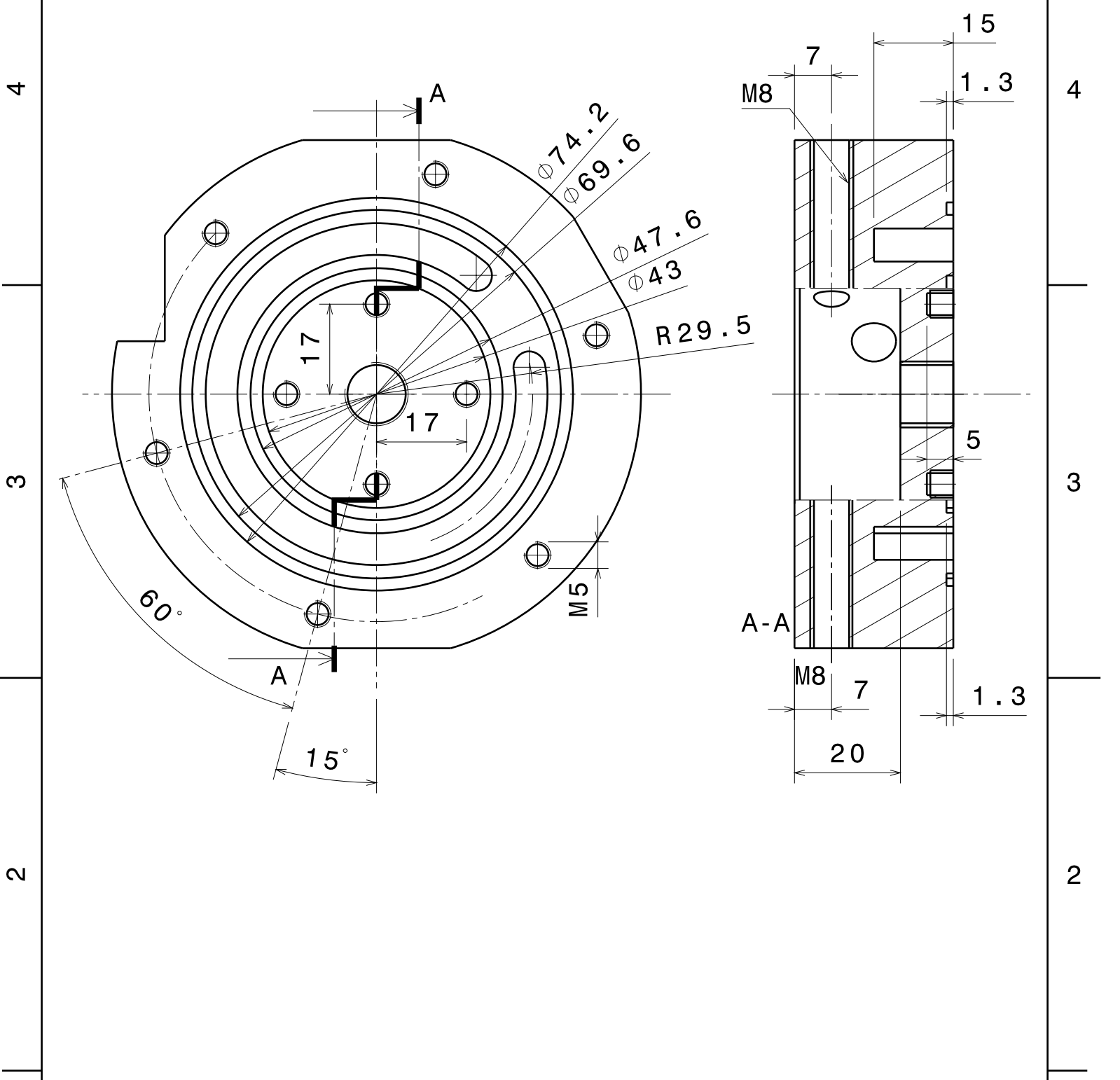
This drawing is our property; it can't be reproduced or communicated without our written agreement.

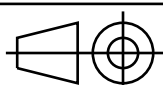
4  
3  
2  
1

4  
3  
2  
1

D

A



DESIGNED BY: <b>T. Veltzke</b>	
DATE: <b>June 1. 2010</b>	
MATERIAL: <b>Stainless Steel</b>	
<b>1.4301</b>	
SIZE <b>A4</b>	
SCALE <b>1:1</b>	WEIGHT (kg)

<h1>Part with inlet chamber (2)</h1>	
DRAWING NUMBER <b>1-2</b>	
SHEET <b>2/4</b>	

I	-
H	-
G	-
F	-
E	-
D	-
C	-
B	-
A	-

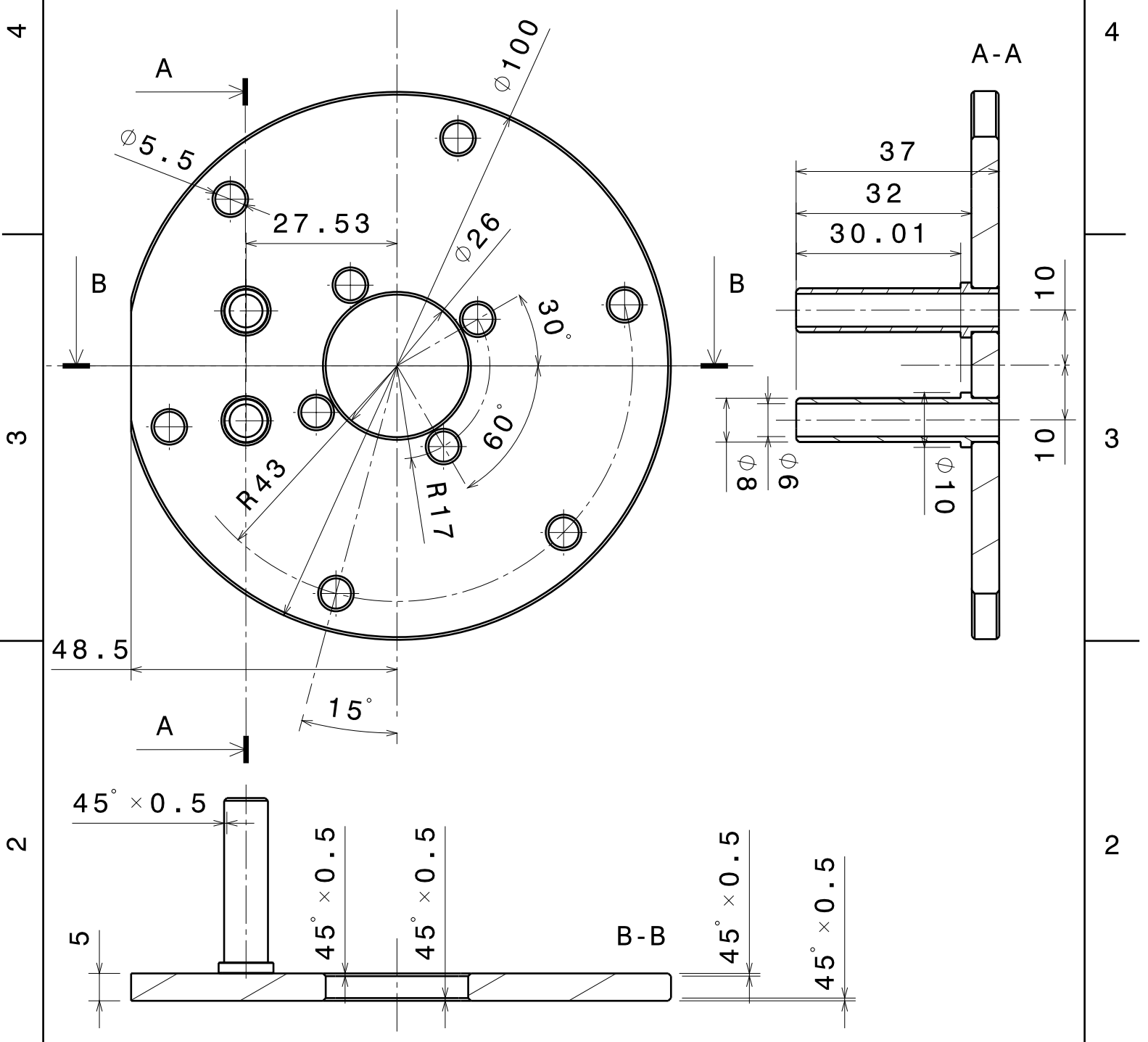
This drawing is our property; it can't be reproduced or communicated without our written agreement.

4  
3  
2  
1

4  
3  
2  
1

D

A



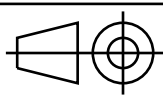
DESIGNED BY:  
T. Veltzke

DATE:  
June 1. 2010

MATERIAL:  
Stainless Steel  
1.4301

SIZE  
**A4**

SCALE  
**1:1**



**Cover with pipe sockets (inlet)**

**Gas Flow Apparatus**

DRAWING NUMBER  
**1-3**

SHEET  
**3/4**

I	-
H	-
G	-
F	-
E	-
D	-
C	-
B	-
A	-

This drawing is our property; it can't be reproduced or communicated without our written agreement.

4  
3  
2  
1

4  
3  
2  
1

D

A

4

4

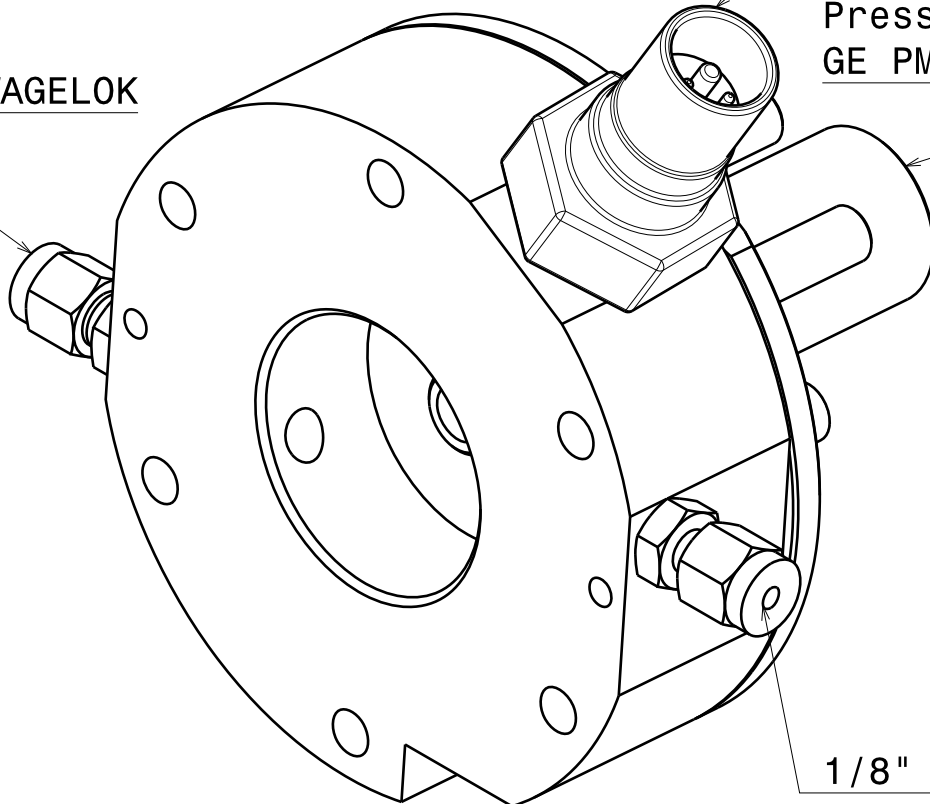
PT1000, WIKA TF35

Pressure gauge  
GE PMP4070

1/8" SWAGELOK

3

3



1/8" SWAGELOK

2

2

DESIGNED BY:  
T. Veltzke  
DATE:  
June 1. 2010

Part with inlet  
chamber (assembled)

I	-
H	-
G	-
F	-
E	-
D	-
C	-
B	-
A	-

1

1

SIZE  
**A4**

Gas Flow Apparatus

SCALE  
**1:1**

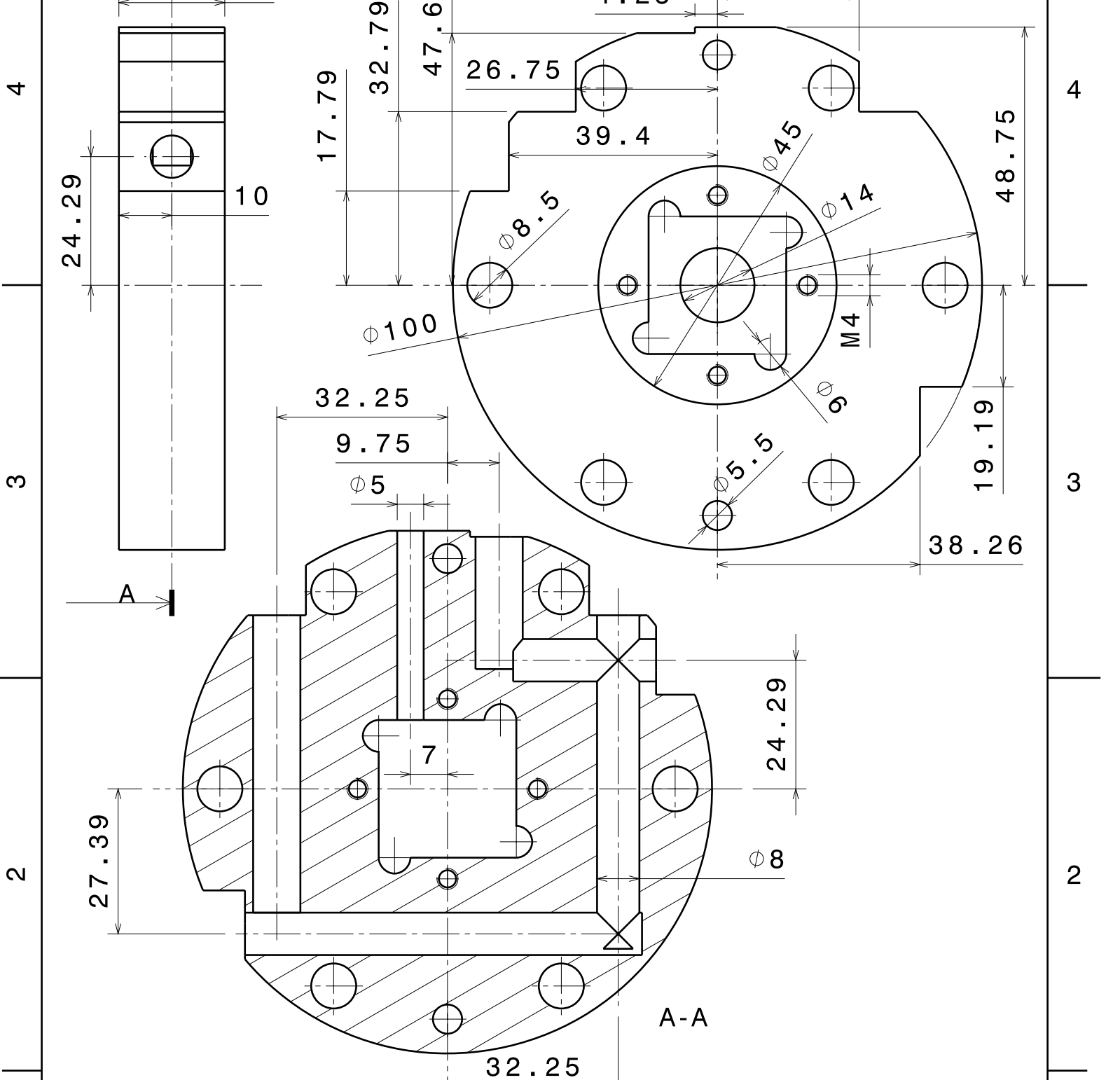
WEIGHT (kg)  
DRAWING NUMBER  
**1-4**

SHEET  
**4/4**

This drawing is our property; it can't be reproduced or communicated without our written agreement.

D

A

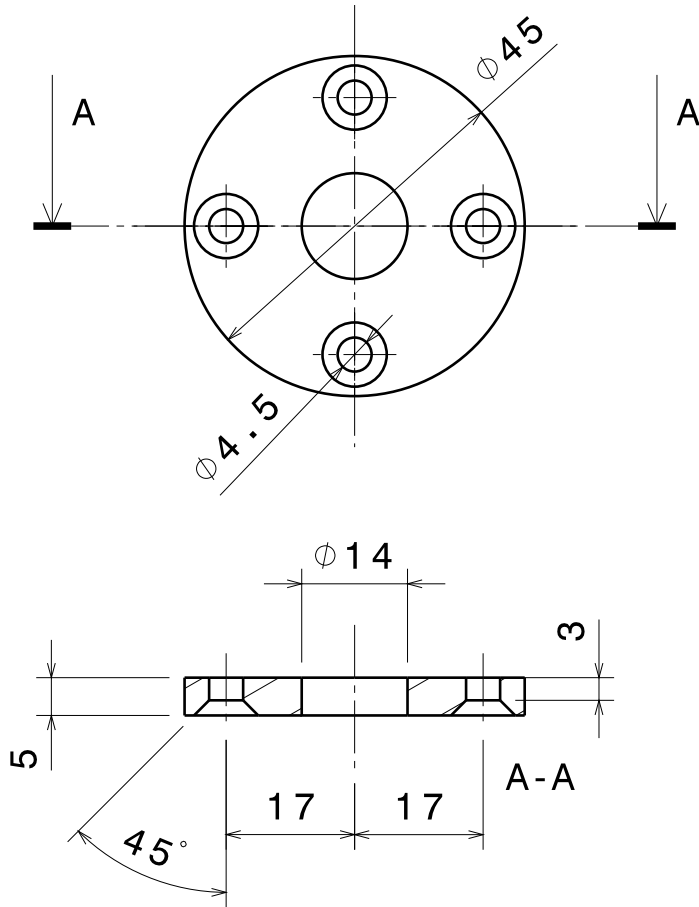


DESIGNED BY: <b>T. Veltzke</b>	
DATE: <b>June 3. 2010</b>	
MATERIAL: <b>Stainless Steel</b>	
<b>1.4301</b>	
SIZE <b>A4</b>	
SCALE <b>1:1</b>	WEIGHT (kg)

<h1>Channel fixture</h1>	
<b>2-1</b>	
DRAWING NUMBER	
<b>1/3</b>	
SHEET	

I	-
H	-
G	-
F	-
E	-
D	-
C	-
B	-
A	-

This drawing is our property; it can't be reproduced or communicated without our written agreement.



DESIGNED BY:  
**T. Veltzke**  
 DATE:  
**June 3. 2010**  
 MATERIAL:  
**Stainless Steel**  
**1.4301**

# Cover for fixture

SIZE  
**A4**

## Gas Flow Apparatus

SCALE  
**1:1**

DRAWING NUMBER  
**2-2**

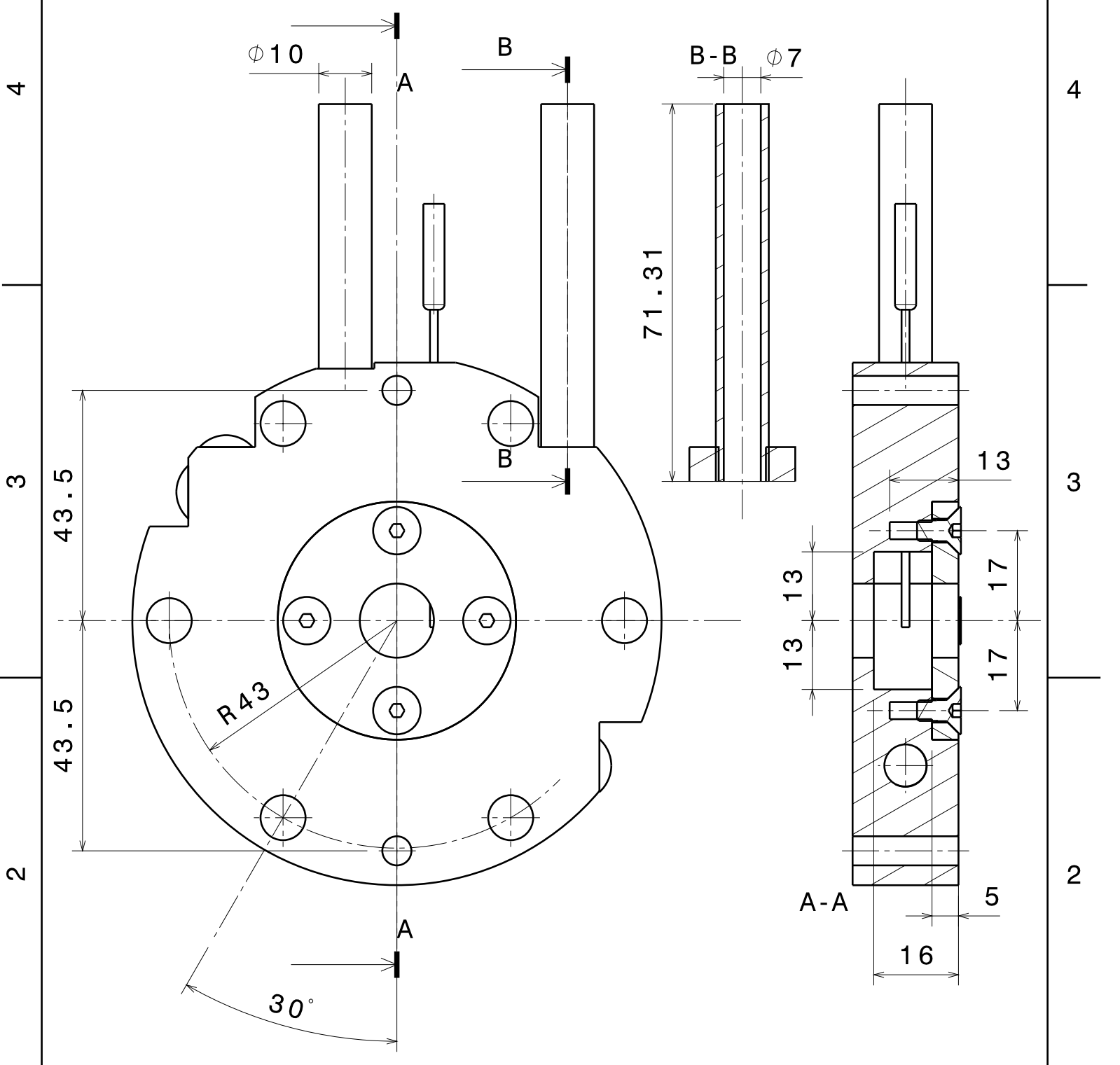
SHEET  
**2/3**

I	-
H	-
G	-
F	-
E	-
D	-
C	-
B	-
A	-

This drawing is our property; it can't be reproduced or communicated without our written agreement.

D

A



DESIGNED BY: <b>T. Veltzke</b>	
DATE: <b>June 3. 2010</b>	
MATERIAL: <b>Stainless Steel</b>	
<b>1.4301</b>	
SIZE <b>A4</b>	
SCALE <b>1:1</b>	WEIGHT (kg)

**Assembling drawing  
fixture**

**Gas Flow Apparatus**

**2-3**

I	-
H	-
G	-
F	-
E	-
D	-
C	-
B	-
A	-

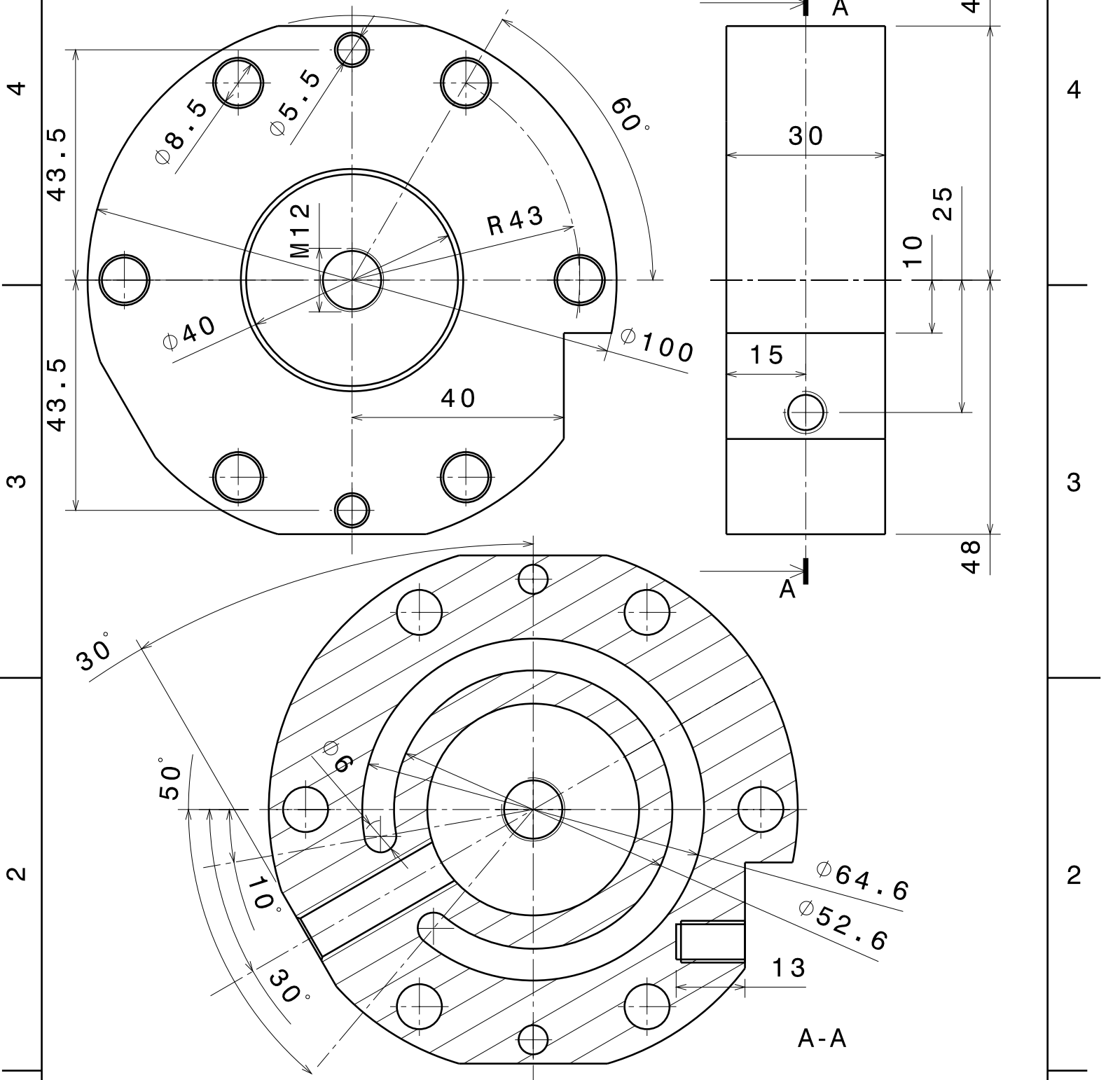
This drawing is our property; it can't be reproduced or communicated without our written agreement.

4  
3  
2  
1

4  
3  
2  
1

D

A



DESIGNED BY: <b>T. Veltzke</b>	
DATE: <b>June 1. 2010</b>	
MATERIAL: <b>Stainless Steel</b>	
<b>1.4301</b>	
SIZE <b>A4</b>	
SCALE <b>1:1</b>	WEIGHT (kg)

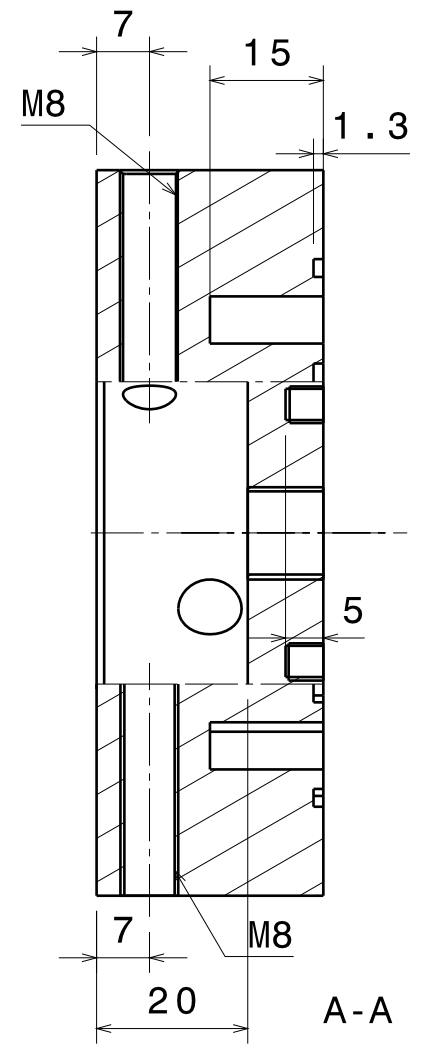
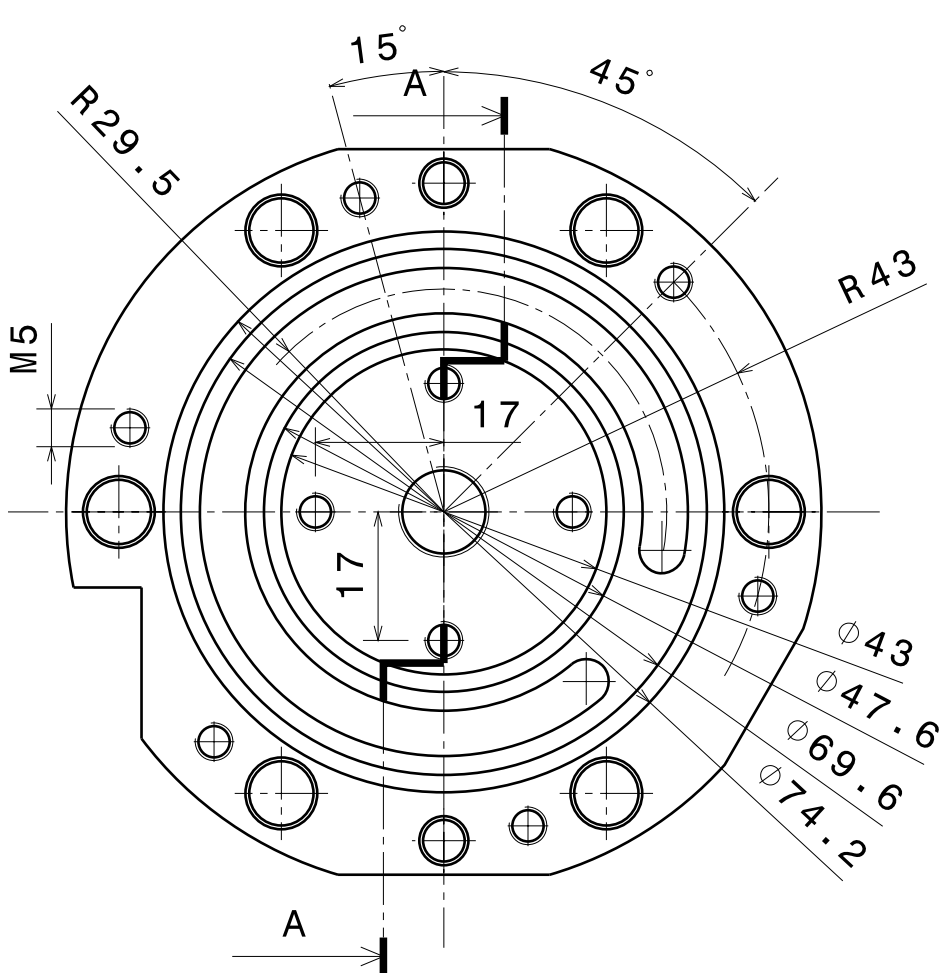
<h1>Part with outlet chamber (1)</h1>	
DRAWING NUMBER <b>3-1</b>	
SHEET <b>1/4</b>	

I	-
H	-
G	-
F	-
E	-
D	-
C	-
B	-
A	-

This drawing is our property; it can't be reproduced or communicated without our written agreement.

4  
3  
2  
1

4  
3  
2  
1



DESIGNED BY: T. Veltzke	
DATE: June 1. 2010	
MATERIAL: Stainless Steel 1.4301	
SIZE <b>A4</b>	
SCALE <b>1:1</b>	WEIGHT (kg)

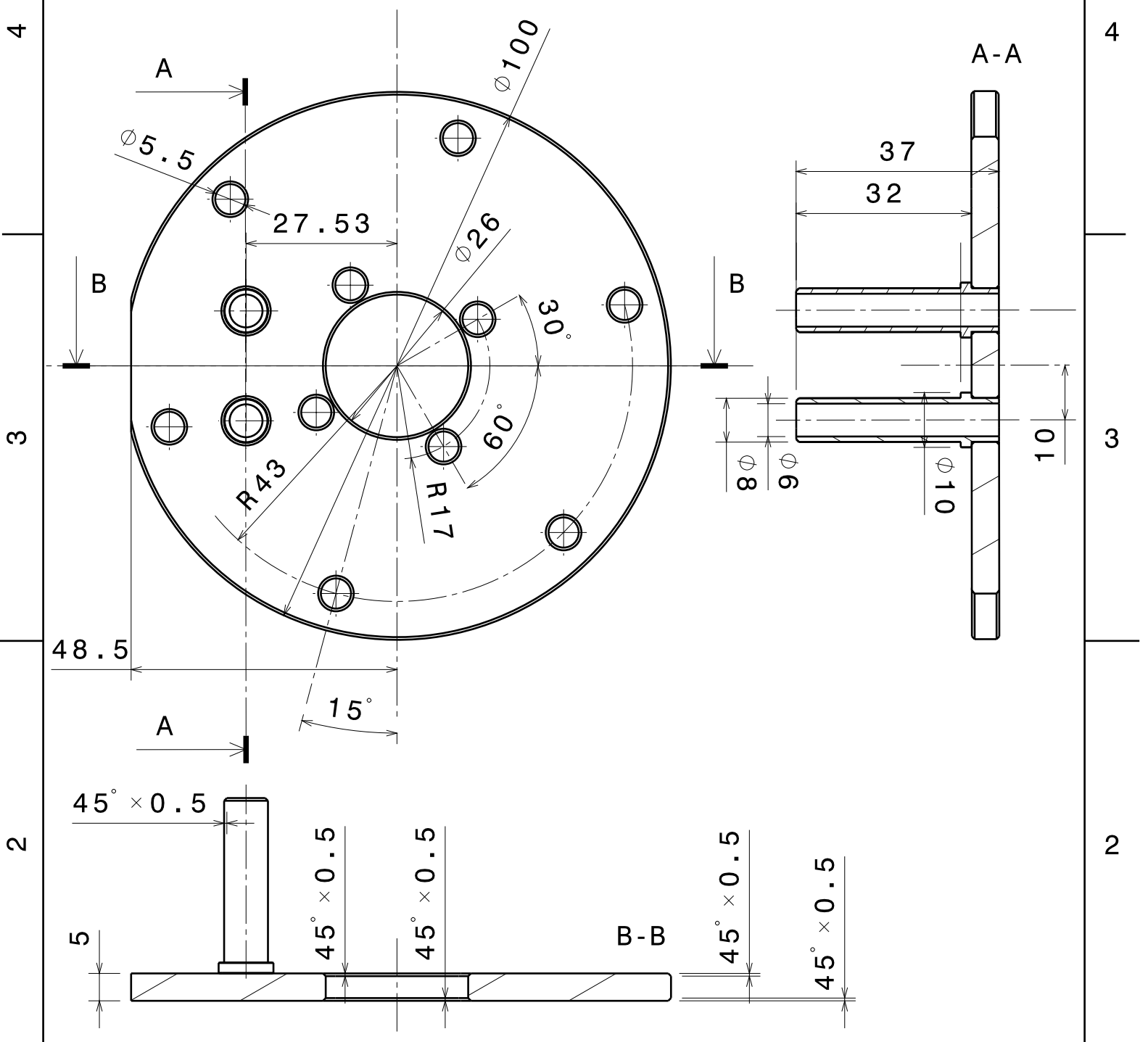
<h1>Part with outlet chamber (2)</h1>	
DRAWING NUMBER <b>3-2</b>	
SHEET <b>2/4</b>	

I	-
H	-
G	-
F	-
E	-
D	-
C	-
B	-
A	-

This drawing is our property; it can't be reproduced or communicated without our written agreement.

D

A



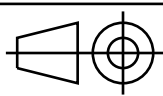
DESIGNED BY:  
T. Veltzke

DATE:  
June 1. 2010

MATERIAL:  
Stainless Steel  
1.4301

SIZE  
A4

SCALE  
1:1



**Cover with pipe sockets (outlet)**

**Gas Flow Apparatus**

DRAWING NUMBER  
3-3

SHEET  
3/4

I	-
H	-
G	-
F	-
E	-
D	-
C	-
B	-
A	-

This drawing is our property; it can't be reproduced or communicated without our written agreement.

4  
3  
2  
1

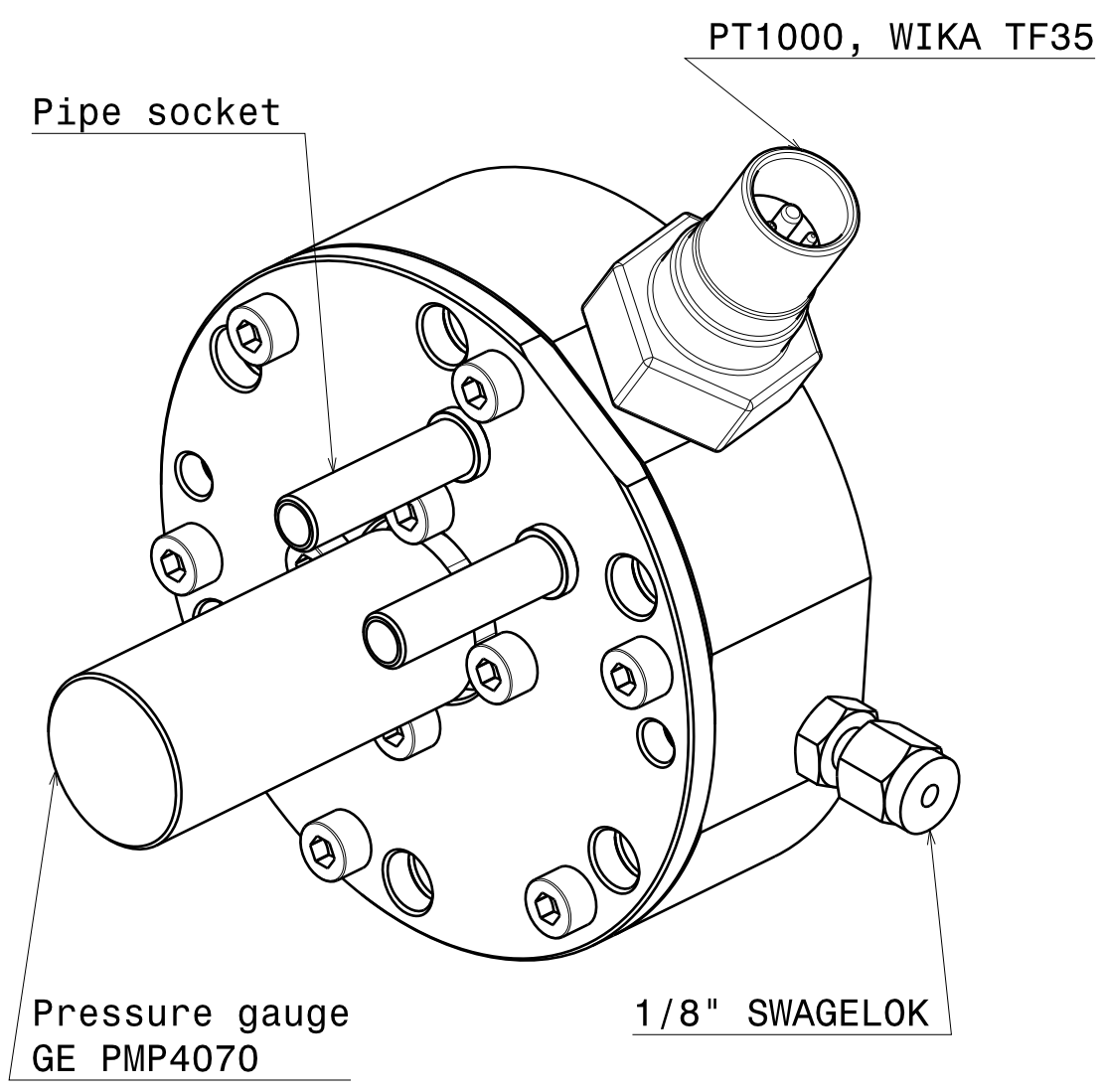
4  
3  
2  
1

D

A

4  
3  
2  
1

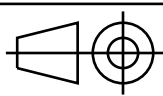
4  
3  
2  
1



DESIGNED BY:  
T. Veltzke  
DATE:  
June 1. 2010

# Part with outlet chamber (assembled)

SIZE  
**A4**



## Gas Flow Apparatus

SCALE  
**1:1**

WEIGHT (kg)  
DRAWING NUMBER  
**3-4**

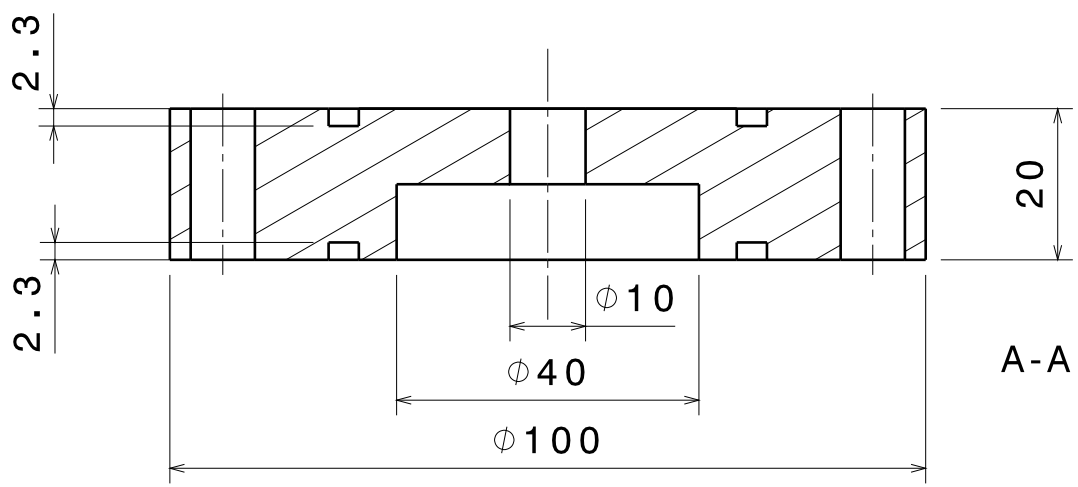
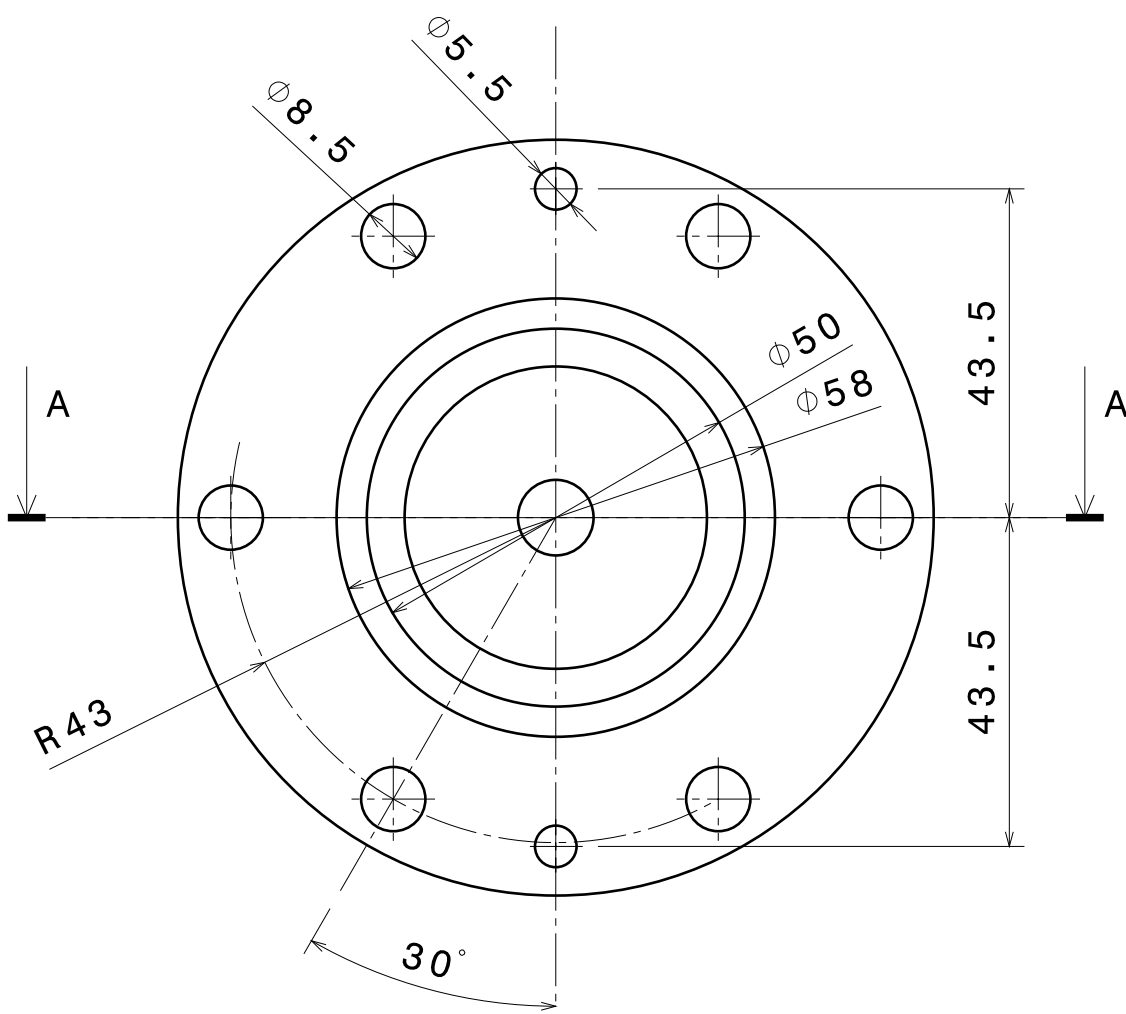
SHEET  
**4/4**

I	-
H	-
G	-
F	-
E	-
D	-
C	-
B	-
A	-

This drawing is our property; it can't be reproduced or communicated without our written agreement.

D

A



DESIGNED BY: <b>T. Veltzke</b>	
DATE: <b>May 28. 2010</b>	
MATERIAL: <b>Stainless Steel</b>	
<b>1.4301</b>	
SIZE <b>A4</b>	
SCALE <b>1:1</b>	WEIGHT (kg)

<h1>Sealing disk</h1>	
DRAWING NUMBER <b>4</b>	SHEET <b>1/1</b>

I	-
H	-
G	-
F	-
E	-
D	-
C	-
B	-
A	-

This drawing is our property; it can't be reproduced or communicated without our written agreement.

D

A



**Specification for Serial#: 3152950**

**Sales Number:** D06872.1.1  
**Transducer Type:** PMP 4070  
**Part Number:** A4070-06A  
**Pressure Range:** 1.6 bar a  
**Supply Voltage:** 15 to 32 Vdc  
**Output Voltage:** 0 to 10 V  
**Mounting Torque:** 20 Nm  
**Pressure Connection:** M12x15-24DEG INTCONE

**Non-Linearity & Hysteresis:** max +/- 0.04 % BSL  
**Temperature Error Band:** max +/- 1.00 % FRO  
**Compensated Temperature Range:** +0 °C to +50 °C

**Electrical Connection:**  
 Cable Length: N/A  
 Positive Supply: Pin 1  
 Negative Supply: Pin 2  
 Positive Output: Pin 3  
 Negative Output: N/A  
 Internal 'R' Cal Facility: N/A  
 Screen: See Application Data

**Date Issued:** 10th Jun 2010

**Application Data**

1. It is very important to use the stated supply polarity since the transducer uses an active regulation circuit.

# OEM-Einschraub-Thermometer mit Steckeranschluss Typ TF35

WIKA Datenblatt TE 67.10

## Anwendungen

Mobilhydraulik  
Maschinenbau  
Kompressoren  
Automotive  
Kälte-, Heizungs-, Klima- und Lüftungstechnik

## Leistungsmerkmale

Messbereiche von -50 ... +300 °C  
Sehr hohe Vibrationsfestigkeit  
Kompakte Bauform  
Elektrischer Anschluss über Steckverbindung



Einschraub-Thermometer Typ TF35

## Beschreibung

Messelement, Toleranz  
WIKA verwendet beim Einschraub-Thermometer Typ TF35 standardmäßig folgende Messelemente:

NTC,  $R_{25} = 2,5 \text{ k}\Omega \pm 5 \%$   
NTC,  $R_{25} = 10 \text{ k}\Omega \pm 5 \%$   
Pt100, Klasse B nach DIN EN 60 751  
Pt1000, Klasse B nach DIN EN 60 751  
Ni1000, DIN 43 760  
KTY10-6  
KTY11-6  
KTY81-210

Andere auf Anfrage

Platinelemente bieten den Vorteil, dass sie internationalen Normen entsprechen (IEC 751 / DIN EN 60 751).

Nickelemente sind ebenfalls genormt, jedoch nicht international. Material- und produktionsspezifische Merkmale hingegen schließen eine Normung von Halbleiterelementen wie z. B. NTC's und KTY aus. Daher sind diese nur begrenzt untereinander austauschbar.

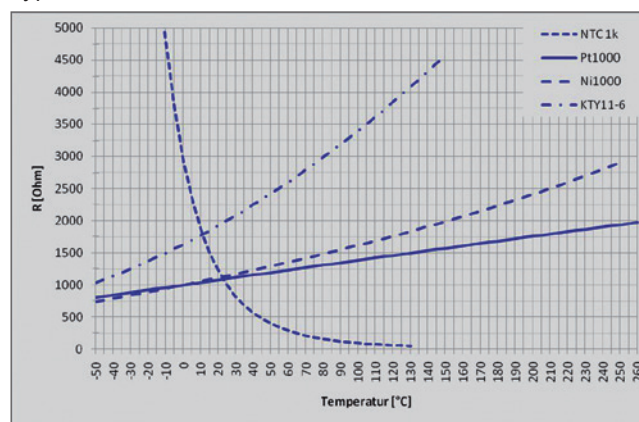
Weitere Vorteile von Platinelementen sind eine bessere Langzeitstabilität und Temperaturzyklus-Fähigkeit, ein größerer Temperaturbereich sowie eine hohe Messgenauigkeit und Linearität.

Eine hohe Messgenauigkeit und Linearität ist mit NTC's ebenfalls erreichbar, jedoch in einem sehr eingeschränkten Temperaturbereich.

Temperaturbereich	-	++	++	+	-
Genauigkeit	-	++	++	+	-
Linearität	-	++	++	+	++
Langzeitstabilität	+	++	++	++	+
Internationale Standards	-	++	++	+	-
Temperaturempfindlichkeit [dR/dT]	++	-	+	+	+
Einfluss der Zuleitung	++	-	+	+	+

Die nachstehenden Kennlinien zeigen die typischen Kurvenverläufe der WIKA-Standardmesselemente in Abhängigkeit der Temperatur sowie die typischen Toleranzkurven.

### Typische Kennlinienverläufe



### Schaltungsart:

Die Einschraub-Thermometer Typ TF35 werden in 2-Leiter-Schaltung ausgeführt.

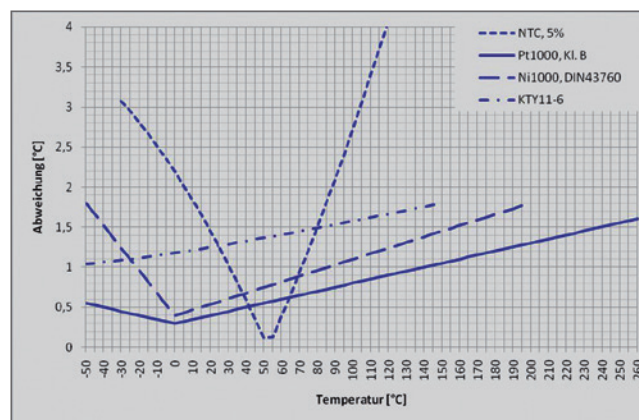
Bei einer Ausführung in 2-Leiter-Schaltung trägt der Leitungswiderstand der Anschlussleitung zum Messwert bei und muss berücksichtigt werden.

Als Richtwert gilt bei Kupferleitung mit Querschnitt 0,22 mm<sup>2</sup>: 0,162 Ω/m → 0,42 °C/m bei Pt100

Alternativ kann eine Ausführung mit Pt1000 gewählt werden, bei der der Einfluss der Zuleitung mit 0,04 °C/m um den Faktor 10 geringer ist. Dies ist ebenso bei einem Ni1000-Sensorelement.

Noch weniger macht sich der Zuleitungswiderstand entsprechend des Grundwiderstandes R<sub>25</sub> bei einem KTY bzw. NTC-Element bemerkbar.

### Typische Toleranzkurven



## Temperaturbereiche

### Mediumtemperatur (Messbereich)

Der Messbereich hängt im Wesentlichen vom Messelement ab:

Messelement	Messbereich
NTC	-40 ... +130 °C
Pt100	-50 ... +200 °C / -50 ... +300 °C
Pt1000	-50 ... +200 °C / -50 ... +300 °C
Ni1000	-50 ... +200 °C
KTY	-50 ... +150 °C

### Umgebungstemperatur

Die zulässige Umgebungstemperatur ist abhängig vom elektrischen Anschluss:

Elektrischer Anschluss	Umgebungstemperatur
AMP Junior Power Timer	-40 ... +150 °C
FASTON-Flachstecker	-40 ... +150 °C
Gerätestecker Deutsch DT04-2P	-40 ... +150 °C
Bajonett-Steckverbinder DIN 72 585	-40 ... +140 °C
Rundsteckverbinder M12 x 1	-40 ... +100 °C

### Hinweis:

Aufgrund der kurzen Baulänge besteht die Möglichkeit, dass die Temperatur am Stecker auf unzulässig hohe Werte steigt. Dies muss bei der Ausführung der Messstelle unbedingt berücksichtigt werden.

#### Werkstoff

Messing

CrNi-Stahl 1.4305

Andere auf Anfrage

#### Durchmesser D

7,5 mm

6,0 mm

5,0 mm

4,0 mm

Andere auf Anfrage

#### Prozessanschluss

Einschraubgewinde:

G ¼ B

G ⅜ B

M10 x 1,5

M12 x 1,5

M14 x 1,5

R¼-ISO7

R ⅜-ISO7

¼" NPT

Andere auf Anfrage

#### Einbaulänge U

28 mm

30 mm

40 mm

50 mm

60 mm

65 mm

Andere auf Anfrage

Die Ansprechzeit wird im wesentlichen beeinflusst durch das verwendete Schutzrohr (Durchmesser, Material) den Wärmeübergang vom Schutzrohr zum Messelement die Strömungsgeschwindigkeit des Mediums

Durch den Aufbau der Einschraub-Thermometer Typ TF35 ist eine optimale Wärmeübertragung vom Medium zum Messelement gegeben.

Die nachstehende Tabelle zeigt die typischen Ansprechzeiten der Einschraub-Thermometer Typ TF35:

Schutzrohr Werkstoff	Durchmesser	Ansprechzeit	
		t <sub>0,5</sub>	t <sub>0,9</sub>
Messing	7,5 mm	2,2 s	6 s
CrNi-Stahl	7,5 mm	2,5 s	6,5 s

Hinweis:

Zur Verbesserung der Ansprechzeit kann ein kleinerer Schutzrohrdurchmesser gewählt werden.

## Vibrationsfestigkeit

Durch den speziellen Einbau der verwendeten Messelemente ist die Vibrationsfestigkeit der Einschraub-Thermometer Typ TF35 sehr hoch.

Die nach DIN EN 60 751 (IEC 751) bereits für erhöhte Anforderungen definierten Beschleunigungswerte von 3 g werden weit übertroffen.

Je nach Einbausituation, Medium, Temperatur und Einbaulänge beträgt die Vibrationsfestigkeit bis zu 10 g.

## Schockfestigkeit

Bis 500 g, je nach Einbausituation, Medium und Temperatur

## Betriebsdruck

Max. 600 bar, je nach Medium, Temperatur und Schutzrohrausführung

## Elektrischer Anschluss

Stecker AMP Junior Power Timer

FASTON-Flachstecker 6,3 x 0,8 mm

FASTON-Flachstecker 4,8 x 0,8 mm

Rundsteckverbinder M12 x 1

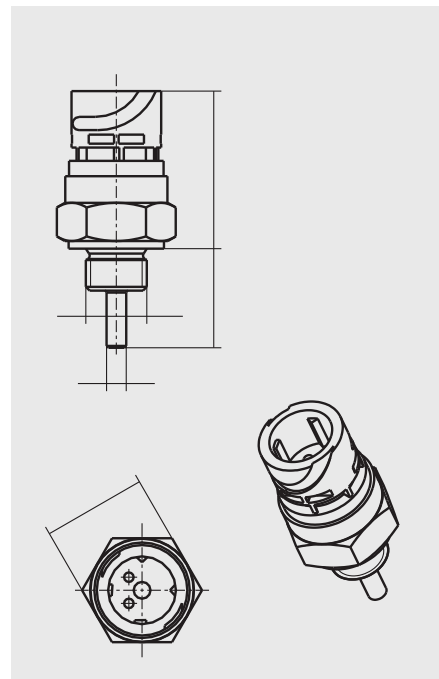
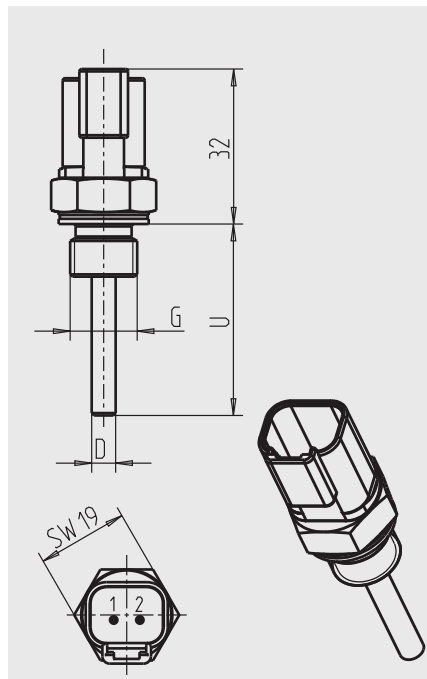
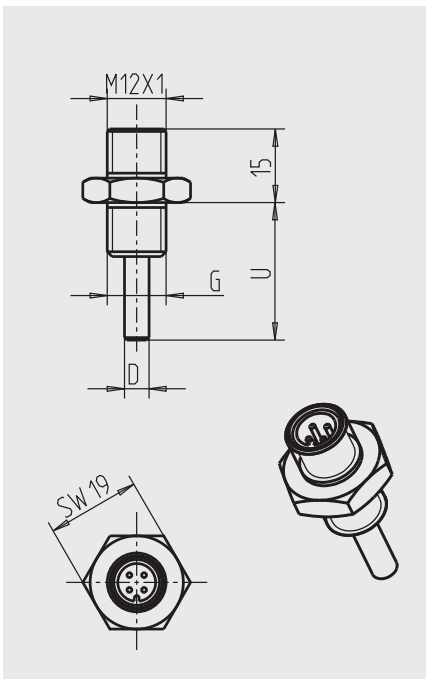
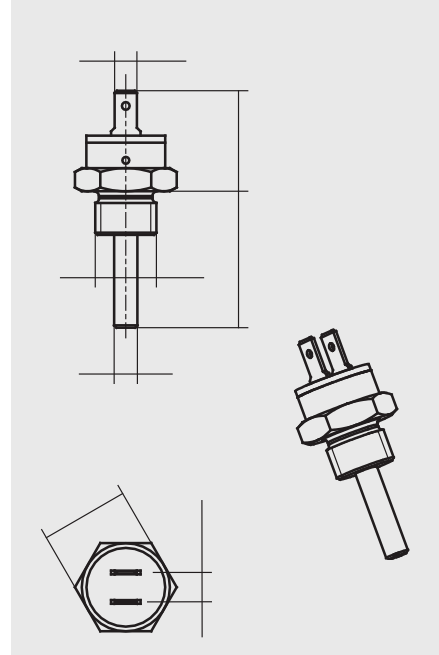
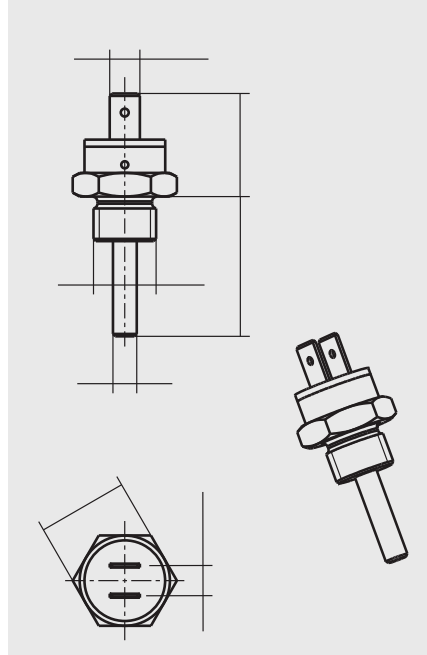
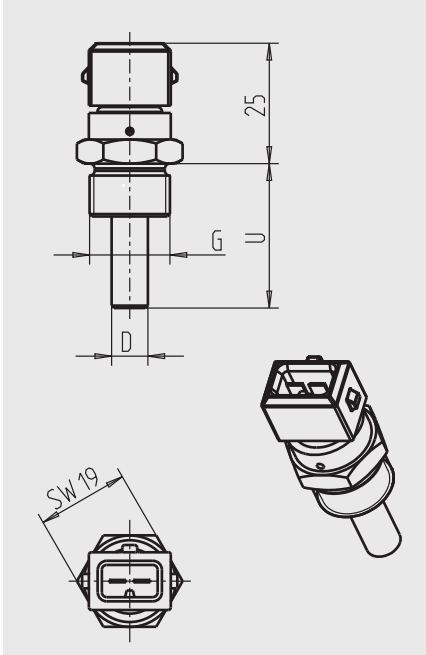
Gerätestecker Deutsch DT04-2P

Bajonett-Steckverbinder, DIN 72 585

Andere Anschlüsse auf Anfrage

## Gehäuseschutzart

IP 66 / IP 67 im gesteckten Zustand



## Bestellangaben

Typ / Messbereich / Messelement / Toleranz / Schutzrohrwerkstoff und -durchmesser / Prozessanschluss / Einbaulänge / Elektrischer Anschluss

Änderungen und den Austausch von Werkstoffen behalten wir uns vor.

Die beschriebenen Geräte entsprechen in ihren Konstruktionen, Maßen und Werkstoffen dem derzeitigen Stand der Technik.



WIKAL Alexander Wiegand SE & Co. KG  
 Alexander-Wiegand-Straße 30  
 63911 Klingenberg/Germany  
 Tel. (+49) 9372/132-0  
 Fax (+49) 9372/132-406  
 E-mail info@wika.de  
 www.wika.de

---



---

**CALIBRATION CERTIFICATE**


---



---

**FLUID NO. 1 OF 5**

CERTIFICATE NO. BHTC69/CL9/847372

Calibration by comparison

Calibration date: 16 Oct 2009

We hereby certify that the instrument mentioned below has been calibrated in accordance with the stated values and conditions. The calibration standards used are traceable to national standards of the Dutch Metrology Institute VSL.

**Calibrated instrument**

Type Flow meter (D)  
 Serial number M9207915A  
 Model number F-110C-002-AGD-11-V  
 Rated accuracy\*  $\pm(2\%FS)$

**Calibration standard**

Type Flow controller (D)  
 Serial number M7208826A  
 Certificate no. BKL002/JST/832013  
 Uncertainty  $\pm 0.5\% Rd$

**Customer conditions**

Fluid **N2**  
 Flow **0.7000 mln/min**  
 Pressure **1004.0..1010.0 mbar (a)**  
 Temperature **20.0 °C**

**Calibration conditions**

Fluid AiR  
 Flow 0.6967 mln/min (equivalent flow)  
 Pressure 5.0 bar (a)  
 Temperature 23.5 °C  
 Atm. pressure 1019.4 hPa (a)

**Calibration and Conversion results**

Point	Calibrated flow	Conversion factor	Customer flow**	Output signal	
	AiR		N2		
1	0.0000 mln/min	-	0.0000 mln/min	0.00%	4.000 mA
2	0.2747 mln/min	1.005	0.2760 mln/min	39.43%	10.309 mA
3	0.5495 mln/min	1.005	0.5520 mln/min	78.86%	16.618 mA
4	0.8244 mln/min	1.005	0.8283 mln/min	118.33%	22.932 mA***

The measurement uncertainty of the calibrated AiR flow is  $\pm 0.5\% Rd$ .

The measured deviation between the flow indicated by the calibrated instrument and the reference flow indicated by the calibration standard is less than  $\pm 0.36\% Rd$ .

**Notes**

Flow unit mln/min is defined at conditions 0.00 °C, 1013.25 hPa (a).

\* Rated accuracy is specified under calibration conditions.

\*\* The calibrated flow is converted to customer fluid and/or conditions using Bronkhorst High-Tech FLUIDAT® software.

\*\*\* Analog output above 20 mA cannot be guaranteed.

Measurement uncertainties are based upon 95% (k=2) confidence limits. Although the item calibrated meets the specifications and performance at the time of calibration, due to any number of factors, this does not imply continuing conformance to the specifications.

More detailed information about the used calibration method can be found on <http://www.bronkhorst.com/certificates>.

Calibrator S.B.

QC N.d.R.

Date 25 Aug 2010

Copy printed by G.B.

---



---

**CALIBRATION CERTIFICATE**


---



---

**FLUID NO. 2 OF 5**

CERTIFICATE NO. BHTC69/CL9/847373

Calibration by comparison

Calibration date: 16 Oct 2009

We hereby certify that the instrument mentioned below has been calibrated in accordance with the stated values and conditions. The calibration standards used are traceable to national standards of the Dutch Metrology Institute VSL.

**Calibrated instrument**

Type Flow meter (D)  
 Serial number M9207915A  
 Model number F-110C-002-AGD-11-V  
 Rated accuracy\*  $\pm(2\%FS)$

**Calibration standard**

Type Flow controller (D)  
 Serial number M7208826A  
 Certificate no. BKL002/JST/832013  
 Uncertainty  $\pm 0.5\% Rd$

**Customer conditions**

Fluid **CO2**  
 Flow **0.7000 mln/min**  
 Pressure **4.0..10.0 mbar (g)**  
 Temperature **20.0 °C**

**Calibration conditions**

Fluid AiR  
 Flow 0.9309 mln/min (equivalent flow)  
 Pressure 5.0 bar (a)  
 Temperature 23.5 °C  
 Atm. pressure 1019.4 hPa (a)

**Calibration and Conversion results**

Point	Calibrated flow	Conversion factor	Customer flow**	Output signal	
	AiR		CO2		
1	0.0000 mln/min	-	0.0000 mln/min	0.00%	4.000 mA
2	0.2747 mln/min	0.750	0.2061 mln/min	29.45%	8.712 mA
3	0.5495 mln/min	0.751	0.4126 mln/min	58.95%	13.432 mA
4	0.8244 mln/min	0.752	0.6197 mln/min	88.52%	18.164 mA
5	1.099 mln/min	0.752	0.8271 mln/min	118.15%	22.904 mA***

The measurement uncertainty of the calibrated AiR flow is  $\pm 0.5\% Rd$ .

The measured deviation between the flow indicated by the calibrated instrument and the reference flow indicated by the calibration standard is less than  $\pm 0.36\% Rd$ .

**Notes**

Flow unit mln/min is defined at conditions 0.00 °C, 1013.25 hPa (a).

\* Rated accuracy is specified under calibration conditions.

\*\* The calibrated flow is converted to customer fluid and/or conditions using Bronkhorst High-Tech FLUIDAT® software.

\*\*\* Analog output above 20 mA cannot be guaranteed.

Measurement uncertainties are based upon 95% (k=2) confidence limits. Although the item calibrated meets the specifications and performance at the time of calibration, due to any number of factors, this does not imply continuing conformance to the specifications.

More detailed information about the used calibration method can be found on <http://www.bronkhorst.com/certificates>.

Calibrator S.B.

QC N.d.R.

Date 25 Aug 2010

Copy printed by G.B.

---



---

**CALIBRATION CERTIFICATE**


---



---

**FLUID NO. 3 OF 5**

CERTIFICATE NO. BHTC69/CL9/847383

Calibration by comparison

Calibration date: 16 Oct 2009

We hereby certify that the instrument mentioned below has been calibrated in accordance with the stated values and conditions. The calibration standards used are traceable to national standards of the Dutch Metrology Institute VSL.

**Calibrated instrument**

Type Flow meter (D)  
 Serial number M9207915A  
 Model number F-110C-002-AGD-11-V  
 Rated accuracy\*  $\pm(2\%FS)$

**Calibration standard**

Type Flow controller (D)  
 Serial number M7208826A  
 Certificate no. BKL002/JST/832013  
 Uncertainty  $\pm 0.5\% Rd$

**Customer conditions**

Fluid **CH4**  
 Flow **0.7000 mln/min**  
 Pressure **4.0..10.0 mbar (g)**  
 Temperature **20.0 °C**

**Calibration conditions**

Fluid AiR  
 Flow 0.8996 mln/min (equivalent flow)  
 Pressure 5.0 bar (a)  
 Temperature 23.5 °C  
 Atm. pressure 1019.4 hPa (a)

**Calibration and Conversion results**

Point	Calibrated flow		Conversion factor	Customer flow**	
	AiR	CH4		CH4	Output signal
1	0.0000 mln/min		-	0.0000 mln/min	0.00% 4.000 mA
2	0.2747 mln/min		0.779	0.2140 mln/min	30.57% 8.891 mA
3	0.5495 mln/min		0.779	0.4278 mln/min	61.12% 13.779 mA
4	0.8244 mln/min		0.778	0.6416 mln/min	91.66% 18.666 mA
5	1.099 mln/min		0.778	0.8552 mln/min	122.18% 23.548 mA***

The measurement uncertainty of the calibrated AiR flow is  $\pm 0.5\% Rd$ .

The measured deviation between the flow indicated by the calibrated instrument and the reference flow indicated by the calibration standard is less than  $\pm 0.36\% Rd$ .

**Notes**

Flow unit mln/min is defined at conditions 0.00 °C, 1013.25 hPa (a).

\* Rated accuracy is specified under calibration conditions.

\*\* The calibrated flow is converted to customer fluid and/or conditions using Bronkhorst High-Tech FLUIDAT® software.

\*\*\* Analog output above 20 mA cannot be guaranteed.

Measurement uncertainties are based upon 95% (k=2) confidence limits. Although the item calibrated meets the specifications and performance at the time of calibration, due to any number of factors, this does not imply continuing conformance to the specifications.

More detailed information about the used calibration method can be found on <http://www.bronkhorst.com/certificates>.

Calibrator S.B.

QC N.d.R.

Date 25 Aug 2010

Copy printed by G.B.

---



---

**CALIBRATION CERTIFICATE**


---



---

**FLUID NO. 4 OF 5**

CERTIFICATE NO. BHTC69/CL9/847385

Calibration by comparison

Calibration date: 16 Oct 2009

We hereby certify that the instrument mentioned below has been calibrated in accordance with the stated values and conditions. The calibration standards used are traceable to national standards of the Dutch Metrology Institute VSL.

**Calibrated instrument**

Type Flow meter (D)  
 Serial number M9207915A  
 Model number F-110C-002-AGD-11-V  
 Rated accuracy\*  $\pm(2\%FS)$

**Calibration standard**

Type Flow controller (D)  
 Serial number M7208826A  
 Certificate no. BKL002/JST/832013  
 Uncertainty  $\pm 0.5\% Rd$

**Customer conditions**

Fluid He  
 Flow 1.000 mln/min  
 Pressure 4.0..10.0 mbar (g)  
 Temperature 20.0 °C

**Calibration conditions**

Fluid AiR  
 Flow 0.7112 mln/min (equivalent flow)  
 Pressure 5.0 bar (a)  
 Temperature 23.5 °C  
 Atm. pressure 1019.4 hPa (a)

**Calibration and Conversion results**

Point	Calibrated flow	Conversion factor	Customer flow**	Output signal	
	AiR		He		
1	0.0000 mln/min	-	0.0000 mln/min	0.00%	4.000 mA
2	0.2747 mln/min	1.409	0.3872 mln/min	38.72%	10.196 mA
3	0.5495 mln/min	1.407	0.7734 mln/min	77.34%	16.374 mA
4	0.8244 mln/min	1.405	1.159 mln/min	115.87%	22.539 mA***

The measurement uncertainty of the calibrated AiR flow is  $\pm 0.5\% Rd$ .

The measured deviation between the flow indicated by the calibrated instrument and the reference flow indicated by the calibration standard is less than  $\pm 0.36\% Rd$ .

**Notes**

Flow unit mln/min is defined at conditions 0.00 °C, 1013.25 hPa (a).

\* Rated accuracy is specified under calibration conditions.

\*\* The calibrated flow is converted to customer fluid and/or conditions using Bronkhorst High-Tech FLUIDAT® software.

\*\*\* Analog output above 20 mA cannot be guaranteed.

Measurement uncertainties are based upon 95% (k=2) confidence limits. Although the item calibrated meets the specifications and performance at the time of calibration, due to any number of factors, this does not imply continuing conformance to the specifications.

More detailed information about the used calibration method can be found on <http://www.bronkhorst.com/certificates>.

Calibrator S.B.

QC N.d.R.

Date 25 Aug 2010

Copy printed by G.B.

---



---

**CALIBRATION CERTIFICATE**


---



---

**FLUID NO. 5 OF 5**

CERTIFICATE NO. BHTC69/CL9/847387

Calibration by comparison  
Calibration date: 16 Oct 2009

We hereby certify that the instrument mentioned below has been calibrated in accordance with the stated values and conditions. The calibration standards used are traceable to national standards of the Dutch Metrology Institute VSL.

**Calibrated instrument**

Type Flow meter (D)  
Serial number M9207915A  
Model number F-110C-002-AGD-11-V  
Rated accuracy\*  $\pm(2\%FS)$

**Calibration standard**

Type Flow controller (D)  
Serial number M7208826A  
Certificate no. BKL002/JST/832013  
Uncertainty  $\pm 0.5\% Rd$

**Customer conditions**

Fluid **H2**  
Flow **0.7000 mln/min**  
Pressure **4.0..10.0 mbar (g)**  
Temperature **20.0 °C**

**Calibration conditions**

Fluid AiR  
Flow 0.6932 mln/min (equivalent flow)  
Pressure 5.0 bar (a)  
Temperature 23.5 °C  
Atm. pressure 1019.4 hPa (a)

**Calibration and Conversion results**

Point	Calibrated flow	Conversion factor	Customer flow**	Output signal	
	AiR		H2		
1	0.0000 mln/min	-	0.0000 mln/min	0.00%	4.000 mA
2	0.2747 mln/min	1.012	0.2781 mln/min	39.73%	10.357 mA
3	0.5495 mln/min	1.011	0.5554 mln/min	79.34%	16.695 mA
4	0.8244 mln/min	1.009	0.8321 mln/min	118.87%	23.019 mA***

The measurement uncertainty of the calibrated AiR flow is  $\pm 0.5\% Rd$ .

The measured deviation between the flow indicated by the calibrated instrument and the reference flow indicated by the calibration standard is less than  $\pm 0.36\% Rd$ .

**Notes**

Flow unit mln/min is defined at conditions 0.00 °C, 1013.25 hPa (a).

\* Rated accuracy is specified under calibration conditions.

\*\* The calibrated flow is converted to customer fluid and/or conditions using Bronkhorst High-Tech FLUIDAT® software.

\*\*\* Analog output above 20 mA cannot be guaranteed.

Measurement uncertainties are based upon 95% (k=2) confidence limits. Although the item calibrated meets the specifications and performance at the time of calibration, due to any number of factors, this does not imply continuing conformance to the specifications.

More detailed information about the used calibration method can be found on <http://www.bronkhorst.com/certificates>.

Calibrator S.B.

QC N.d.R.

Date 25 Aug 2010

Copy printed by G.B.

---

**CALIBRATION CERTIFICATE**

---

We herewith certify that the instrument mentioned below has been calibrated in accordance with the stated values and conditions. The calibration standards used are traceable to national standards of the Dutch Metrology Institute VSL.

== Identifications ==

	<u>Calibrated Instrument</u>	<u>Calibration Standard</u>
Type :	Flow controller (D)	Piston Prover
Serial number :	M10203787A	80363
Model number :	F-201CV-ABD-11-Z	FPP T-005-TD
Certificate no. :	BHTG29/940762	BKL001/801385

== Conditions ==

	<u>Customer</u>		<u>Calibration</u>
Fluid :	N2	Fluid :	AiR
Pressure :	2.6 bar (a)	Pressure :	5.0 bar (a)
Temperature :	20 °C	Temperature :	23.5 °C
Flow (*) :	10 mln/min	Room temperature :	23.5 °C
Output range :	0 - 100 %	Atm. pressure :	1025 hPa

== Results ==

Nominal Flow Setting	Calibrated Output Signal	Customer Flow (*)	Deviation
0.0 %	0.0000 %	0.0000 mln/min	0.0 %FS
25.0 %	24.96 %	2.498 mln/min	0.0 %FS
50.0 %	50.01 %	4.994 mln/min	0.1 %FS
75.0 %	74.96 %	7.507 mln/min	-0.1 %FS
100.0 %	99.99 %	10.03 mln/min	-0.3 %FS

== Notes ==

- \* Reference conditions of flow units: 0.00 °C, 1013.25 hPa (a).
- \* The calibrated flow is converted to customer flow using Bronkhorst High-Tech FLUIDAT® software.

Calibrator : B.H.

Date : 19 May 2010

Signed : .....

QC : .....

## USB-6211/6215 Pinout

Figure A-2 shows the pinout of the USB-6211 and USB-6215.

For a detailed description of each signal, refer to the *I/O Connector Signal Descriptions* section of Chapter 3, *Connector and LED Information*.

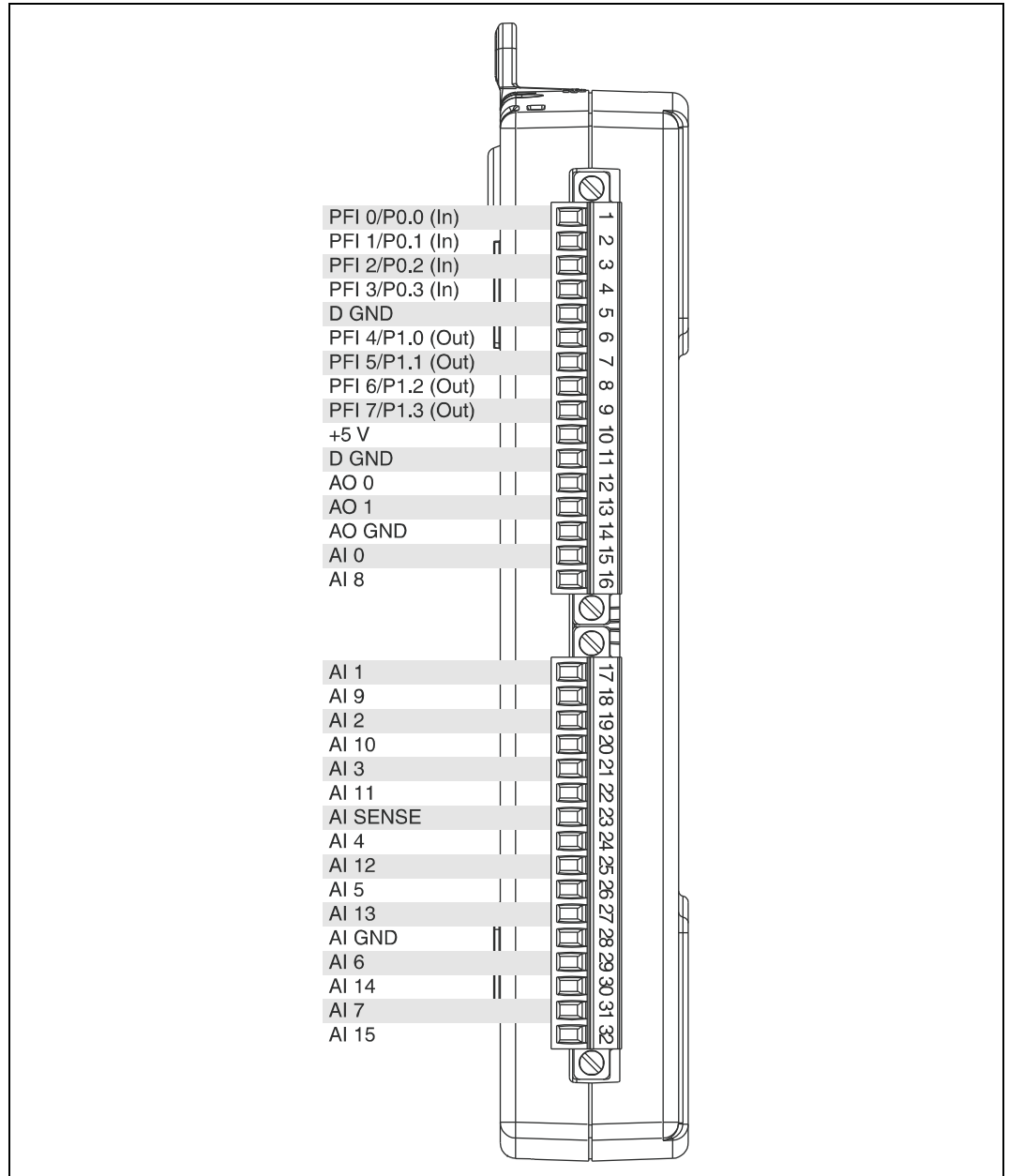


**Figure A-2.** USB-6211/6215 Pinout



# APPENDIX B

The second appendix contains all experimental raw data obtained on test channels according to section 5.1. All measurements are performed under isothermal conditions by means of the measuring procedure described in section 5.2.3. In each of the following tables, information about experimental conditions is given in caption.

**Table B.1:** Experimental results obtained on uniform channel *RC20* with different working gases. Data is shown in Figure 5.8 on page 73. Measurements are performed under isothermal conditions at different temperatures. Units of values are as follows:  $p$  in (kPa);  $\theta$  in ( $^{\circ}\text{C}$ );  $\dot{m}$  in ( $\times 10^{-9}$  kg s $^{-1}$ ).

$p_i$	$p_o$	$\theta_i$	$\theta_o$	$\dot{m}$	$p_i$	$p_o$	$\theta_i$	$\theta_o$	$\dot{m}$
<i>Carbon dioxide</i>									
110.0668	100.0365	20.7678	20.7802	2.8390	110.1345	100.0911	20.7986	20.8145	2.8754
102.1522	100.0191	20.7770	20.7906	0.3905	127.7801	97.6760	39.9726	40.1812	7.6022
115.1080	100.0831	20.7867	20.7989	4.4927	132.7813	97.6859	40.0016	40.1941	9.1952
130.1698	100.1675	20.7948	20.8083	9.7899					
<i>Nitrogen</i>									
110.0995	99.8358	20.0777	20.0587	1.2538	146.7097	100.6527	20.3243	20.4411	8.6562
124.9844	99.8533	20.0911	20.0716	4.4020	148.7279	100.6770	20.3181	20.4372	9.1254
134.9826	99.8684	20.0930	20.0775	6.5499	150.7372	100.7023	20.3192	20.4390	9.5713
104.7533	100.2243	20.3394	20.4570	0.4198	152.7560	100.7351	20.3210	20.4346	10.0372
105.3849	100.2324	20.3375	20.4578	0.5323	104.3402	100.1198	35.0197	35.0747	0.4393
105.8820	100.2392	20.3408	20.4584	0.6194	106.3438	100.1504	35.0714	35.1018	0.7356
106.3636	100.2431	20.3371	20.4525	0.6873	108.3227	100.1639	35.0950	35.1454	1.0246
106.8937	100.2528	20.3336	20.4509	0.7796	110.3648	100.1663	35.1024	35.1612	1.3232
107.3871	100.2599	20.3300	20.4507	0.8760	114.3671	100.1888	35.1329	35.1868	2.0236
107.9051	100.2681	20.3273	20.4519	0.9588	118.3823	100.2077	35.1400	35.2111	2.6663
108.4043	100.2715	20.3287	20.4537	1.0414	122.3814	100.2305	35.1359	35.2129	3.3183
108.9080	100.2767	20.3296	20.4440	1.1170	126.4097	100.2553	35.1401	35.2211	4.0763
109.4091	100.2874	20.3291	20.4485	1.2149	130.4406	100.2868	35.1886	35.2529	4.8027
109.9481	100.2931	20.3249	20.4553	1.3087	138.4815	100.3408	35.2641	35.3119	6.3260
110.4544	100.3030	20.3272	20.4478	1.3940	142.5250	100.3802	35.3066	35.3598	7.1030
112.4668	100.3167	20.3316	20.4498	1.7556	146.5630	100.4150	35.3292	35.3904	7.8866
114.4707	100.3383	20.3245	20.4516	2.1127	150.8175	100.4453	35.3312	35.4045	8.7416
116.4805	100.3516	20.3300	20.4453	2.4911	155.6129	100.4851	35.3376	35.4137	9.7778
118.4757	100.3604	20.3259	20.4426	2.8563	106.6090	100.4786	49.6652	49.7490	0.4936
120.5026	100.3757	20.3268	20.4446	3.2413	108.6360	100.4896	49.6958	49.7623	0.7724
122.5038	100.3905	20.3284	20.4487	3.6212	110.6383	100.5027	49.6882	49.7570	1.0468
124.5176	100.4111	20.3270	20.4495	4.0274	114.6437	100.5252	49.6752	49.7566	1.6561
126.5705	100.4348	20.3315	20.4438	4.4115	122.6949	100.5619	49.6737	49.7555	2.9395
128.5697	100.4479	20.3212	20.4406	4.8328	126.7096	100.5894	49.6596	49.7564	3.5736
130.5809	100.4680	20.3217	20.4394	5.2364	130.7584	100.6097	49.6730	49.7519	4.2757
132.5852	100.4915	20.3234	20.4436	5.6319	134.7734	100.6347	49.6657	49.7536	4.9686
134.6097	100.5142	20.3222	20.4346	6.0512	138.7799	100.6598	49.6866	49.7754	5.6947

136.6324	100.5421	20.3207	20.4380	6.4986	142.7836	100.6904	49.6956	49.7870	6.4135
138.8271	100.5640	20.3277	20.4418	6.9096	146.8137	100.7134	49.6970	49.7902	7.1513
140.6600	100.5849	20.3270	20.4395	7.3467	150.8450	100.7496	49.7039	49.7953	7.9189
142.6808	100.6057	20.3298	20.4476	7.7864	155.8800	100.7869	49.7069	49.7955	8.9162
144.7032	100.6305	20.3273	20.4400	8.2390					

**Table B.2:** Experimental results obtained on *Al-3* with CO<sub>2</sub> as working gas. Recalculated raw data is shown in Figure 6.3 on page 83. Measurements are performed under isothermal conditions. Units of values are as follows:  $p$  in (kPa);  $\theta$  in ( $^{\circ}$ C);  $\dot{m}$  in ( $\times 10^{-9}$  kg s $^{-1}$ ).

$p_i$	$p_o$	$\theta_i$	$\theta_o$	$\dot{m}$	$p_i$	$p_o$	$\theta_i$	$\theta_o$	$\dot{m}$
<i>Nozzle direction</i>									
23.0493	3.0140	20.9581	21.0320	2.6337	44.4679	4.4944	20.9602	21.0419	7.4982
28.4143	3.3753	20.9466	21.0221	3.7148	55.1848	5.2192	20.9736	21.0493	10.5890
33.7763	3.7466	20.9344	21.0162	4.8987	66.1918	5.9806	20.9771	21.0588	14.2405
39.1417	4.1230	20.9404	21.0204	6.2083	22.9631	2.9526	20.9926	21.0669	2.5511
44.5191	4.5079	20.9371	21.0171	7.6009	28.3101	3.3099	20.9928	21.0655	3.6147
55.2463	5.2426	20.9365	21.0156	10.7135	33.6586	3.6739	20.9935	21.0686	4.8107
66.2826	6.0228	20.9296	21.0160	14.3977	39.0161	4.0372	21.0077	21.0818	6.1124
23.0337	3.0146	20.9500	21.0255	2.5791	44.3989	4.4210	21.0087	21.0845	7.5279
28.3792	3.3779	20.9531	21.0303	3.6388	55.1425	5.1676	21.0131	21.0953	10.6845
33.7338	3.7409	20.9574	21.0284	4.8325	66.1462	5.9368	21.0157	21.0959	14.4237
39.0934	4.1095	20.9621	21.0350	6.0953					
<i>Diffusor direction</i>									
23.0876	3.0266	20.7392	20.8271	2.4650	44.4704	4.4735	20.9785	21.0559	7.0612
28.4097	3.3626	20.7514	20.8411	3.4537	55.1726	5.1861	20.9782	21.0562	10.0725
33.7446	3.7084	20.7812	20.8682	4.5599	66.1791	5.9574	20.9887	21.0695	13.6746
39.1058	4.0720	20.8074	20.8984	5.7841	22.9279	2.8680	20.7939	20.8780	2.3795
44.4716	4.4461	20.8306	20.9190	7.1300	28.2698	3.2126	20.8244	20.9119	3.3663
55.1824	5.1696	20.8565	20.9468	10.1097	33.6281	3.5801	20.8468	20.9322	4.4668
66.2153	5.9404	20.8669	20.9631	13.7193	38.9563	3.9326	20.8660	20.9507	5.6844
23.1011	3.0558	20.9190	21.0074	2.3886	44.3288	4.3036	20.8763	20.9630	7.0106
28.4241	3.3932	20.9371	21.0215	3.3914	55.0365	5.0263	20.8860	20.9734	9.9676
33.7672	3.7546	20.9411	21.0252	4.5126	66.0779	5.8064	20.9025	20.9933	13.5637
39.1137	4.1077	20.9614	21.0370	5.7312					

**Table B.3:** Experimental results obtained on *Si-5* with CO<sub>2</sub> as working gas. Recalculated raw data is shown in Figure 6.1 on page 80. Measurements are performed under isothermal conditions without varying temperature. Units of values are as follows:  $p$  in (kPa);  $\theta$  in ( $^{\circ}$ C);  $\dot{m}$  in ( $\times 10^{-9}$  kg s $^{-1}$ ).

$p_i$	$p_o$	$\theta_i$	$\theta_o$	$\dot{m}$	$p_i$	$p_o$	$\theta_i$	$\theta_o$	$\dot{m}$
<i>Nozzle direction</i>									
12.2343	2.1531	21.1052	21.1986	1.1513	28.7030	3.7197	21.2806	21.3719	5.2514
15.0085	2.4351	21.1327	21.2318	1.7689	34.2151	4.2368	21.2802	21.3714	7.0108
17.7470	2.6891	21.1380	21.2316	2.3961	45.2085	5.2415	21.2864	21.3746	11.0370
20.4918	2.9449	21.1556	21.2604	3.0453	56.4596	6.2681	21.2890	21.3770	15.8757
23.2455	3.2031	21.1794	21.2796	3.7561	12.7243	2.6561	21.2103	21.2723	1.1461
28.7277	3.7024	21.1897	21.2938	5.3178	15.4197	2.8757	21.2372	21.3000	1.7550
34.2209	4.2092	21.2046	21.3027	7.0547	18.1375	3.1096	21.2417	21.3047	2.3746
45.1965	5.2064	21.2173	21.3144	11.0729	20.8723	3.3522	21.2524	21.3136	3.0378

56.4372	6.2319	21.2316	21.3247	15.9074	23.6080	3.6009	21.2677	21.3264	3.7534
12.2014	2.1582	21.2533	21.3372	1.1083	29.0236	4.0360	21.2832	21.3365	5.3265
14.9396	2.4203	21.2707	21.3617	1.7043	34.4882	4.5114	21.2886	21.3416	7.0863
17.6985	2.6855	21.2866	21.3793	2.3053	45.4116	5.4503	21.2928	21.3468	11.1259
20.4444	2.9488	21.2897	21.3812	2.9799	56.6454	6.4661	21.2999	21.3527	15.9655
23.2110	3.2147	21.2889	21.3786	3.6735					
<i>Diffusor direction</i>									
12.3269	2.2203	21.4508	21.5223	0.9338	29.0254	4.0259	21.2506	21.3250	4.6252
15.0550	2.4615	21.4522	21.5252	1.4091	34.4493	4.4620	21.2650	21.3338	6.1950
17.8007	2.7101	21.4396	21.5089	1.9533	45.3301	5.3494	21.2709	21.3408	9.8305
20.5224	2.9416	21.4265	21.4928	2.5089	56.5055	6.3027	21.2887	21.3544	14.3194
23.2612	3.1943	21.4117	21.4812	3.1479	12.0555	1.9955	21.2431	21.3366	0.9285
28.6775	3.6228	21.4046	21.4716	4.5140	14.9919	2.4410	21.2481	21.3399	1.4379
34.1473	4.1017	21.4068	21.4725	6.0758	17.7796	2.7350	21.2537	21.3461	1.9668
45.0841	5.0577	21.3846	21.4526	9.7385	20.5620	3.0305	21.2538	21.3428	2.5523
56.3677	6.0840	21.4063	21.4725	14.2457	23.3460	3.3284	21.2480	21.3378	3.1745
12.8550	2.7939	21.1585	21.2393	1.0021	28.8081	3.8133	21.2556	21.3458	4.5578
15.5516	2.9982	21.1943	21.2781	1.5125	34.3103	4.3214	21.2554	21.3415	6.1505
18.2494	3.2076	21.1898	21.2720	2.0471	45.2502	5.2781	21.2532	21.3435	9.8184
20.9446	3.4141	21.2160	21.2962	2.6281	56.4663	6.2811	21.2578	21.3444	14.3248
23.6260	3.6031	21.2314	21.3093	3.2321					

**Table B.4:** Experimental results obtained on *Si-7* with CO<sub>2</sub> as working gas. Recalculated raw data is shown in Figure 6.3 on page 83. Measurements are performed under isothermal conditions without varying temperature. Units of values are as follows:  $p$  in (kPa);  $\theta$  in ( $^{\circ}$ C);  $\dot{m}$  in ( $\times 10^{-9}$  kg s $^{-1}$ ).

$p_i$	$p_o$	$\theta_i$	$\theta_o$	$\dot{m}$	$p_i$	$p_o$	$\theta_i$	$\theta_o$	$\dot{m}$
<i>Nozzle direction</i>									
23.0926	3.0334	21.5798	21.5960	2.2992	55.4585	5.4977	21.5710	21.6458	10.7700
28.4863	3.4468	21.5882	21.6129	3.3888	66.5719	6.4067	21.5919	21.6633	14.7532
33.8895	3.8690	21.5988	21.6201	4.6011	77.4734	7.3196	21.6054	21.6771	18.7808
44.6758	4.6831	21.6092	21.6311	7.4371	22.8604	2.8453	21.3599	21.4530	2.2937
55.5145	5.5407	21.6220	21.6418	10.7923	28.2511	3.2623	21.3936	21.4781	3.3821
66.6277	6.4257	21.6340	21.6568	14.7781	33.6778	3.6912	21.3988	21.4851	4.6331
77.4741	7.3136	21.6471	21.6694	18.7797	44.4877	4.5145	21.4212	21.4987	7.4964
22.8078	2.8205	21.5288	21.6189	2.2264	55.3387	5.3706	21.4313	21.5168	10.8608
28.2562	3.2796	21.5303	21.6232	3.3267	66.4455	6.2599	21.4528	21.5324	14.8500
33.7165	3.7426	21.5371	21.6270	4.5477	77.3136	7.1505	21.4669	21.5453	18.8058
44.5618	4.5961	21.5441	21.6280	7.4099					
<i>Diffusor direction</i>									
22.7559	2.7899	21.4232	21.4783	1.9840	22.6879	2.6709	21.4469	21.5432	1.9194
22.7923	2.6812	21.4098	21.4731	1.9700	28.0594	3.0579	21.4724	21.5674	2.8638
33.5592	3.4676	21.4462	21.5014	4.0035	33.4416	3.4534	21.4881	21.5768	3.9623
44.3501	4.2795	21.4619	21.5167	6.5776	44.2168	4.2462	21.4991	21.5878	6.5127
55.1564	5.1017	21.4755	21.5283	9.6523	55.0269	5.0623	21.5093	21.5951	9.6012
66.3243	5.9936	21.4960	21.5498	13.3728	66.1025	5.9138	21.5220	21.6065	13.2938
77.1693	6.8628	21.5071	21.5616	17.4175	76.9175	6.7456	21.5363	21.6171	17.3091

**Table B.5:** Experimental results obtained on *Si-9* with various working gases. CO<sub>2</sub> data is shown in Figure 6.1b on page 80 and together with argon data in Figure 6.4 on page 85. Recalculated CO<sub>2</sub> data is shown in Figure 6.2 on page 81 and Figure 6.3 on page 83. Argon and oxygen data are used for calculation of diodicity  $D$  which is plotted in Figure 6.3. Nitrogen data is used to perform the Anderson-Darling test in section 5.2.5. All measurements are performed under isothermal conditions with partially varying temperature. Units of values are as follows:  $p$  in (kPa);  $\theta$  in ( $^{\circ}\text{C}$ );  $\dot{m}$  in ( $\times 10^{-9} \text{ kg s}^{-1}$ ).

$p_i$	$p_o$	$\theta_i$	$\theta_o$	$\dot{m}$	$p_i$	$p_o$	$\theta_i$	$\theta_o$	$\dot{m}$
<i>Argon, nozzle direction</i>									
$\theta_{\text{nom}} = 7^{\circ}\text{C}$									
30.0714	4.8827	6.8696	6.7153	1.2441	35.5802	5.4379	21.4004	21.3237	1.4140
35.2258	5.0757	6.9823	6.8356	1.6872	51.1754	6.0365	21.4153	21.3365	3.0542
50.9246	5.7745	7.0311	6.8890	3.4415	66.8194	6.6934	21.4151	21.3368	5.0404
$\theta_{\text{nom}} = 25^{\circ}\text{C}$									
66.6457	6.4972	7.0478	6.9091	5.5792	30.3764	5.1737	25.9321	25.8861	0.9709
30.1754	4.9848	7.0509	6.9165	1.1276	35.5253	5.3712	26.0947	26.0412	1.3346
35.3607	5.2061	7.0513	6.9195	1.6780	51.1092	5.9721	26.1710	26.1234	2.8974
51.0123	5.8623	7.0589	6.9412	3.4490	66.7351	6.6275	26.2167	26.1681	4.7991
66.7039	6.5489	7.0605	6.9376	5.5817	35.5704	5.4582	26.2557	26.2049	1.2279
30.2020	5.0458	7.0464	6.9259	1.1357	51.1460	6.0433	26.2605	26.2137	2.7988
35.4235	5.2623	7.0349	6.9172	1.7044	66.7774	6.6882	26.2717	26.2206	4.7258
51.0666	5.9059	7.0320	6.9147	3.4838	35.6512	5.5335	26.2742	26.2258	1.1609
66.7716	6.6132	7.0188	6.9072	5.6399	51.2135	6.1149	26.2765	26.2279	2.7696
29.9692	4.8020	7.0165	6.9072	1.1448	66.8417	6.7516	26.2791	26.2309	4.6881
35.1943	5.0318	7.0082	6.9001	1.7133	$\theta_{\text{nom}} = 30^{\circ}\text{C}$				
50.8693	5.6993	7.0072	6.9013	3.4903	30.4238	5.2472	30.6833	30.6042	1.0256
66.5824	6.4315	7.0210	6.8991	5.6272	35.6198	5.4375	30.8869	30.8123	1.3481
$\theta_{\text{nom}} = 15^{\circ}\text{C}$									
30.3139	5.1261	15.3835	15.2809	1.1238	51.1583	6.0191	31.0177	30.9262	2.8755
35.5197	5.3320	15.4385	15.3407	1.6244	66.8013	6.6667	31.0757	30.9893	4.7373
51.1399	5.9567	15.4695	15.3761	3.3075	30.4588	5.3312	31.1029	31.0282	0.7432
66.8097	6.6454	15.4982	15.4039	5.3420	35.6731	5.5239	31.1179	31.0397	1.2346
30.3871	5.2114	15.5061	15.4158	1.0552	51.2270	6.0940	31.1261	31.0513	2.7846
35.5798	5.4176	15.5097	15.4231	1.5608	66.8540	6.7213	31.1219	31.0346	4.6729
51.1904	6.0355	15.5106	15.4226	3.2575	35.4961	5.3500	31.1515	31.0743	1.1091
66.8525	6.7093	15.5004	15.4084	5.3088	51.0621	5.9284	31.1669	31.0900	2.6275
30.4885	5.3386	15.4770	15.3896	1.0539	66.6951	6.5755	31.1805	31.0976	4.4917
35.6962	5.5390	15.4868	15.4012	1.5655	35.3971	5.2496	31.1160	31.0376	1.1648
51.2791	6.1439	15.5003	15.4154	3.2532	50.9907	5.8440	31.1139	31.0346	2.7476
66.9546	6.8078	15.5349	15.4300	5.2924	66.6583	6.5239	31.1076	31.0260	4.6180
$\theta_{\text{nom}} = 21^{\circ}\text{C}$									
30.1904	5.0312	21.3456	21.2717	0.9652	51.0768	5.9614	31.1139	31.0403	2.6680
35.3853	5.2374	21.3369	21.2555	1.4762	66.7025	6.5902	31.1252	31.0535	4.4965
51.0070	5.8558	21.3600	21.2846	3.1418	35.5674	5.4483	31.1201	31.0333	1.0511
66.6763	6.5328	21.3637	21.2853	5.1411	51.1339	6.0272	31.1133	31.0327	2.6215
30.3631	5.2138	21.3887	21.3100	0.8992	66.7634	6.6580	31.1281	31.0556	4.4768
35.5746	5.4152	21.3886	21.3093	1.4301	30.3099	5.1149	30.7531	30.6870	0.8859
51.1644	6.0210	21.3921	21.3126	3.0962	35.4516	5.3100	30.9292	30.8604	1.2587
66.8113	6.6822	21.3972	21.3196	5.0762	51.0385	5.8944	31.0281	30.9460	2.7632
30.3960	5.2381	21.3957	21.3200	0.9049	66.6630	6.5331	31.0680	30.9945	4.6139
<i>Argon, diffusor direction</i>									
$\theta_{\text{nom}} = 7^{\circ}\text{C}$									
35.3732	5.2178	6.8920	6.9293	1.6460	140.4622	100.4562	21.4543	21.3897	7.4088
50.9364	5.8029	6.9432	6.9801	3.2213	30.1332	4.9899	21.4640	21.4079	0.7269
66.5934	6.4644	6.9667	7.0216	5.2010	35.3066	5.1732	21.4760	21.4260	1.1616
29.9963	4.8509	7.0044	7.0550	1.0115	50.8728	5.7372	21.4743	21.4152	2.6499
					66.4803	6.3628	21.4705	21.4116	4.4660



29.3329	4.2692	21.3275	21.3264	1.6568	50.3245	20.3309	21.3275	21.3264	3.4908
49.9646	4.9359	21.3200	21.3197	4.5715	65.5269	20.5428	21.3266	21.3263	6.2062
21.6403	4.0558	21.3266	21.3263	0.8217	80.7506	20.7918	21.3200	21.3197	9.5400
19.0879	4.0000	21.3140	21.3147	0.5657	45.4156	20.4252	21.3140	21.3147	2.8054
27.1951	4.2265	21.2993	21.2995	1.4693	50.4785	20.4888	21.3068	21.3049	3.6271
20.3790	5.2505	21.3068	21.3049	0.6600	65.6736	20.6897	21.2994	21.2960	6.3301
22.9454	5.3186	21.2994	21.2960	0.9187	80.8933	20.9259	21.3200	21.3197	9.6243
30.6260	5.5182	21.2925	21.2891	1.7587	45.1616	20.1764	21.3140	21.3147	2.6663
35.7663	5.6729	21.2759	21.2666	2.4115	50.2330	20.2421	21.3263	21.3140	3.4554
51.2557	6.1656	21.6058	21.4419	4.7019	65.4008	20.4269	21.3147	21.2993	6.1371
66.8040	6.7306	21.6070	21.4442	7.5346	80.6133	20.6513	21.2995	21.2995	9.3774
20.4551	5.3461	21.6077	21.4424	0.6531	45.5918	20.5885	21.3049	21.3049	2.7868
23.0263	5.4107	21.5909	21.4307	0.9071	50.6409	20.6463	21.3266	21.3263	3.6103
30.7091	5.6112	21.5832	21.4238	1.7557	65.8184	20.8400	21.3140	21.3147	6.3434
35.8521	5.7619	21.5543	21.4002	2.4070	81.0333	21.0645	21.2993	21.2995	9.6807

*Carbon dioxide, diffusor direction*

18.4235	3.4357	21.6018	21.4377	0.4621	55.7546	10.6585	21.3200	21.3197	4.7946
21.0362	3.5320	21.6033	21.4388	0.6916	71.0789	11.0029	21.2994	21.2960	7.6249
28.8101	3.8181	21.6057	21.4418	1.4545	35.8067	10.6684	21.3275	21.3264	1.9365
34.0148	4.0369	21.6083	21.4475	2.0494	40.9101	10.7557	21.3200	21.3197	2.6010
49.6664	4.6918	21.6073	21.4434	4.1567	56.1518	11.0251	21.3266	21.3263	4.9146
65.4129	5.4379	21.6105	21.4465	6.8421	71.4793	11.3576	21.3200	21.3197	7.7399
18.7775	3.7217	21.6058	21.4419	0.4234	35.5245	10.4152	21.3266	21.3263	1.8435
21.3565	3.8048	21.6070	21.4442	0.6399	40.6100	10.4985	21.3140	21.3147	2.5023
29.0838	4.0486	21.6057	21.4418	1.3806	55.8739	10.7771	21.2993	21.2995	4.7991
34.2556	4.2377	21.6083	21.4475	1.9677	71.1889	11.1180	21.3068	21.3049	7.6338
49.8445	4.8369	21.3275	21.3264	4.0758	35.7844	10.6954	21.2994	21.2960	1.8575
65.5176	5.5150	21.3200	21.3197	6.7587	40.9273	10.8527	21.3275	21.3264	2.5184
50.0073	4.9976	21.3266	21.3263	4.1085	56.2821	11.2273	21.3200	21.3197	4.8535
34.5655	4.5211	21.5389	21.3884	2.0120	71.7403	11.7069	21.3266	21.3263	7.7055
29.4520	4.3998	21.6018	21.4377	1.4407	34.8702	19.8814	21.3140	21.3147	1.3426
21.7868	4.2208	21.6033	21.4388	0.6896	37.4562	19.9399	21.2993	21.2995	1.5461
19.2479	4.1753	21.6057	21.4418	0.4703	45.0376	20.0554	21.3068	21.3049	2.5105
18.7588	3.6819	21.6083	21.4475	0.4390	50.1577	20.1710	21.2994	21.3275	3.2893
21.2980	3.7326	21.6073	21.4434	0.6519	65.4039	20.4294	21.3264	21.3200	5.9565
20.4084	5.3045	21.6105	21.4465	0.5701	80.7375	20.7657	21.3197	21.3266	9.1247
22.9640	5.3627	21.6077	21.4419	0.8087	34.9605	19.9485	21.3263	21.3140	1.3522
30.6299	5.5405	21.6070	21.4442	1.5936	37.4735	19.9694	21.3147	21.2993	1.4789
35.7572	5.6775	21.6058	21.4424	2.1853	45.0239	20.0388	21.2995	21.3068	2.7203
51.1933	6.1311	21.5909	21.4307	4.3162	50.0828	20.0980	21.3049	21.2994	3.2936
66.7109	6.6669	21.5832	21.4238	7.0063	65.2510	20.2793	21.2960	21.2925	5.9482
20.5332	5.4409	21.5543	21.4002	0.5598	80.4647	20.4958	21.2891	21.2759	9.0902
23.0874	5.5005	21.3275	21.3264	0.7971	35.5354	20.5494	21.6077	21.4424	1.3673
30.7487	5.6751	21.3200	21.3197	1.5688	38.0801	20.5741	21.5909	21.4307	1.5083
35.8779	5.8133	21.3263	21.3140	2.1781	45.6289	20.6477	21.3275	21.3264	2.5724
51.2919	6.2402	21.3147	21.2993	4.3107	50.6804	20.7026	21.3266	21.3263	3.3440
66.7975	6.7587	21.2995	21.3068	7.0063	65.8697	20.8902	21.3200	21.3197	6.0261
20.4587	5.3578	21.3275	21.3264	0.5719	81.0910	21.1118	21.3140	21.3147	9.2024
23.0083	5.4146	21.3266	21.3263	0.8067	35.0140	20.0447	21.3068	21.3049	1.3276
30.6761	5.5936	21.3200	21.3197	1.5953	37.5400	20.0646	21.2994	21.2960	1.4552
35.8018	5.7298	21.5832	21.4238	2.1914	45.1217	20.1407	21.3200	21.3197	2.7156
51.2323	6.1804	21.5543	21.4002	4.3236	50.1883	20.1996	21.3140	21.3147	3.2895
66.7467	6.7120	21.5299	21.3782	7.0199	65.3500	20.3769	21.3263	21.3140	5.9590
35.4255	10.2958	21.2994	21.2960	1.8485	80.5704	20.5979	21.3147	21.2993	9.1230
40.4861	10.3759	21.3275	21.3264	2.5110					

*Nitrogen, nozzle direction*

33.1048	8.1172	21.1982	21.1851	1.6015	135.2949	110.2890	21.3667	21.3352	4.1995
38.2581	8.2657	21.2067	21.1930	2.0693	140.3272	110.3268	21.3644	21.3320	5.2363
53.6911	8.7107	21.2019	21.1839	3.6384	155.4005	110.4142	21.3640	21.3321	8.4748
69.2157	9.2322	21.2118	21.1968	5.4376	170.7139	110.5168	21.3679	21.3327	12.0221
17.9339	7.9374	21.3144	21.3141	0.2819	135.4341	110.4362	21.3396	21.3129	4.2220
20.4570	7.9842	21.3401	21.3424	0.4558	140.4577	110.4677	21.3549	21.3251	5.2403
23.0171	8.0427	21.3772	21.3763	0.6599	155.5494	110.5589	21.3593	21.3278	8.4951
25.6054	8.1055	21.4053	21.4094	0.8756	170.8571	110.6626	21.3632	21.3313	12.0420
33.2454	8.2721	21.4024	21.4006	1.5702	130.1826	100.1629	21.3809	21.3311	4.8905
38.3774	8.4073	21.4249	21.4215	2.0801	140.2374	100.2267	21.3852	21.3339	6.9025
53.8257	8.8243	21.4434	21.4395	3.7792	150.3088	100.3028	21.3872	21.3372	9.0171
69.3082	9.3260	21.4463	21.4412	5.6925	130.2820	100.2576	21.3902	21.3407	4.8733
17.8695	7.8625	21.4358	21.4403	0.2548	140.3358	100.3236	21.3987	21.3462	6.8939
20.4084	7.9189	21.4449	21.4465	0.4246	150.4021	100.3963	21.3987	21.3485	9.0115
22.9672	7.9841	21.4535	21.4527	0.5795	29.5699	4.4984	21.1277	21.0659	1.2436
25.5377	8.0482	21.4706	21.4738	0.7568	34.7282	4.6813	21.2220	21.1572	1.7839
33.2380	8.2377	21.4805	21.4809	1.3454	50.3395	5.3109	21.3053	21.2448	3.4142
38.3497	8.3803	21.4814	21.4830	1.7754	66.0422	6.0292	21.3581	21.3043	5.2191
53.8034	8.8179	21.4835	21.4828	3.2809	29.6771	4.6034	21.4285	21.3774	1.0516
20.1290	7.6200	21.5003	21.4990	0.3489	34.8707	4.8194	21.4277	21.3721	1.4503
22.6667	7.6901	21.4920	21.4908	0.5179	29.5411	4.4723	21.4011	21.3498	1.0589
25.2450	7.7655	21.4890	21.4890	0.7042	34.7543	4.6874	21.4127	21.3556	1.4801
25.7333	8.2382	21.4621	21.4622	0.7095	29.5751	4.4864	21.4341	21.3800	1.0102
23.2038	8.2197	21.4644	21.4643	0.5310	34.7932	4.7041	21.4351	21.3799	1.4311
20.6880	8.2034	21.4616	21.4582	0.3661					

*Nitrogen, diffusor direction*

15.2877	7.7986	21.1885	21.1775	0.1470	26.1182	8.5772	21.1867	21.1648	0.8330
17.8603	7.8408	21.1854	21.1724	0.2817	23.6006	8.5661	21.2065	21.1832	0.6586
20.3900	7.8884	21.1702	21.1555	0.4461	21.1191	8.5554	21.2031	21.1788	0.5158
22.9287	7.9400	21.1620	21.1487	0.6377	18.6041	8.5390	21.1735	21.1509	0.3795
25.4954	7.9961	21.1703	21.1605	0.8293	16.1058	8.5212	21.1455	21.1187	0.2460
33.1558	8.1479	21.1732	21.1556	1.4396	18.6368	8.5675	21.1417	21.1177	0.3925
38.3039	8.2891	21.1382	21.1162	1.9368	21.1862	8.6225	21.1400	21.1116	0.5370
53.6708	8.6625	21.1689	21.1468	3.5145	23.7468	8.6771	21.1362	21.1067	0.7017
69.1472	9.1302	21.1774	21.1567	5.3004	26.2839	8.7402	21.1355	21.1065	0.8592
15.1648	7.6642	21.1682	21.1515	0.1602	33.9497	8.8977	21.1369	21.1060	1.3937
17.6959	7.7098	21.1602	21.1423	0.3092	39.0611	9.0286	21.1383	21.1102	1.7771
20.2648	7.7664	21.1611	21.1391	0.4518	54.4466	9.4071	21.1321	21.1016	3.1437
22.8120	7.8210	21.1528	21.1356	0.6203	17.7471	7.7436	21.4277	21.4188	0.1922
25.3731	7.8814	21.1640	21.1463	0.7687	20.2937	7.7992	21.4509	21.4421	0.3506
33.0269	8.0449	21.1755	21.1580	1.2987	22.8529	7.8606	21.4537	21.4477	0.5006
38.1880	8.1820	21.1689	21.1504	1.6982	25.4094	7.9184	21.4596	21.4533	0.6626
53.5921	8.5807	21.1717	21.1519	3.0413	33.0865	8.0912	21.4498	21.4445	1.1939
15.2691	7.7685	21.1594	21.1452	0.1514	38.2285	8.2274	21.4674	21.4598	1.5681
17.8345	7.8297	21.1556	21.1396	0.2870	130.1411	100.1528	21.4031	21.3713	4.7898
20.4012	7.8946	21.1504	21.1339	0.4296	140.2939	100.3165	21.4091	21.3769	6.7837
22.9752	7.9675	21.1435	21.1264	0.5751	150.4839	100.5064	21.4142	21.3772	8.8753
25.5300	8.0406	21.1451	21.1303	0.7396	135.3281	110.3366	21.4114	21.3736	4.0990
33.2272	8.2318	21.1332	21.1176	1.2624	140.4911	110.5038	21.4025	21.3626	5.1356
38.3718	8.3873	21.1316	21.1167	1.6526	155.7105	110.7307	21.4139	21.3738	8.3266
53.8246	8.8228	21.1278	21.1096	2.9972	171.3572	111.1771	21.4157	21.3718	11.8486
25.3819	7.8121	21.1189	21.0955	0.8285	136.1557	111.1756	21.3819	21.3474	4.1614
33.0472	7.9846	21.1111	21.0921	1.3354	141.2070	111.2275	21.3852	21.3469	5.1752
38.1687	8.1181	21.0972	21.0774	1.7098	156.3220	111.3394	21.3855	21.3472	8.3979
53.5652	8.5248	21.1044	21.0828	3.0358	171.6665	111.4771	21.3934	21.3555	11.9012
53.7057	8.7305	21.1991	21.1736	3.6295	130.3559	100.3475	21.2842	21.2480	4.8547
69.1757	9.2021	21.1987	21.1767	5.4138	140.4137	100.4118	21.2833	21.2498	6.8415

53.8955	8.9069	21.1852	21.1583	3.4756	150.4746	100.4838	21.2981	21.2634	8.9530
38.6368	8.6412	21.1718	21.1455	1.9487	135.5656	110.5722	21.3932	21.3591	4.1810
33.5928	8.5909	21.1475	21.1205	1.5303	140.5986	110.6057	21.3945	21.3595	5.1958
23.0925	8.0674	21.1723	21.1482	0.6713	155.6877	110.7001	21.3958	21.3612	8.4050
25.6391	8.1294	21.1789	21.1548	0.8326	171.0070	110.8046	21.3987	21.3618	11.9069
33.3072	8.2993	21.1698	21.1463	1.3497	29.5342	4.3564	21.1275	21.0451	0.9654
38.4388	8.4365	21.1837	21.1574	1.7360	34.7206	4.5616	21.2274	21.1451	1.3075
53.8414	8.8390	21.1848	21.1606	3.0693	29.7320	4.6091	21.3949	21.3329	0.9667
38.9903	8.9471	21.0754	21.0456	1.8875	34.9376	4.8099	21.3821	21.3186	1.3010
54.3446	9.3275	21.0899	21.0554	3.2482	29.6416	4.5048	21.4073	21.3480	0.8891
69.7891	9.7846	21.1122	21.0805	4.8804	34.7924	4.7001	21.4082	21.3493	1.2529
54.0069	9.0014	21.1930	21.1675	3.0680	29.7258	4.6048	21.4041	21.3438	0.8789
38.7603	8.7269	21.1883	21.1618	1.7452	34.9183	4.8000	21.4064	21.3443	1.2560
33.6948	8.6731	21.1754	21.1537	1.3504					
<i>Oxygen, nozzle direction</i>									
30.1390	4.9748	21.3409	21.2627	1.0998	51.0438	5.9026	21.3378	21.2626	3.1028
35.3388	5.1820	21.3532	21.2814	1.5774	65.5994	5.8650	21.3403	21.2632	4.8769
50.9463	5.8093	21.3613	21.2879	3.0726	30.1139	4.9573	21.3433	21.2700	1.1532
66.1183	5.9890	21.3650	21.2911	4.8677	35.3229	5.1682	21.3435	21.2720	1.5926
30.2365	5.0836	21.3568	21.2868	1.1682	50.9336	5.7933	21.3415	21.2681	3.0824
35.4383	5.2896	21.3468	21.2756	1.6145	66.6136	6.4747	21.3446	21.2723	4.8521
<i>Oxygen, diffuser direction</i>									
35.0539	4.8893	21.1732	21.1054	1.4318	35.1453	5.0349	21.4327	21.3774	1.2678
50.6320	5.5003	21.2753	21.2048	2.7313	50.7251	5.6194	21.4462	21.3895	2.6108
66.3200	6.1793	21.3298	21.2725	4.3427	66.3519	6.2643	21.4485	21.3955	4.2397
29.9995	4.8339	21.3634	21.3088	0.9829	29.9162	4.7654	21.1928	21.1287	0.9829
35.1655	5.0283	21.3818	21.3266	1.3760	35.0615	4.9595	21.3467	21.3014	1.3058
50.7383	5.6090	21.4013	21.3459	2.6859	50.6318	5.5438	21.4216	21.3762	2.6200
66.3854	6.2595	21.4231	21.3701	4.3043	66.2711	6.1970	21.4696	21.4194	4.2149
30.0654	4.9458	21.4247	21.3716	0.9431	30.0002	4.8923	21.5065	21.4683	0.8628
35.2554	5.1358	21.4252	21.3709	1.3244	35.1909	5.0864	21.5268	21.4826	1.2482
50.8353	5.7093	21.4334	21.3794	2.6567	50.7519	5.6645	21.5438	21.4939	2.5679
66.4568	6.3479	21.4360	21.3792	4.2735	66.3725	6.3082	21.5738	21.5189	4.1692
29.9675	4.8382	21.4308	21.3759	0.8623					

**Table B.6:** Experimental results obtained on silanized *Si-9* with carbon dioxide and argon as working gases. Data is plotted in Figure 6.4 on page 85. Measurements are performed under isothermal conditions without varying temperature. Units of values are as follows:  $p$  in (kPa);  $\theta$  in ( $^{\circ}\text{C}$ );  $\dot{m}$  in ( $\times 10^{-9} \text{ kg s}^{-1}$ ).

$p_i$	$p_o$	$\theta_i$	$\theta_o$	$\dot{m}$	$p_i$	$p_o$	$\theta_i$	$\theta_o$	$\dot{m}$
<i>Argon, nozzle direction</i>									
36.6080	6.4500	20.9301	20.7964	2.7862	93.9851	53.8190	20.9752	20.8332	7.5806
46.9584	6.8100	20.9263	20.7949	4.3341	104.0903	53.9599	20.9721	20.8262	10.1952
57.3554	7.1920	20.9259	20.7910	6.0995	114.2596	54.1308	20.9792	20.8292	12.9892
67.7526	7.6060	20.9248	20.7922	8.0329	104.6336	54.4922	20.9696	20.8240	10.2480
40.1900	10.0449	20.9489	20.8110	2.7725	94.9073	54.7619	20.9572	20.8152	7.6752
50.4484	10.2890	20.9465	20.8104	4.4090	85.1213	54.9696	20.9577	20.8158	5.2796
60.7016	10.5575	20.9464	20.8113	6.2382	95.2532	55.1045	20.9541	20.8103	7.6879
71.0082	10.8643	20.9492	20.8121	8.2296	105.3835	55.2474	20.9579	20.8131	10.3038
45.1730	15.0161	20.9506	20.8127	3.0330	115.5589	55.4190	20.9667	20.8232	13.1391
55.3626	15.2005	20.9521	20.8163	4.7613	34.3044	4.1392	20.9893	20.8541	2.3874
65.5737	15.4109	20.9527	20.8151	6.6008	44.8109	4.6336	20.9906	20.8549	3.9031

75.7939	15.6488	20.9543	20.8183	8.7113	55.2979	5.1425	20.9932	20.8576	5.6088
55.0710	24.9203	20.9504	20.8141	3.5674	65.8238	5.6687	20.9950	20.8576	7.5316
65.2220	25.0581	20.9552	20.8207	5.4535	130.4070	100.3948	21.4536	21.3881	7.1754
75.3640	25.2179	20.9627	20.8243	7.5400	140.4622	100.4562	21.4543	21.3897	10.3723
85.5378	25.3957	20.9642	20.8234	9.8193	150.5220	100.5275	21.4594	21.3875	13.8197
70.2190	40.0519	20.9734	20.8323	4.4142	120.4584	100.4462	21.4639	21.3958	5.6745
80.3199	40.1650	20.9725	20.8314	6.5503	28.1969	4.0331	20.9809	20.8447	1.5486
90.4339	40.3033	20.9756	20.8321	8.8772	38.6489	4.4903	20.9770	20.8420	2.9297
100.5837	40.4495	20.9670	20.8233	11.4299	49.1237	4.9751	20.9882	20.8494	4.5293
83.8392	53.6988	20.9798	20.8369	5.1677	59.6250	5.4785	20.9905	20.8510	6.3202

*Argon, diffusor direction*

35.8810	3.7163	21.0398	20.8839	2.1661	71.1840	11.0233	21.0141	20.8570	7.3148
46.3742	4.2164	21.0354	20.8741	3.6122	49.6663	19.5090	21.0197	20.8700	2.9605
56.8927	4.7278	21.0321	20.8709	5.2158	59.8238	19.6594	21.0240	20.8690	4.5846
67.3994	5.2473	21.0276	20.8650	6.9472	69.9997	19.8206	21.0259	20.8698	6.4369
54.9583	4.7973	21.0046	20.8436	4.8707	80.1769	20.0160	21.0315	20.8743	8.4334
44.6213	4.4506	20.9842	20.8241	3.3819	73.1796	43.0355	21.0256	20.8704	4.3548
34.2901	4.1183	20.9644	20.8067	2.0576	83.2875	43.1340	21.0321	20.8743	6.4564
49.9346	4.7797	20.9590	20.7985	4.1273	93.4204	43.2590	21.0378	20.8789	8.7691
60.4219	5.2595	20.9650	20.8043	5.8026	103.5502	43.4045	21.0379	20.8753	11.2385
66.7292	5.5701	20.9784	20.8175	6.9013	26.7308	6.5479	21.0308	20.8815	1.0014
130.2480	100.2331	21.4482	21.4026	7.6279	36.9716	6.8083	21.0363	20.8852	2.1527
140.3103	100.3046	21.4528	21.4028	11.3027	47.2889	7.1108	21.0424	20.8927	3.5491
150.3732	100.3790	21.4512	21.3946	15.2135	57.6183	7.4470	21.0429	20.8912	5.1200
130.3123	100.3116	21.4406	21.3935	7.9408	50.5642	7.4092	21.0205	20.8696	3.9971
140.3747	100.3775	21.4465	21.3975	11.5604	40.4349	7.2640	20.9986	20.8468	2.6084
150.4543	100.4546	21.4485	21.3943	15.3384	30.2915	7.1157	20.9934	20.8412	1.3603
35.9493	5.7657	20.9908	20.8327	2.1419	52.8792	7.7187	21.0118	20.8544	4.3629
46.2735	6.1007	20.9878	20.8270	3.4844	60.1176	7.9598	21.0160	20.8619	5.5503
56.6428	6.4767	20.9929	20.8328	5.0363	67.3730	8.2248	21.0156	20.8624	6.8152
67.0431	6.8852	20.9937	20.8326	6.8083	29.5460	4.3567	21.0454	20.8816	1.5060
40.4152	10.2448	21.0001	20.8445	2.4238	39.9192	4.7537	21.0502	20.8920	2.7644
50.6425	10.4715	21.0098	20.8520	3.8473	50.3528	5.1904	21.0397	20.8818	4.2271
60.8926	10.7295	21.0101	20.8542	5.4634					

*Carbon dioxide, nozzle direction*

34.1379	4.0391	21.1989	20.7368	2.6323	40.6102	10.5191	21.1796	20.7295	3.0594
44.5480	4.4604	21.1845	20.7184	4.1286	50.8051	10.7198	21.1728	20.7169	4.6965
55.0228	4.9251	21.1600	20.6906	5.8449	61.0402	10.9597	21.1799	20.7263	6.5300
65.4835	5.4100	21.1457	20.6759	7.8219	71.2930	11.2311	21.1940	20.7399	8.5974
34.2576	4.1534	21.1439	20.6768	2.6396	40.4209	10.3689	21.2034	21.0652	2.8686
44.6620	4.5761	21.1513	20.6878	4.1315	50.6115	10.5682	21.1768	21.0350	4.4778
55.1057	5.0290	21.1760	20.7135	5.8389	60.8426	10.8043	21.1654	21.0194	6.3243
65.5784	5.5148	21.2066	20.7471	7.8193	71.1140	11.0790	21.1485	21.0142	8.4026
34.0187	3.9457	21.0238	20.8676	2.5580	50.3247	20.2444	21.2123	20.7589	3.7248
44.4469	4.3870	21.0242	20.8634	4.0231	60.4652	20.3908	21.2194	20.7663	5.5562
54.9160	4.8631	21.0538	20.8901	5.7411	70.6362	20.5647	21.2281	20.7723	7.5810
65.4020	5.3602	21.0656	20.9202	7.7040	80.8163	20.7580	21.2371	20.7798	9.8480
55.1570	5.1269	21.1879	21.0484	5.6786	50.5262	20.4451	21.2318	20.7672	3.7050
44.9130	4.8879	21.2389	21.1045	3.9376	60.6669	20.5884	21.2323	20.7677	5.5394
34.6807	4.6574	21.2659	21.1347	2.4362	70.8163	20.7552	21.2346	20.7789	7.5872
45.0741	5.0622	21.2767	21.1430	3.9142	81.0157	20.8865	21.0422	20.5930	10.1101
55.4995	5.4919	21.2849	21.1460	5.6407	50.2201	20.1541	21.1446	21.0000	3.5766
65.9465	5.9531	21.2702	21.1306	7.5920	60.3508	20.2980	21.1392	20.9941	5.4071
35.7285	5.6408	21.2289	20.7699	2.7192	70.5013	20.4564	21.1392	20.9939	7.4670
46.0517	5.9732	21.2325	20.7711	4.2178	80.6890	20.6529	21.1442	21.0069	9.7220
56.4241	6.3532	21.2439	20.7797	5.9687	120.0583	89.9810	21.2581	20.7613	8.5581

66.8285	6.7666	21.2534	20.7928	7.9477	130.1882	90.1194	21.2704	20.7799	11.9392
35.8565	5.7690	21.2390	20.7785	2.6881	140.6144	90.2674	21.2832	20.7901	15.6415
46.1665	6.0867	21.2360	20.7732	4.2221	151.1856	90.8512	21.3045	20.8140	18.8631
56.5107	6.4388	21.2302	20.7707	5.9788	142.2235	91.8845	21.2804	20.7950	15.8316
67.0012	6.9334	21.2011	20.7424	8.0070	132.4397	92.3844	21.2591	20.7766	12.1483
56.9928	6.9147	21.1642	20.7032	6.0676	132.6667	92.6052	21.2645	20.7803	12.1654
46.8763	6.7920	21.1574	20.6982	4.3097	143.0576	92.7205	21.2598	20.7794	15.9137
46.9525	6.8656	21.1519	20.6913	4.3154	153.1826	92.8537	21.2686	20.7869	18.8748
57.2627	7.1845	21.1498	20.6896	6.0908	120.0543	90.0167	21.1486	21.0073	8.4212
67.6031	7.5345	21.1545	20.6937	8.0856	130.1791	90.1520	21.1535	21.0109	11.8386
35.6726	5.6122	21.1450	21.0044	2.5557	140.7411	90.4353	21.1522	21.0166	15.4959
46.0094	5.9511	21.1388	20.9946	4.0737	150.9426	90.7225	21.1344	20.9957	18.8402
56.3704	6.3250	21.1301	20.9965	5.8297	141.8029	91.5731	21.0956	20.9560	15.6232
66.7747	6.7432	21.1678	21.0475	7.8029	132.1538	92.1241	21.0746	20.9322	12.0077
40.4262	10.3360	21.1756	20.7238	3.0617	122.6018	92.5668	21.0911	20.9493	8.6021
50.6321	10.5558	21.1762	20.7261	4.6595	132.8287	92.8107	21.1634	21.0327	12.0175
60.8825	10.8119	21.1737	20.7206	6.5084	143.3006	93.0358	21.2056	21.0758	15.7934
71.1697	11.1074	21.1771	20.7213	8.5734	153.4735	93.2860	21.2488	21.1182	18.8660

*Carbon dioxide, diffusor direction*

34.2538	4.0674	21.0947	20.6882	2.2830	40.4980	10.3986	20.8830	20.7646	2.8564
44.6248	4.4556	21.0911	20.6861	3.6654	50.6796	10.5923	20.9021	20.7788	4.3282
55.0463	4.8957	21.0908	20.6840	5.2770	60.8980	10.8200	20.9220	20.7934	6.0625
65.5272	5.3825	21.1510	20.7636	7.0856	71.1522	11.0831	20.9499	20.8188	8.0154
34.0947	4.0032	20.9418	20.7916	2.3039	50.3380	20.2071	21.1908	20.8109	3.5424
44.4869	4.4020	20.9657	20.8193	3.6335	60.5029	20.3687	21.1875	20.8115	5.2718
54.9094	4.8422	20.9973	20.8496	5.2089	70.6401	20.5089	21.1824	20.8011	7.2140
65.3689	5.3139	21.0030	20.8539	7.0510	80.9538	20.8422	21.1919	20.8127	9.4011
55.1532	5.0894	20.9691	20.8230	5.2426	71.2700	21.1828	21.2078	20.8295	7.2782
44.9461	4.8678	20.9531	20.8115	3.6801	61.4058	21.3129	21.1884	20.8104	5.3648
34.7470	4.6575	20.9263	20.7933	2.3419	61.5089	21.4114	21.1901	20.8116	5.3785
45.1018	5.0209	20.9174	20.7863	3.6932	71.6343	21.5537	21.1914	20.8142	7.3486
55.4817	5.4144	20.9147	20.7818	5.3139	81.7294	21.6467	21.1866	20.8070	9.5282
65.9107	5.8501	20.9075	20.7736	7.1705	50.3327	20.2491	20.9148	20.7819	3.5983
35.9044	5.7304	21.3191	20.9407	2.3305	60.4559	20.3863	20.9465	20.8135	5.3079
46.1896	6.0372	21.3557	20.9783	3.7698	70.6168	20.5553	20.9733	20.8422	7.2216
56.5359	6.4049	21.3791	21.0000	5.4158	80.8016	20.7409	20.9961	20.8596	9.3871
66.9483	6.8216	21.3883	21.0129	7.2633	119.8687	89.7883	21.1889	20.8028	8.5114
35.7811	5.6868	21.4190	21.0570	2.1801	129.9279	89.8593	21.1895	20.8021	11.8425
46.0744	5.9910	21.3440	20.9623	3.6322	140.3162	89.9620	21.1940	20.8090	15.5084
56.4391	6.3577	21.2782	20.9005	5.3058	150.4480	90.0962	21.1991	20.8091	18.8387
66.8449	6.7686	21.2452	20.8637	7.2099	120.1902	90.1082	21.1553	20.7698	8.5410
35.7363	5.6224	20.6979	20.5812	2.5567	130.2820	90.2120	21.1442	20.7605	11.8813
46.0273	5.9270	20.7193	20.5996	3.9468	140.7164	90.3514	21.1426	20.7559	15.5670
56.3674	6.2761	20.7548	20.6321	5.5575	150.8749	90.5194	21.1450	20.7571	18.8582
66.7551	6.6713	20.8194	20.6984	7.4039	120.1498	90.0748	21.1475	20.7648	8.5095
40.5503	10.4429	21.2254	20.8492	2.7701	130.2714	90.1945	21.1479	20.7571	11.8692
50.7456	10.6371	21.2143	20.8356	4.2660	140.6918	90.3251	21.1468	20.7558	15.5220
60.9670	10.8620	21.2154	20.8329	5.9871	150.8559	90.4994	21.1498	20.7603	18.8474
71.2438	11.1263	21.2089	20.8285	7.9567	71.2082	11.0896	21.1831	20.8035	7.8798
40.5317	10.4190	21.1959	20.8202	2.6024	60.9650	10.8323	21.1881	20.8075	5.8984
50.7443	10.6120	21.1947	20.8149	4.1353					